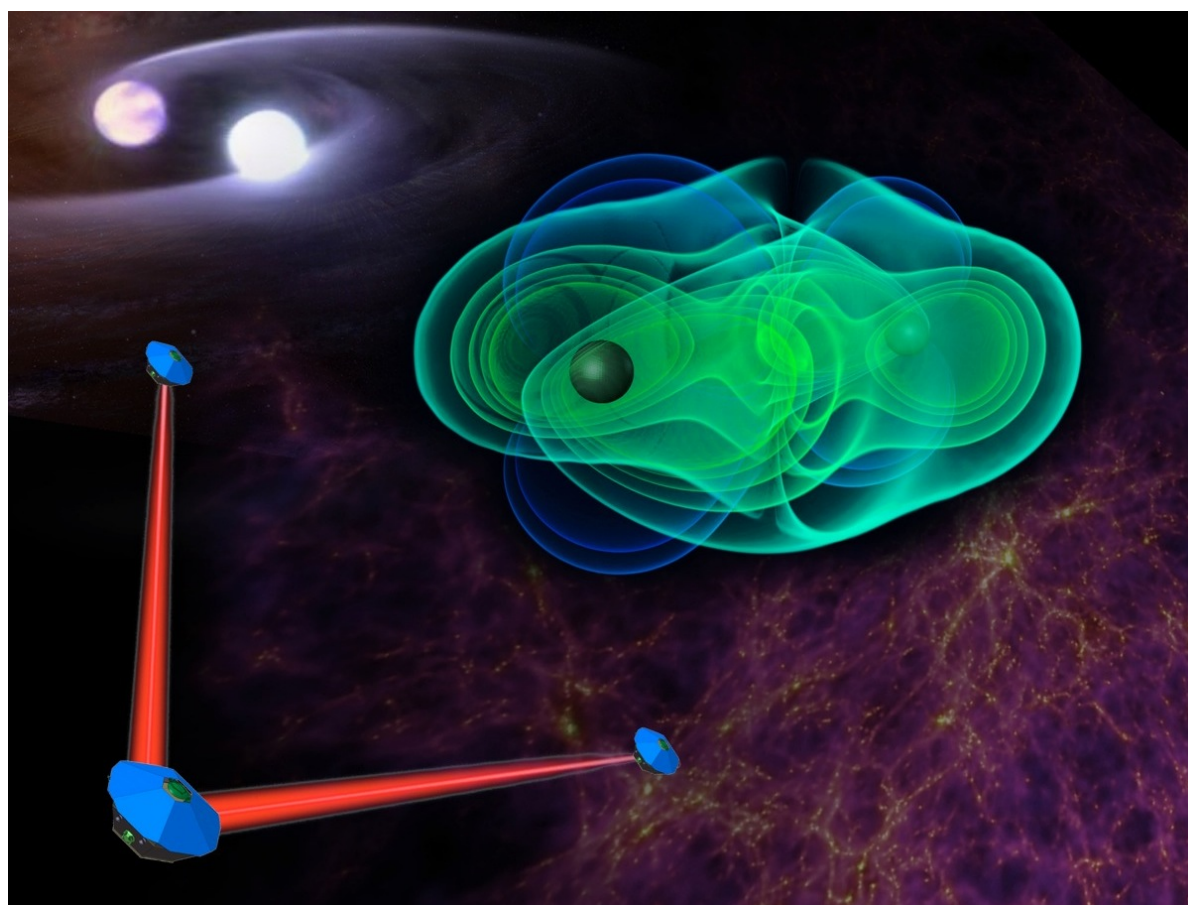


NGO

Revealing a hidden Universe: opening a new chapter of discovery



Assessment Study Report

The electronic version of this document contains hyperlinks that are indicated by color. [Internal links](#) refer to content *within* this document, [external links](#) refer to content *outside* this document and require a connection to the internet.

The picture on the front page was made using the following material

- Numerical simulation of merging black holes
 - Numerical simulation: C. Reisswig, L. Rezzolla (Max Planck Institute for Gravitational Physics (Albert Einstein Institute))
 - Scientific visualisation: M. Koppitz (Zuse Institute Berlin)
- Millenium Simulation Project (SPRINGEL ET AL., 2005)
- White Dwarf Star Spiral (NASA/Tod Strohmayer (GSFC)/Dana Berry (Chandra X-Ray Observatory))
- NGO spacecraft rendering: EADS Astrium

NGO Mission Description

Science Objectives

Through the detection and observation of gravitational waves

- Survey compact stellar-mass binaries and study the structure of the Galaxy
 - Trace the formation, growth, and merger history of massive black holes
 - Explore stellar populations and dynamics in galactic nuclei
 - Confront General Relativity with observations
 - Probe new physics and cosmology
-

Event Rates and Event Numbers

Frequency band	1×10^{-4} Hz to 1 Hz, (3×10^{-5} Hz to 1 Hz as a goal)
Massive black hole mergers	10 yr^{-1} to 100 yr^{-1}
Extreme mass ratio inspirals	10 yr^{-1} to 20 yr^{-1}
Galactic Binaries	~ 3000 resolvable out of a total of $\sim 30 \times 10^6$ in the NGO band

Mission

Duration	2 years science orbit, (~ 4 years including transfer and commissioning)
Orbits	Three drag-free satellites in heliocentric orbits,
Spacecraft bus	Provides power, communication, and AOCS on science orbit. Micronewton propulsion system, magnetically and gravitationally controlled design, power supply from solar cells
AOCS	Derived from test mass position and received laser, star tracker as backup
<i>Pointing</i>	Spacecraft attitude jitter $< 10 \text{ nrad}/\sqrt{\text{Hz}}$
<i>S/C</i>	Mass (three spacecraft incl. payload): 865 kg
<i>Power</i>	Science mode: 493 W
Propulsion module	Used during transfer, chemical propulsion
<i>Mass</i>	Dry mass (three modules): 1509 kg
<i>Power</i>	Transfer phase: 147 W maximum
Constellation	Equilateral triangle, “mother” S/C at one vertex, “daughter” S/C at the two other vertices, 1×10^6 km armlength, trailing Earth by 20° , inclined by 60° with respect to the ecliptic. Armlength variation $< 1\%$, angular variation $\pm 0.8^\circ$, rel. velocity between S/C < 20 m/s
Communications	Data generation rate 17 kbps per S/C, downlink via ESA ground stations, X-band, downlink data rate 200 kbps during 8 hours contact. Contact schedule: every 48 hours to one of the S/C, max. 6 days latency, max. 12 hour latency during preferred periods.
Total Mass	Including margin, launch adapter and propellant
<i>Mother</i>	1703 kg
<i>2 Daughters</i>	3585 kg
Power per S/C	Including margin and conversion losses:
<i>Mother</i>	638 W
<i>Daughter</i>	548 W
Launcher	1 + 1 Soyuz (1 Mother-S/C-P/M + 2 Daughter-S/C-P/M)

Instruments, 2 (1) per **Mother-S/C** (**Daughter-S/C**)

Laser	2 W output power (EOL), wavelength 1064 nm, frequency stability (pre-stabilised) $282 \text{ Hz}/\sqrt{\text{Hz}}$, fractional power stability $10^{-3}/\sqrt{\text{Hz}}$
Optical bench	low- CTE material (Zerodur), monolithic construction (hydroxy-catalysis bonding)
Interferometry	heterodyne interferometry, $18 \text{ pm}/\sqrt{\text{Hz}}$ requirement. Inter-S/C ranging to ~ 1 m, clock tone transfer
GRS	$46 \text{ mm} \times 46 \text{ mm} \times 46 \text{ mm}$ test mass made from AuPt alloy (73:27), electrostatically controlled, optical readout, residual acceleration $3 \times 10^{-15} \text{ m/s}^2/\sqrt{\text{Hz}}$ (10^{-9} m/s^2 at DC)
Telescope	20 cm off-axis telescope. Changing inter-S/C angle compensated by telescope movement.
<i>Mass</i>	Net mass per payload: Mother 282 kg, Daughter 154 kg
<i>Power</i>	Payload power consumption: Mother 282 W, Daughter 192 W

Foreword

The first mission concept studies for a space-borne gravitational wave observatory can be traced back to activities in the 1980s at the **Joint Institute for Laboratory Astrophysics** (JILA) leading to a first full description of a mission comprising three drag-free spacecraft in a heliocentric orbit, then named Laser Antenna for Gravitational-radiation Observation in Space (LAGOS). In the early 1990s, LISA was proposed to ESA, first to the then M3-cycle, later as a cornerstone to the “Horizon 2000 Plus” programme, as captured in the first “Yellow Book” of 1996. At this time LISA consisted of six spacecraft, but showed already the key features of the later LISA and today’s NGO: Interferometric measurement of distances, long baselines (5×10^6 km in those days), drag-free spacecraft based on inertial sensors, and the familiar “cartwheel”-orbits. The number of spacecraft was reduced to the current three in a series of cost-reduction exercises in 1996 and 1997, resulting in an update of the first Yellow Book in 1998. As well in 1997, the then study team and ESA’s Fundamental Physics Advisory Group (FPAG) recommended to carry out LISA in collaboration with NASA, laying the grounds for the joint formulation study that was to commence later.

The first industrial study on LISA published its final report in July 2000, proposing a mission design for that has in essence survived till today – three spacecraft, a separation of spacecraft and propulsion module and a measurement principle that had been refined, but saw little change in the underlying principles. In 2001 following the spirit of a collaborative mission, the two science teams formed by each agency (ESA and NASA) joined forces formed a single science team.

Equally in 2001, LISA became part of the Beyond Einstein programme of NASA as one of the great observatories. In 2003, LISA underwent a first of a series of US reviews aimed at technology readiness that culminated with LISA being identified as the mission with the highest readiness in NASA’s Beyond Einstein programme.

From 2005 to 2010, the joint formulation study was conducted by ESA and NASA. During that time both agencies ran their own technology development activities in a coordinated fashion, so that critical technology areas saw activities by both agencies for risk reduction.

When ESA formulated the Cosmic Vision 2015–2025 programme in 2005, and started the assessment phase in 2007, LISA was identified early on as one of the potential candidates for the L1 launch slot. In early 2011, LISA was presented to the advisory structure of ESA as a formal candidate for the L1 launch slot. Shortly after, in a response to the evolving programmatic framework in the US, it was decided that all L missions were to undergo a reformulation under the premise of an “ESA-led” mission.

Over the last decade, the scientific objectives and requirements for LISA, and subsequently NGO, underwent many refinements, described in this report. Today, computational tools are available to assess the impact of changes in the sensitivity on the science output, leading to science requirements that are traceable to the scientific objectives. Furthermore, the scientific community rose to the challenge of demonstrating the feasibility of the data analysis, closing the loop between science objectives and science output.

This report summarises the design of the reformulated mission and the payload that are the result of the recent industrial activity and ESA’s Concurrent Design Facility. It is evident that the design inherits quite some detail from previous studies, in particular for LISA and LISA Pathfinder, together with many contributions from technology development activities, either sponsored by ESA or undertaken by laboratories and institutes in Europe and the US on national funding.

Authors

This report has been authored by the members of the NGO science working team:

Oliver Jennrich (chair)	ESA	
Pierre Binetruy	APC Paris	France
Monica Colpi	University of Milano Bicocca	Italy
Karsten Danzmann	AEI Hannover	Germany
Philippe Jetzer	University of Zurich	Switzerland
Alberto Lobo	IEEC Barcelona	Spain
Gijs Nelemans	Radboud University Nijmegen	The Netherlands
Bernard Schutz	AEI Potsdam	Germany
Robin Stebbins (NASA Liason)	NASA GSFC	USA
Tim Sumner	Imperial College	UK
Stefano Vitale	University of Trento	Italy
Henry Ward	University of Glasgow	UK

Acknowledgements

The ESA Formulation study was led by A. Gianolio (ESA Project Manager), O. Jennrich (ESA Study Scientist), Paul McNamara (ESA LPF Project Scientist), and L. d’Arcio (ESA Optical Engineer) with the support of B. Johlander, L. Scalamiero, and Z. Sodnik. The Science Operations activity was supported by D. Texier. The industrial support activity was conducted by EADS Astrium UK and Germany.

Much scientific support was given to NGO from scientists that were not members of the science working but contributed significantly to this report, either directly or through work regarding the previous study (in alphabetical order):

Pau Amaro-Seoane (AEI), Berangere Argence (APC), Stuart Aston (Birmingham), Sofiane Aoudia (AEI), Gerard Auger (APC), Stas Babak (AEI), John Baker (GSFC), Simon Barke (AEI), Matthew Benacquista (UTB), Emanuele Berti (U Mississippi), Iouri Bykov (AEI), Martin Caldwell (RAL), Jordan Camp (GSFC), Chiara Caprini (IPhT), John Conklin (Stanford), Dan deBra (Stanford), Luciano Di Fiore (Naples), Christian Diekmann (AEI), Jean-Francois Dufaux (APC), Alejandro Bohe (IAP), Juan Jose Esteban Delgado (AEI), Ewan Fitzsimons (U Glasgow), Roland Fleddermann (AEI), Jonathan Gair (U Cambridge), Antonio Garcia (AEI), Catia Grimani (Urbino) Felipe Guzman (AEI/GSFC), Hubert Halloin (APC), Tupper Hyde (GSFC), Ian Harris (JPL), Gerhard Heinzel (AEI), Martin Hewitson (AEI) Steven Hochman (U Florida), Daniel Hollington (Imperial College), Nick Jedrich (GSFC), Mac Keiser (Stanford), Christian Killow (Glasgow), William Klipstein (JPL), Joachim Kullmann (AEI), Ryan Lang (GSFC), Tyson Littenberg (GSFC), Jeffrey Livas (GSFC), Achmed Mansoor (GSFC), Kirk McKenzie (JPL), Sean McWilliams (GSFC), Stephen Merkowitz (GSFC), Shawn Mitryk (U Florida), Anneke Monsky (AEI), Guido Müller (U Florida), Miquel Nofrarias (AEI), Kenji Numata (GSFC), Mike Perreux-Lloyd (U Glasgow), Antoine Petiteau (APC and AEI) Eric Plagnol (APC), Moshe Pniel (JPL), Scott Pollack (University of Washington), Ed Porter (APC), Alix Preston (UF), Volker Quetschke (UTB), Dave Robertson (Glasgow), Albrecht Rüdiger (AEI), Josep Sanjuan (IEEC Barcelona), B. Sathyaprakash (U Cardiff), Alberto Sesana (AEI), Daniel Shaddock (ANU), Diana Shaul (Imperial College), Ben Sheard (AEI), Robert Spero (JPL), Frank Steier (AEI), Ke-Xun Sun (Stanford), Dylan Sweeney (U Florida), David Tanner (UF), Michael Troebs (AEI), Glenn de Vine (JPL), Marta Volonteri (University of Michigan), Vinzenz Wand (AEI), Gudrun Wanner (AEI), Brent Ware (JPL), Peter Wass (U Trento/Imperial College), Bill Weber (U Trento), Yanan Yu (U Florida), Michele Vallisneri (JPL), Marta Volonteri (U Michigan), Alberto Vecchio (U Birmingham), Andreas Zoellner (Stanford)

The members of the former joint science team, whose work formed the foundation of many of the details reported were Karsten Danzmann (AEI Hannover), Thomas A Prince (JPL), Pierre Binetruy (APC Paris), Peter Bender (JILA), Sasha Buchman (Stanford University), Joan Centrella (NASA GSFC), Massimo Cerdonio (INFN Padua), Neil

Cornish (Montana State University), Mike Cruise (University of Birmingham), Curt J Cutler (JPL), Lee Sam Finn (PennState University), Jens Gundlach (University of Washington), Craig Hogan (Fermilab), Jim Hough (University of Glasgow), Scott A. Hughes (MIT), Philippe Jetzer (University of Zurich), Alberto Lobo (IEEC Barcelona), Piero Madau (UC Santa Cruz), Yannick Mellier (IAP), Sterl Phinney (Caltech), Douglas O. Richstone (University of Michigan), Bernard Schutz (AEI Potsdam), Robin Stebbins (NASA GSFC), Tim Sumner (Imperial College), Kip Thorne (Caltech), Jean-Yves Vinet (Observatoire de Côte d'Azur), Stefano Vitale (University of Trento)

Contact

Please direct all comments and questions to **O. Jennrich**.

Contents

NGO Mission Description	i
Foreword	iii
Authors	v
1. Executive Summary	1
2. Scientific Objectives	5
2.1. NGO Science Objectives	5
2.2. Gravitational Waves – An Overview	5
2.2.1. What are gravitational waves?	6
2.2.2. How are gravitational waves detected?	7
2.2.3. The gravitational wave universe in the NGO band	9
2.3. Ultra-Compact Binaries	12
2.3.1. Overview	12
2.3.2. Instrument verification	13
2.3.3. NGO as a workhorse: thousands of new binaries	14
2.3.4. The foreground of Galactic gravitational waves	15
2.3.5. Studying the astrophysics of compact binaries using NGO	16
2.3.6. Studies of galactic structure with NGO	20
2.4. Astrophysical Black Holes	22
2.4.1. Overview	22
2.4.2. Black holes in the realm of the observations	23
2.4.3. The merger of galaxies, the coalescing of their black holes	26
2.4.4. Dual, binary and recoiling AGN in the cosmic landscape	28
2.4.5. Seed black holes	30
2.4.6. Evolving massive black hole spins via coalescence and accretion events	30
2.4.7. Cosmological massive black hole merger rate	32
2.4.8. Massive black hole binaries as gravitational waves sources: what can NGO discover?	33
2.4.9. Parameter estimation on fiducial massive black hole population models	37
2.5. Extreme mass ratio inspirals and astrophysics of dense stellar systems	40
2.5.1. Extreme Mass Ratio Inspirals in galactic nuclei	40
2.5.2. A probe of galactic dynamics	42
2.5.3. A probe of the masses of stellar and massive black holes	42
2.5.4. Detecting extreme mass ratio inspirals with NGO	43
2.5.5. Estimating the event rates of extreme mass ratio inspirals for NGO	46
2.5.6. Black hole coalescence events in star clusters	47
2.6. Confronting General Relativity with Precision Measurements of Strong Gravity	48
2.6.1. Setting the stage	48
2.6.2. Testing strong-field gravity: The inspiral, merger, and ringdown of massive black hole binaries	50
2.6.3. Extreme mass ratio inspirals: precision probes of Kerr spacetime	53
2.6.4. Intermediate mass ratio binaries	54
2.6.5. The mass of the graviton	55

2.7. Cosmology	56
2.7.1. New physics and the early universe	56
2.7.2. Cosmological measurements with NGO	60
3. The NGO concept	63
3.1. NGO design concept	63
3.2. Measurement scheme	65
3.3. Data Analysis	66
3.3.1. General principles	67
3.3.2. Templates	67
3.3.3. Algorithms	68
3.3.4. Mock Data Challenge	68
4. Scientific Requirements	71
4.1. Science Requirements Overview	71
4.1.1. Science requirements rationale	71
4.2. Observation Requirements	72
4.3. Instrument Sensitivity Model	74
4.3.1. ISM Description	74
4.3.2. Instrument sensitivity function	74
4.3.3. Instrument Noise Model	76
4.3.4. ISM Validation	77
4.3.5. Noise Model validation	78
4.4. Performance Requirements	80
5. Payload	83
5.1. Optical System	84
5.1.1. Optical bench	84
5.1.2. Optical assembly tracking mechanism	88
5.2. Phase measurement	88
5.2.1. Clock noise removal	89
5.3. Disturbance Reduction System	90
5.3.1. Principle of operation	90
5.3.2. Environmental requirements	92
5.3.3. Gravitational Reference Sensor	92
5.4. Telescope	96
5.5. Laser System	98
5.5.1. Laser frequency noise suppression	99
6. Mission Design	103
6.1. Overview	103
6.2. Spacecraft Design	103
6.3. Micropropulsion design	105
6.3.1. FEPP thrusters	106
6.3.2. Cold gas thrusters	106
6.3.3. Radiofrequency ion thrusters	107
6.4. Propulsion module design	107
6.4.1. S/C-P/M Separation System	109
6.4.2. Propulsion Subsystem	109
6.5. Mission Analysis	110
6.5.1. Overview	110
6.5.2. Launch and Early Operations Phase	110

6.5.3. Transfer	110
6.5.4. Science orbit	111
6.6. Mission budgets	113
6.6.1. Mass and power budget	113
6.6.2. RF link budgets	113
7. Mission Operations	115
7.1. Introduction	115
7.2. Science Products	115
7.3. Mission Phases	116
7.3.1. Launch and Early Operations Phase	116
7.3.2. Cruise Phase	116
7.3.3. Commissioning Phase	117
7.3.4. Calibration phase	118
7.3.5. Science Operations Phase	118
7.3.6. Post-operations Phase	119
7.4. Mission Operations Elements	119
7.4.1. Ground Segment	119
7.4.2. Flight Operations	119
7.5. Science Operations Elements	119
7.5.1. Science Operation Centre	119
7.5.2. Data processing centre	120
7.5.3. Instrument Operations Teams	120
7.5.4. Data Archive	122
8. Management	123
8.1. Instrument procurement strategy	123
8.2. Project Scientist and Science Team	124
8.3. Data analysis	124
8.3.1. Data Rights	124
A. The Evolution of LISA to NGO	125
A.1. General architecture	125
A.2. Galactic binaries	125
A.3. Astrophysical Black Holes	126
A.4. EMRI	127
A.5. Testing General Relativity	127
A.6. Cosmology	128
Acronyms	129
Bibliography	131

1. Executive Summary

Einstein's theory of spacetime and gravity, general relativity, predicts that suitably accelerated masses produce propagating vibrations that travel through spacetime at the speed of light. These gravitational waves (as the vibrations are called) are produced abundantly in the universe and permeate all of space. Measuring them will add an altogether new way to explore what is happening in the universe: rather than studying the propagation and transformation of conventional particles and fields in spacetime, as all science has done up to now, **NGO** will sense vibrations of the fabric of spacetime itself. Studying these signals will convey rich new information about the behaviour, structure, and history of the physical universe, and about physics itself. When gravitational waves become observable they will provide a new and uniquely powerful probe of the extremes of spacetime, from the Big Bang to black holes, to address the deep questions that have emerged in mankind's never-ending quest to understand the cosmos: what powered the Big Bang, what happens to space and time in black holes and what is the mysterious dark energy accelerating the expansion of the universe?

NGO is a space mission designed to measure gravitational radiation over a broad band at low frequencies, from about 0.1 mHz to 1 Hz, a band where the universe is richly populated by strong sources of gravitational waves. It measures signals from a wide range of different sources that are of strong interest to the astrophysics of black hole and galaxy formation, and also to tests of general relativity and to cosmology: massive black holes merging in galaxies at all distances; massive black holes consuming smaller compact objects; known binary compact stars and stellar remnants; members of known populations of more distant binaries; and probably other sources, possibly including relics of the extremely early Big Bang, which are as yet unknown. These strong signals convey detailed information addressing a wide range of science, addressing scientific questions raised by ESA's Cosmic Vision programme, such as "What are the fundamental laws of the universe?" and "How did the universe originate and what is it made of?"

NGO will study in detail the signals from thousands of stellar-mass close binaries in the Galaxy and give information on the extreme endpoints of stellar evolution. **NGO** provides distances and detailed orbital and mass parameters for hundreds of the most compact binaries, a rich trove of information for detailed mapping and reconstruction of the history of stars in our Galaxy, and a source of information about tidal and non-gravitational influences on orbits associated with the internal physics of the compact remnants themselves.

NGO will determine how and when the massive black holes present in most galactic nuclei today have formed and grown over cosmic time. **NGO** will explore almost all the mass-redshift parameter space relevant for reconstructing their evolution at look back times. The gravitational wave signal from coalescing black holes reveals their spin and redshifted mass, and the distribution of masses and spins will be studied for a distinction among different formation scenarios. Black holes are expected to transit into the mass interval to which **NGO** is sensitive along the course of their cosmic evolution, and thus their coalescences will be the cleanest tracers of the assembly of galaxies.

NGO will bring a new perspective to the study of galactic nuclei. Orbits of stellar black holes captured by massive black holes at the centre of galaxies evolve by gravitational radiation. By capturing their signal, **NGO** will offer the deepest view of nearby galactic nuclei, providing information on the space density of compact objects, and on the star's dynamics around massive black holes.

NGO will observe highly relativistic black hole-black hole coalescences providing exceptionally strong tests of the predictions of General Relativity. By capturing the signal of merging binary black holes, where maximally warped vacuum spacetimes travel at near the speed of light interacting strongly with each other, **NGO** will trace the full nonlinear dynamics of the theory of gravity. By capturing the signal of stellar black holes skimming the horizon of a large massive black hole at the centre of a galaxy, **NGO** will measure the mass, spin and quadrupole moment of the central object testing its level of Kerr-ness; thus testing for the first time the black hole hypothesis, and the no-hair conjecture.

NGO will probe new physics and cosmology with gravitational waves, and search for unforeseen sources of

gravitational waves. The **NGO** frequency band in the relativistic early Universe corresponds to horizon scales where phase transitions of new forces of nature or extra dimensions of space may have caused catastrophic, explosive bubble growth and gravitational wave production. **NGO** is capable of detecting a stochastic background from such events from about 100 GeV to about 1000 TeV, if gravitational waves in the **NGO** band were produced with sufficient efficiency.

Although gravitational waves have never been directly detected, the existence of gravitational waves is in little doubt as their effects have been measured precisely, if indirectly. Any theory of gravity consistent with special relativity will exhibit gravitational waves, and the predictions of general relativity should be quantitatively reliable for **NGO** because the long-standing best evidence for gravitational waves is the orbital decay of the Hulse-Taylor binary pulsar, which radiates at frequencies only marginally below **NGO**'s operating band. Therefore **NGO** will be able to detect the gravitational waves predicted by any reasonable theory of gravity.

In the same way that electromagnetic radiation accompanies acceleration of electric charges, gravitational radiation accompanies quadrupolar acceleration of any kind of mass or energy, perturbing spacetime with a dimensionless metric-strain amplitude. **NGO** senses this by monitoring the changes in the distances between inertial test masses. **NGO** uses precision laser interferometry across 10^6 km of space to compare separations between test masses that are protected by the spacecraft from non-gravitational disturbances. **NGO** coherently measures spacetime strain variations, including frequency, phase, and polarisation, all of which reflect large-scale properties of the systems that produce them and are therefore direct traces of the motions of distant matter.

NGO is an astronomical observatory of unprecedented versatility and range. Its all-sky field of view ensures that it can observe every source of gravitational waves, without having to compromise between observations. Its coherent mode of observing allows it to resolve and distinguish overlapping signals and locate them on the sky. Its unparalleled sensitivity allows it to study sources within the Galaxy and out to the edge of the universe. Finally, **NGO**'s wide frequency band (four decades in frequency, equivalent to the span from near infrared to radio frequency in the electromagnetic sector) allows it to study similar sources of widely different masses and cosmological redshifts. Because gravitational waves penetrate all regions of time and space with almost no attenuation, **NGO** can sense waves from the densest regions of matter, the earliest stages of the Big Bang, and the most extreme warpings of spacetime near black holes. In particular, **NGO** can observe objects that are shielded from electromagnetic observations by other stars or dust, such as binary systems close to or beyond the galactic center.

The key components of the **NGO** mission concept are the interferometric measurement of the changes of a large baseline (10^6 km), free-falling test masses that define the endpoints of the baseline, suitable orbits of the spacecraft to avoid orbit maintenance (and hence disturbances on the test masses) and a mission lifetime of two years. The principle of interferometric measurements is always the comparison between the phase of two electromagnetic waves. However, the large distance between the **NGO** spacecraft makes it necessary to extend the classical concept of an interferometer somewhat, so that the measurement scheme somewhat resembles doppler spacecraft tracking. **NGO** employs a “Mother” spacecraft and two “Daughter” spacecraft. The **Mother-S/C** sends out a laser beam to each of the **Daughter-S/C** that compare the phase of the received light with the phase of a local laser, record the phase measurement and in turn send out light from the local laser to the **Mother-S/C** where a similar measurement takes place. The recorded phase measurements are transmitted to ground where they are suitably combined to extract the change in the inter-spacecraft distance caused by gravitational waves. The free-falling test masses ensure that the spacecraft follow purely gravitational orbits which minimises the acceleration noise that could otherwise mask the small gravitational wave signals. However, the orbits of the spacecraft are locally maintained, *i.e.* there is no “formation flying” with **NGO**. The changes of the inter-spacecraft distance that are caused by the natural evolution of the orbits are well outside the sensitive frequency range for **NGO**. The lifetime of the mission strikes a compromise between the number of events for transient sources (*i.e.* massive black hole mergers) and the stability of the constellation and the level of consumables.

The classical distinction between spacecraft and payload doesn't fit **NGO** very well, as the spacecraft is not just providing the infrastructure for the instruments, but must be designed and built with the gravitational requirements of the free-falling test masses in mind. The usual structural and thermal analysis of the spacecraft has therefore been extended to include gravitational effects as well to ensure that the requirements on gravity gradient at the position of the test masses is fully met. In addition, the payload controls the position of the spacecraft during

science operations, rendering the spacecraft effectively a part of the instrument. The importance of the co-design (and the co-operation) of spacecraft and payload is captured in the term “sciencecraft”. The core features of the payload have been stable since more than a decade: the interferometric measurement system, the telescope, the gravitational reference sensor, and the micropropulsion system. Their design has evolved and over the time has now reached considerable maturity. Many of the design features of, *e.g.*, the optical bench have been shown in laboratory prototypes, during testing of the **LISA Pathfinder** (LPF), and will finally be demonstrated on orbit during LPF operations. The disturbance reduction system (DRS) for **NGO** is identical to the one that is being built as the flight model for LPF, and the NGO baseline design allows to accommodate the micropropulsion system that will be used on LPF. Other critical components of **NGO**, which are not needed for LPF, have been demonstrated experimentally to meet the requirements of **NGO**, such as the phasemeter post-processing techniques to remove the residual laser phase noise (**TDI**).

Data analysis, the extraction of the science from the **NGO** data, had been conjectured to be a problem in the past. The community rose to the challenge of proving that not only the instrument can deliver data that in principle allow to assess the science questions, but that the techniques and concepts to extract the source parameters from the data streams are available and can be applied. A key component for that demonstration are the ability to create high-fidelity waveforms for the sources, having a well-understood signal simulator for the mission, and being able to extract the source parameters from the simulated signals, which has been developed by the **NGO** project. The community-organised **Mock LISA Data Challenge** (MLDC) can be given credit to demonstrate the feasibility of the **NGO** data analysis. Having started in 2005, the **MLDC** is based on blind challenges of increasing complexity – from a few sources in the first challenge to the full combination of all likely sources in the data stream in the most recent fourth challenge. Scientific research groups from all over the world developed, tested and implemented a wide variety of techniques, so that we are now in the position to assert that **NGO** data analysis is not only feasible, but that a proof-of-concept for the actual data analysis is at hand.

The data produced by **NGO** will be made public after a short period (6 months TBD) in form of a publically accessible catalogue that includes the identified sources and their parameters as well as the basic strain measurements and the software tools to analyse those data streams. The foreseen time between data ingestion and catalogue updates is necessary to ensure the quality of the data and to extract the parameters of those sources to a suitable degree of precision. During this time, the data will be accessible to the Science Team members; participation of independent scientists in the Science Team is foreseen. The catalogue will be updated during the course of the mission to incorporate the increasing precision of the parameters for continuous or quasi-continuous sources (compact binaries and extreme mass ratio inspirals).

Transient events, such as massive black hole mergers, will be announced as soon as possible to allow the community to plan for electromagnetic co-observation of a merger event.

2. Scientific Objectives

2.1. NGO Science Objectives

The science objectives for **NGO** are as follows:

1. Survey compact stellar-mass binaries and study the structure of the Galaxy
 - 1.1 Elucidate the formation and evolution of Galactic stellar-mass compact binaries and thus constrain the outcome of the common envelope phase and the progenitors of (type Ia) supernovae.
 - 1.2 Determine the spatial distribution of stellar mass binaries in the Milky Way.
 - 1.3 Improve our understanding of white dwarfs, their masses, and their interactions in binaries, and enable combined gravitational and electromagnetic observations
2. Trace the formation, growth and merger history of massive black holes.
 - 2.1 Trace the formation, growth and merger history of massive black holes with masses $10^5 M_{\odot} - 10^7 M_{\odot}$ during the epoch of growth of quasi-stellar objects and widespread star formation ($0 < z < 5$) through their coalescence in galactic halos.
 - 2.2 Capture the signal of coalescing massive black hole binaries with masses $2 \times 10^4 M_{\odot} - 10^5 M_{\odot}$ in the range of $5 < z < 10$ when the universe is less than 1 Gyr old.
3. Explore stellar populations and dynamics in galactic nuclei
 - 3.1 Characterise the immediate environment of massive black holes in $z < 0.7$ galactic nuclei from extreme mass ratio capture signals.
 - 3.2 Discovery of intermediate-mass black holes from their captures by massive black holes.
4. Confront General Relativity with observations
 - 4.1 Detect gravitational waves directly and measure their properties precisely
 - 4.2 Test whether the central massive objects in galactic nuclei are consistent with the Kerr black holes of General Relativity.
 - 4.3 Perform precision tests of dynamical strong-field gravity.
5. Probe new physics and cosmology with gravitational waves
 - 5.1 Measure the spectrum of cosmological backgrounds, or set upper limits on them in the 10^{-4} Hz to 10^{-1} Hz band.
 - 5.2 Search for gravitational wave bursts from cosmic string cusps and kinks.

2.2. Gravitational Waves – An Overview

Almost everything we know about the universe we have learned from light: since ancient times, electromagnetic waves have been messengers from the cosmos to our eyes, and later to our telescopes and our antennas. More recently, we have begun to parse the messages of more exotic carriers such as the elusive neutrinos from the Sun and beyond. We are now ready to add an altogether new modality to science: sensing vibrations of the very fabric of spacetime. Gravitational waves will add a many-voiced soundtrack to the rich imagery of the cosmos (see HOGAN, 2006).

In EINSTEIN'S 1915 General Theory of Relativity (GR), the geometry of spacetime is not a passive setting for the dynamics of matter and energy, but an equally dynamic player. Matter and energy cause spacetime curvature, which in its turn guides the free fall of matter and energy. Remarkably, spacetime can support curvature without

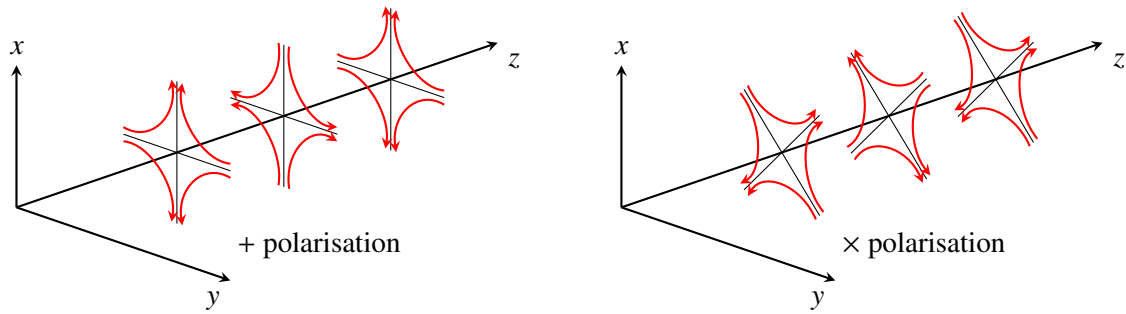


Figure 2.1.: Gravitational waves propagating along the z axis act in the x - y -plane. The two different polarisations (“+” and “ \times ”) exert different forces (red arrows).

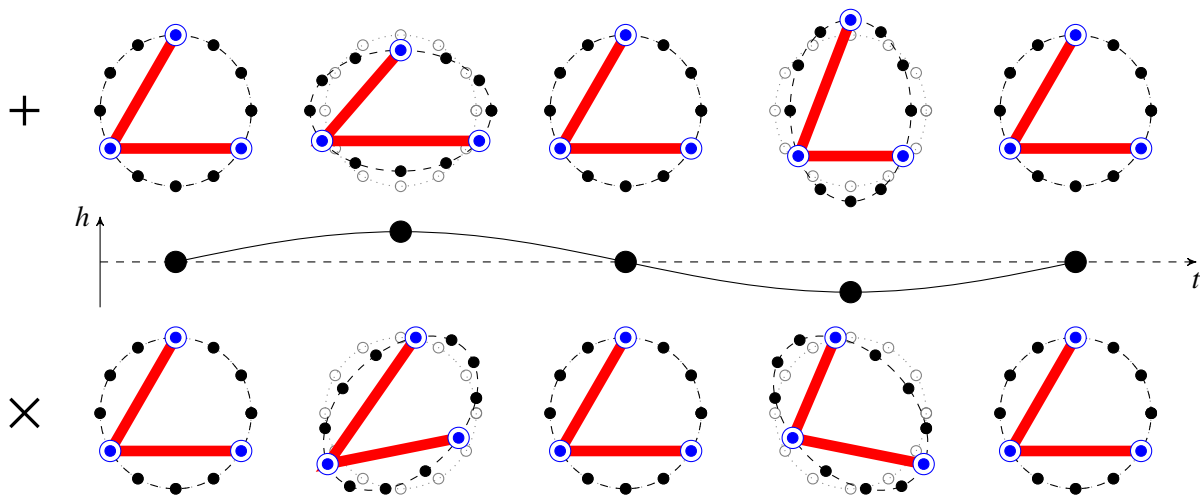


Figure 2.2.: A cartoon illustrating the passage of a gravitational wave through a ring of masses. Four phases of one cycle of the spatial distortion by a wave normal to the plane of the figure are shown both for the plus (“+”, upper row) and cross (“ \times ”, lower row) polarisations. Three of the masses in the ring are used to represent the three NGO spacecraft, and the time-varying changes in the red arms show what the NGO interferometer would measure.

any matter: black holes, the densest masses in the universe, are objects of pure spacetime wrapped around itself; gravitational waves are self-sustaining, undulatory excitations of spacetime, carrying energy and travelling at the speed of light. Unlike electromagnetic radiation (but much like neutrinos) gravitational waves interact very weakly with matter, and can penetrate anything almost without losing intensity. This makes them powerful probes of faraway regions and extreme conditions, but it also makes them very hard to detect. Only recently has technology advanced to the point of building apparatus sensitive enough to measure the minute effects of gravitational waves on matter.

Gravitational waves will reveal the most violent events in the universe, the collision and coalescence of two black holes. During the final orbits before the merger, the power radiated in gravitational waves reaches 10^{49} W, independent of the involved masses (the energy, however, depends on the masses), a thousand times more luminous than all the stars in all the galaxies in the visible universe put together. These mergers will allow us to test how well Einstein’s equations work in such extreme conditions, offering us insight into the strongest and most violently dynamic spacetimes Nature has produced since the Big Bang.

2.2.1. What are gravitational waves?

Electromagnetic waves are self-sustaining oscillations of the electric and magnetic fields, propagating through spacetime. By contrast, gravitational waves are oscillations of spacetime itself (see THORNE, 1987; and FLANAGAN & HUGHES, 2005, for reviews). Einstein predicted gravitational waves shortly after developing GR, but the first

experimental verification of their existence had to wait over 60 years, until the binary pulsar observations by HULSE & TAYLOR starting in 1974 (HULSE & TAYLOR, 1974).

According to GR, gravitational waves propagate at the speed of light, acting tidally by stretching and squeezing any extended distribution of matter or energy through which they pass. This warping action is transverse to the direction of wave propagation. Gravitational waves contain two dynamical degrees of freedom, which can be identified with the “+” (plus) and “×” (cross) polarisations, corresponding to the axes associated with the stretching and squeezing (see figure 2.1). A pure “+” polarisation squeezes along the x -axis and stretches along the y -axis, and then the other way round one half-cycle later (figure 2.2). It is a particular property of GR that gravitational waves come in only two polarisations. Other theories of gravity predict as many as five different polarisations and the absence (or indeed presence) of such polarisations will serve as a further test of GR (EARDLEY ET AL., 1973).

Just as electromagnetic waves are generated by accelerated charges, gravitational waves are generated by accelerated masses. Because of charge conservation, an oscillating charge dipole is the lowest-order time dependent distribution that can produce electromagnetic waves; because of mass and momentum (*i.e.*, mass dipole) conservation, a variable mass *quadrupole* is needed to produce gravitational waves – technically it is the second time derivative of the transverse-traceless part of the quadrupole moment that generates gravitational waves (FOR A BOOK REVIEW SEE MAGGIORE, 2007).

Electromagnetic waves arise from the interactions of atoms, nuclei, or other particles within astrophysical sources and they are typically generated in numerous individual emitting volumes, much smaller than the astrophysical object of interest, so the wavelength of radiation is also much smaller than the object. For this reason, electromagnetic waves permit us to image the object if it is close enough or big enough. But the short wavelength has a disadvantage: typically, we receive an incoherent superposition of radiation from many independent regions in the source. If the source is not close enough to be resolved, then it is often a difficult and uncertain job to model the emission process well enough to go from the information we get about many different wavelength-scale regions up to the much larger scale of the entire astrophysical system.

By contrast, gravitational waves are generated by the bulk mass distribution of the objects, so their wavelength is typically comparable to or larger than the size of the entire emitting region, *e.g.* for two black holes orbiting each other and losing energy by gravitational radiation, the wavelength of the gravitational waves is 10 to 20 times the radius of the orbit. Thus, gravitational wave observations do not generally allow imaging, and the extraction of information from waveforms proceeds, *e.g.*, with audio-like methods such as time-frequency analysis or matched filtering. Because gravitational waves are emitted coherently from the entirety of the astrophysical object, they provide direct information about the object’s large-scale structure. Moreover, observations of gravitational waves allow us to extract information from the phase of the wave as well as its amplitude or intensity. The phase evolution often carries more information about the detailed dynamics of the emitter than the amplitude does.

2.2.2. How are gravitational waves detected?

Einstein’s great epiphany was that gravity is the manifestation of the curvature of spacetime, the background for all the interactions of matter and energy. Freely falling test bodies (small compared to the spacetime curvature and undisturbed by other forces) thread spacetime along geodesics, the straightest paths possible through this curved arena. Nearby, approximately parallel geodesics are pushed together and pulled apart by spacetime curvature. Gravitational waves are waves of spacetime curvature and are experienced by test bodies as an oscillating change in their relative distance.

To understand how this principle is used to detect gravitational waves, it is useful to visualise an idealised Michelson laser interferometer (see figure 2.3) whose components are floating freely in space, at rest with each other, and far removed from any gravitating bodies. The power measured by a photodetector at the exit port of the interferometer is a simple function of the phase difference of the two light beams that are divided at the beamsplitter, propagated along the two arms, and recombined at the exit port. Incoming gravitational waves (consider for simplicity a plane gravitational wave, propagating perpendicularly to the plane of the interferometer, with “+” polarisation aligned with the two arms) alternately increase the distance experienced by light travelling along one arm and decrease the distance along the other, creating oscillations in the power measured at the exit port. This is the basic principle of ground-based interferometric detectors such as LIGO and Virgo.

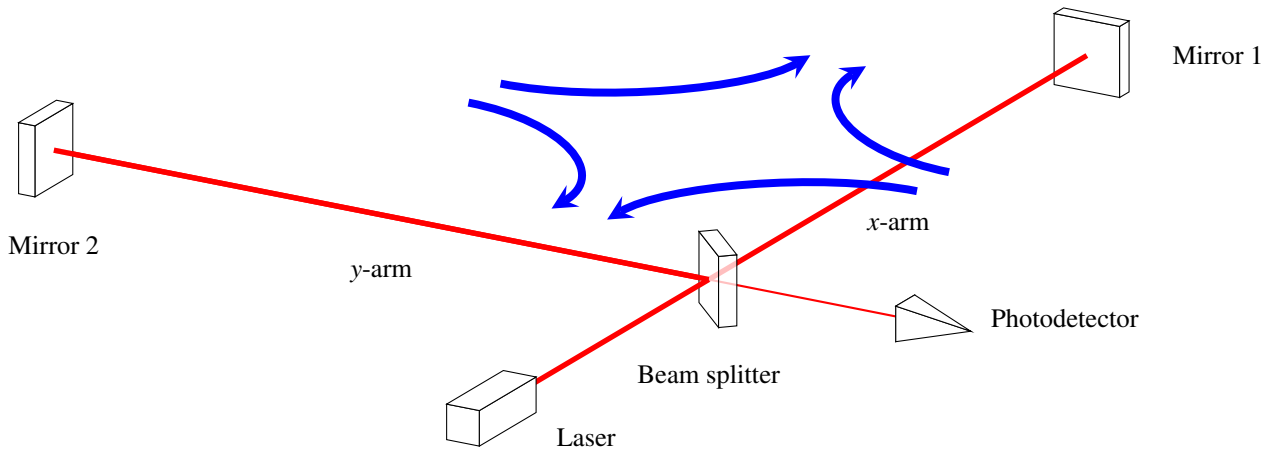


Figure 2.3.: *Idealised Michelson interferometer with laser, beam splitter, end mirrors, and photodetector at the exit port. The blue arrows represent a perpendicularly propagating, linearly polarised gravitational wave.*

NGO brings the Michelson measurement concept to the grander scale and much quieter environment of space. While ground-based detectors are naturally limited by the Earth’s curvature to kilometre armlengths, **NGO** is about a million times larger. As gravitational waves cause a *strain*, *i.e.* a fractional length change, longer arms undergo bigger changes, so **NGO** can achieve 10^{-21} strain resolution by measuring displacements of the order of fractions of a picometer. Combining this with the absence of seismic and gravity-gradient noise, **NGO** achieves sensitivity to the low-frequency gravitational waves emitted by large massive systems. Thus, while advanced ground-based detectors may observe neutron stars or stellar-mass black holes coalescing out to distances of hundreds of megaparsecs, **NGO** will be sensitive to massive black hole coalescences out to redshifts of $z \sim 10$, allowing it to fathom the earliest stages of galaxy formation.

While **NGO** can be thought of as a “Michelson interferometer in space”, its actual implementation is quite different from a conventional Michelson interferometer. The experimental approach is closer to that of spacecraft Doppler tracking, in which the observed quantity is the frequency change in the signal from a distant spacecraft. In **NGO**, the “Mother” spacecraft (Mother-S/C) sends a beam of laser light to each of the two “Daughter” spacecraft (Daughter-S/C), and in turn receives a beam from each of them. The received laser light is coherently combined at a photodetector with the light from an on-board reference laser, and the relative phase (or frequency difference when the time derivation is taken) is recorded as a beat signal. The beat signals recorded at each of the three spacecraft are delayed in time and recombined in a technique called time-delay interferometry (TDI) (TINTO & LARSON, 2005) which essentially creates a virtual Michelson interferometer whose output signals represent the basic **NGO** science data stream.

NGO as an astronomical observatory for gravitational waves has some characteristics that are different from observatories of electromagnetic radiation. It will help to understand the range and versatility of **NGO**’s observations as described in this document if we make some of these differences explicit below.

First, **NGO** has a large intrinsic dynamic range: it could in principle measure accurately signals over an amplitude range of 10^5 or an energy range of 10^{10} . This is because it measures tiny changes in separations between the test masses and therefore always operates in a linear regime. **NGO** is designed to study signals well below its mean noise level (extracting them by matched filtering) up to the strongest expected sources in the universe.

Second, **NGO** has a very large frequency range, spanning four decades, limited at high frequencies by its size and at low frequencies by the difficulty of isolating the test masses. This means that, unlike optical, ultraviolet, or infrared observatories, **NGO** is less likely to miss distant sources because they are cosmologically red-shifted to lower frequencies: indeed, it will be able to study the populations of objects out to the highest redshifts.

Third, **NGO** has all-sky acceptance of signals; it sweeps three different quadrupolar antenna patterns across the sky as it orbits the Sun, so that its sensitivity for all but the shortest transient sources is fairly isotropic. Unlike any imaging electromagnetic observatory, **NGO** is not pointed, so it does not miss any signals once they are above its noise level. This property is particularly important as it allows **NGO** to detect strong transient events such as

black hole coalescences without having to point at the source; the strongest events in the universe are necessarily transient, because they radiate far too much energy to be sustained in a steady state. Although **NGO** is an all-sky detector, it can nevertheless reconstruct event positions through its data analysis, by analysing phase modulation (Doppler effects) and amplitude modulation of the signals, which are available thanks to the detector's coherent observations. **NGO** can also separate thousands of simultaneously superimposed signals because it uses phase information to resolve them, so its all-sky acceptance does not lead to confusion except where there are very large numbers of sources.

Finally, **NGO** is not troubled by absorption, scattering, or obscuration in any of its observations, as gravitational waves interact very weakly with matter. The best illustration of this is in searching for a cosmological background of radiation from inflation: **NGO** can in principle see right back to the end of the inflationary epoch, through all stages of decoupling, symmetry breaking, and particle creation. Gravitational waves will also give us our deepest views of the interiors of very dense environments, our only direct information about black holes, leading to their unequivocal identification, and to our first chance to observe any possible structures in the electrically neutral dark matter in the universe.

We also note that **NGO** (as all interferometric gravitational wave detectors) observes the *amplitude* of the gravitational wave (or wave strain) h , *i.e.* the fractional amount of the stretching and squeezing discussed above. As the amplitude h falls off only as $1/r$, strong sources of gravitational waves (such as the binary inspirals of massive black holes, which **NGO** will see with amplitude signal-to-noise ratio (SNR) of more than 1000 at a redshift $z = 1$), can essentially be detected out to arbitrarily large redshifts. A further consequence of measuring the amplitude is the practise to express the sensitivity as an amplitude spectral density, *i.e.*, the square root of the more commonplace power spectral density, as the amplitude spectral density relates more closely to the measurement. As strain is a dimensionless quantity, strain amplitude spectral density has the peculiar units of inverse square root of hertz.

The distinctive characteristics of gravitational waves ensure that they will provide a unique new channel to study the universe, complementing information gathered over decades from electro-magnetic (EM) channels, and probing previously inaccessible dense and dark regions of the universe. The potential for discovery and surprise is great.

2.2.3. The gravitational wave universe in the **NGO** band

Although gravitational waves have not been detected directly yet, we know enough about the contents of the universe to make reasonably accurate assessments about some of their sources that **NGO** will observe (see HUGHES, 2003; HUGHES, 2006, for reviews). As discussed earlier, in the same way that accelerated electric charges generate electromagnetic radiation, accelerated mass and energy generate gravitational radiation. The periodic motion of a system of mass M and size R at a (luminosity) distance D creates gravitational waves with a strain amplitude of about $h \sim (GM/(Rc^2))^2(R/D)$, with a frequency determined by the frequency of the motion. The shapes and strengths of the observed waves give us details about the structure and behaviour of the system that produced them.

The strongest waves are generated by systems with the largest gravitational fields GM/R , which correspond to large masses and small sizes and are generated by the interactions of black holes, which have $GM/(Rc^2) \approx 1$. The lightest black holes (remnants of single stars, with about ten times the mass of the Sun) emit at the highest frequencies, in the 100 Hz band, accessible to ground-based detectors. Figure 2.4 depicts the different frequency bands and the different source classes for **NGO** and ground-based detectors, such as **LIGO**.

By contrast, the strongest sources in the far lower **NGO** band (between 0.1 mHz to 1 Hz) are the massive black holes at the centres of galaxies; these are the remnants of the process of galaxy formation, with about 10^4 to 10^7 times the mass of the Sun (M_\odot). Optical, radio, and X-ray astronomy have produced abundant evidence that nearly all galaxies have massive black holes in their central nucleus, and that some of them even have two.

Mergers of massive black holes (MBHs) happen frequently: galaxies are continually forming, in a hierarchical fashion, starting from the mergers of smaller galaxies, and whenever two galaxies merge their central black holes sink to the centre and find each other. **MBH** mergers are so powerful that **NGO** can detect them out to a wide range of redshifts, extending back to the first protogalaxies at $z \sim 15$. Estimates from standard galaxy formation theory suggest that **NGO** will detect massive black hole coalescences about once or twice every week (VOLONTERI,

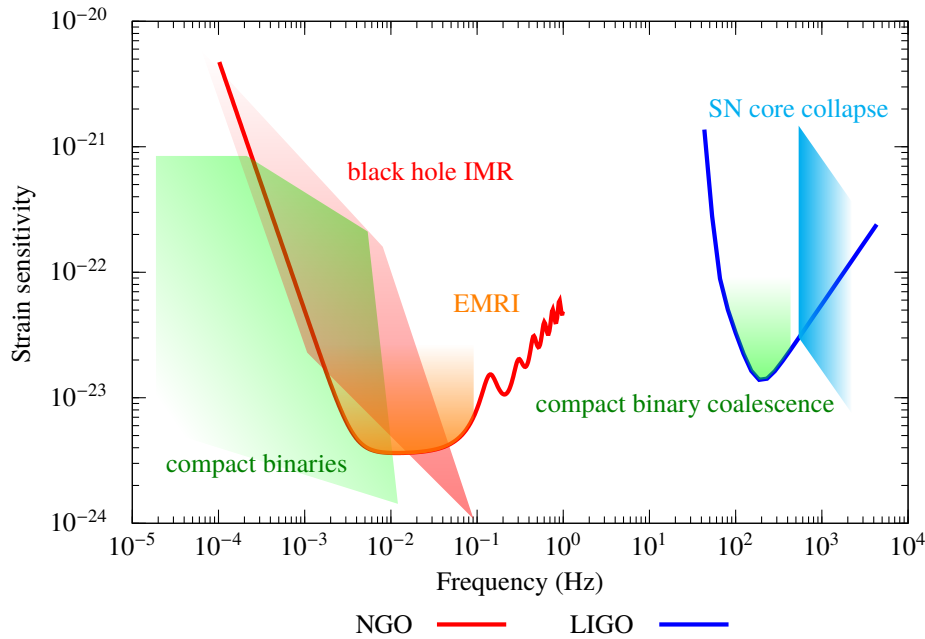


Figure 2.4.: Comparison between the NGO sensitivity (red curve) and the sensitivity of present ground-based detectors such as LIGO (blue curve). While having about the same strain sensitivity, NGO covers a much lower frequency range than LIGO and aims for different astrophysical sources. NGO is sensitive to the inspiral, merger and ringdown (IMR) of massive black hole binaries (in red), the quasi-monochromatic signal from compact binaries (in green) and the extreme mass ratio inspirals (EMRIs, in orange). Ground based detectors operate in the acoustic frequency range and are sensitive to the coalescence of compact binaries (in green) and “burst” events like supernovae core collapses (in cyan). While the compact binaries observed by NGO and ground based detectors are in principle the same systems, they are separated by millions of years of evolution. Note that in this plot the strain sensitivities are compared, that take into account the differences in integration time.

2006), but predictions are very uncertain at the high-redshift end, which is beyond the reach of electromagnetic observations. NGO will lift the veil of these cosmic “dark ages”, providing a direct record of the history of galaxy formation and central black hole growth in the observable universe.

Smaller galactic objects can also be captured (and eventually consumed) by the central black hole. Compact objects such as degenerate dwarfs, neutron stars, and black holes sometimes will be driven by chance encounters into a close orbit around the MBH: a dance of death that they will repeat for many revolutions until they finally plunge into the black hole’s event horizon. The gravitational waves from these extreme mass-ratio inspirals (EMRIs) encode a detailed map of spacetime geometry around the MBH. The history and environment of the black hole leave no imprint on this geometry, which is a very pure and beautiful solution (the Kerr metric) of the equations of GR. Thus, EMRI signals will test Einstein’s theory by probing the most accurately predicted structures in all of astrophysics.

In addition to black holes, many other known systems in our universe can produce gravitational waves in NGO’s frequency band. Soon after it is turned on, NGO will quickly detect a handful of nearby verification binary stars, which have known periods and positions (and even assigned names), and which will appear in the NGO data with predictable, distinctive signatures.

A large Galactic population of undiscovered degenerate-dwarf binaries will be observed all across the NGO band; we know from electromagnetic observations that such objects exist in our vicinity, but NGO will detect thousands of individual binaries throughout the Galaxy. At low frequencies millions more binaries from across the Galaxy will blend together into a confusion background in the NGO data, which will nevertheless teach us about the statistics of their population. At higher frequencies, the binaries have more powerful signals, and are farther apart in frequency space, allowing NGO to characterise each individually. At high frequencies, NGO may also detect the background signal from the degenerate binaries in other distant galaxies, allowing us to place constraints on cosmic star formation rates.

Given that all forms of matter and energy couple to gravity, it seems likely that the universe will treat **NGO** to yet other gravitational wave sources that we cannot anticipate on the basis of our electromagnetic observations. This is especially true for observations at very high redshifts, where **NGO** may give us the very first clues to the unknown conditions of matter and energy in the very early universe.

In the relativistic early universe, the **NGO** frequency band corresponds to the Terascale frontier, where the phase transitions of exotic fields or extra spatial dimensions may have caused catastrophic and explosive bubble growth, with efficient gravitational wave production. **NGO** will also probe superstrings, relics of the early universe predicted in some versions of string theory. These exotic structures, which are completely invisible except for the gravitational waves they emit, could produce strong, distinctive **NGO** signatures; they could provide direct evidence that all forms of matter and energy, and possibly even spacetime itself, are ultimately made of quantum strings.

2.3. Ultra-Compact Binaries

NGO science objectives and investigations relevant to this section

1. Survey compact stellar-mass binaries and study the structure of the Galaxy
 - 1.1 Elucidate the formation and evolution of Galactic stellar-mass compact binaries and thus constrain the outcome of the common envelope phase and the progenitors of (type Ia) supernovae.
 - 1.2 Determine the spatial distribution of stellar mass binaries in the Milky Way.
 - 1.3 Improve our understanding of white dwarfs, their masses, and their interactions in binaries, and enable combined gravitational and electromagnetic observations

The NGO Science Objectives are listed in chapter 2.

2.3.1. Overview

The most numerous sources in the low-frequency gravitational wave band are ultra-compact binary stars which are double stars in which two compact objects such as white dwarfs, neutron stars and stellar mass black holes orbit each other with short periods. They have relatively weak gravitational wave signals in comparison to massive black hole binaries, but are numerous in the Galaxy and even the Solar neighbourhood.

Several thousand systems are expected to be detected individually, with their parameters determined to high precision, while the combined signals of the millions of compact binaries in the NGO band will form a foreground signal. This is in contrast to less than 50 ultra-compact binaries known today. The number of detections will allow to study entire populations of binaries in great detail. In particular, the most numerous sources are double white dwarfs which are one of the candidate progenitors of type Ia supernovae and related peculiar supernovae. NGO will determine the merger rate of these binaries. The detailed knowledge of the ultra-compact binary population also constrains the formation of these binaries and thus many preceding phases in binary evolution. This has a strong bearing on our understanding of many high-energy phenomena in the universe such as supernova explosions, gamma-ray bursts and X-ray sources as they share parts of the evolution history of the binaries detectable by NGO.

As many of the Galactic sources are rather close (within a few kpc), they will be detectable at high SNR (often larger than 50), allowing detailed studies of individual binaries. For many hundreds, the frequency and phase evolution can be studied, enabling the study of the physics of tides and mass transfer in unprecedented detail. The extreme conditions of short orbital periods, strong gravitational fields and high mass-transfer rates are unique in astrophysics.

The NGO measurements will provide different information to what can be deduced from electromagnetic detections. In particular, NGO's capability to determine distances and inclinations, as well as the fact that the gravitational wave signals are unaffected by interstellar dust provide significant advantages over other detection techniques. Compared to Gaia, NGO will observe a quite different population. Gravitational wave observations allow us to determine the distances to binaries that are right in the Galactic centre rather than to those close to the Sun. The distance determinations will make it possible to map the distribution of many compact binaries in the Galaxy, providing a new method to study Galactic structure. The inclination determinations allow the study of binary formation by comparing the average angular momentum of the binaries to that of the Galaxy. Electromagnetic observations and gravitational wave observations are complementary to one another; dedicated complementary observing programs as well as public data releases will allow simultaneous and follow-up electromagnetic observations of binaries identified by NGO.

A number of guaranteed detectable sources are known to date from electromagnetic observations. Some of these can be used to verify instrument performance by looking for a gravitational signal at twice the orbital period and comparing the signal with expectations. In addition, once NGO has detected several nearby binaries and determined their sky position they can be observed optically thus providing an additional quantitative check on instrument sensitivity.

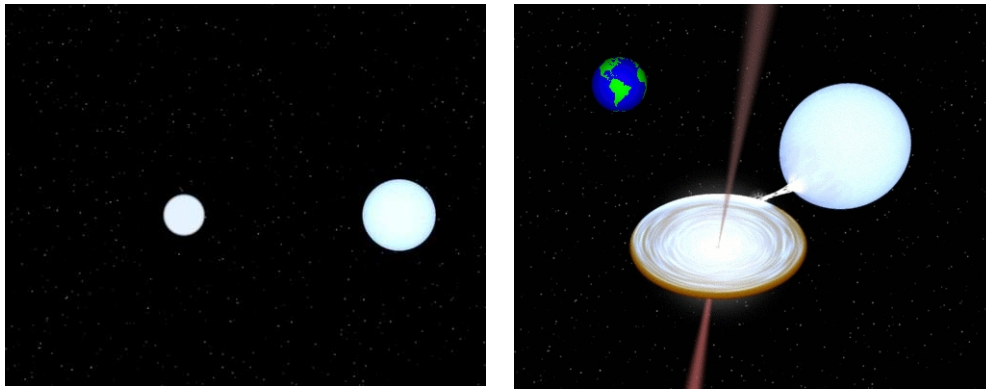


Figure 2.5.: Artist impression of a detached double white dwarf binary (left) and an interacting binary in which a neutron star accretes material from a white dwarf donor. The Earth is shown to set the scale. Courtesy BinSim by Rob Hynes.

2.3.2. Instrument verification

Of the known ultra-compact binaries, 8 will be detected by NGO as verification binary. Upcoming wide-field and synoptical surveys will discover more before the NGO launch.

There are currently about 50 known ultra-compact binaries. They come in two flavours, systems in which the two stars are well apart, called detached binaries and binaries in which the two stars are so close together that mass is flowing from one star to the other, called interacting binaries (see figure 2.5)

A subset of the known ultra-compact binaries have been recognised as instrument verification sources, as they should be detected in a few weeks to months and thus can be used to verify the performance of the instrument (STROEER & VECCHIO, 2006). The most promising verification binaries are the shortest-period interacting binaries HM Cnc (RX J0806.3+1527), V407 Vul, ES Cet and the recently discovered 12 minute period detached system SDSS J0651+28 (BROWN ET AL., 2011) (see figure 2.6). For a decade it has remained unclear if the measured periods of HM Cnc and V407 Vul were actually orbital periods, but recent results from the Keck telescope on HM Cnc (ROELOFS ET AL., 2010) show conclusively that this system has an orbital period of 5.4 minutes. As V407 Vul has almost identical properties, this implies that this also really is a binary with an orbital period of 9.5 minutes.

As the signal from the verification binaries is essentially monochromatic with a well known frequency within the NGO mission time, astrophysical effects (see section 2.3.5) will not hamper their detection.

As more and more wide field and synoptical surveys are done, the number of ultra-compact binaries is gradually increasing and is expected to continue to do so in the future. Already several new binaries have been found in the Sloan Digital Sky Survey (SDSS) and the Palomar Transient Factory (PTF) (LEVITAN ET AL., 2011; RAU ET AL., 2010) while surveys such as Pan-Starrs, the European Galactic Plane Surveys (EGAPS) and in the future Large Synoptic Survey Telescope (LSST) will also find new systems. However, most of these systems found have relatively long orbital periods (longer than about 30 minutes). Two pilot surveys in principle capable of finding ultra-compact binaries with periods less than 30 minutes are underway or will start soon: the Rapid Time Survey (RATS) (BARCLAY ET AL., 2011) and the OmegaWhite survey.

Interacting ultra-compact binaries with neutron star accretors are strong X-ray sources and new discoveries are expected, both through the continued monitoring of the sky to search for X-ray transients with RXTE, MAXI and other satellites, as well as through dedicated X-ray and optical surveys of the Galactic bulge that are currently happening (JONKER ET AL., 2011). With these developments, the number of verification sources available for NGO will be several tens allowing detailed tests of the performance of the instrument.

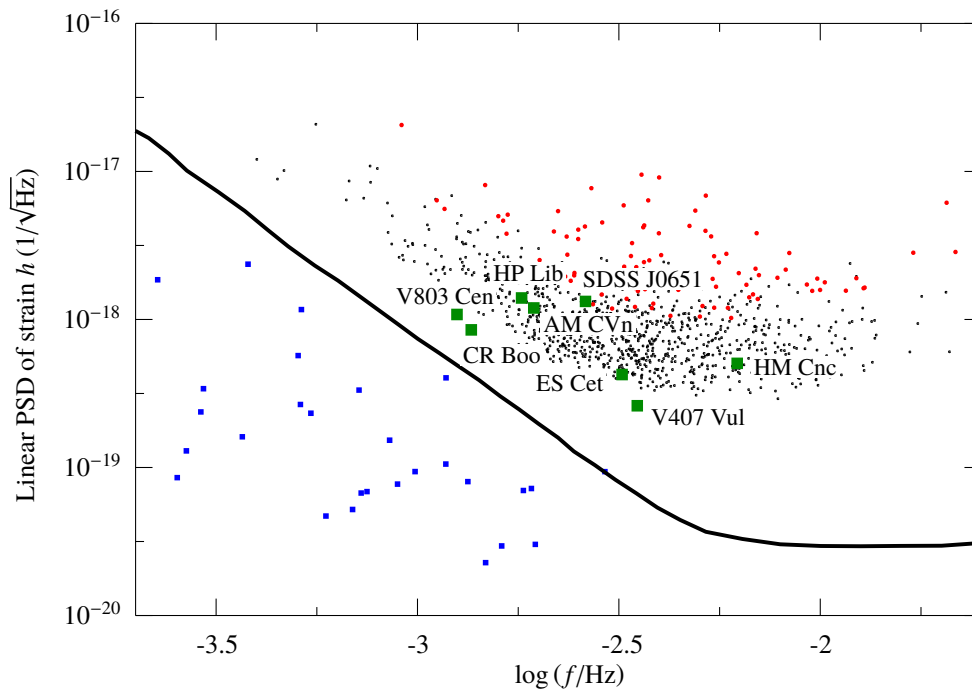


Figure 2.6.: Gravitational wave strain versus frequency for the verification binaries and the brightest binaries expected from a simulated Galactic population of ultra-compact binaries. The solid line show the sensitivity of NGO. Verification binaries are shown as green squares with their names indicated, blue squares are other known binaries. Strongest 100 simulated binaries are shown in red, strongest 1000 as black dots. Integration time for the binaries is two years. Based on BROWN ET AL. (2011); ROELOFS ET AL. (2006, 2010) for the known binaries and NELEMANS ET AL. (2004) for the simulation.

2.3.3. NGO as a workhorse: thousands of new binaries

NGO will detect about 3000 double white dwarf binaries individually. Most have orbital periods between 5 and 10 minutes and have experienced at least one common-envelope phase and thus put its physics to a critical test. These sources are exactly the population which has been proposed as progenitors of normal type Ia as well as peculiar supernovae. If formation of all ultra-compact binaries is enhanced in globular clusters by dynamical interactions, NGO will measure that.

Ultra-compact binaries will completely dominate the number of source detections by NGO. Current estimates suggest the numbers of resolved compact binaries that will be detected by NGO to be in the thousands (WEBBINK, 2010). The shortest period systems will be the most numerous, the majority having periods between 5 and 10 minutes. NGO will revolutionise our knowledge of such a population, especially given that only two of the known fifty sources have periods less than ten minutes. As these systems are relatively short lived and faint, there is no hope to detect such systems in significant numbers by any other means than via gravitational radiation as there are only several thousand expected to exist in the whole Galaxy. Their detection will allow us to test different models for the common-envelope phase, a significant uncertainty in our understanding of binary evolution and many high-energy phenomena. The internal statistical accuracy delivered by the sheer number of detected sources will ensure that the common-envelope phase will be put to the most critical test expected in the midterm future. The same population can be used to constrain models for type Ia supernovae and peculiar supernovae, as well as the formation of ultra-compact binaries in globular clusters.

The outcome of the common envelope phase

Only a minority of the stars in the universe are single, leaving the majority to be part of a binary, a triple or a higher-order system. On the order of half of the binaries formed with sufficiently small orbital separation, so that the stars will interact during the evolution of the components into giants or super giants. Especially for low-mass stars, the majority of interactions are unstable and will lead to runaway mass transfer. Based on the observed

short orbital periods of binaries that have passed this stage it is argued that somehow the companion of the giant ends up inside the giant's outer layers. During that common envelope phase, (dynamical) friction reduces the velocity of the companion, leading to orbital shrinkage and transfer of angular momentum from the orbit into the envelope of the giant. Along with angular momentum, orbital energy is deposited in the envelope, whose matter is then unbound from the giant's core, leading to a very compact binary consisting of the core of the giant and the original companion (PACZYNSKI, 1976).

Virtually all compact binaries and most of the systems giving rise to high-energy phenomena (such as X-ray binaries, relativistic binary pulsars and possibly gamma-ray bursts) have experienced at least one common-envelope phase. Given the importance of this phase in high-energy astrophysics, our understanding of the physics and our ability to predict the outcome of the common-envelope phase are poor. Theoretical progress to understand the phase from first physical principles is slow (*e.g.* TAAM & RICKER, 2010; TAAM & SANDQUIST, 2000) and the standard formalism described above has been challenged by observational tests (DE MARCO ET AL., 2011; NELEMANS & TOUT, 2005).

Comparison of the parameters of the thousands of binaries detected by NGO with model predictions will provide a direct test of the different proposed outcomes of the common-envelope phase and our understanding of the preceding binary evolution in general.

Type Ia supernovae and sub-luminous supernovae

Type Ia supernovae have been the heralds of a new paradigm in Cosmology: cosmic acceleration (PERLMUTTER ET AL., 1999; RIESS ET AL., 1998A) for which the 2011 Nobel Prize in Physics was awarded. However, there are different scenarios proposed for the progenitors of SN Ia, one is the merger of two (carbon-oxygen) white dwarfs that are brought together via gravitational wave radiation (PAKMOR ET AL., 2010) which is exactly the population NGO will be probing. By determining the number of systems in the Galaxy and their period distribution, the rate at which they will merge will be measured. By comparing that to the inferred SNIa rate for an Sbc galaxy, the viability of this progenitor scenario will be determined. The significant efforts in the past decade to find more supernovae and the advent of wide field optical surveys have revealed a host of new types of supernovae (KASLIWAL ET AL., 2010; PERETS ET AL., 2010, 2011; SULLIVAN ET AL., 2011). Some of these have been suggested to originate in the interaction between two white dwarfs at very short periods, again exactly the population to which NGO is sensitive (PERETS ET AL., 2010; WALDMAN ET AL., 2011).

Formation of ultra-compact binaries in globular clusters

Globular clusters have a strong overabundance of bright X-ray sources per unit mass compared to the field, probably due to dynamical interactions. Many of these have turned out to be so-called ultra-compact X-ray binaries, in which a neutron star accreted material from a white dwarf companion in a very compact orbit, exactly the type of sources that NGO may see. However, it is not clear if the same enhancement will operate for the much more numerous white dwarf binaries.

The angular resolution that can be achieved with NGO is such that globular clusters can be resolved, so that the cluster sources can be distinguished from the Galactic disc sources. This enables NGO to determine the number of ultra-compact binaries in globular clusters and thus to provide a direct test of the overabundance of white dwarf binaries in globular clusters. That in turn can be used to test models for dynamical interactions in clusters.

2.3.4. The foreground of Galactic gravitational waves

The millions of ultra-compact binaries that will not be individually detected by NGO will form a detectable foreground from which the global properties of the whole population can be determined.

At frequencies below a few mHz the number of sources in the Galaxy is so large (6×10^7 to 8×10^7 , *see e.g.* RUITER ET AL., 2010; YU & JEFFERY, 2010) that only a small percentage, the brightest sources, will be *individually* detected.

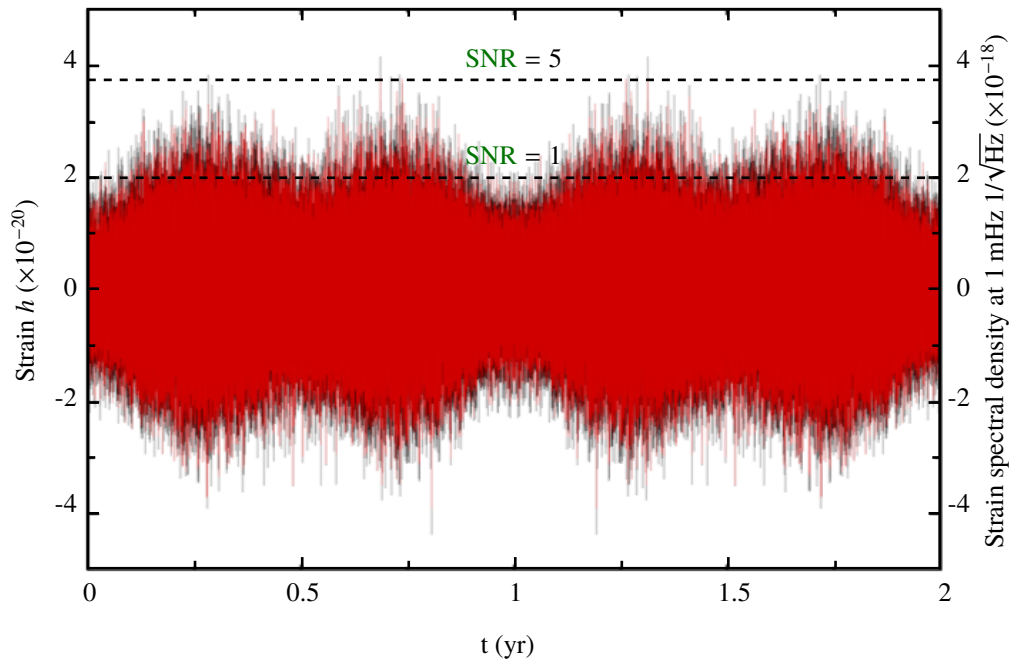


Figure 2.7.: Level of the Galactic gravitational wave signal as a function of time. Black is the total signal, the red after removal of the resolved binaries. The yearly variation of the Galactic foreground can clearly be seen. The dashed lines give the associated SNR for the contribution of the foreground signal to the total signal. For most of the time, the SNR varies between 1 and 5. The scale on the right y-axis indicates the approximate level of the galactic foreground “noise” at 1 mHz. Based on the RUITER ET AL. (2009) Galactic model.

The vast majority will form an unresolved *foreground* signal in the detector, which is quite different from and much stronger than any diffuse extragalactic *background* (FARMER & PHINNEY, 2003).

This foreground is often described as an additional noise component, which is misleading for two reasons. The first is that there is a lot of astrophysical information in the foreground. The overall level of the foreground is a measure of the total number of ultra-compact binaries, which gives valuable information given the current uncertainty levels in the normalisation of the population models. The spectral shape of the foreground also contains information about the homogeneity of the sample, as simple models of a steady state with one type of binary predict a very distinct shape. In addition, the geometrical distribution of the sources can be detected by NGO.

Due to the concentration of sources in the Galactic centre and the inhomogeneity of the NGO antenna pattern, the foreground is strongly modulated over the course of a year, with time periods in which the foreground is more than a factor two lower than during other periods (EDLUND ET AL., 2005). The characteristics of the modulation can be used to learn about the distribution of the sources in the Galaxy as the different Galactic components (thin disk, thick disk, halo) contribute differently to the modulation, and their respective amplitude can be used to, for example, set upper limits to the halo population (e.g. RUITER ET AL., 2009).

2.3.5. Studying the astrophysics of compact binaries using NGO

By studying the binaries that NGO detected in detail, the physics of tides in white dwarfs and mass-transfer stability will be constrained. The physics of the actual merger of two white dwarfs is uncertain and will be tested by either detection or non-detection of this event. NGO will discover the complete Galactic population of short-period neutron star and black hole binaries and thus determine their local merger rate.

Although the effect of gravitational radiation on the orbit will dominate the evolution of the binaries detected by NGO, additional physical processes will cause strong deviations from the simple point-mass approximation. The two most important interactions that occur are tides – when at least one of the stars in a binary system is not in co-rotation with the orbital motion or when the orbit is eccentric – and mass transfer. Because many

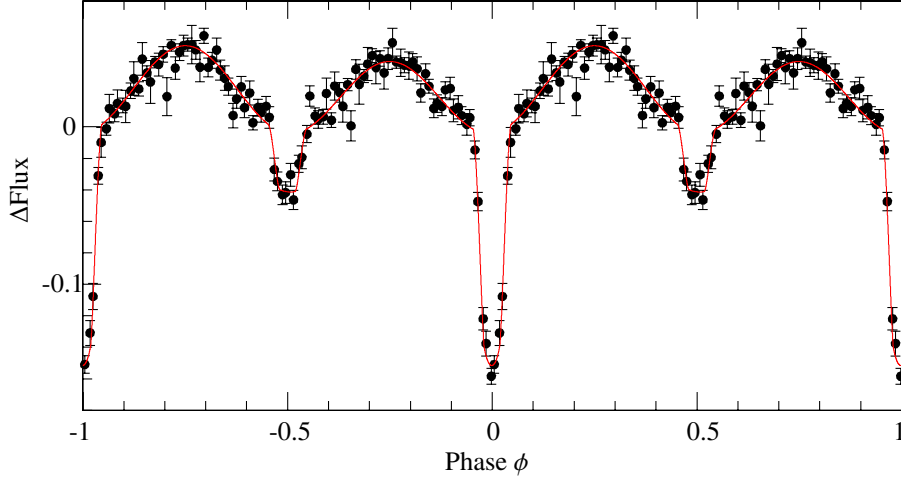


Figure 2.8.: Lightcurve of SDSS J0651+28, folded on the 12 minute orbital period. Except for the two eclipses at phase $\phi = 0$ and $\phi = 0.5$, the sinusoidal variation due to the tidal distortion of the primary white dwarf. From BROWN ET AL. (2011)

binaries will be easily detected, these interactions do not hamper their discovery, but instead will allow tests of the physics underlying these deviations. By providing a completely complementary approach, gravitational wave measurements are optimal to the study of short period systems in contrast to the current bias towards bright electromagnetic systems and events.

Physics of tidal interaction

NGO measurements of individual short-period binaries will give a wealth of information on the physics of tides and the stability of the mass transfer. For detached systems with little or no interaction, the frequency evolution is well understood as that of two point masses. The strain amplitude h , the frequency f and its derivatives then are connected by

$$h \propto \mathcal{M}^{5/3} f^{2/3} D^{-1} \quad \text{with} \quad \mathcal{M} = \frac{(m_1 m_2)^{3/5}}{(m_1 + m_2)^{1/5}} \quad (2.1)$$

$$\dot{f} \propto \mathcal{M}^{5/3} f^{11/3} \quad (2.2)$$

$$\ddot{f} = \frac{11}{3} \frac{\dot{f}}{f} \quad (2.3)$$

where \mathcal{M} is the chirp mass, m_1, m_2 the masses of the binary constituents and D the distance. Thus the measurement of h, f, \dot{f} provides chirp mass and distance; the additional measurement of \ddot{f} would give a direct test of the dominance of gravitational wave radiation in the frequency evolution. Tidal interaction between white dwarfs in detached systems before the onset of mass transfer will give rise to distinct deviations of the frequency evolution as compared to systems with no or little tidal interaction. The strength of the tidal interaction is virtually unknown, with estimates ranging over many orders of magnitude (MARSH ET AL., 2004), although the high temperature of the white dwarf in the recently discovered 12 min double white dwarf (figure 2.8) may suggest efficient tidal heating (PIRO, 2011). Knowledge of the strength of the tides is important not only for understanding the physics of tides in general and of white dwarf interiors, but has important consequences for the tidal heating (and possibly optical observability) of NGO sources and the stability of mass transfer between white dwarfs (FULLER & LAI, 2011; MARSH, 2011; RACINE ET AL., 2007; WILLEMS ET AL., 2010).

In globular clusters, dynamical interactions may produce eccentric double white dwarf systems, which can be used to constrain white dwarf properties and masses (VALSECCHI ET AL., 2011).

Physics of mass-transfer stability

Detached ultra-compact binaries will evolve to shorter and shorter periods due to the angular momentum loss through gravitational wave radiation. At sufficiently short orbital period (a few minutes) one of the stars becomes larger than its Roche lobe – the equipotential surface that crosses the minimum of the potential between the two stars – and material “leaks” out of the potential well of one star upon the other star. Depending on the difference between the change of the radius of this star and the Roche lobe upon mass transfer, there may be positive or negative feedback, leading to either limited, stable mass transfer, or a runaway mass-transfer instability.

For double white dwarfs and white dwarf-neutron star binaries the stability of the ensuing mass transfer has important consequences, for the number of detectable sources, as well as for a number of open astrophysical questions. The stable systems will form interacting binaries, AM CVn systems or ultra-compact X-ray binaries, that can be detected through their gravitational wave (GW) emissions. **NGO** will detect a number of detached double white dwarfs and AM CVn systems that are so close to the onset of mass transfer that the stability of the mass transfer can be tested directly by comparing their numbers. In addition, **NGO** will detect several ultra-compact X-ray binaries at the very early stages of mass transfer, providing a test of the mass transfer stability in these systems as well (MARSH, 2011).

For AM CVn systems, a major uncertainty in the mass-transfer stability is again the tidal interaction between the two white dwarfs. Most likely the mass transfer will proceed via the direct impact configuration: due to the proximity of the two stars, the mass transfer stream lands directly on the surface of the accreting white dwarf, rather than wrapping around the accreting stars and interacting with itself to form a flat accretion disk in the plane of the orbit (MARSH & STEEGHS, 2002; WEBBINK, 1984). The stability of the mass transfer depends critically on the tidal interaction between the two white dwarfs (MARSH ET AL., 2004): In the absence of any tidal interaction, there will be additional angular momentum loss from the orbit due to the transfer of angular momentum from the orbit to the accreting star which will consequently spin up. This is different from cases where the accretion is via a disc for which most of the angular momentum generally is stored in the disc and eventually via very efficient tidal interaction put back into the orbit. Efficient tidal coupling between the accreting star and the companion has the ability to return the angular momentum back to the orbit (SEE D’SOUZA ET AL., 2006; RACINE ET AL., 2007), thus reducing the magnitude of the spin-up.

The difference between efficient and inefficient tidal coupling is rather dramatic: the fraction of double white dwarfs estimated to survive the onset of mass transfer can drop from about 20 % to 0.2 % (NELEMANS ET AL., 2001) depending on assumptions about the tidal coupling. This difference is easily measurable with **NGO**. Short-term variations in the secular evolution of the systems experiencing mass transfer will change the frequency evolution, but are likely to be rare and will not prevent the detection of these systems (STROEER & NELEMANS, 2009).

For ultra-compact X-ray binaries, the stability issue is completely different. At the onset, the mass transfer is orders of magnitude above the Eddington limit for a neutron star (the mass transfer rate at which the potential energy liberated in the accretion can couple to the infalling gas to blow it away). For normal stars and white dwarfs, this would likely lead to a complete merger of the system, but the enormous amount of energy liberated when matter is falling into the very deep potential well of a neutron star allows matter to be dumped on it at rates up to a thousand times the Eddington limit if the white dwarf has a low mass (SEE YUNGELSON ET AL., 2002). This allows the formation of ultra-compact X-ray binaries from white dwarf-neutron star pairs. **NGO** will unambiguously test this prediction by detecting several tens of ultra-compact X-ray binaries with periods between 5 and 20 minutes.

Double white dwarf mergers

The 80 % to 99.8 % of the double white dwarfs that experience run-away mass transfer and merger give rise to quite spectacular phenomena. Mergers of double white dwarfs have been proposed as progenitors of single subdwarf O and B stars, R Corona Borealis stars and maybe all massive white dwarfs (e.g. WEBBINK, 1984). In addition, the merger of a sufficiently massive double white dwarf can be a trigger for type Ia supernova events (SEE PAKMOR ET AL., 2010). Alternatively, if the merger does not lead to an explosion, a (rapidly spinning) neutron star will be formed. This is one possible way to form isolated millisecond radio pulsars as well as magnetars, which have been proposed as sites for short gamma-ray bursts (e.g. LEVAN ET AL., 2006).

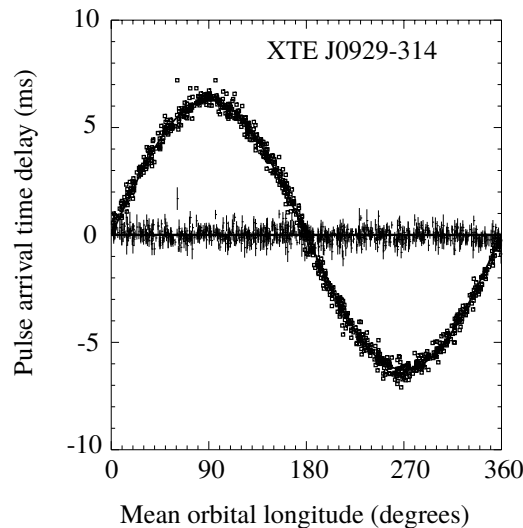


Figure 2.9.: Imprint of the 40 min orbital period on the arrival times of the (5.4 ms) X-ray pulsations in the ultra-compact X-ray binary XTE J0929-314. From GALLOWAY ET AL. (2002).

There is severe uncertainty about how the actual merger process takes place. Original estimates were that it is a truly dynamical process, taking one or two orbits only. If that is true, is not expected that **NGO** will witness the actual merger of a double white dwarf as the event rate in our Galaxy is too low. It will just detect the shortest-period binaries known, expected at a period of about two minutes and give an extremely good estimate of their merger rate. However, if the actual merger takes many orbits as recently found in simulations (DAN ET AL., 2011), **NGO** may observe them directly, thus testing these theories.

By measuring (chirp) masses and coalescence times, **NGO** will directly determine the merger rate for double white dwarfs with different masses which can then be compared with the rates and population of their possible descendants determined by other means (STROEER ET AL., 2011).

Neutron star and black hole binaries

The current observational and theoretical estimates of the formation rate of neutron star binaries are highly uncertain and predict several tens of neutron star binaries to be detected by **NGO** (e.g. BELCZYNSKI ET AL., 2010; NELEMANS ET AL., 2001). The number of ultra-compact stellar-mass black hole binaries in the Galaxy is even more uncertain (e.g. BELCZYNSKI ET AL., 2002); furthermore, these binaries are likely to be detectable only through their **GW** emission as they are electromagnetically quiet. **NGO** will thus constrain the formation rate estimates and the numbers of neutron star binaries and ultra-compact stellar mass black hole binaries. As the systems can be seen throughout the Galaxy, the samples for all these populations will be *complete at the shortest periods*. Thus, the sample will be independent of selection effects such as those present in radio pulsar surveys and X-ray surveys that pick up only transient X-ray sources. In addition, by the time **NGO** will fly, Advanced **LIGO** and Virgo will likely have detected a number of double neutron star mergers from far away galaxies, so these measurements together will test our ability to extrapolate our population models from our own galaxy to the rest of the universe.

A special situation might arise in the millisecond X-ray pulsars in ultra-compact X-ray binaries. In the last decade, observations of X-ray pulsations from many ultra-compact X-ray binaries have enabled astrophysicists to determine the rotation rate of the neutron star in the binary using the **NASA** mission **Rossi X-Ray Timing Explorer** (RXTE) (WIJNANDS, 2010). As had been expected on theoretical grounds, neutron stars are spinning rapidly several hundred times per second due to the angular momentum gained from infalling matter. The measurements give credence to the idea that these rapidly spinning neutron stars observed as millisecond radio pulsars are descendants of accreting neutron stars in binary systems (e.g. BHATTACHARYA & VAN DEN HEUVEL, 1991). However, the exact role of ultra-compact binaries in the formation of these pulsars has yet to be established. The distribution of spin periods discovered in X-ray binaries suggests additional neutron star angular momentum loss on top of the plasma physics interaction between the accretion and magnetic field of the spinning neutron stars

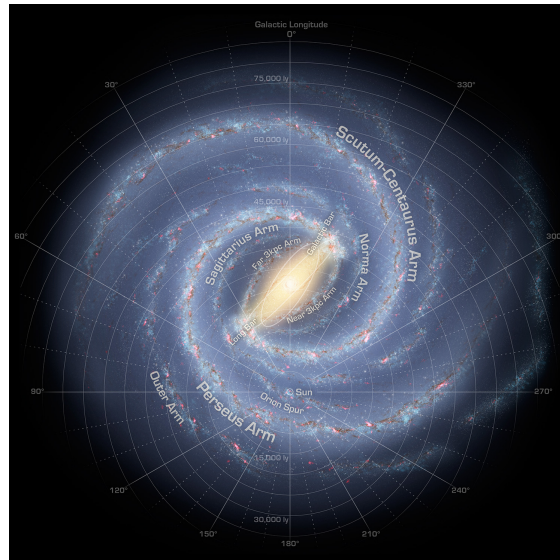


Figure 2.10.: *Spitzer GLIMPSE model of the Milky Way, showing bulge, bar and spiral arms. The resolved binaries are expected to trace the old stellar populations of the Milky Way. Courtesy NASA/JPL-Caltech/R. Hurt (SSC/Caltech)*

(CHAKRABARTY ET AL., 2003) which could be due to strong gravitational wave emission (BILDSTEN, 1998; but see WATTS ET AL., 2008; and PATRUNO ET AL., 2011). In that case, ultra-compact X-ray binaries might be the only sources that could be studied simultaneously with **NGO** and ground based detectors, with **NGO** detecting the orbital period and the ground based detector detecting the neutron star spin period (figure 2.9).

2.3.6. Studies of galactic structure with NGO

NGO will measure the sky position and distance of several hundred binaries, constraining the mass distribution in the Galaxy and providing an independent distance estimate to the Galactic centre. The level and shape of the Galactic foreground will constrain the relative contributions of thin disk, thick disk and halo populations and their properties. For several hundred sources the orbital inclination will be determined to better than 10 degrees, allowing to test if binaries are statistically aligned with the Galactic disk.

One of the major capabilities of **NGO** is that it will determine distances for hundreds of compact binaries by measuring their \dot{f} (see equation (2.2)). The ability of **NGO** to determine distances depends on the mission lifetime, as larger life times lead to more accurate \dot{f} measurements. The directional dependence of the Galactic foreground as well as the directional accuracy for the resolved systems allow a statistical assessment of the contributions of the different Galactic components (see figure 2.10) such as the Galactic bulge (with its bar), the thin and thick disc and the Galactic halo.

The *Galactic centre* is one of the most interesting areas of the Galaxy, with a central massive black hole surrounded by a dense assembly of stars with intriguing properties. Dynamical effects, in particular mass segregation, will lead to many interactions close to the central black hole so that wide binaries will become tighter or will be disrupted (FOR A REVIEW SEE ALEXANDER, 2005). This likely leads to an increase in the number of ultra-compact binaries as well as the possibility of **EMRIs** (see 2.5.1). **NGO** will allow to put much more stringent constraints on these populations than current observations (SEE *e.g.* ROELOFS ET AL., 2007), which are limited by the electromagnetic faintness of the sources, or theoretical predictions, which are limited by our current understanding of the processes leading to compact binary formation. Distance determinations to the many ultra-compact binaries around the Galactic centre will allow for an independent distance determination.

The level and shape of the double white dwarf foreground as well as the distribution of resolved sources will provide information on the *scale height* of the ultra-compact binary population (BENACQUISTA & HOLLEY-BOCKELMANN, 2006) in the *disc of the Galaxy*.

The distribution of sources in the *Galactic halo* will be significantly different from the other Galactic components. In principle the halo population is expected to be much smaller than the rest of the Galaxy (RUITER ET AL., 2009; YU & JEFFERY, 2010), but it might be enhanced as the formation and evolution of binaries in the halo may have been quite different. Such old and metal-poor population can locally be studied only in globular clusters, where the formation and evolution of binaries is generally completely altered by dynamical effects. Two of the known **AM CVn** systems may belong to the halo. They have very low metal abundances and have anomalous velocities. If true this implies that a large number of **AM CVn** stars are in the halo, maybe as many as in the rest of the Galaxy. The **NGO** directional sensitivity will immediately pick up any strong halo population if it exists.

Finally, for many of the resolved sources the **NGO** measurements will also provide an accurate estimate of their orbital inclination. For the first time, this will give hints on the dynamics of the formation of binaries from interstellar clouds, because it will test if the the angular momentum vectors of the binaries are in a statistical way related to the overall angular momentum of the Galaxy.

2.4. Astrophysical Black Holes

NGO science objectives and investigations relevant to this section

2. Trace the formation, growth and merger history of massive black holes.
 - 2.1 Trace the formation, growth and merger history of massive black holes with masses $10^5 M_{\odot} - 10^7 M_{\odot}$ during the epoch of growth of quasi-stellar objects and widespread star formation ($0 < z < 5$) through their coalescence in galactic halos.
 - 2.2 Capture the signal of coalescing massive black hole binaries with masses $2 \times 10^4 M_{\odot} - 10^5 M_{\odot}$ in the range of $5 < z < 10$ when the universe is less than 1 Gyr old.

Cosmic Vision scientific questions addressed by this section

- 3.3 Matter under extreme conditions
Probe gravity theory in the very strong field environment of black holes and other compact objects, and the state of matter at supra-nuclear energies in neutron stars
- 4.2 The universe taking shape
Find the very first gravitationally-bound structures that were assembled in the universe – precursors to today’s galaxies, groups and clusters of galaxies – and trace their evolution to the current epoch
- 4.3 The evolving violent universe
Trace the formation and evolution of the supermassive black holes at galaxy centres – in relation to galaxy and star formation – and trace the life cycles of matter in the universe along its history

The NGO Science Objectives are listed in chapter 2.

2.4.1. Overview

Astrophysical black holes appear to come in nature into two flavours: the “stellar mass” black holes of $3 M_{\odot}$ to approximately $100 M_{\odot}$ resulting from the core collapse of very massive stars, and the “supermassive” black holes of $10^6 M_{\odot} - 10^9 M_{\odot}$ that, according to the accretion paradigm, power the luminous quasi-stellar objects (QSOs). The former light up the X-ray sky, albeit only in our neighbourhood, as stellar mass black holes fade below detection limits for larger distances. The latter are detected as active galactic nuclei (AGN), over the whole cosmic time available to our current telescopes. Electromagnetic evidence of black holes of mass in the range of approximately $100 M_{\odot}$ and $10^6 M_{\odot}$ is less common, due to the intrinsic difficulty of detecting such faint sources in external galaxies. However, it is in this mass interval, elusive to electromagnetic observations, that the history of supermassive black hole growth is imprinted.

Supermassive black holes inhabit bright galaxies, and are ubiquitous in our low-redshift universe. The discovery of close correlations between the mass of the supermassive black hole with key properties of the host has led to the notion that black holes form and evolve in symbiosis with their galaxy host. In agreement with the current paradigm of hierarchical formation of galactic structures and with limits imposed by the cosmic X-ray background light, astrophysical black holes are believed to emerge from a population of *seed* black holes with masses from about $100 M_{\odot} - 10^5 M_{\odot}$, customarily called *intermediate mass black holes*. The mass and spin of these black holes change sizably in these interactions as they evolve over cosmic time through intermittent phases of copious accretion and merging with other black holes in galactic halos. In a galactic merger, the black holes that inhabit the two colliding galaxies, spiral in, under the action of dynamical friction, and *pair* on sub-galactic scales forming a Keplerian binary: *binary black holes* thus appear as inescapable outcome of galaxy assembly. When two massive black holes coalesce, they become one of the loudest sources of gravitational waves in the universe.

NGO is expected to target coalescing binaries of $10^5 M_{\odot} - 10^7 M_{\odot}$ during the epoch of widespread cosmic star formation ($0 < z < 6$), and to capture the signal of a coalescing binary of $10^4 M_{\odot} - 10^5 M_{\odot}$ out to redshift $z \lesssim 20$, much beyond the era of the earliest known QSOs. Gravitational waveforms carry information on the spins of the black holes that New Gravitational wave Observatory (NGO) will measure with exquisite precision, providing a diagnostic of the mechanism of black hole growth. The detection of coalescing black holes not only

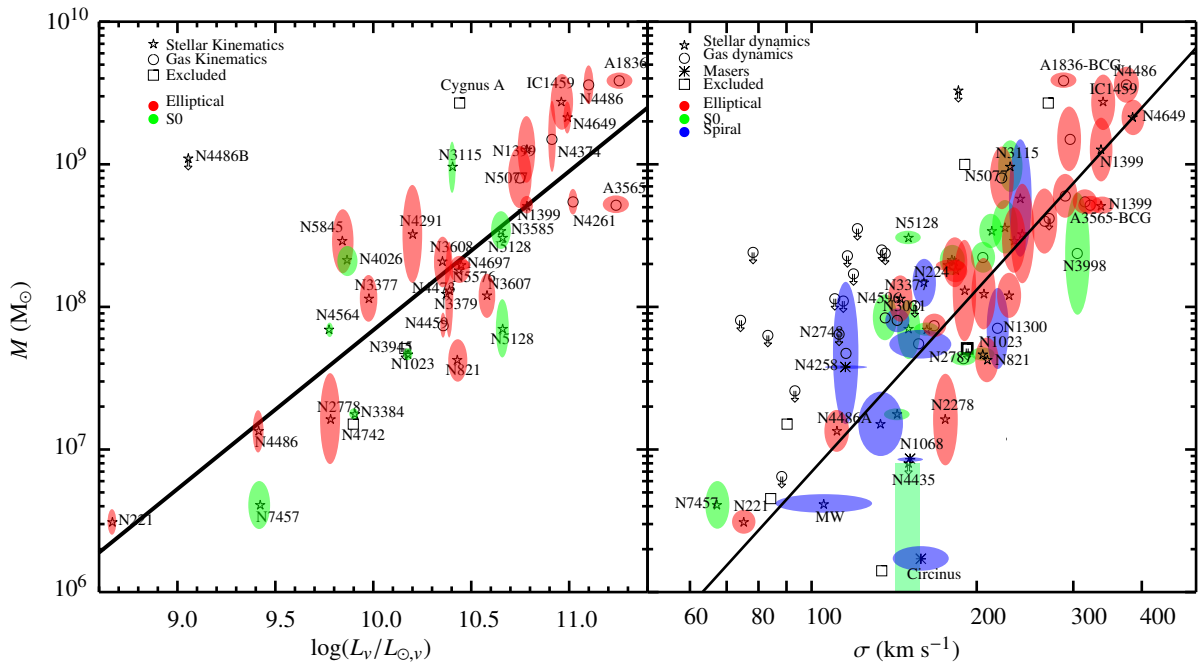


Figure 2.11.: The correlation between the black hole mass M_{\bullet} and the luminosity of the host galaxy's stellar bulge (left), and the host galaxy's bulge velocity dispersion σ (right) for all detections in galaxies near enough for current instruments to resolve the region in which the black hole mass dominates the stellar and gas dynamics (ADAPTED FROM GÜLTEKIN ET AL., 2009)

will shed light into the phases of black hole growth and QSO evolution, but will pierce deep into the hierarchical process of galaxy formation.

2.4.2. Black holes in the realm of the observations

Supermassive black holes appear to be a key component of galaxies. They are ubiquitous in near bright galaxies and share a common evolution. The intense accretion phase that supermassive black holes experience when outshining as QSOs and AGN erase information on how and when the black holes formed. It is this information that NGO aims at unravelling.

Dormant and active supermassive black holes

QSOs are active nuclei that are so luminous that they often outshine their galaxy host. They are sources of electromagnetic energy, with radiation emitted across the spectrum, almost equally, from X-rays to the far-infrared, and in a fraction of cases, from γ -rays to radio waves. Their variability on short timescales reveals that the emitting region is compact, only a few light hours across.

There is now scientific consensus that the electromagnetic power from QSOs and from the less luminous AGNs results from accretion onto a supermassive black hole of $10^7 M_{\odot} - 10^9 M_{\odot}$ (KROLIK, 1999; SALPETER, 1964; ZEL'DOVICH & NOVIKOV, 1964). Escaping energy in the form of radiation, high velocity plasma outflows, and ultra relativistic jets is generated with high efficiency ($\varepsilon \sim 10\%$, higher than nuclear reactions) just outside the event horizon, through magnetic and viscous stresses on parcels of gas orbiting in the gravitational potential of the black hole. The accretion paradigm has been, and still is, at the heart of the hypothesis of black holes as being “real” sources in our cosmic landscape. NGO will offer the new perspective of revealing these black holes as powerful sources of gravitational waves.

Massive black holes are tiny objects compared to their host galaxies. The event horizon of a Kerr black hole of mass M_{\bullet} has size $R_{\text{horizon}} \sim GM_{\bullet}/c^2$ far smaller than the optical radius of the galaxy host, $R_{\text{horizon}} \sim 10^{-11} R_{\text{gal}}$.

The distance to which a black hole affects the kinematics of stars (the gravitational influence radius) is $R_{\text{grav}} \sim GM_{\bullet}/\sigma^2$ that as well is small compared to the optical radius of the host, $R_{\text{grav}} \sim 10^{-4} R_{\text{gal}}$ (σ is the

velocity dispersion of the stars of the galactic bulge). For a long time the QSO and more generally the AGN phenomena were depicted as caused by a process exclusively confined to the nuclear region of the host.

This picture of disjoint black hole and galaxy evolution changed with the advent of the Hubble Space Telescope (HST) (FERRARESE & FORD, 2005). Observations of almost all bright galaxy spheroids in the near universe by HST reveal that the velocities of stars and gas start to rise in a Keplerian fashion at their centres, highlighting the presence of a dark point-mass which dominates the central gravitational potential. The same observations provide the mass of this dark object, hypothesised to be a quiescent black hole. The proximity of these galaxies to Earth allows for a full optical characterisation of the host, and this has ultimately led to the discovery of tight correlations (depicted in figure 2.11 from GÜLTEKIN ET AL.) between the black hole mass M_{\bullet} and the luminosity and velocity dispersion σ of the stars (FERRARESE & MERRITT, 2000; GEBHARDT ET AL., 2000). The relations state that galaxy spheroids with higher stellar velocity dispersions, *i.e.* with deeper gravitational potential wells and accordingly higher stellar masses and luminosities, host heavier central black holes with little dispersion in the correlation. Thus more massive galaxies grow more massive black holes: the black hole “sees” the galaxy that it inhabits, and the galaxy “sees” the black hole at its centre despite its small influence radius (HÄRING & RIX, 2004; MAGORRIAN ET AL., 1998; MARCONI & HUNT, 2003).

Consensus is rising that the $M_{\bullet} - \sigma$ relation of figure 2.11 is fossil evidence of a *co-evolution of black holes and galaxies*. The relation may have been rising along the course of galactic mergers and in episodes of self-regulated accretion, but its true origin and evolution at look-back times is still unclear (DI MATTEO ET AL., 2005; HOPKINS ET AL., 2008; KING, 2003; SILK & REES, 1998).

The census of black holes, from the study of the kinematics of stars and gas in nearby galaxies, has further led to the estimate of the black hole local mass density: $\rho_{\bullet} \sim 2 \times 10^5 M_{\odot} \text{Mpc}^{-3} - 5 \times 10^5 M_{\odot} \text{Mpc}^{-3}$ (LAUER ET AL., 2007; MARCONI ET AL., 2004). Whether this mass density traces the initial conditions, *i.e.* the mass since birth, obtained at most by rearranging individual masses via coalescences, or the mass acquired via major episodes of accretion in AGN phases can only be inferred using information resulting from the AGN demographics and from studies of the X-ray cosmic background.

Two arguments provide clues about how much of the black hole growth occurred through accretion of gas, in phases when the black hole is active as AGN. The first is the existence of a limiting luminosity for an accreting black hole, corresponding to when the radiation pressure force equals gravity. Above this limit material that would be responsible of the emission can not fall onto the black hole, as it is pushed away. This limit is the Eddington luminosity $L_E = 4\pi GM_{\bullet} m_p c / \sigma_T \sim 10^{46} \text{erg s}^{-1} (M_{\bullet} / 10^8 M_{\odot})$ (σ_T and m_p are the Thomson cross section and proton mass). The AGN luminosity L is normally a fraction $f_E \lesssim 1$ of the Eddington luminosity since as soon as L approaches L_E , the radiation pressure force against gravity self-regulates the accretion flow to $L \sim L_E$, providing also a lower bound to M_{\bullet} . The second is that “light is mass”, *i.e.* that any light output from accretion (at a luminosity level $L = \varepsilon \dot{M} c^2$) increases the black hole’s mass at a rate $dM_{\bullet}/dt = (1 - \varepsilon)\dot{M}$, where \dot{M} is the rest-mass accreted per unit time, and ε the accretion efficiency, *i.e.* how much of the accreted mass is converted into radiation. Accordingly, the black hole’s mass increases in relation to the self-regulated flow in an exponential fashion with an e -folding time $\tau_{\text{BH}} \approx 4.7 \times 10^8 \varepsilon [f_E (1 - \varepsilon)]^{-1} \text{yr}$. For $\varepsilon \approx 0.1$ (typical of radiatively efficient accretion onto a non-rapidly rotating black hole) and $f_E \approx 0.1$, this timescale is short (about 3%) compared to the age of the universe, indicating that black holes can enhance their mass via accretion by orders of magnitude.

Active black holes in galaxies are known to contribute to the rise of a cosmic X-ray background resulting mostly from unresolved and obscured AGN of mass $10^8 M_{\odot} - 10^9 M_{\odot}$, in the redshift interval $0.5 < z < 3$ (MERLONI, 2004). As energy from accretion is equivalent to mass, the X-ray light present in the background mirrors the increment in mass experienced by the black holes, over cosmic history due to accretion. This mass-density increment is found to be $\Delta\rho_{\bullet} \approx 3.5 \times 10^5 (\varepsilon/0.1)^{-1} M_{\odot} \text{Mpc}^{-3}$ (MARCONI ET AL., 2004; SOLTAN, 1982). As the contribution to the local (zero redshift) black hole mass density ρ_{\bullet} results from black holes of comparable mass $10^8 M_{\odot} - 10^9 M_{\odot}$, the close match between the two independent measures, ρ_{\bullet} and $\Delta\rho_{\bullet}$, indicates that radiatively efficient accretion ($\varepsilon \approx 0.1$) played a large part in the building of supermassive black holes in galaxies, from redshift $z \sim 3$ to now. It further indicates that information residing in the initial mass distribution of the, albeit unknown, black hole seed population is erased during events of copious accretion, along the course of cosmic evolution.

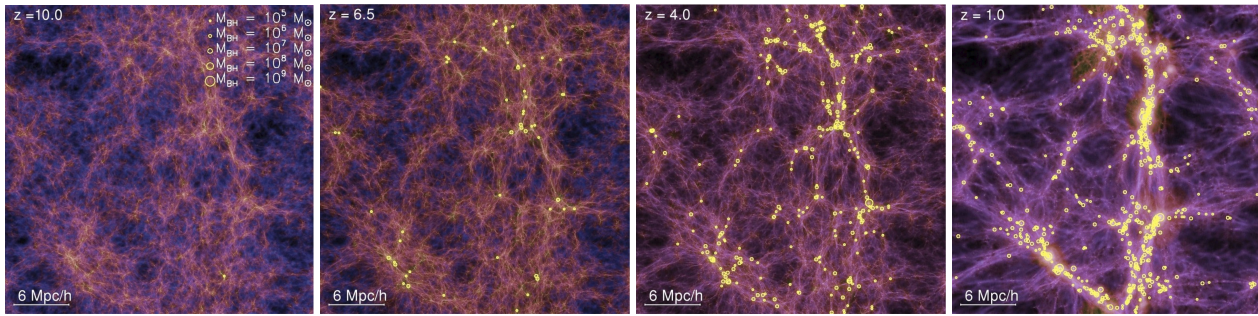


Figure 2.12.: A state-of-art hydrodynamical simulation by DI MATTEO ET AL. (2008) visualising the cosmic evolution of the baryonic density field and of their embedded black holes, in the Λ CDM cosmology. Each panel shows the same region of space ($33.75 h^{-1}$ Mpc on a side) at different redshift, as labelled. The circles mark the positions of the black holes, with a size that encodes the mass, as indicated in the top left panel (numerical force resolution limits the lowest black hole mass to $10^5 M_{\odot}$). The projected baryonic density field is colour-coded with brightness proportional to the logarithm of the gas surface density. The images show that the black holes emerge in halos starting at high redshift (as early as $z \sim 10$) and later grow by gas inflows that accompany the hierarchical build-up of ever larger halos through merging. As the simulation evolves, the number of black holes rapidly increases and larger halos host increasingly larger black holes. No black holes as massive as $10^9 M_{\odot}$ are present in the simulated box because they are extremely rare.

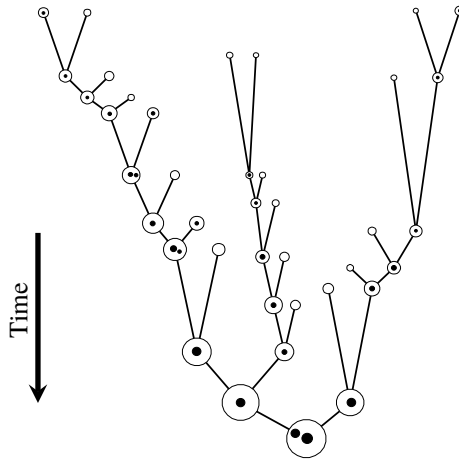


Figure 2.13.: A cartoon of the merger-tree history for the assembly of a galaxy and its central black hole, through the mergers of smaller galaxies and the coalescences of their black holes.

Massive black holes in the cosmological framework

Black holes are expected to transit into the mass interval to which **NGO** is sensitive along the course of their cosmic evolution. **NGO** will then map and mark the loci where galaxies form and cluster, using black holes as clean tracers of their assembly by capturing gravitational waves emitted during their coalescence, that travelled undisturbed from the sites where they originated.

These key findings hint in favour of the existence, at any redshift, of an underlying population of black holes of a smaller variety, with masses of $10^4 M_{\odot} - 10^7 M_{\odot}$ that grew in mass along cosmic histories inside their galaxies, through episodes of merging and accretion. The evolution of black holes mimics closely that of their host galaxies within the currently favoured cosmological paradigm: a universe dominated by cold dark matter (CDM). Observations show that the mass content of the universe is dominated by **CDM**, with baryons contributing only at a 10 % level to the **CDM**, and that the spectrum of primordial density perturbations contains more power at lower masses (MO ET AL., 2010). Thus, at the earliest epoch, the universe was dominated by small density perturbations. Regions with higher density grow in time, to the point they decouple from the Hubble flow and collapse and virialise forming self gravitating halos. The first objects that collapse under their own self-gravity are small halos that grow bigger through mergers with other halos and accretion of surrounding matter. This is a bottom

up path, and the process is known as hierarchical clustering. As halos cluster and merge to build larger ones, baryons follow the Λ CDM halo potential well and, similarly, black holes form and evolve in the same bottom-up fashion (VOLONTERI ET AL., 2003; WHITE & REES, 1978; WYTHE & LOEB, 2002). State-of-the-art hydrodynamical cosmological simulations (DI MATTEO ET AL., 2008) illustrate (figure 2.12) where and when the massive black hole form and how they are connected with the evolving background baryonic density field. As illustrated in figure 2.12 and as inferred in statistical models based on the extended Press-Schechter formalism, most of the black holes transit into the mass interval for which **NGO** is sensitive during their cosmic evolution (VOLONTERI ET AL., 2003). Figure 2.13 sketches and simplifies conceptually the complex net terminating with the formation of a bright galaxy at zero redshift, highlighting the sites where black holes form, cluster within halos, pair with other black holes, and eventually coalesce.

Black holes in the sensitivity window of **NGO**

Middleweight black holes of $10^5 M_{\odot}$ are observed in the near universe, but knowledge is rather incomplete. **NGO** will investigate a mass interval which is fundamental to understand the origin and growth of supermassive black holes and to which we are blind with our current electromagnetic techniques. Due to the transparency of the universe to gravitational waves at any redshift, **NGO** will explore black holes of $10^4 M_{\odot} - 10^5 M_{\odot}$ out to a redshift $z \lesssim 20$, tracing the rise of the population.

Is there any observational evidence of black holes of this variety in the universe, relevant for **NGO**? The Milky Way hosts in its bulge a black hole of $4 \times 10^6 M_{\odot}$ (GHEZ ET AL., 2008; GILLESSEN ET AL., 2009), providing an example of a black hole that does *not* fall into the population traced by the luminous **QSOs**. Black holes in the mass range $10^5 M_{\odot} - 10^7 M_{\odot}$ are now increasingly found in low mass spiral galaxies and dwarfs with and without a bulge (KUO ET AL., 2011; XIAO ET AL., 2011). Evidence also exists that some of these low mass black holes of $M < 10^5 M_{\odot}$ cohabit nuclear star clusters (BEKKI & GRAHAM, 2010; FERRARESE ET AL., 2006; WEHNER & HARRIS, 2006). Dwarf galaxies in the galactic field are believed to undergo a quieter merger and accretion history than their brighter analogues. They may represent the nearest example of low mass halos from which galaxy assembly took off. Dwarf galaxies are thus the preferred site for the search of pristine black holes (VOLONTERI & NATARAJAN, 2009). NCG 4359, a close-by bulgeless, disk dwarf is a compelling example, as it houses a black hole of only $3.6 \times 10^5 M_{\odot}$ (PETERSON ET AL., 2005). This key discovery shows that nature provides a channel to black hole formation also in galaxies with potential wells much shallower than those of the massive spheroids. These middleweight mass black holes were likely numerous at very high redshifts, but are almost invisible given their low intrinsic luminosity. If present, they would also become invisible to electromagnetic observations near redshift $z \gtrsim 11$ as close to this redshift the intergalactic medium becomes opaque to their light, due to intervening absorption of the neutral hydrogen (FAN ET AL., 2006B; MIRALDA-ESCUDE, 1998). ULAS J1120+0641 holds the record of being the further distant known **QSO**, at redshift $z = 7.085 \pm 0.003$, and hosts a very massive black hole of $\sim 2 \times 10^9 M_{\odot}$ (MORTLOCK ET AL., 2011). Its light was emitted before the end of the reionisation, *i.e.* before the theoretically predicted transition of the interstellar medium from an electrically neutral to an ionised state. **NGO** can discover middleweight black holes beyond redshift $z \gtrsim 11$, probing their rise during the early stages of galaxy formation and clustering.

2.4.3. The merger of galaxies, the coalescing of their black holes

The path of black holes to coalescence in a galaxy merger is complex as various physical mechanisms involving the interaction of the black holes with stars and gas need to be at play and work effectively, acting on different scales from kpc down to 10^{-3} pc. Only at the smallest scales gravitational waves guide the inspiral to coalescence. **NGO** will trace the last phase of this evolution, when the black hole horizons are about to touch.

A grand collision between two galaxies of comparable mass (called major merger) is a destructive event or more correctly a transformation, as the two galaxies, after merging, form a new galaxy with a new morphology. Individual stars do not collide during the merger as they are tiny compared to the distances between them. Their energy however varies violently in the interaction, as the gravitational potential changes widely with time when

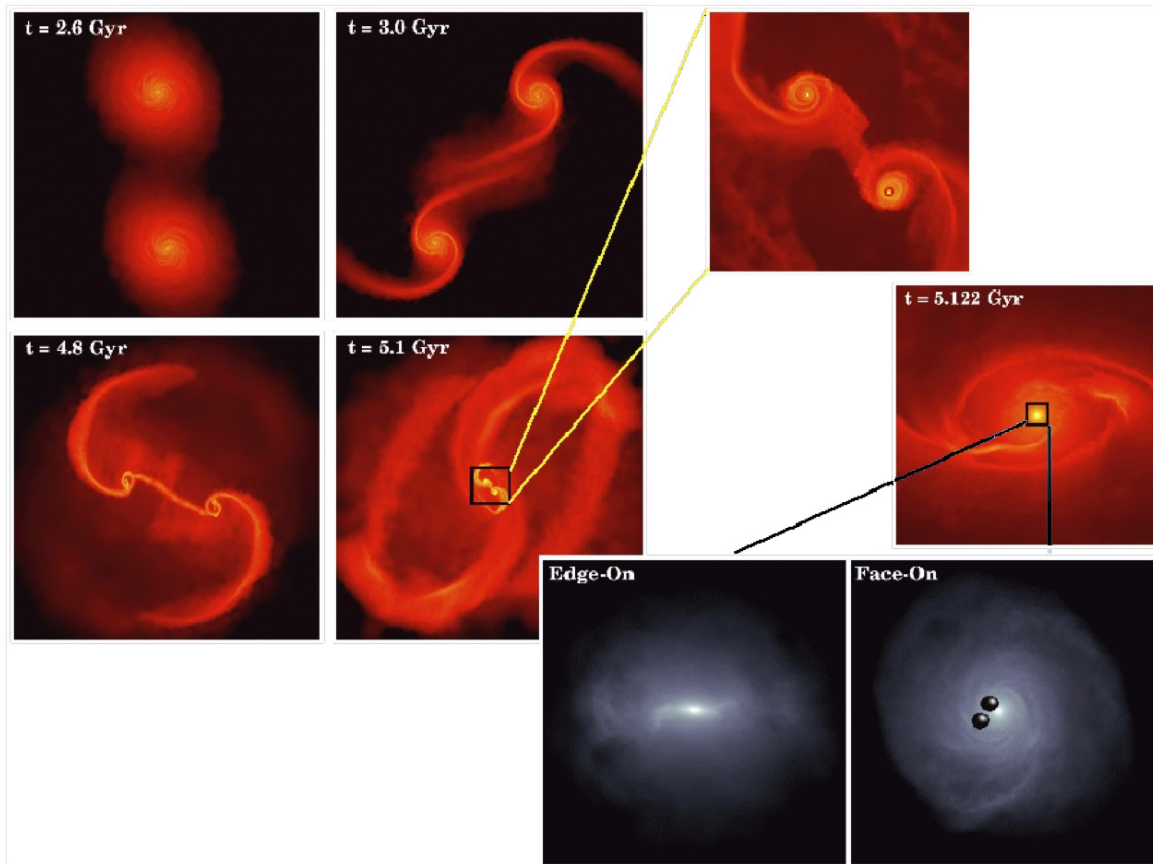


Figure 2.14.: The different stages of the merger between two identical Milky-Way-like gas-rich disc galaxies (FROM MAYER ET AL., 2007). The panels show the density maps of the gas component in logarithmic scale, with brighter colours for higher densities. The four panels to the left show the large-scale evolution at different times. The boxes are 120 kpc on a side (top) and 60 kpc on a side (bottom). During the interaction tidal forces tear the galactic discs apart, generating spectacular tidal tails and plumes. The panels to the right show a zoom in of the very last stage of the merger, about 100 million years before the two cores have fully coalesced (upper panel), and 2 million years after the merger (middle panel), when a massive, rotating nuclear gaseous disc embedded in a series of large-scale ring-like structures has formed. The boxes are now 8 kpc on a side. The two bottom panels, with a grey colour scale, show the detail of the inner 160 pc of the middle panel; a massive nuclear disc, shown edge-on (left) and face-on (right), forms in the aftermath of the merger (of $10^9 M_{\odot}$). The two black holes continue to sink inside the disc and form a Keplerian binary; they are shown in the face-on image.

the new galaxy forms. Gas clouds collide instead along the course of the merger: new stars form, and streams of gas flow in the nuclear region of the newly forming galaxy. Massive black holes in a grand collision behave like stars, and a key question rises, relevant to the science case for **NGO**: *Do black holes coalesce as their galaxies merge?*

The fate of black holes in merging galaxies can only be traced using numerical simulations at the limits of current numerical resolution. Not only single black holes are tiny, but also binary black holes are. They form a binary system when the mass in stars enclosed in the binary orbit becomes negligible compared to the total mass M of the binary, and the Keplerian velocities of the two black holes exceed the velocity σ of the stars. This occurs when their relative separation a_B decreases below their gravitational influence radius GM/σ^2 , i.e. when $a_B \lesssim 10^{-4} - 10^{-5} R_{\text{gal}}$. Binary black holes on the verge of coalescing within less than a Hubble time are even smaller, as they touch when their separation is of the size of the event horizon. The timescale for coalescence by gravitational waves only is a sensitive function of the binary separation, scaling as a_B^4 (PETERS, 1964). Therefore, gravitational waves guide the inspiral only when the separation is less than a critical value $a_{\text{GW}} \sim 0.003 a_B (M/10^6 M_{\odot})^{1/4}$ that is of 0.01 pc – 0.001 pc for a circular binary in the **NGO** mass interval. Typical orbital periods at a_{GW} are of a few years to tens of years, and the relative velocities of the holes are as high as 3000 km/s – 5000 km/s.

Black holes have to travel a distance from 0.1 kpc – 10 kpc down to 0.01 pc – 0.001 pc, before entering the gravitational wave inspiral regime in a galaxy. Given the huge dynamical range, different physical mechanisms are guiding their sinking (COLPI & DOTTI, 2011). We can distinguish four phases for the dynamics of black holes on their way to and after merging: the *pairing phase* (I) when the black holes pair on galactic scales following the dynamics of the galaxies they inhabit until they form a Keplerian binary (on pc scales);(II) the *binary phase*, when the Keplerian binary continues to harden at the centre of the galaxy remnant;(III) the *GW phase*, when black hole inspiral is dominated by loss of energy and angular momentum by GW; and finally(IV) the *recoiling phase* when the now single black hole either oscillates or escapes the galaxy following gravitational recoil.

In major merger of galaxies the black holes pair under the action of dynamical friction acting on the disc or bulge which they inhabit, and in this way are driven toward the centre of the forming new galaxy (BEGELMAN ET AL., 1980). Pairing occurs on the timescale of a galactic merger of a few billion years. A few million years after the new galaxy has formed, a Keplerian binary forms on the scale of 1 pc – 10 pc, under the action of dynamical friction by stars and gas: figure 2.14 shows the collision of two galactic gaseous discs in a simulated merger of two galaxies similar to the Milky Way. The merger ends with the formation of a Keplerian binary immersed in a central massive nuclear disc (MAYER ET AL., 2007). The subsequent hardening of the binary orbit (phase II) is controlled by the inflow of stars from larger radii, and by the gas rotating around in a circum-binary disc (COLPI & DOTTI, 2011; MERRITT & MILOSAVLJEVIĆ, 2005). In gas rich environments, and for black holes of mass smaller than about $10^7 M_{\odot}$, gas-dynamical torques on the binary suffice to drive the system down to the gravitational wave inspiral domain if the gas does not fragment in stars (CUADRA ET AL., 2009; GOULD & RIX, 2000). . In gas poor galaxies, stars, that are ubiquitous, can scatter individually off the black holes, causing the binary to harden progressively (MERRITT & MILOSAVLJEVIĆ, 2005; QUINLAN, 1996; SESANA ET AL., 2007A, 2008A). . These stars approach the binary from nearly radial orbit, and shrink the binary down to the GW phase, if they are present in sufficient number to carry away the energy and angular momentum necessary for the decay down to a_{GW} . These stars, ejected with high velocities, are lost by the galaxy, and the timescale of binary hardening depends on the rate at which new stars are supplied from far-out distances. Self-consistent high resolution direct N-body simulations indicate that the stellar potential of the remnant galaxy retains, in response to the anisotropy of the merger, a sufficiently high degree of rotation and triaxiality to guarantee a large reservoir of stars on centrophilic orbits that can interact with the black holes down to the transit from the binary phase to the GW phase (BERCZIK ET AL., 2006; KHAN ET AL., 2011; PRETO ET AL., 2011). When coalescence occurs the new black hole retains memory of the orbit orientation relative to the black hole spins prior to merge “recoiling”, as gravitational waves are emitted anisotropically (BAKER ET AL., 2008B). The kicked black hole, that moves away from the centre, may return after a few oscillations down to the nuclear regions of the host galaxy, or escape the galaxy depending on the magnitude of the recoil (GUALANDRIS & MERRITT, 2008).

2.4.4. Dual, binary and recoiling AGN in the cosmic landscape

Dual AGN, *i.e.* active black holes observed during their pairing phase, offer the view of what we may call the galactic “precursors” of black hole binary coalescences. They are now discovered in increasing numbers, in large surveys. By contrast, evidence of binary and recoiling AGN is poor, as the true nature of a number of candidates is not yet established fully. NGO only will offer the unique view of an imminent binary merger by capturing its loud gravitational wave signal.

Surprisingly, the closest example of an imminent merger is in our Local Group. Andromeda (M31) along with a handful of lesser galaxies does not follow Hubble’s law of cosmic expansion: it is falling toward us at a speed of about 120 km/s. M31 is a member of a group of galaxies, including the Milky Way, that form a gravitationally bound system, the Local Group. M31 and the Milky Way each house a massive black hole (VAN DER MAREL ET AL., 1994) and are on a collision course, with a merger possibly before the Sun expands into a red giant (COX & LOEB, 2008). Observations are now revealing the presence of many colliding galaxies in the universe, and in a number of cases two active black holes are visible through their X-ray or radio emission, as highlighted in figure 2.15. More than two hundred dual AGN have been recently discovered in the large SDSS survey (LIU ET AL., 2011), challenging our notions on the mechanisms that trigger AGN activity, and offering the view of galactic mergers in their very early phases.

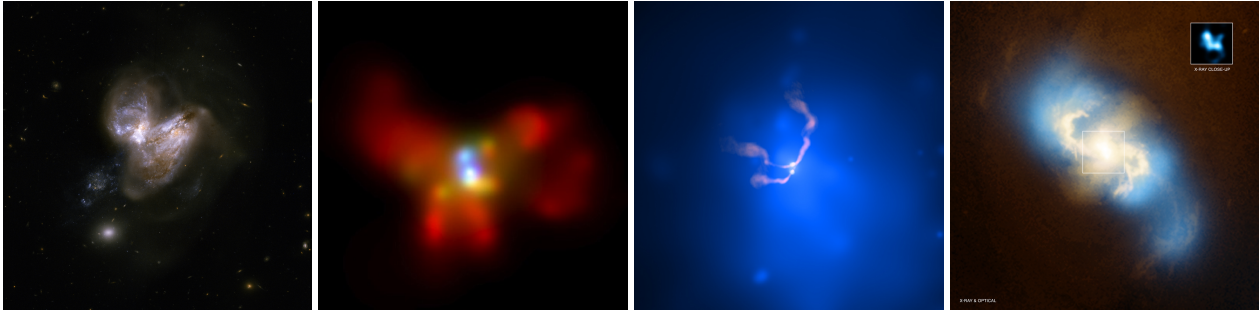


Figure 2.15.: Active black holes in colliding galaxies. Arp 299 (leftmost panel) is the interacting system resulting from the collision of two gas-rich spirals, and hosts a dual AGN, *i.e.* two black holes “active” during the pairing phase. The accreting black holes are visible in the X-rays and are located at the optical centres of the two galaxies, at a separation of 4.6 kpc (BALLO ET AL., 2004). X-ray view of NGC 6240 (middle left panel) an ultra luminous infrared galaxy considered to be a merger in a well advanced phase (KOMOSSA ET AL., 2003). X-ray observations with the Chandra Observatory let to the discovery of two strong hard X-ray unresolved sources embedded in the diluted soft X-ray emission (red) of a starburst. The dual AGN are at a separation of 700 pc. Composite X-ray (blue)/radio (pink) image of the galaxy cluster Abell 400 (middle right panel) showing radio jets immersed in a vast cloud of multimillion degree X-ray emitting gas that pervades the cluster. The jets emanate from the vicinity of two supermassive black holes (a dual radio-loud AGN) housed in two elliptical galaxies in the very early stage of merging. Composite optical and X-ray image of NGC 3393 (rightmost panel), a spiral galaxy with no evident signs of interaction. In its nucleus, two active black holes have been discovered at a separation of only 150 pc (FABBIANO ET AL., 2011). The closeness of the black holes embedded in the bulge, provide a hitherto missing observational point to the study of galaxy-black hole evolution: the phase when the black holes are close to forming a Keplerian binary. The regular spiral morphology and predominantly old circum-nuclear stellar population of this galaxy, indicates that a merger of a dwarf with a large spiral led to the formation of the binary (CALLEGARI ET AL., 2011).

By contrast, the existence of binary AGN, *i.e.* of two active black holes when bound in a Keplerian fashion, is still debatable at the observational level, as they are rare objects, difficult to identify (VOLONTERI ET AL., 2009). Two cases deserve attention. The first is the case of 0402+379, a radio source in an elliptical galaxy showing two compact flat-spectrum radio nuclei, only 7 pc apart (RODRIGUEZ ET AL., 2006). The second case is OJ 287, a source displaying a periodic variability of 12 years that has been interpreted as being a Keplerian binary with evidence of orbital decay by emission of GW (VALTONEN ET AL., 2008). A number of sub-parsec binary black hole candidates have been found in large surveys based on the recognition that gas clouds orbiting one/two black hole(s) can leave an imprint in the optical spectra of the AGN, *i.e.* large velocities offsets among various emission lines, . but further observations will be necessary to assess their true nature (ERACLEOUS ET AL., 2011; TSALMANTZA ET AL., 2011). Recoiling AGN, *i.e.* recoiling black holes observed in an active phase (LOEB, 2007; MERRITT ET AL., 2009B), , have been searched recently, and several groups claim (or disclaim) a discovery (BOGDANOVIĆ ET AL., 2009; CIVANO ET AL., 2010; DOTTI ET AL., 2009B; JONKER ET AL., 2010; KOMOSSA ET AL., 2008). If confirmed, these discoveries would unmistakably prove that black hole coalescences are unescapable events that occur in the universe.

The most remarkable, albeit indirect, evidence of coalescence events is found in bright elliptical galaxies that are believed to be product of mergers. Bright elliptical galaxies show light deficits (cores) in their surface brightness profiles, *i.e.* lack of stars in their nuclei, and this missing light correlates with the mass of the central black hole (KORMENDY & BENDER, 2009; MERRITT, 2006). Thus, cores are evidence of a history of binary black holes that scour out the nuclear stars via three-body scattering prior to merge (BOYLAN-KOLCHIN ET AL., 2004; GUALANDRIS & MERRITT, 2008). . Lastly, mergers change the black hole’s spin directions according to angular momentum conservation: reorientation of the black hole spin following coalescence can explain the X-shaped radio galaxies where an old dim jet coexists with a new jet with different orientation (MERRITT & EKERS, 2002). If the jet is launched along the black hole spin, X-shaped jets would be sign again of accomplished coalescence events.

2.4.5. Seed black holes

The path of formation of the first black holes in galaxies is unknown. There exist major uncertainties in the physical mechanism(s) conducive to the gravitational collapse of a system, either a star or a very massive quasi-star, into a black hole. The mass of seed black holes ranges from a few hundred to few hundred thousand solar masses, depending on the formation mechanism. Seed black holes later grow, following different evolutions according to their different formation path and clustering inside dark matter halos, and **NGO** aims at disentangling different routes of evolution. **NGO** will considerably reduce the uncertainty about the nature of the seed population, as the number of observed mergers and the inferred masses will allow to decide among the different models or, in the case of concurrent models, determine their prevalence.

Models of hierarchical structure formation predict that galaxy sized dark matter halos start to become common at redshift $z \sim 10 - 20$ (MO ET AL., 2010). This is the beginning of the non linear phase of density fluctuations in the universe, and hence also the epoch of baryonic collapse leading to star and galaxy formation. Different populations of seed black holes have been proposed in the range $100 M_{\odot} - 10^6 M_{\odot}$ (VOLONTERI, 2010). *Small* mass seeds ($100 M_{\odot} - 1000 M_{\odot}$) may result from the collapse of the first generation of stars (Pop III) that form from unstable metal-free gas clouds, at $z \sim 20$ and in halos of $10^6 M_{\odot}$ (ABEL ET AL., 2002; OMUKAI & PALLA, 2003; TEGMARK ET AL., 1997). Pop III stars as massive as $260 M_{\odot}$ or larger collapse directly into a black hole of similar mass after only about 2 Myr (HEGER ET AL., 2003; MADAU & REES, 2001). *Large* seeds may form in heavier halos (of $10^8 M_{\odot}$ from the collapse of unstable gaseous discs of $10^4 M_{\odot} - 10^6 M_{\odot}$. This route, ending with the formation of a very massive quasi-star, is possible if an intense ultraviolet background light and a highly turbulent velocity field suppress gas-cloud fragmentation, in an environ of low metallicity (BEGELMAN ET AL., 2006; LODATO & NATARAJAN, 2006). The massive quasi-star burns hydrogen and helium in its core and collapses into a black hole, as shown in numerical simulations (MONTERO ET AL., 2011; SHIBATA & SHAPIRO, 2002).

The subsequent step is to follow the evolution of the black hole seeds according to the growth of the halos they inhabit, and the mode of accretion (VOLONTERI & BEGELMAN, 2010). This is a complex, model-dependent process that **NGO** can trace, probing coalescences of growing seeds out to very large redshift.

2.4.6. Evolving massive black hole spins via coalescence and accretion events

Masses and spins evolve dramatically following coalescence and accretion events. The spin offers the best diagnostics on whether the black holes prior to coalescence have experienced either coherent or chaotic accretion episodes. Both, mass and spin, are directly encoded into the gravitational waves emitted during the merger process. **NGO** will measure the masses and spins of the black holes prior to coalescence, offering unprecedented details on how black hole binaries have been evolving along of the course of the galactic merger and along cosmic history.

Astrophysical black holes are fully described by the mass M_{\bullet} and angular momentum \mathbf{J} , referred to as spin. The modulus of \mathbf{J} is usually specified in terms of the dimensionless spin parameter a_{\bullet} defined so that $J = a_{\bullet}(GM_{\bullet}^2/c)$. For a specified mass M_{\bullet} , a black hole described by **GR** cannot have $a_{\bullet} > 1$, without showing a naked singularity (and this is forbidden by the Cosmic Censorship conjecture). Both coalescences and accretion change M_{\bullet} , J (or a_{\bullet}) and the orientation of \mathbf{J} in a significant manner.

Spins in black hole coalescences

With the advent of numerical relativity, it became possible to accurately determine the evolution of the initial spins of the black holes to the final spin of the remnant black hole in a merger event (BAKER ET AL., 2006B; CAMPANELLI ET AL., 2006A; CENTRELLA ET AL., 2010; PRETORIUS, 2005; REZZOLLA ET AL., 2008A).

Numerical relativity simulations for equal mass, non spinning black holes find a spin $a_{\bullet} = 0.68646 \pm 0.00004$ (SCHEEL ET AL., 2009) for the merged black hole, resulting from the angular momentum of the orbit. Extrapolation of black hole coalescences with large initial spins (larger than approximately 0.9) exactly aligned with the orbital angular momentum find a final $a_{\bullet} = 0.951 \pm 0.004$ (MARRONETTI ET AL., 2008). When mergers occur with retro- and pro-grade orbits equally distributed, as it is expected in the case of astrophysical black holes, the average spin

of the merger remnant is about 0.7, close to the expectation for non spinning holes (BERTI & VOLONTERI, 2008; HUGHES & BLANDFORD, 2003)

For almost any configuration of spins and mass ratio, the emission pattern of the gravitational wave is anisotropic, leading to a *gravitational recoil* (CAMPANELLI ET AL., 2007; GONZÁLEZ ET AL., 2007; LOUSTO & ZLOCHOWER, 2011B). Numerical studies show that initial non-spinning black holes, or binaries with spins aligned with the orbital angular momentum are recoiling with a velocity below about 200 km/s. By contrast, the recoil is dramatically larger, up to approximately 5000 km/s, for binaries of comparable mass and black holes with large spins in peculiar non-aligned configurations (LOUSTO & ZLOCHOWER, 2011A). Thus unexpectedly, spins (regulated by coalescence and accretion) affect the retention fraction of black holes in galactic halos, and this has consequences on the overall evolution of black holes in galaxies. (SCHNITTMAN & BUONANNO, 2007; VOLONTERI ET AL., 2010).

Spin and black hole accretion

The evolution of mass and spin of astrophysical black are strongly correlated, also when considering accretion. Spins determine directly the radiative efficiency $\varepsilon(a_\bullet)$ and so the rate at which mass is increasing. In radiatively efficient accretion discs (SHAKURA & SUNYAEV, 1973), ε varies from 0.057 (for $a_\bullet = 0$) to 0.151 (for $a_\bullet = 0.9$) and 0.43 (for $a_\bullet = 1$). Accretion on the other hand determines black hole spins since matter carries with it angular momentum (the angular momentum at the innermost stable circular orbit of a Kerr black hole). A non-rotating black hole is spun-up to $a_\bullet = 1$ after increasing its mass by a factor $\sqrt{6}$, for prograde accretion (BARDEEN, 1970). Conversely, a maximally rotating black hole is spun-down by retrograde accretion to $a_\bullet \sim 0$, after growing by a factor $\sqrt{3/2}$.

Accretion imposes limits on the black hole spin. Gas accretion from a geometrically thin disc limits the black-hole spin to $a_\bullet^{\text{acc}} = 0.9980 \pm 0.0002$, as photons emitted by the disc and with angular momentum anti-parallel to the black hole spin are preferentially captured, having a larger cross section, limiting its rotation (THORNE, 1974). The inclusion of a jet, as studied in magneto-electrodynamic simulations, reduces this limit to $a_\bullet^{\text{jet}} \approx 0.93$ (GAMMIE ET AL., 2004), and changes in the accretion geometry produce a similar effect (POPHAM & GAMMIE, 1998).

How black holes are fed from the large scale down to the hole's influence radius (R_{grav}) is presently unknown, and the spin is sensitive to the way gas is accreted with time (VOLONTERI ET AL., 2007). Two limiting modes of accretion can occur. *Coherent accretion* refers to accretion from a geometrically thin disc, lasting longer than a few e -folding times. During coherent accretion the black hole can more than double its mass, bringing its spin up to the limit imposed by basic physics, either a_\bullet^{acc} or a_\bullet^{jet} . By contrast, *chaotic accretion* refers to a succession of accretion episodes that are incoherent, *i.e.* randomly oriented. The black hole can then either spin up or spin down and spin-down occurs when counter-rotating material is accreted, *i.e.* when the angular momentum \mathbf{L} of the disc is strongly misaligned with respect to \mathbf{J} (*i.e.* $\mathbf{J} \cdot \mathbf{L} < 0$). If accretion proceeds via short-lived, uncorrelated episodes with co-rotating and counter-rotating material equally probable, spins tend to be small (KING & PRINGLE, 2006): counter-rotating material spins the black hole down more than co-rotating material spins it up, as the innermost stable orbit of a counter-rotating test particle is located at a larger radius than that of a co-rotating particle, and accordingly carries a larger orbital angular momentum.

The direction of the black hole spin is also an important element in the study of black holes. In a viscous accretion disc that is misaligned with the spin of the black hole, Lense-Thirring precession of the orbital plane of fluid elements warps the disc, forcing the gas close to the black hole to align (either parallel or anti-parallel) with the spin of the black hole. Warping is a rapid process that causes alignment of the disc out to $100 R_{\text{horizon}} - 10^3 R_{\text{horizon}}$ (depending on a_\bullet , BARDEEN & PETERSON, 1975). Following conservation of total angular momentum, the black hole responds to the warping through precession and alignment, due to dissipation in the disc, evolving into a configuration of minimum energy where the black hole and disc are aligned (KING ET AL., 2005; PEREGO ET AL., 2009). This process is short (10^5 yrs) compared to the typical accretion time scale allowing astrophysical black holes to evolve into a quasi-aligned spin-orbit configuration prior to coalescence (DOTTI ET AL., 2010).

2.4.7. Cosmological massive black hole merger rate

Coalescence rates, as a function of redshift and in different mass bins, can only be inferred theoretically, using statistical models for the hierarchical build-up of cosmic structures. These models, firmly anchored to low redshift observations, indicate that the expected detection rates for **NGO** range between few and few hundred per year.

As **NGO** creates a new exploratory window on the evolution of black holes, covering a mass and redshift range that is out of the reach of current (and planned) instruments, its expected detection rate is by definition, observationally unconstrained. Today, we can probe dormant black holes down to masses of about $10^5 M_\odot$ in the local universe only, and their massive (*i.e.* heavier than $10^8 M_\odot$) active counterpart out to redshift $\gtrsim 6$ (FAN ET AL., 2006A). Any estimate of the **NGO** detection rate necessarily has to rely on extrapolations based on theoretical models matching the properties of the observable black holes population.

Observationally, the black hole merger rate can be inferred only at relatively low redshift, by counting the fraction of close pairs in deep galaxy surveys. Given a galaxy density per co-moving megaparsec cube n_G , a fraction of close pair ϕ , and a characteristic merger timescale \mathcal{T}_M , the merger rate density of galaxies (number of mergers per year per co-moving megaparsec cube), is given by $\dot{n}_M = \phi n_G / (2\mathcal{T}_M)$. Estimates of \dot{n}_M have been produced by several groups in the last decade (see XU ET AL., 2011 for a review), using deep spectroscopic galaxy surveys like **COMBO**, **COSMOS** and **DEEP2**. Surveys are obviously flux limited, and usually an absolute magnitude cutoff (which translate into a stellar mass lower limit) is applied to obtain a complete sample of galaxy pairs across a range of redshifts. The galaxy merger rate is therefore fairly well constrained only at redshift $z \lesssim 1$ for galaxies with stellar mass larger than approximately $10^{10} M_\odot$. From compilation of all the measurement (XU ET AL., 2011), typical average massive galaxy merger rates \dot{n}_M at $z < 1$ lie in the range $5 \times 10^{-4} < \dot{n}_M < 2 \times 10^{-3} h_{100}^3 \text{Mpc}^{-3} \text{Gyr}^{-1}$. By applying the black hole-host relations (GÜLTEKIN ET AL., 2009), the galaxy stellar mass cutoff is converted into a lower limit to the hosted black hole mass. Assuming a black hole occupation fraction of one (appropriate for massive galaxies) and integrating over the appropriate co-moving cosmological volume, this translates into an *observational* estimate of the *massive black hole merger rate* for $z < 1$ and $M > \text{few} \times 10^6 M_\odot$. These estimates can be compared to the rate predicted by Monte Carlo merger trees (VOLONTERI ET AL., 2003) based on the **EPS** (LACEY & COLE, 1993; PRESS & SCHECHTER, 1974), which are used to reconstruct the black hole assembly, and thus to infer **NGO** detection rates, in the Λ CDM cosmology. The evolutionary path can be traced back to very high redshift ($z > 20$) with high resolution via numerical **EPS** Monte Carlo realisations of the merger hierarchy. SESANA ET AL. (2008B) carried a detailed comparison of the merger rate predicted by such models in the $z < 1$ and $M > \text{few} \times 10^6 M_\odot$ range with those inferred by galaxy pair counting, finding a generally broad consistency within a factor of 2.

On the theoretical side, merger rates of massive black holes can be computed from semi-analytic galaxy formation models coupled to massive N-Body simulations tracing the cosmological evolution of dark matter halo (BERTONE ET AL., 2007; DE LUCIA ET AL., 2006; GUO ET AL., 2011), such as the Millennium Run (SPRINGEL ET AL., 2005). These models are generally bound to the limiting resolution of the underlying N-body simulations, and are therefore complete only for galaxy masses larger than approximately $10^{10} M_\odot$. In a companion study SESANA ET AL. also showed that the merging black hole mass functions predicted by **EPS** based merger trees are in excellent agreement with those extracted by semi-analytic galaxy formation model, in the mass range $M > 10^7 M_\odot$, where semi-analytic models can be considered complete. Merger rates obtained by **EPS** merger trees are therefore firmly anchored to low redshift observations and to theoretical galaxy formation models. Nevertheless, the lack of observations in the mass range of interest for **NGO** leaves significant room for modelling, and theoretical astrophysicists have developed a large variety of massive black hole formation scenarios that are compatible with observational constraints (BEGELMAN ET AL., 2006; KOUSHIAPPAS ET AL., 2004; LODATO & NATARAJAN, 2006; VOLONTERI ET AL., 2003). The predicted coalescence rate in the **NGO** window depends on the peculiar details of the models, ranging from a handful up to few hundred events per year (ENOKI ET AL., 2004; HAEHNELT, 1994; KOUSHIAPPAS & ZENTNER, 2006; RHOOK & WYITHE, 2005; SESANA ET AL., 2004, 2005, 2007B; WYITHE & LOEB, 2003). A recent compilation, encompassing a wide variety of assembly history can be found in (SESANA ET AL., 2011).

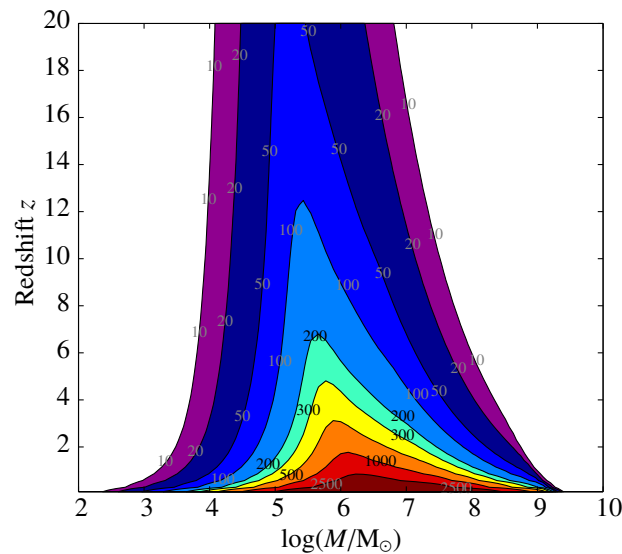


Figure 2.16.: Constant-contour levels of the sky and polarisation angle-averaged signal-to-noise ratio (SNR), for equal mass non-spinning binaries as a function of their total mass M and cosmological redshift z . The total mass M is measured in the rest frame of the source. SNR is computed using PhenomC waveforms (SANTAMARÍA ET AL., 2010) that includes the three phases of black hole coalescence (inspiral, merger, and ring-down, as described in the text).

2.4.8. Massive black hole binaries as gravitational waves sources: what can NGO discover?

Current electromagnetic observations are probing only the tip of the massive black hole distribution in the universe, targeting black holes with large masses, between $10^7 M_{\odot} - 10^9 M_{\odot}$. Conversely, NGO will be able to detect the gravitational waves emitted by black hole binaries with total mass (in the source rest frame) as small as $10^4 M_{\odot}$ and up to $10^7 M_{\odot}$, out to a redshift as remote as $z \sim 20$.

NGO is unique as it offers the opportunity of *directly* measuring the black hole spins.

NGO will detect fiducial sources out to redshift $z \lesssim 10$ with $\text{SNR} \gtrsim 10$ and so it will explore almost all the mass-redshift parameter space relevant for addressing scientific questions on the evolution of the black hole population. Redshifted mass will be measured to an unprecedented accuracy, up to the 0.1% – 1% level, whereas absolute errors in the spin determination are expected to be in the range 0.01 to 0.1, allowing reconstructing the cosmic evolution of massive black holes.

In the NGO window of detectability massive black hole binary coalescence is a three-step process comprising the *inspiral, merger, and ring-down* (FLANAGAN & HUGHES, 1998). The inspiral stage is a relatively slow, adiabatic process in which the black holes spiral together on near-circular orbits. The black holes have a separation wide enough so that they can be treated analytically as point particles within the post-Newtonian (PN) approximation of their binding energy and radiated flux (BLANCHET, 2006). The inspiral is followed by the dynamical coalescence, in which the black holes plunge and merge together, forming a highly distorted, perturbed remnant. At the end of the inspiral, the black holes velocities approach $v/c \sim 1/3$. At this stage, the PN approximation breaks down, and the system can only be described solving for the Einstein equation with direct numerical simulations. The distorted remnant settles into a stationary Kerr black hole as it *rings down*, by emitting gravitational radiation. This latter stage can be, again, modelled analytically in terms of black hole perturbation theory. At the end of the ring-down the final black hole is left in a quiescent state, with no residual structure besides its Kerr spacetime geometry.

In the recent years, there has been a major effort in constructing accurate GW waveforms inclusive of the inspiral merger and ring-down phases (BAKER ET AL., 2006B; CAMPANELLI ET AL., 2006A; HANNAM ET AL., 2007; PRETORIUS, 2005). The full waveform is computationally very demanding even for few orbital cycles. Full waveforms can be designed by stitching together the analytic PN waveform of the early inspiral with (semi)phenomenologically described merger and the ring-down forms (DAMOUR ET AL., 2011; PAN ET AL., 2011; SANTAMARÍA ET AL., 2010), calibrated against available numerical data. In the following estimations we will mostly employ phenomenological

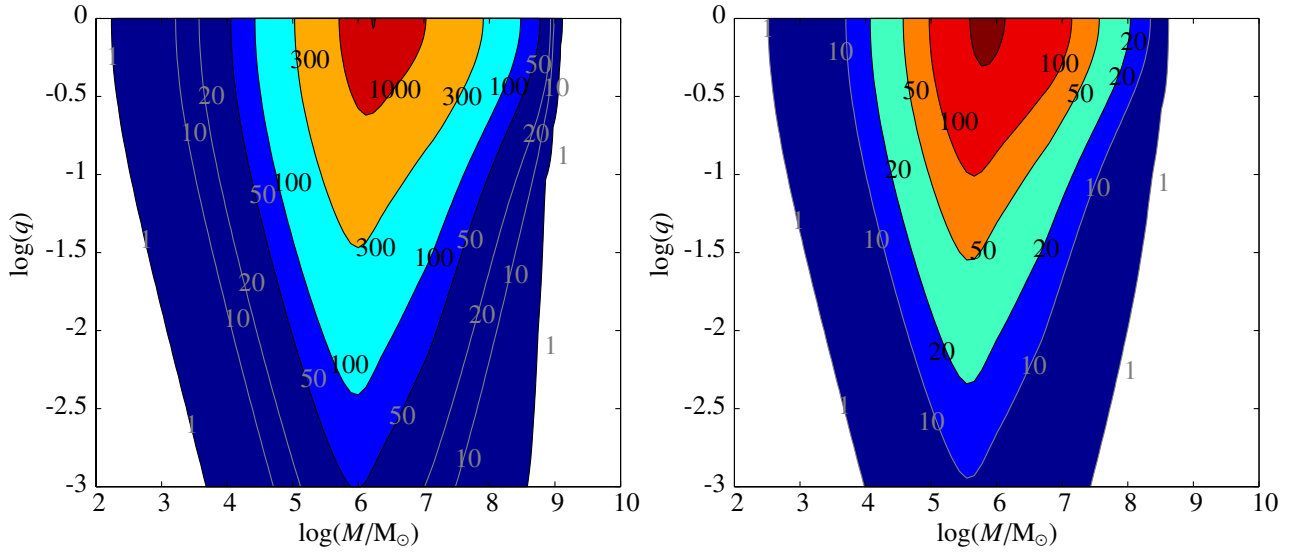


Figure 2.17.: The figure shows constant-contour levels of the sky and polarisation angle averaged signal-to-noise ratio (SNR) for non-spinning binaries, at cosmological redshift $z = 1$ (left panel) and $z = 4$, (right panel) in the M - q plane, where M is the total mass of the binary in the source rest frame, and q is the mass ratio. The SNR is computed from the full non spinning PhenomC waveform including inspiral, merger and ring-down, as in figure 2.16.

waveforms constructed in frequency domain as described in SANTAMARÍA ET AL. (2010). Self consistent waveforms of this type are available for non spinning binaries and for binaries with aligned spins (the so called PhenomC waveforms). In the case of binaries with misaligned spins, we use hybrid waveforms stitching together precessing PN waveforms for inspiral to PhenomC waveforms for the merger and ring-down by projecting the orbital angular momentum and individual spins onto the final momentum of the distorted black hole after merger. Given a waveform model we can probe NGO performances by computing the SNR generated in the detector by a GW source with any given set of parameters, in the relevant astrophysical range.

Detector performance

Figure 2.16 shows NGO SNR contour plots of equal mass coalescing binaries, in the rest-frame-total mass M and redshift z plane. Here we use PhenomC waveforms for non spinning binaries, and the SNR is averaged over all possible source sky locations and wave polarisation, for one-year observation. The plot highlights the capabilities of NGO in covering almost all the mass-redshift parameter space relevant to massive black hole astrophysics. It is of importance to emphasise that current electromagnetic observations are probing only the tip of the massive black hole distribution in the universe. Our current knowledge of massive black holes is bound to instrument flux limits, probing only the mass range $10^7 M_\odot - 10^9 M_\odot$ at $0 \lesssim z \lesssim 7$. Conversely, NGO will be able to detect the gravitational waves emitted by sources with total mass (in the source rest frame) as small as $10^4 M_\odot$, inaccessible to any other astrophysical probe, except in the near neighbourhoods. A binary with total mass in the interval $10^4 M_\odot - 10^7 M_\odot$ can be detected out to a redshift as remote as $z \sim 20$ with a $\text{SNR} \gtrsim 10$. By contrast, a binary as massive as a few $10^8 M_\odot$ can be detected with high SNR in our local universe ($z \lesssim 1$). Binaries with total mass between $10^5 M_\odot - 10^7 M_\odot$ can be detected with a $\text{SNR} \gtrsim 100$, between $0 \lesssim z \lesssim 5$. These intervals in mass and redshift can be considered as optimal for the census of the black hole population in the universe.

Figure 2.17 shows constant-contour levels of the SNR expected from binaries with different mass ratios q (defined as $q = m_2/m_1$ where m_2 is the mass of the less massive black hole in the binary) located at redshift $z = 1$ and $z = 4$. The plots show first the fading of the signal that occurs with decreasing q , as unequal mass binaries have lower strain amplitudes than equal mass binaries. Plots show also the fading of the signal with increasing redshift, and thus with increasing luminosity distance. Notice however that even at $z = 4$, binaries in the mass range $10^5 M_\odot - 10^7 M_\odot$ with mass ratio $q \lesssim 10^{-1}$ can be detected with $\text{SNR} \gtrsim 20$.

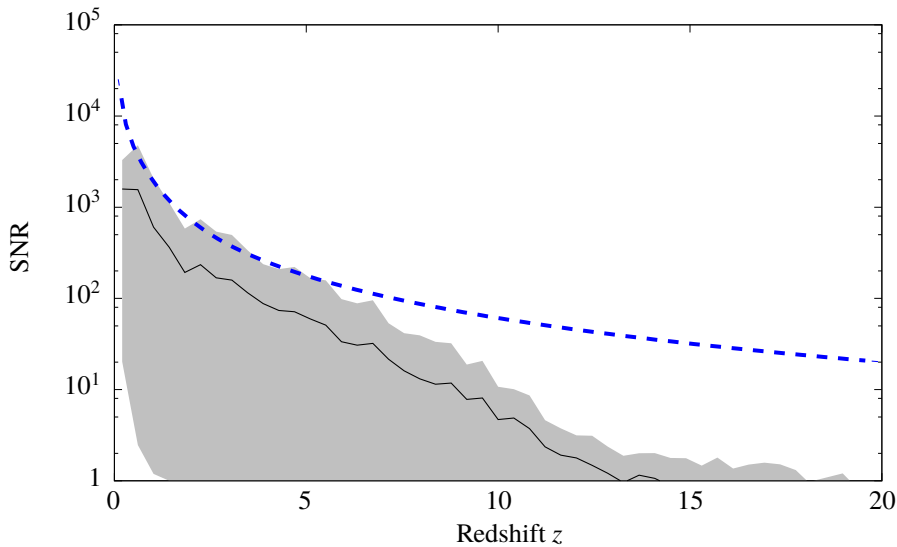


Figure 2.18.: SNR distribution as a function of cosmological redshift, computed using the inspiral, merger and ring-down waveform PhenomC for spinning binaries (SANTAMARÍA ET AL., 2010). The solid line corresponds to the mean value, and the grey area to the distribution corresponding to 10th and 90th percentile of SNR distribution. These results are based on a catalogue of 15360 sources obtained combining 25 realisations of each of the four fiducial massive black hole evolution models. The dashed-blue line indicates the sky-averaged SNR, for one year of integration, computed for an equal mass coalescing binary of $10^6 M_{\odot}$: the SNR is computed without including a model for the astrophysical evolution of the black holes, showing directly the instrument performance (SESANA ET AL., 2011).

Parameter estimation

Figures 2.16 and 2.17 describe the detectability of single events, and for these individual events, it is possible to extract information on the physical parameters of the source. Waveforms carry information on the redshifted mass (the mass measured at the detector is $(1 + z)$ the mass at the source location) and spin of the individual black holes prior to coalescence. The measure of the mass and spin is of importance in Astrophysics. Except for the Galactic centre, the mass of the astrophysical black holes is estimated with uncertainties ranging from 15 % to a factor of about 2, depending on the technique used, and the type of source. As far as spin is concerned, its measure is only indirect, and it is derived through modelling of the spectrum, or of the shape of emission lines, mainly by fitting the skewed relativistic $K\alpha$ iron line. There are few notable examples, but uncertainties are still large. By contrast, spins leave a distinctive peculiar imprint in the GW waveform.

In section 2.4.5 and section 2.4.6 we explored different routes to seed black hole formation and to their subsequent assembly and growth through mergers and accretion episodes. Different physically motivated assumptions lead to different black hole evolution scenarios, and, as highlighted above, the lack of observational constraints allowed theoretical astrophysicists to develop a large variety of massive black holes formation scenarios. To assess the astrophysical impact of NGO, we simulate observations assuming a fiducial set of four cosmological black hole evolution scenarios: SE refers to a model where the seeds have small (S) mass about $100 M_{\odot}$ (from Pop III stars only), and accretion is coherent, *i.e.* resulting from extended (E) accretion episodes: SC refers to a model where seeds are small but accretion is chaotic (C), *i.e.*, resulting from uncorrelated episodes; and finally LE and LC refer to a model where the seed population is heavy (L stands for large seeds of $10^5 M_{\odot}$) and accretion is extended and chaotic, respectively. The models are close to those used in previous studies by the LISA performance evaluation task force (ARUN ET AL., 2009). The only difference is that in the extended accretion model, spins are not assumed to be perfectly aligned to the binary orbital angular momentum. The angles of misalignment relative to the orbit are drawn randomly in the range 0° to 20° , consistent with the finding of recent hydrodynamical simulations of binaries forming in wet mergers (DOTTI ET AL., 2010). These models encompass a broad range of plausible massive black hole evolution scenarios, and we use them as a testbed for NGO capabilities in a fiducial astrophysical context. Each massive black hole binary, coalescing at redshift z , is characterised by the (rest frame) total mass $M = m_1 + m_2$ (with m_1 and m_2 the mass of the primary and

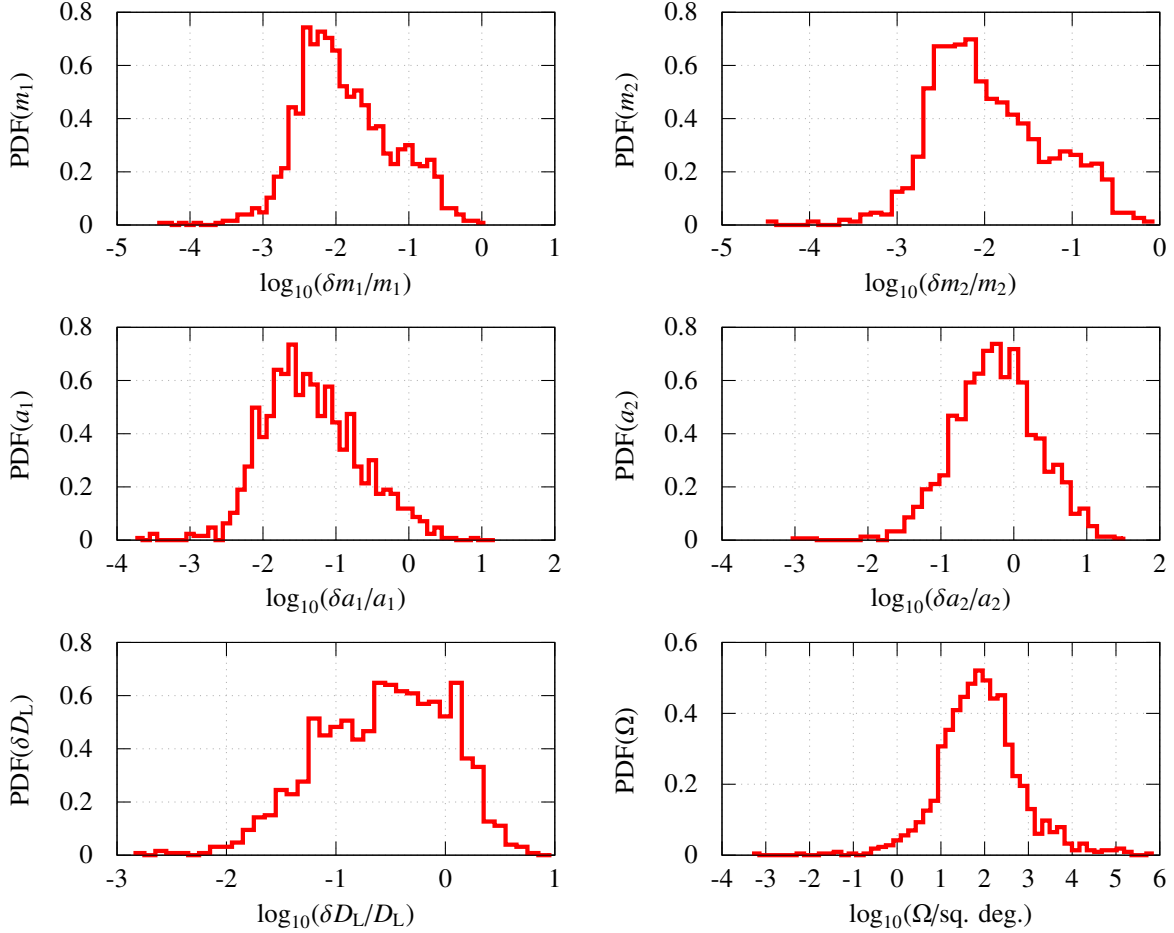


Figure 2.19.: Parameter estimation accuracy evaluated on a source catalogue, obtained combining ten Monte Carlo realisations of the coalescing massive black hole binary population, predicted by the four SE-SC-LE-LC models. The top panels show the distributions of the fractional errors in the estimation of the redshifted masses of the primary (left) and secondary (right) black hole. The middle panels show the absolute error distributions on the measurement of the primary (left) and secondary (right) black hole spin, while the bottom panels show the D_L fractional error distribution on the luminosity distance D_L , and the sky location accuracy $\Delta\Omega$ (in deg^2). Errors are evaluated considering full waveforms.

secondary black hole), mass ratio $q = m_2/m_1$, spin vectors \mathbf{J}_1 and \mathbf{J}_2 ; spin moduli are indicated with a_1 and a_2 . The orientation of the spins are drawn as described above for the extended (E) models, and completely random for the chaotic (C) models. Here we generate several Monte Carlo realisations of each model and we sum-up all the generated sources in a single “average” catalogue (we will consider models separately in the next section). Catalogues are generated by selecting M , q , z , a_1 , a_2 according to the distribution predicted by the individual models, and by randomising other source parameters (sky location, polarisation, inclination, initial phase, coalescence time) according to the appropriate distribution.

Figure 2.18 shows the average source SNR as a function of the source redshift. According to the simulated models, NGO will detect sources with $\text{SNR} \gtrsim 10$ out to $z \lesssim 10$. Note that the astrophysical capabilities of NGO are not limited by the detector design, but by the population of astrophysical sources. If there were a coalescing black hole binary of $10^4 M_\odot - 10^6 M_\odot$ out to redshift $z \sim 20$, NGO would reveal such a source. Our models, and accordingly our SNR distribution, do not include such an event.

Figure 2.19 shows error distributions in the source parameter estimation, for all the events in the combined catalogue. We used a hybrid approach of joining inspiral with PhenomC waveforms, as described above, to evaluate uncertainties based on the Fisher matrix approximation. It is found that individual black hole redshifted masses can be measured with unprecedented precision, *i.e.* with an error of 0.1% – 1%, on both components. No other astrophysical tool has the capability of reaching a comparable accuracy. As far as spins are concerned,

the analysis shows that the spin of the primary massive black hole can be measured with an exquisite accuracy, to a 0.01 to 0.1 absolute uncertainty. This precision in the measure mirrors the fact that the primary black hole leaves a bigger imprint in the waveform. The measurement is more problematic for a_2 that can be either determined to an accuracy of 0.1, or remain completely undetermined, depending on the source mass ratio and spin amplitude. We emphasise that the spin measure is a neat, direct measurement, that does not involve complex, often degenerate, multi-parametric fits of high energy emission processes.

The source luminosity distance error D_L has a wide spread, usually ranging from 50% to only few percent. Note that this is a direct measurement of the luminosity distance to the source, which, again, cannot be directly obtained (for cosmological objects) at any comparable accuracy level by any other astrophysical means. **NGO** is a full sky monitor, and the localisation of the source in the sky is also encoded in the waveform pattern. Sky location accuracy is typically estimated in the range 10 to 1000 square degrees.

2.4.9. Parameter estimation on fiducial massive black hole population models

NGO observations have the potential of constraining the astrophysics of massive black holes along their entire cosmic history, in a mass and redshift range inaccessible to conventional electromagnetic observations.

NGO will be an *observatory*. The goal is not only to detect sources, but also to extract valuable astrophysical information from the observations. While measurements for individual systems are interesting and potentially very useful for making strong-field tests of **GR** (see section 2.6.2), the properties of the set of massive black hole binary mergers that are observed which will carry the most information for astrophysics. Gravitational wave observations of multiple binary mergers may be used together to learn about their formation and evolution through cosmic history.

After signal extraction and data analysis, these observations will provide a catalogue of coalescing binaries, with measurements of several properties of the sources (masses, mass ratio, spins, distances, etc) and estimated errors. The interesting questions to ask are the following: *can we discriminate among different massive black hole formation and evolution scenarios on the basis of gravitational wave observations alone?* Given a set of observed binary coalescences, what information can be extracted about the underlying population? For example, will gravitational wave observations alone tell us something about the mass spectrum of the seed black holes at high redshift that are inaccessible to conventional electromagnetic observations, or about the poorly understood physics of accretion? This question was extensively tackled in (SESANA ET AL., 2011) in the context of LISA.

Selection among a discrete set of models

First we consider a discrete set of models. In the general picture of massive black hole cosmic evolution, the population is shaped by the *seeding process* and the *accretion history*. The four models we consider here are the same that were used and described by the LISA performance evaluation task force (ARUN ET AL., 2009), and follow their naming convention introduced in section 2.4.6: SE, SC, LE, and LC. We test here if **NGO** observations will provide enough information that will enable us to discriminate among the models, assuming that the universe is well described by one of these.

Each model predicts a *theoretical* distribution of coalescing massive black hole binaries. A given dataset D of observed events can be compared to a given model A by computing the likelihood $p(D|A)$ that the observed dataset D is a realisation of model A . When testing a dataset D against a pair of models A and B , we assign probability $p_A = p(D|A)/(p(D|A) + p(D|B))$ to model A , and probability $p_B = 1 - p_A$ to model B . The probabilities p_A and p_B are a measure of the relative confidence we have in model A and B , given an observation D . Once the **NGO** data set is available, each model comparison will yield this single number, p_A , which describes the confidence that model A is correct. Without an actual observed data only a statistical likelihood for achieving a certain confidence with future **NGO** observations can be obtained.

From independent realisations of the population of coalescing massive black hole binaries in the universe predicted by each of the four models, simulated gravitational wave observations are created by producing datasets D of observed events (including measurement errors), which were then statistically compared to the theoretical models. Considering only sources that are observed with a **SNR** larger than eight, setting a confidence threshold

Table 2.1.: Summary of all possible comparisons of the pure models. Results are for one year of observation with NGO. We take a fixed confidence level of $p = 0.95$. The numbers in the upper-right half of each table show the fraction of realisations in which the row model will be chosen at more than this confidence level when the row model is true. The numbers in the lower-left half of each table show the fraction of realisations in which the row model cannot be ruled out at that confidence level when the column model is true. In the left table we consider the trivariate M , q , and z distribution of observed events; in the right table we also include the observed distribution of remnant spins, S_r .

	Without spins					With spins			
	SE	SC	LE	LC		SE	SC	LE	LC
SE	×	0.48	0.99	0.99	SE	×	0.96	0.99	0.99
SC	0.53	×	1.00	1.00	SC	0.13	×	1.00	1.00
LE	0.01	0.01	×	0.79	LE	0.01	0.01	×	0.97
LC	0.02	0.02	0.22	×	LC	0.02	0.02	0.06	×

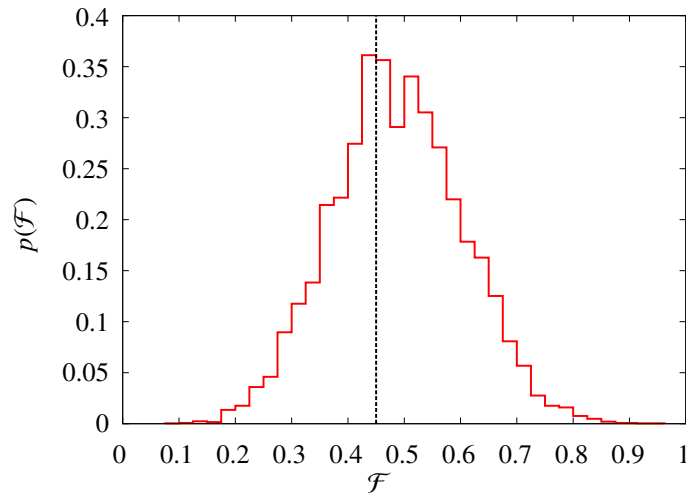


Figure 2.20.: Likelihood distribution of the mixing fraction \mathcal{F} , for a particular realisation of the model $\mathcal{F}[SE] + (1 - \mathcal{F})[LE]$. The true mixing parameter, marked by a dashed vertical line, was $\mathcal{F} = 0.45$.

of 0.95, and determining the fraction of realisations of model A yield a confidence $p_A > 0.95$ when compared to an alternative model B . This procedure is then repeated for every pair of models. For simplicity, only observations of **GW** from circular, non-spinning binaries were modelled. Therefore, each coalescing black hole binary in the population is characterised by only three intrinsic parameters – redshift z , mass M , and mass ratio q . The *theoretical* trivariate distribution in these parameters predicted by the models are compared to the *observed* values in the dataset D . In terms of gravitational waveform modelling, the analysis can therefore be considered extremely conservative.

Results are shown in the left hand panel of table 2.1, for a one year observation. The vast majority of the pair comparisons yield a 95 % confidence in the true model for almost all the realisations — we can perfectly discriminate among different models. Similarly, we can always rule out the alternative (false) model at a 95 % confidence level. Noticeable exceptions are the comparisons of models LE to LC and SE to SC, *i.e.*, among models differing by accretion mode only. This is because the accretion mode (efficient versus chaotic) particularly affects the spin distribution of the coalescing systems, which was not considered here. To extend this work, the analysis of the distribution of the merger remnant spins S_r was included and compared to the *theoretical* distribution predicted by the models to the *observed* values (including determination errors once again). The spin of the remnant can be reasonably determined in about 30 % of the cases only; however, adding this information, allows to almost perfectly discriminate between the LE and LC and the SE and SC models, as shown in the right hand panel of table 2.1.

Constrains on parametric models

In the preceding section we demonstrated the potential of **NGO** to discriminate among a discrete set of “pure” models given a priori. However, the true massive black hole population in the universe will probably result from a mixing of known physical processes, or even from a completely unexplored physical mechanism. A meaningful way to study this problem is to construct parametric models that depend on a set of key physical parameters, λ_i , describing, for instance, the seed mass function and redshift distribution, the accretion efficiency etc. and to investigate the potential of **NGO** to constrain these parameters. Such a parametric family of models is not available at the moment, but we can carry out a similar exercise by mixing two of our pure models, A and B , to produce a model in which the number of events of a particular type is given by $\mathcal{F}[A] + (1 - \mathcal{F})[B]$, where $[A]$ is the number of events of that type predicted by model A , $[B]$ is the corresponding number predicted by model B and \mathcal{F} is the “mixing fraction”. In this case we generate datasets D from a mixed model with a certain unknown \mathcal{F} , and we estimate the \mathcal{F} parameter by computing the likelihood that the data D is drawn from a mixed distribution, as a function of \mathcal{F} . A specific example is shown in figure 2.20. Here the underlying model is $\mathcal{F}[\text{SE}] + (1 - \mathcal{F})[\text{LE}]$, with $\mathcal{F} = 0.45$. **NGO** observations will allow us to pin-down the correct value of the mixing parameter with an uncertainty of ~ 0.1 . More complex examples of multi-model mixing can be found in (SESANA ET AL., 2011). Although highly idealised, this exercise demonstrate the potential of **NGO** observations to constrain the physics and astrophysics of massive black holes along their entire cosmic history, in a mass and redshift range inaccessible to conventional electromagnetic observations.

2.5. Extreme mass ratio inspirals and astrophysics of dense stellar systems

NGO science objectives and investigations relevant to this section

3. Explore stellar populations and dynamics in galactic nuclei
 - 3.1 Characterise the immediate environment of massive black holes in $z < 0.7$ galactic nuclei from extreme mass ratio capture signals.
 - 3.2 Discovery of intermediate-mass black holes from their captures by massive black holes.

Cosmic Vision scientific questions addressed by this section

- 3.3 Matter under extreme conditions

Probe gravity theory in the very strong field environment of black holes and other compact objects, and the state of matter at supra-nuclear energies in neutron stars

The NGO Science Objectives are listed in chapter 2.

Introduction – the Galactic Centre: a unique laboratory

The discovery, in the local universe, of dark, massive objects lurking at the centres of nearly all bright galaxies is one of the key findings of modern-day astronomy, the most spectacular being the case of the dark object in our OWN Galaxy (GHEZ ET AL., 2008; GILLESSEN ET AL., 2009). The nucleus of the Milky Way is one hundred times closer to Earth than the nearest large external galaxy Andromeda, and one hundred thousand times closer than the nearest QSO. Due to its proximity, it is the only nucleus in the universe that can be studied and imaged in great detail. The central few parsecs of the Milky Way house gas cloud complexes in both neutral and hot phases, a dense luminous star cluster, and a faint radio source SgrA* of extreme compactness (3 to 10 light minutes across). Observations, using diffraction-limited imaging and spectroscopy in the near-infrared, have been able to probe the densest region of the star cluster and measure the stellar dynamics of more than two hundred stars within a few light days of the dynamic centre. The latter is coincident, to within 0.1 arcsec, with the compact radio source SgrA*. The stellar velocities increase toward SgrA* with a Kepler law, implying the presence of a $(4 \pm 0.06 \pm 0.35) \times 10^6 M_{\odot}$ central dark mass (GILLESSEN ET AL., 2009). This technique has also led to the discovery of nearly thirty young stars that orbit the innermost region: the so called S0 (or S stars). These young stars are seen to move on Keplerian orbits, with S02 (or S2) the showcase star orbiting the putative black hole on a highly eccentric (0.88) orbit with a period of 15.9 years. The periapsis of this orbit requires a lower limit on the density of the dark point-like mass concentration of more than $10^{13} M_{\odot} \text{pc}^{-3}$ (MAOZ, 1998). Additionally, a lower limit of more than $10^{18} M_{\odot} \text{pc}^{-3}$ can be inferred from the compactness of the radio source (GENZEL ET AL., 2010). These limits provide compelling evidence that the dark point-mass at SgrA* is a black hole. A cluster of dark stars of this mass and density (e.g. composed of neutron stars, stellar black holes or sub-stellar entities such as brown dwarfs, planets and rocks) can not remain in stable equilibrium for longer than 10^7 years (MAOZ, 1998), and the only remaining, albeit improbable, hypothesis is a concentration of heavy bosons (a boson star, (COLPI ET AL., 1986)) or of hyperlight black holes (MAOZ, 1998, $M_{\bullet} < 0.005 M_{\odot}$). Overall, the measurements are consistent with a system composed of a massive black hole, and an extended close-to-isotropic star cluster, with the young S0 (or S) stars the only population showing a collective rotation pattern in their orbits.

2.5.1. Extreme Mass Ratio Inspirals in galactic nuclei

NGO will bring a new revolutionary perspective to the study of galactic nuclei. NGO will offer the deepest view of galactic nuclei, exploring regions to which we are blind using current electromagnetic techniques and probing the dynamics of stars in the space-time of a Kerr black hole, by capturing the gravitational waves emitted by stellar black holes orbiting the massive black hole.

Can we probe the nearest environs of a massive black hole other than the Galactic centre? Massive black holes are surrounded by a variety of stellar populations, and among them are compact stars. White dwarfs, neutron stars, and stellar black holes all share the property that they reach the last stable orbit around the central massive black hole before they are tidally disrupted. A compact star can either plunge directly toward the event horizon of the massive black hole, or gradually spiral in and fall into the hole, emitting gravitational waves. The latter process is the one of primary interest for **NGO**. Gravitational waves produced by inspirals of stellar compact objects into massive black holes are observable by **NGO**. The mass of the compact object is typically of the order of a few solar masses, while the mass of the central black holes detectable by **NGO** is from $10^4 M_{\odot}$ to $10^7 M_{\odot}$. Because the mass ratio for these binaries is typically around 10^5 , these sources are commonly referred to as **extreme mass-ratio inspirals (EMRIs)**.

The extreme mass ratio ensures that the inspiralling object essentially acts as a test particle in the background space-time of the central massive black hole. **EMRI** detections thus provide the best means to probe the environment of an astrophysical black hole and its stellar surroundings. White dwarfs, neutron stars, and stellar black holes can all in principle lead to observable **EMRI** signals. However, stellar black holes, being the most massive, are expected to dominate the observed rate for **NGO**, for two reasons: mass segregation tends to concentrate the heavier compact stars nearer the massive black hole, and black hole inspirals have higher signal-to-noise, and so can be seen within a much larger volume.

Three different mechanisms for the production of **EMRIs** have been explored in the literature. The oldest and best-understood mechanism is the diffusion of stars in angular-momentum space, due to two-body scattering. Compact stars in the inner 0.01 pc will sometimes diffuse onto very high eccentricity orbits, such that gravitational radiation will then shrink the orbit's semi-major axis and eventually drive the compact star into the massive black hole. Important physical effects setting the overall rate for this mechanism are mass segregation, which concentrates the more massive stellar black holes ($\approx 10 M_{\odot}$) close to the central black hole, and resonant relaxation, which increases the rate of orbit diffusion in phase-space (HOPMAN & ALEXANDER, 2006B): the orbits of stars close to a massive black hole are nearly Keplerian ellipses, and these orbits exert long term torques on each other, which can modify the angular momentum distribution of the stars and enhance the rate of **EMRI**'s formation (GÜRKAN & HOPMAN, 2007). However, subtle relativistic effects can reduce the estimated rates from relaxation processes (MERRITT ET AL., 2011). In addition to the two-body scattering mechanism, other proposed channels for **EMRIs** are tidal disruption of binaries that pass close to the central black hole (MILLER ET AL., 2005), and creation of massive stars (and their rapid evolution into black holes) in the accretion discs surrounding the central massive black hole (LEVIN, 2007). Tidal break up of incoming stellar binaries may already have been seen in the Milky Way following the remarkable discovery of a number of so-called hypervelocity stars observed escaping from our Galaxy (*e.g.*, BROWN ET AL., 2009). They are believed to be the outcome of an ejection following the break-up of two bound stars by the tidal field of SgrA*. All these mechanisms give specific predictions on the eccentricity and inclination of **EMRI** events that can be extracted from the gravitational wave signal (MILLER ET AL., 2005).

When the orbital separation between the two objects is small, of the order of few horizon radii from the large black hole, energy is radiated away in gravitational waves, and the semimajor axis of the orbit shrinks. Radiation is emitted over hundreds of thousand of orbits as the object inspirals to the point where it is swallowed by the central massive black hole. Over short periods of time, the emitted radiation can be thought of as a snapshot that contains detailed information about the physical parameters of the binary. The detection of the emitted gravitational wave signal will give us very detailed information about the orbit, the mass, and spin of the massive black hole as well as the mass of the test object (GAIR ET AL., 2010A; HOPMAN, 2009; PRETO & AMARO-SEOANE, 2010).

The measurement of even *a few* **EMRIs** will give astrophysicists a totally new and different way of probing dense stellar systems determining the mechanisms that shape stellar dynamics in the galactic nuclei and will allow us to recover the information on the emitting system with a precision which is not only unprecedented in the history of astrophysics, but beyond that of any other technique (AMARO-SEOANE ET AL., 2007; BABAK ET AL., 2010; PORTER, 2009).

2.5.2. A probe of galactic dynamics

The detection of EMRI will allow us to infer properties of the stellar environment around a massive black hole, so that our understanding of stellar dynamics in galactic nuclei will be greatly improved.

The centre-most part of the stellar spheroid, *i.e.* the *galactic nucleus*, constitutes an extreme environment in terms of stellar dynamics. With stellar densities higher than $10^6 \text{ M}_\odot \text{pc}^{-3}$, and relative velocities exceeding 100 km/s collisional processes, *i.e.* collective gravitational encounters among stars, are important in shaping the density profiles of stars. The mutual influence between the massive black hole and the stellar system occurs thanks to various mechanisms. Some are global, like the capture of stars via collisional relaxation, or accretion of gas lost by stars through stellar evolution, or adiabatic adaptation of stellar orbits to the increasing mass of the black hole. Others involve a very close interaction like the tidal disruption of a star, or the formation of an EMRI.

The distribution of stars around a massive black hole is a classical problem in stellar dynamics (BAHCALL & WOLF, 1976, 1977), of importance for EMRI is the distribution of stellar black holes. Objects more massive than the average star, such as stellar black holes, tend to segregate at the centre of the stellar distribution in the attempt to reach, through long-distance gravitational encounters, equipartition of kinetic energy. A dense, strongly mass-segregated cusp of stellar black holes is expected to form near a massive black hole, and such a cusp plays a critical role in the generation of EMRIs. The problem of the presence of a dark cusp has been addressed, for the Galactic centre, by different authors, from a semi-analytical and numerical standpoint (FREITAG ET AL., 2006A,C; HOPMAN & ALEXANDER, 2006A; SIGURDSSON & REES, 1997). A population of stellar black holes can leave an imprint on the dynamics of the S0 (or S) stars, at the Galactic centre, inducing a Newtonian retrograde precession on their orbits (MOUAWAD ET AL., 2005). Current data are not sufficient to provide evidence of such deviations from Keplerian orbits so that the existence of a population of stellar black holes is yet to be confirmed (GILLESSEN ET AL., 2009; MERRITT ET AL., 2009A).

2.5.3. A probe of the masses of stellar and massive black holes

Detection of EMRIs from black holes in the NGO mass range, that includes black holes similar to the Milky Way's, will enable us to probe the population of central black holes in an interval of masses where electromagnetic observations are challenging. NGO's EMRIs can be detected up to $z \simeq 0.5 - 0.7$ allowing to explore a volume of several tens of Gpc^3 and discover massive black holes in dwarf galaxies that are still elusive to electromagnetic observations. NGO will also measure the mass of the stellar black hole. This will provide invaluable information on the mass spectrum of stellar black holes, and on the processes giving rise to compact stars.

It is very difficult to measure the mass of black holes, both of the massive and stellar variety. In the case of massive black holes, methods based on following the innermost kinematics are difficult for low-mass massive black holes; *i.e.*, between 10^5 M_\odot and 10^7 M_\odot . These black holes have low intrinsic luminosities even when they are active, making detection hard. Performing dynamical measurements at these masses through stellar kinematic requires extremely high spatial resolution. Nowadays with adaptive optics we could optimistically hope to get a handful of measurements through stellar kinematic about 5 kpc away, although future 20 m – 30 m telescopes can reach up the Virgo cluster (16.5 Mpc). Exquisite gas-dynamical measurements are possible for only a handful of active black holes using water megamaser spots in a Keplerian circumnuclear disk (KUO ET AL., 2011). Still, the black hole in the centre of our own galaxy lies in this range, and placing constraints on the mass function of low-mass black holes has key astrophysical implications. Observations show that the masses of black holes correlate with the mass, luminosity and the stellar velocity dispersion of the host (GÜLTEKIN ET AL., 2009). These correlations imply that black holes evolve along with their hosts throughout cosmic time. One unanswered question is whether this symbiosis extends down to the lowest galaxy and black hole masses due to changes in the accretion properties (MATHUR & GRUPE, 2005), dynamical effects (VOLONTERI ET AL., 2007), or cosmic bias (VOLONTERI & NATARAJAN, 2009). NGO will discover the population of massive black holes in galaxies smaller than the Milky Way, that are difficult to access using other observational techniques, and provide insights on the co-evolution of black holes and their hosts.

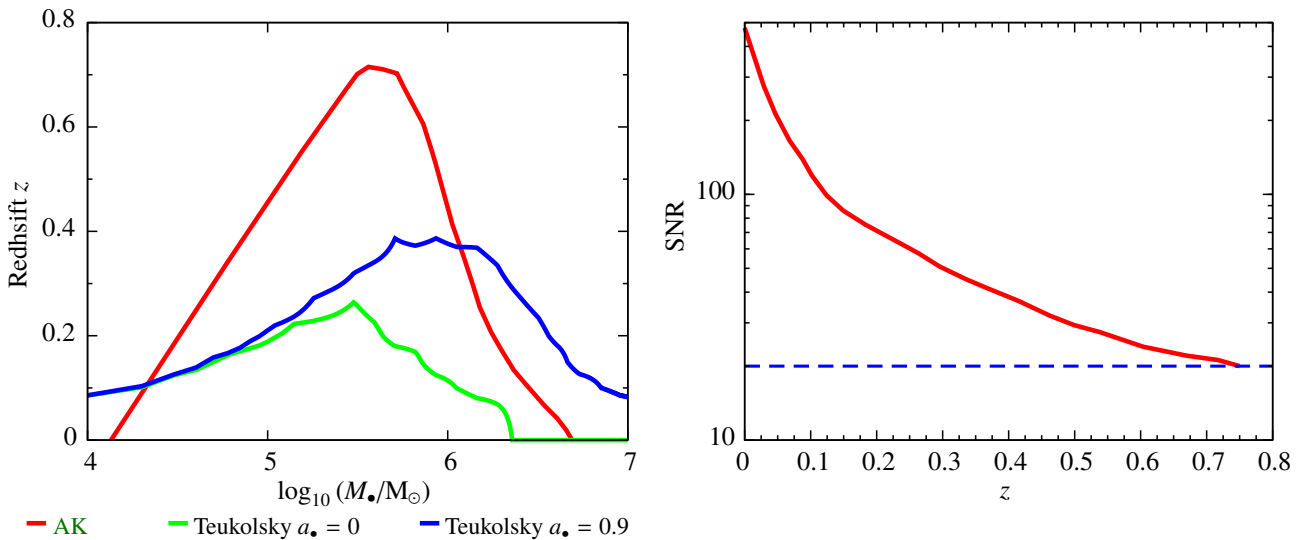


Figure 2.21.: Left: The maximum detectable redshift z (or horizon) for EMRIs assuming a two year mission lifetime, and a $SNR = 20$. The red curve is computed using the analytic waveform model and has a maximum redshift of $z \sim 0.7$ for black hole masses at the source rest-frame of $4 \times 10^5 M_{\odot}$. The green and blue curves are sky-averaged horizons, computed using the Teukolsky waveform model, for two different values of the spin of the central black holes, $a_{\bullet} = 0$ (green) and $a_{\bullet} = 0.9$ (blue).

Right: The distribution of maximum EMRI SNRs versus redshift for NGO. The dashed horizontal line denotes the SNR threshold of 20.

Difficulties, albeit of different nature, exist in measuring the masses and mass distribution of stellar black holes. Stellar black holes are observed as accreting X-ray sources in binaries. According to stellar evolution, black holes result from the core collapse of very massive stars, and their mass is predicted to be in excess of the maximum mass of a neutron star, which is still not fully constrained. Depending on the state of nuclear matter, this limit varies from about $1.6 M_{\odot}$ to about $3 M_{\odot}$ (SHAPIRO & TEUKOLSKY, 1986). The maximum mass of a stellar black hole is not constrained theoretically, and is known to depend sensitively on the metallicity of the progenitor star. The masses of stellar black holes are inferred using Kepler’s third law, or through spectral analysis of the emission from the hole’s accretion disc. These techniques can be used only for black holes in a binary system. Current measurements indicate a range for stellar black holes from about $5 M_{\odot}$ up to $20 M_{\odot}$, but uncertainties in the estimate can be as large as a factor of two (OROSZ, 2003). In addition, stellar black holes in interacting binaries are a very small and probably strongly biased fraction of the total stellar black hole population. Their progenitors are stars that have lost their hydrogen mantle due to mass transfer and thus formed in a different way than the vast majority of stellar black holes. NGO will measure the mass of the stellar black holes again with unprecedented precision providing invaluable insight on the process of star formation in the dense nuclei of galaxies, where conditions appear extreme.

2.5.4. Detecting extreme mass ratio inspirals with NGO

NGO will detect EMRI events out to redshift $z \sim 0.7$ in normal galaxies with high SNR and in the mass interval $10^4 M_{\odot} \lesssim M \lesssim 5 \times 10^6 M_{\odot}$. NGO will measure the mass and spin of the large, massive black hole with a precision to better than a part in 10^4 . This will enable us to characterise the population of central massive black holes in an interval of masses where electromagnetic observations are poor, incomplete or even missing, providing information also on their spins. NGO will also measure with equivalent precision the mass of the stellar black hole in the EMRI event, and also the orbital eccentricity at plunge. These observations will provide insight on the way stars and their remnants are forming and evolving in the extreme environment of a galactic nucleus.

EMRIs are compact stars moving on relativistic orbits around a massive black hole. As the compact object spends most of its time in the strong field regime, its orbit is very complex and difficult to model. While not fully realistic, a set of phenomenological waveforms have been developed (BARACK & CUTLER, 2004), the “Analytic

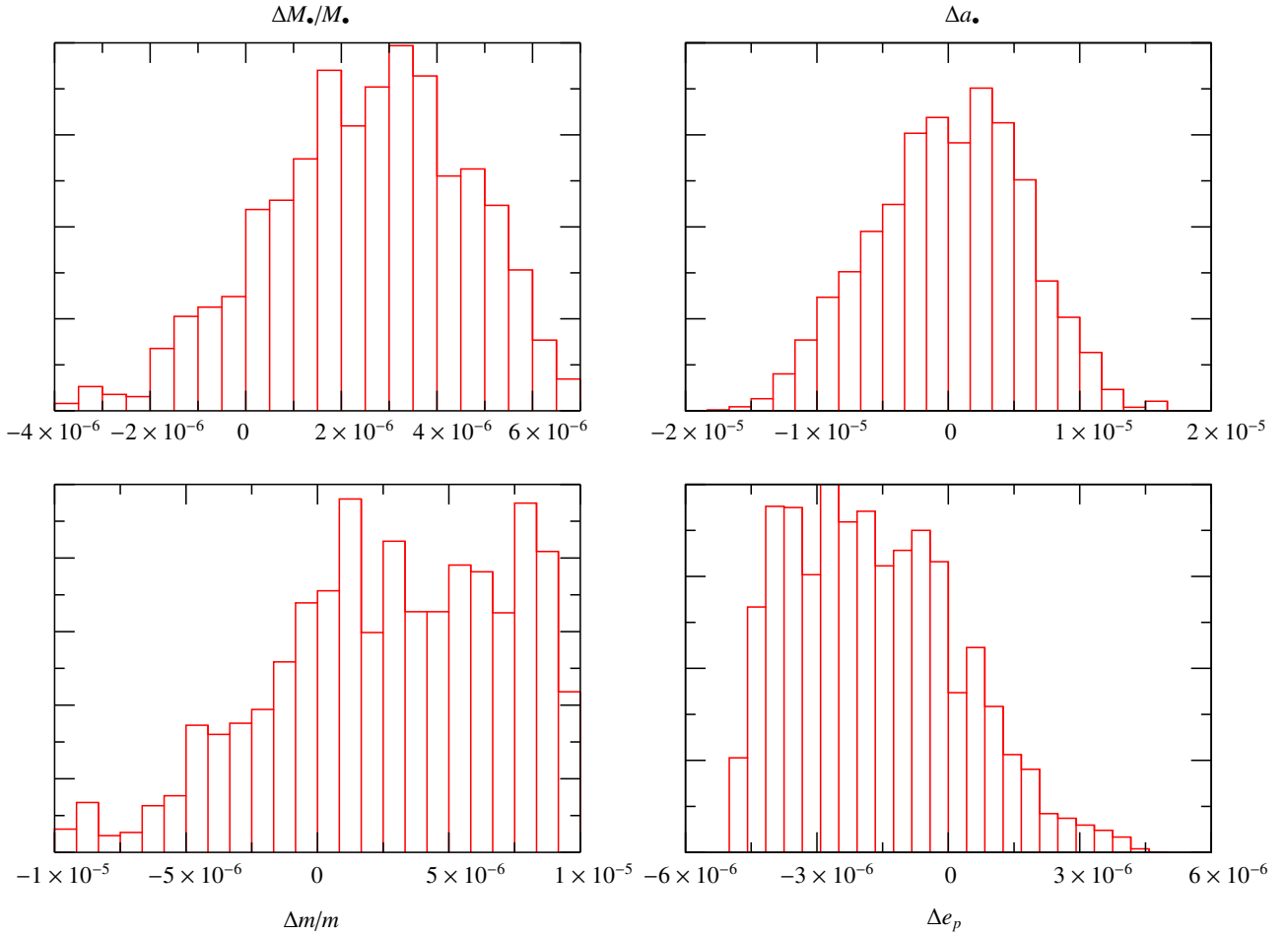


Figure 2.22.: The distribution of errors from a Markov Chain Monte Carlo analysis for a source at $z = 0.55$ with an SNR of 25. The plot shows the error distributions for the central black holes mass M_{\bullet} and spin a_{\bullet} , the mass of the compact object m and the eccentricity at plunge e_p .

Kludge” (AK) waveforms, which fully capture the complexity of the model. These waveforms are defined by a 14 dimensional parameter set, of which the most physically relevant are the masses of the central black hole and of the compact object, M_{\bullet} and m respectively, the spin of the massive black hole a_{\bullet} , the eccentricity of the orbit at plunge, e_p , the sky position of the source with respect to the detector, and the luminosity distance to the source, D_L . In addition to these approximate models, more accurate EMRI waveform models have been computed using perturbation theory, in which the inspiraling object is regarded as a small perturbation to the background spacetime of the large black hole. The perturbation theory framework was first outlined by TEUKOLSKY (1973) and gave rise to the Teukolsky equation. However, solution of this equation is computationally expensive, and results have only recently been obtained for a selection of generic orbits (DRASCO & HUGHES, 2006). Nonetheless, results have been fully tabulated for certain restricted types of orbit. For the calculations described here we will use data for circular-equatorial orbits (FINN & THORNE, 2000; GAIR, 2009A). We can use both models to compute the maximum detectable redshift, or the horizon for EMRI detection, as a function of mass.

To calculate the detection limit of EMRI for NGO using the AK waveforms, we must perform a Monte Carlo simulation over the waveform parameters. We explore the mass range $10^4 M_{\odot} \lesssim M_{\bullet} \lesssim 5 \times 10^6 M_{\odot}$. As not much is known about the distribution of spins or eccentricities for EMRI, we consider uniform distributions for the spins in the range $-0.95 \leq a_{\bullet} \leq 0.95$, and for eccentricities at plunge in the interval $0.05 \leq e_p \leq 0.4$. We fix the mass of the inspiraling body to $10 M_{\odot}$ to represent the inspiral of a stellar black hole as these are expected to dominate the event rate (GAIR ET AL., 2004). The detection horizon for neutron star and white dwarf inspirals is significantly less than for black holes. The final assumption required is to set a threshold of detection. While a SNR threshold of 30 was thought to be justified in the past, advances in search algorithms have recently

Table 2.2.: Estimated number of *EMRI* events detectable by *NGO*. The first three columns shows the results computed using the Teukolsky waveform model, assuming all black holes have fixed spin of 0, 0.5 or 0.9. The last column shows results computed using the analytic kludge waveform model.

Waveform model	Teukolsky with black hole spin			Analytic Kludge
	$a_{\bullet} = 0$	$a_{\bullet} = 0.5$	$a_{\bullet} = 0.9$	
Number of events	30	35	55	50

demonstrated that *EMRI* with *SNR* about 20 is sufficient for detection (BABAK ET AL., 2010; CORNISH, 2011; GAIR ET AL., 2008A) allowing us to assume a threshold of an *SNR* of 20 in this analysis.

Assuming a mission lifetime T of two years, and plunge times between $0 \text{ yr} \leq t_p \leq 5 \text{ yr}$, a large scale Monte Carlo simulation was run over all 14 parameters. In figure 2.21 (left) we plot the maximum detectable redshift z (also referred to as horizon) as a function of intrinsic mass of the massive black hole. Systems with intrinsic mass in the range from $10^4 M_{\odot} \leq M_{\bullet} \leq 5 \times 10^6 M_{\odot}$ are detectable in the local universe at redshift of $z \lesssim 0.1$, while systems in the range from $10^5 M_{\odot} \leq M_{\bullet} \leq 10^6 M_{\odot}$ should be detectable by *NGO* to $z \sim 0.7$, corresponding to a co-moving volume of about 70 Gpc^3 .

Figure 2.21 (left) also shows the maximum redshift z as a function of the mass of the central massive black hole, computed for circular-equatorial inspirals using the Teukolsky equation for the same masses of the inspiralling compact object and massive black holes. This curve shows the sky-averaged horizon, *i.e.*, the maximum redshift at which the *SNR* averaged over inclinations and orientations of the *EMRI* system reaches the threshold value of 20. The Teukolsky results are only available for a few selected values of the spin of the central black hole. We therefore show the horizon assuming all the central black holes have a spin of $a_{\bullet} = 0$, and assuming all the black holes have spin of $a_{\bullet} = 0.9$. The Teukolsky horizon appears significantly lower than the *AK* horizon, but this is a result of the sky-averaging approximation – the sky averaged *SNR* is expected to be a factor of about 2.5 lower than the *SNR* of an “optimally oriented” binary. The *AK* horizon was computed using a Monte Carlo simulation over orientations and sky locations for the source and will therefore approach the value for an optimally-oriented binary. The difference between the sky-averaged Teukolsky horizon and the *AK* horizon is therefore consistent with the expected level of difference. The maximum horizon for the Teukolsky curves is at a similar value for the mass of the central black hole as the *AK* results – somewhat lower for $a_{\bullet} = 0$ and higher for $a_{\bullet} = 0.9$, as we would expect since inspirals into more rapidly spinning black holes emit radiation at higher frequencies, which shifts the peak sensitivity to higher masses. For the same reason, we see that the *NGO* horizon is at a higher redshift for more rapidly spinning central black holes.

In figure 2.21 (right) we plot the distribution of maximum *SNRs* as a function of redshift for the Monte Carlo simulation performed using the *AK* waveforms. Nearby *EMRIs* will be detectable with *SNRs* of many tens, with *SNRs* of 30 being available to $z = 0.5$. *EMRIs* can be detected with an *SNR* of 20 up to $z \simeq 0.7$, up to a volume of about 70 Gpc^3 , encompassing the last 6×10^9 years of the universe.

EMRIs are the most complex sources to model and to search for. However, if they can be detected, this complexity will allow us to estimate the parameters of the system with great accuracy (BABAK ET AL., 2010; CORNISH, 2011; GAIR ET AL., 2008A). For an *EMRI* detected with a certain *SNR*, the parameter estimation does not strongly depend on the detector configuration since any detected *EMRI* will be observed for many waveform cycles. The parameter estimation achievable with *NGO* is therefore the same as published results for *LISA* (BARACK & CUTLER, 2004; HUERTA & GAIR, 2009). For any *EMRI* observed with *SNR* above the detection threshold of 20, we expect to measure the mass M_{\bullet} and spin a_{\bullet} of the central massive black hole with a precision to better than a part in 10^4 . This is illustrated in Figure 2.22 that shows the results from a Markov Chain Monte Carlo analysis (CORNISH & PORTER, 2006) of a source at $z = 0.55$ with *SNR* = 25. The plots show the distribution of errors for a particular source that would be recovered by analysing the data from the detector. Results are shown for the mass M_{\bullet}/M_{\odot} and spin a_{\bullet} of central black hole, the mass m/M_{\bullet} of the stellar black hole, and the eccentricity at plunge e_p . Our analysis also shows that the luminosity distance D_L to the source is determined with an accuracy of less than 1 % and the source sky location can be determined to around 0.2 square degrees. While the *SNR* is quite low for this source, the level of accuracy in the estimation of parameters is clear.

2.5.5. Estimating the event rates of extreme mass ratio inspirals for NGO

The estimated detection rates based on the best available models of the black hole population and the EMRI rate per galaxy, are about 50 events with a two year NGO mission, with a factor of $\lesssim 2$ uncertainty from the waveform modelling and lack of knowledge about the likely system parameters. An additional uncertainty, of at least an order of magnitude, arises from the uncertain astrophysics. Even with a handful of events, NGO's EMRIs will be a powerful astrophysical probe of the formation and evolution of massive and stellar black holes.

We can use the horizon distances described in the preceding section to compute the likely number of EMRI events that NGO will detect, if we make further assumptions about the EMRI occurring in the universe. This depends on the black hole population and on the rate at which EMRI occur around massive black holes with particular properties. The latter is poorly known, and we will use results from HOPMAN (2009) and AMARO-SEOANE & PRETO (2011) for the rate of inspirals involving black holes. The rate Γ_{\bullet} is found to scale with the central black hole mass, M_{\bullet} , as $\Gamma_{\bullet} \sim 400 \text{ Gyr}^{-1} (M_{\bullet}/3 \times 10^6 M_{\odot})^{-0.19}$.

We do not consider neutron star and white dwarf inspirals in these rate estimates as the expected number of detections with NGO is less than one in both cases, due to the considerably reduced horizon distance for these events. We therefore fix the mass of the inspiraling body at $10 M_{\odot}$ as in the previous section.

To model the black hole population, we take the mass function of black holes to in the intrinsic mass range $10^4 M_{\odot} \lesssim M_{\bullet} \lesssim 5 \times 10^6 M_{\odot}$. Using the assumption that there is no evolution in the black hole mass function, we sampled sources from a uniform distribution in co-moving volume. These assumptions are consistent with the mass function derived from the observed galaxy luminosity function using the $M_{\bullet} - \sigma$ relation, and excluding Sc-Sd galaxies (ALLER & RICHSTONE, 2002; GAIR, 2009A; GAIR ET AL., 2004). For the results using the AK waveform model, we choose the spin of the central object uniformly in the range $0 \leq a_{\bullet} \leq 0.95$, the eccentricity of the orbit at plunge uniformly in the range $0.05 \leq e_p \leq 0.4$ and all angles to be uniform or uniform in cosine as appropriate. For the Teukolsky based results we do not need to specify the angles as we use a sky and orientation averaged sensitivity, and we do not specify the eccentricity or inclination as the orbits are all circular and equatorial (although we assume equal numbers of prograde and retrograde inspirals). As before, the Teukolsky results are available for fixed values of the spin only so we estimate the event rate assuming that all the black holes have spin 0, 0.5 or 0.9.

It is important also to correctly randomise over the plunge time of the EMRI. For the AK calculation, we choose the plunge time uniformly in $0 \text{ yr} \leq t_p \leq 5 \text{ yr}$, with time measured relative to the start of the NGO observation and assuming an NGO lifetime of 2 years. Although sufficiently nearby events with plunge times greater than 5 years in principle could be detected, it was found that such events contribute less than one event to the total event rate. For the Teukolsky calculation, we evaluated the observable lifetime for every event, which is the amount of time during the inspiral that NGO could start to observe that will allow sufficient SNR to be accumulated over the mission lifetime to allow a detection (GAIR, 2009A).

In table 2.2 we give the results of this calculation for different waveform models and black hole spins, and it is in the range of 25 to 50 events in two years. The predicted number of events depends on the assumptions about the waveform model and the spin of the black holes, but is in the range of 25 to 50 events in two years. The number of events predicted for the AK model is higher because the presence of eccentricity in the system tends to increase the amount of energy radiated in the NGO band. The analytic kludge estimates include randomisation over the black hole spin and the orbital eccentricity and inclination, so the true detection rate is likely to be closer to this number, although this depends on the unknown astrophysical distribution of EMRI parameters. Even with as few as 10 events, GAIR ET AL. (2010) show that the slope of the mass function of massive black holes in the mass range $10^4 M_{\odot} - 10^6 M_{\odot}$ can be determined to a precision of about 0.3, which is the current level of observational uncertainty.

2.5.6. Black hole coalescence events in star clusters

The detection with NGO of even a single coalescence event involving two intermediate mass black holes in colliding star clusters, present in the very local universe, would be a major discovery, and it would have a strong impact in the field of stellar dynamics and stellar evolution in star forming regions.

In closing this section on astrophysical black holes, we explore briefly the possibility that an instrument like NGO will detect coalescences between intermediate mass black holes in the interval $10^2 M_{\odot} - 10^4 M_{\odot}$ that do *not* result from the assembly of dark matter halos, but that originate from *local* coalescence events occurring in star clusters, and under extreme yet unexploited astrophysical conditions. Given the tiny radius of gravitational influence (about 0.01 pc) of such light black holes on the surrounding dense stellar environment, their detection is extremely difficult, and their existence has never been confirmed, though evidence has been claimed in a number of globular clusters (SEE MILLER, 2009; MILLER & COLBERT, 2004, AND REFERENCES THEREIN).

An intermediate mass black hole may form in a young cluster if the most massive stars sink to the cluster's centre due to mass segregation before they evolve and explode. There, they start to physically collide. The most massive star gains more and more mass and forms a runaway star that may collapse to form an intermediate mass black hole (PORTEGIES ZWART ET AL., 2004). . To detect an intermediate mass black with NGO we need either a compact object (e.g., a stellar black hole) inspiralling in one of them (KONSTANTINIDIS ET AL., 2011), or two intermediate mass black holes forming a binary. The formation of a binary of intermediate-mass black holes can be theoretically explained in two different ways. Either via star-cluster star-cluster collisions like those found in the Antennæ galaxy (AMARO-SEOANE & FREITAG, 2006; AMARO-SEOANE ET AL., 2010), or via formation in situ of an intermediate mass black hole binary (GÜRKAN ET AL., 2006).

NGO will typically be able to see systems of binaries of intermediate mass black holes with SNR > 10 out to a few Gpc (SANTAMARÍA ET AL., 2010), and the radiation associated to a stellar black hole plunging onto an intermediate mass black holes in a massive star cluster in the local universe. The huge uncertainties involved in the dynamical formation of intermediate mass black holes in star clusters make difficult to predict event rates, but under favourable conditions few events per year might be observed (AMARO-SEOANE & FREITAG, 2006). The detection of even a single event would have a large importance for astrophysics, probing the existence of black holes in this unexplored mass range, and shedding light in the complex dynamics taking place in the densest stellar clusters.

2.6. Confronting General Relativity with Precision Measurements of Strong Gravity

NGO science objectives and investigations relevant to this section

4. Confront General Relativity with observations
 - 4.1 Detect gravitational waves directly and measure their properties precisely
 - 4.2 Test whether the central massive objects in galactic nuclei are consistent with the Kerr black holes of General Relativity.
 - 4.3 Perform precision tests of dynamical strong-field gravity.

Cosmic Vision scientific questions addressed by this section

- 3.3 Matter under extreme conditions

Probe gravity theory in the very strong field environment of black holes and other compact objects, and the state of matter at supra-nuclear energies in neutron stars

The NGO Science Objectives are listed in chapter 2.

2.6.1. Setting the stage

General Relativity has been extensively tested in the weak field regime both in the solar system and by using binary pulsars. NGO will provide a unique opportunity of confronting GR in the highly dynamical strong field regime of massive black holes.

GR is a theory of gravity in which gravitational fields are manifested as curvature of spacetime. GR has no adjustable parameters other than Newton's gravitational constant, and it makes solid, specific predictions. Any test can therefore potentially be fatal to its viability, and any failure of GR can point the way to new physics. Confronting GR with experimental measurements, particularly in the strong gravitational field regime, is therefore an essential enterprise. In fact, despite its great successes, we know that GR cannot be the final word on gravity, since it is a classical theory that necessarily breaks down at the Planck scale. As yet there is no complete, quantum theory of gravity, and gravitation is not unified with the other fundamental forces. Under such a premise, several stress tests of GR have been proposed, each of them potentially fatal to the theory, however all of them involve low energies and length-scales much larger than the Planck scale.

Although so far GR has passed all the tests to which it has been subjected (WILL, 2006), most of these tests were set in the weak-field regime, in which the parameter $\epsilon = v^2/c^2 \sim GM/(Rc^2)$ is much smaller than one. Here v is the typical velocity of the orbiting bodies, M their total mass, and R their typical separation. For the tests of GR that have been carried out in our Solar System, expected second-order GR corrections to the Newtonian dynamics are of the order $\epsilon \sim 10^{-6} - 10^{-8}$, and so to date it has been sufficient to expand GR equations to the first Post-Newtonian (PN) order. Solar System tests are completely consistent with GR to this order of approximation.

Binary pulsars, which are essentially very stable and accurate clocks with typical orbital velocities $v/c \sim 10^{-3}$ ($\epsilon \sim 10^{-6}$), are excellent laboratories for precision tests of GR (LORIMER, 2008). Current observations of several binary pulsars are perfectly consistent with the GR predictions, with orbits again calculated to the first PN order. Observations of the first binary pulsar to be discovered, PSR 1913+16, also provided the first astrophysical evidence for gravitational radiation, a 2.5-PN-order effect. Loss of energy due to gravitational-wave emission (radiation reaction) causes the binary orbit to shrink slowly; its measured period derivative \dot{P} agrees with GR predictions to within 0.2%, consistent with measurement error bars (WEISBERG & TAYLOR, 2005). Another double pulsar system, PSR J0737-3039 A and B, allows additional tests of GR that were not available prior to its discovery (KRAMER ET AL., 2006). In that system, the orbital period derivative is consistent with GR at the 0.3% level, and the Shapiro delay agrees to within 0.05% with the predictions of GR (KRAMER & WEX, 2009). However, the gravitational fields responsible for the orbital motion in known binary pulsars are not much stronger than

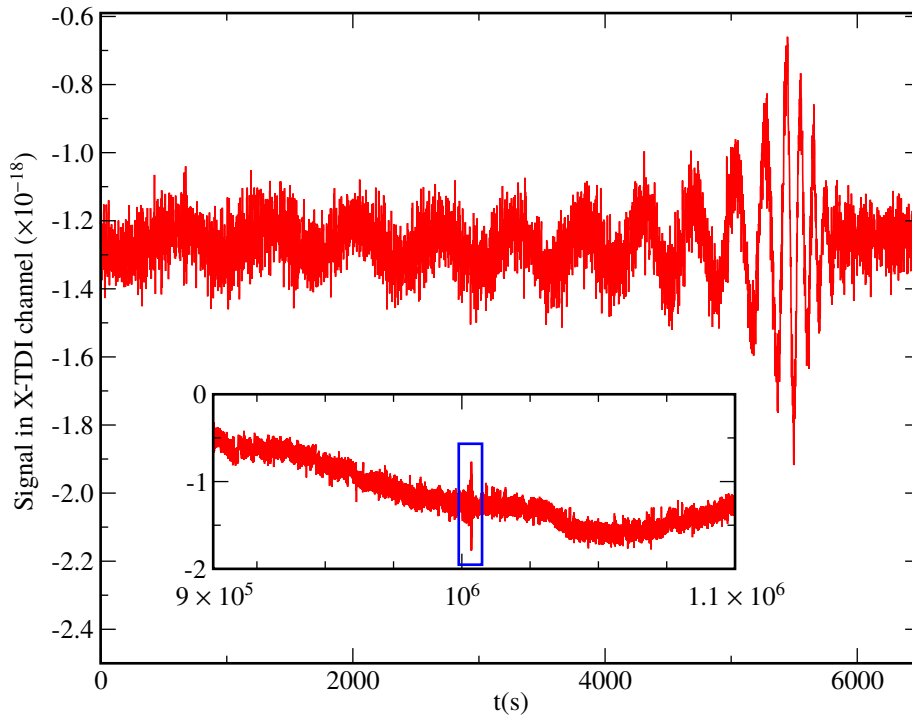


Figure 2.23.: Gravitational wave signal for the final few orbits, plunge, merger and ringdown of a coalescing binary. The total mass of system $M(1+z) = 2 \times 10^6 M_{\odot}$, mass ratio $m_1/m_2 = 2$, spin magnitudes $a_1 = 0.6$ $a_2 = 0.55$, misalignment between spins and orbital angular momentum few degrees, the distance to the source $z = 5$. The inset shows the signal on a larger data span.

those in the Solar System: the semimajor axis of the orbit of PSR 1913+16 is about $1.4 R_{\odot}$. Such weak fields limit the ability of binary pulsars to probe nonlinear GR dynamics. They do provide important tests of strong-field static gravity, as the redshift at the surface of a neutron star is of order 0.2.

NGO observations of coalescing massive black hole binaries, or of stellar-mass compact objects spiralling into massive black holes, will allow us to confront GR with precision measurements of physical regimes and phenomena that are not accessible through Solar System or binary pulsar measurements. The merger of comparable-mass black hole binaries produces an enormously powerful burst of gravitational radiation, which NGO will be able to measure with amplitude SNR as high as a few hundred, even at cosmological distances. In the months prior to merger, NGO will detect the gravitational waves emitted during the binary inspiral; from that inspiral waveform, the masses and spins of the two black holes can be determined to high accuracy. Given these physical parameters, numerical relativity will predict very accurately the shape of the merger waveform, and this can be compared directly with observations, providing an ideal test of pure GR in a highly dynamical, strong-field regime.

Stellar-mass compact objects spiralling into massive black holes will provide a qualitatively different test, but an equally exquisite one. The compact object travels on a near-geodesic of the spacetime of the massive black hole. As it spirals in, its emitted radiation effectively maps out the spacetime surrounding the massive black hole. Because the inspiralling body is so small compared to the central black hole, the inspiral time is long and NGO will typically be able to observe of order 10^5 cycles of inspiral waveform, all of which are emitted as the compact object spirals from 10 horizon radii down to a few horizon radii. Encoded in these waves is an extremely high precision map of the spacetime metric just outside the central black hole. Better opportunities than these for confronting GR with actual strong-field observations could hardly be hoped for.

The Advanced LIGO/Virgo detectors should come online around 2015, and their sensitivity is large enough that they should routinely observe stellar mass black hole coalescences, where the binary components are of roughly comparable mass. However, even the brightest black hole mergers that LIGO and Virgo should observe will still have an amplitude SNR about 10 to 100 times smaller than the brightest massive black hole coalescences that NGO will observe. The precision with which NGO can measure the merger and ringdown waveforms

will correspondingly be better by the same factor when compared to ground-based detectors. The situation is similar for the EMRIs described in the previous section: while ground-based detectors may detect binaries with mass ratios of about 10^{-2} (e.g., a neutron star spiralling into a $100 M_{\odot}$ black hole), in observations lasting approximately 10^2 to 10^3 cycles, the precision with which the spacetime can be mapped in such cases is at least two orders of magnitude worse than what is achievable with NGO's EMRI sources. Thus NGO will test our understanding of gravity in the most extreme conditions of strong and dynamical fields, and with a precision that is two orders of magnitude better than that achievable from the ground.

GR has been extraordinarily fruitful in correctly predicting new physical effects, including gravitational lensing, the gravitational redshift, black holes and gravitational waves. GR also provided the overall framework for modern cosmology, including the expansion of the Universe. However, our current understanding of the nonlinear, strong gravity regime of GR is quite limited. Exploring gravitational fields in the dynamical, strong-field regime could reveal new objects that are unexpected, but perfectly consistent with GR, or even show violations of GR.

The best opportunity for making such discoveries is with an instrument of high sensitivity. Ground-based detectors like LIGO and Virgo will almost certainly always have to detect signals by extracting them from deep in the instrumental noise, and they will therefore depend on prior predictions of waveforms. NGO, on the other hand, will have enough sensitivity that many signals will show themselves well above noise; unexpected signals are much easier to recognize with such an instrument.

2.6.2. Testing strong-field gravity: The inspiral, merger, and ringdown of massive black hole binaries

NGO will be capable of detecting inspiral and/or merger plus ring-down parts of the gravitational wave signal from coalescing massive black hole binaries of comparable mass. For the nearby events ($z \sim 1$) the last several hours of the gravitational wave signal will be clearly seen in the data allowing direct comparison with the waveforms predicted by GR.

NGO's strongest sources are expected to be coalescing black hole binaries where the components have roughly comparable masses, $0.1 < m_2/m_1 < 1$. Their signal at coalescence will be visible by eye in the data stream, standing out well above the noise, as illustrated in figure 2.23.

A black hole binary coalescence can be schematically decomposed into three stages (inspiral, merger, and ringdown), all of which will be observable by NGO for a typical source. The inspiral stage is a relatively slow, adiabatic process, well described by the analytic PN approximation. The inspiral is followed by the dynamical merger of the two black holes, that form a single, highly distorted black hole remnant. Close to merger, the black hole velocities approach $v/c \sim 1/3$ and the PN approximation breaks down, so the waveform must be computed by solving the full Einstein equations via advanced numerical techniques. The distorted remnant black hole settles down into a stationary rotating solution of Einstein's equations (a Kerr black hole) by emitting gravitational radiation. This is the so called "ringdown" phase, where the gravitational wave signal is a superposition of damped exponentials quasi-normal modes (QNMs), and therefore similar to the sound of a ringing bell. While numerical relativity is required to understand the gravitational radiation emitted during merger, the post-merger evolution – i.e., the black hole "quasinormal ringing" – can be modelled using black hole perturbation theory. The final outcome of the ringdown is the Kerr geometry, with a stationary spacetime metric that is determined uniquely by its mass and spin, as required by the black hole "no-hair" theorem.

For equal-mass black hole binaries with total mass M in the range $2 \times 10^5 M_{\odot} < M(1+z) < 2 \times 10^6 M_{\odot}$, where z is the cosmological redshift of the source, the inspiral SNR and post-inspiral (merger plus ring-down) SNR are within an order of magnitude of each other. From a typical NGO observation of the inspiral part of the signal, it will be possible to determine the physical parameters of the binary to extremely high accuracy. Using these parameters, numerical relativity can predict very precisely the merger and ringdown waves. Measurements of the individual masses and spins will allow us to predict the mass and the spin of the remnant black hole (REZZOLLA ET AL., 2008B), which can be directly tested against the corresponding parameters extracted from the ringdown. The merger and ringdown waveforms will typically have an SNR of 10^2 to 10^3 for binary black holes with the total mass $10^5 M_{\odot} < M(1+z) < 6 \times 10^8 M_{\odot}$ at $z = 1$, so an extremely clean comparison will be possible between the observed waveforms and the predictions of GR.

The inspiral stage: comparing inspiral rate with predictions of General Relativity

The inspiral phase could be observed by **NGO** up to a year before the final merger with relatively large **SNR**. Comparison of the observed inspiral rate with **PN** predictions of **GR** will provide a valuable test of **GR** in the regime of strong dynamical gravitational fields.

With orbital velocities v/c typically in the range 0.05 to 0.3, most of the inspiral stage can be well described using high-order **PN** expansions of the Einstein equations. The inspiral waveform is a chirp: a sinusoid that increases in frequency and amplitude as the black holes spiral together. Depending on the source parameters, **NGO** will be able to observe the final stages of the inspiral, for up to one year in some favourable cases. To give a practical reference, when the gravitational-wave frequency sweeps past 0.3 mHz, the time remaining until merger is approximately

$$t = 106.8 \text{ days} \left(\frac{0.25}{\eta} \right) \left(\frac{M(1+z)}{2 \times 10^5 M_{\odot}} \right)^{-5/3} \left(\frac{f}{0.3 \text{ mHz}} \right)^{-8/3} \quad (2.4)$$

where, as above, $M = m_1 + m_2$ is the total mass of the binary and $\eta = m_1 m_2 / M^2$ is the symmetric mass ratio. **NGO** will observe the last 10^2 to 10^4 **GW** inspiral cycles, depending on the total mass and proximity. Since the inspiral signal is quite well understood theoretically, matched filtering can be used to recognise these inspirals up to a year before the final merger, at a time when the total **SNR** is still small. Moreover, as the total **SNR** in the inspiral is quite large in many cases, and such signals are long lived, matched filtering based on the inspiral waveform alone can determine the system parameters to very high accuracy. Both masses can be determined to within a fractional error of about 10^{-2} to 10^{-1} , and the spin of the primary black hole can be measured an accuracy of 10 % or better.

The nonlinear structure of **GR** (and possible deviations from **GR**) could be encoded in a phenomenological way by considering hypothetical modifications of the gravitational wave amplitude and phasing, as proposed by different authors (ARUN ET AL., 2006; YUNES & PRETORIUS, 2009). The relatively large strength of the inspiral gravitational wave signal will allow a sensitive test of **GR** by comparing the rate of the observed inspiral (phase evolution) to predictions of the **PN** approximation to **GR** (CORNISH ET AL., 2011; HUWYLER ET AL., 2011; LI ET AL., 2011; MISHRA ET AL., 2010).

The merger stage: spectacular bursts

The merger of two black holes could be observed by **NGO** throughout the Universe if it falls into the detector band. The observation of the merger could be confronted directly with the predictions of **GR** and, if the inspiral is also observed, could be used for a consistency check between the two parts of the gravitational wave signal.

The inspiral is followed by a dynamical merger that produces a burst of gravitational waves. This is a brief event, comprising a few cycles lasting about $5 \times 10^3 \text{ s} (M/10^6 M_{\odot}) (0.25/\eta)$, yet very energetic: during the merger the gravitational wave luminosity is $L_{\text{GW}} \sim 10^{23} L_{\odot}$, emitting more power than all the stars in the observable Universe. The final merger of massive binaries occurs in the very strong-field, highly nonlinear and highly dynamical regime of **GR**, and is the strongest gravitational wave source that **NGO** is expected to see. **NGO** will be able to see the merger of two $10^4 M_{\odot}$ black hole beyond redshift $z = 20$, and for mergers of two $10^6 M_{\odot}$ black hole at $z = 1$ the **SNR** will be about 2000. As mentioned above, **NGO** observations of the inspiral yield a good measurement of the masses and spins of the black holes. With these in hand, numerical relativity will make a very specific prediction for the merger and ringdown radiation from the system. Comparison with the waveform that **NGO** actually observes will allow us to confront the predictions of **GR** with an ultra-high precision measurement in the fully nonlinear and dynamical regime of strong gravity for the first time.

The ringdown stage: black hole spectroscopy

According to GR the merger leads to a single ringing Kerr black hole characterised by its mass and spin. Detecting two or more quasinormal modes (the individual damped exponential components of the so-called “ringdown” radiation) will allow us to check whether the final object indeed is described only by two parameters in accord with the “no-hair” theorem of GR.

Although numerical relativity waveforms from colliding holes naturally include the ringdown waves, these waves are also well understood analytically. GR predicts, as a consequence of the “no-hair” theorem, that every excited black hole emits gravitational waves until it reaches a time-independent state characterised entirely by its mass and spin. These ringdown waves consist of a set of superposed black hole QNM waves with exponentially damped sinusoidal time dependence, plus a far weaker “tail”. The modes are strongly damped as their energy is radiated away to infinity, so the final ringdown stage is brief, lasting only a few cycles.

The QNM of Kerr black hole can be computed using perturbation theory: the spacetime metric is written as the Kerr metric plus a small perturbation, and Einstein’s equations are expanded to first-order in that perturbation. The solutions can be decomposed into a sum of damped exponentials with complex eigenfrequencies (CHANDRASEKHAR & DETWEILER, 1975) that can be computed to essentially arbitrary accuracy (LEAVER, 1985).

While there are infinitely many modes (corresponding to the angular order and overtone number of the perturbation from the stationary state), the lowest-order modes are the most readily excited and the least strongly damped, so in practise only a few modes are likely to be observed. The frequencies and damping times of these ringdown QNM (TABULATED IN BERTI ET AL., 2009) are completely determined by the mass and the spin of the remnant black hole.

A data analysis strategy based on multi-mode searches will be necessary for an accurate estimation of the mass and spin of the final black hole (BERTI ET AL., 2006, 2007). Furthermore, if we can measure at least two different QNMs in a ringdown signal, the ringdown radiation itself will provide a strong-field test of the hypothesis that the central massive objects in galactic nuclei are indeed Kerr black holes. The reason is that a two-mode signal contains four parameters (the frequencies and damping times of each mode), which must all be consistent with the *same* mass and spin values DREYER ET AL., 2004. Just like we can identify chemical elements via spectroscopic measurements, we can uniquely identify a black hole (determine its mass and spin) from the spectrum of its ringdown radiation.

If GR is correct but the observed radiation is emitted from a different source (exotic proposals include boson stars and gravastars, among others), the spectrum would most certainly be inconsistent with the QNM spectrum of Kerr black holes in GR (BERTI ET AL., 2006; CHIRENTI & REZZOLLA, 2007; PANI ET AL., 2009; YOSHIDA ET AL., 1994). The same should occur if GR does not correctly describe gravity in the extremes of strong fields and dynamical spacetimes. The fact that black hole oscillations should produce different radiation spectra in different theories of gravity is true in general (BARAUSSE & REZZOLLA, 2008), and the spectrum was studied in some specific extensions of GR, such as Einstein-dilaton-Gauss-Bonnet gravity (PANI & CARDOSO, 2009).

The possibility of testing the no-hair theorem with QNMs depends on the accuracy with which frequencies and damping times can be measured, which in turn depends on the SNR of the ringdown signal. As shown in (BERTI, 2006; BERTI ET AL., 2007), SNR larger than 50 should be sufficient to identify the presence of a second mode and use it for tests of the no-hair theorem. This is only marginally achievable with advanced Earth-based detectors, but SNRs of this order should be the norm for the black hole mergers detectable by NGO. Furthermore, recent work showed that multi-mode ringdown waveforms could encode information on parameters of the binary *before merger*, such as the binary’s mass ratio (KAMARETSOS ET AL., 2011), and this would provide further consistency checks on the strong-field dynamics of general relativity.

2.6.3. Extreme mass ratio inspirals: precision probes of Kerr spacetime

NGO will be able to observe the last few years of the inspiral of a stellar mass object into a black hole with mass $10^5 M_\odot - 10^6 M_\odot$ up to $z \sim 0.7$. The large number of observed orbital cycles (about 10^5) will allow us to measure precisely the parameters of the central object including its quadrupole moment. Any deviations in the orbital motion from **GR** predictions will be imprinted in the phase of the gravitational wave. Measurements of the mass, spin and quadrupole moment of the central object will allow us to check whether it is consistent with a **GR** Kerr black hole.

EMRIs are expected to be very clean astrophysical systems, except perhaps in the few percent of galaxies containing accreting massive black holes, where interactions with the accretion disk could possibly affect the **EMRI** dynamics. Over timescales of the order of a day, the orbits of the smaller body are essentially geodesics in the spacetime of the massive black hole. On longer timescales, the loss of energy and angular momentum due to gravitational-wave emission causes the smaller body to spiral in; *i.e.*, the geodesic's “constants” of motion change slowly over time. Over a typical **NGO** observation time (years), **EMRI** orbits are highly relativistic (radius smaller than 10 Schwarzschild radii) and display extreme forms of periastron and orbital plane precession due to the dragging of inertial frames by the massive black hole's spin. shows two sample waveforms, corresponding to short stretches of time.

Given the large amount of **GW** cycles collected in a typical **EMRI** observation (about 10^5), a fit of the observed gravitational waves to theoretically calculated templates will be very sensitive to small changes in the physical parameters of the system. As mentioned above, this sensitivity makes the search computationally challenging, but it allows an extremely accurate determination of the source parameters, once an **EMRI** signal is identified. Assuming that **GR** is correct and the central massive object is a black hole, **NGO** should be able to determine the mass and spin of the massive black hole to fractional accuracy of about 10^{-4} to 10^{-3} for **GW** signals with an **SNR** of 20 (BARACK & CUTLER, 2004).

This level of precision suggests that we can use **EMRI** as a highly precise observational test of the “Kerr-ness” of the central massive object. That is, if we do *not* assume that the larger object is a black hole, we can use gravitational waves from an **EMRI** to map the spacetime of that object. The spacetime outside a stationary axisymmetric object is fully determined by its mass moments M_l and current multipole moments S_l . Since these moments fully characterise the spacetime, the orbits of the smaller object and the gravitational waves it emits are determined by the multipolar structure of the spacetime. By observing these gravitational waves with **NGO** we can therefore precisely characterise the spacetime of the central object. Extracting the moments from the **EMRI** waves is analogous to geodesy, in which the distribution of mass in the Earth is determined by studying the orbits of satellites. Black hole geodesy, also known as holiodesy, is very powerful because Kerr black holes have a very special multipolar structure. A Kerr black hole with mass M_\bullet and spin parameter a_\bullet (in units with $G = c = 1$) has multipole moments given by

$$M_l + iS_l = (ia_\bullet)^l M_\bullet^{l+1} \quad (2.5)$$

Thus, $M_0 = M_\bullet$, $S_1 = a_\bullet M_\bullet^2$, and $M_2 = -a_\bullet^2 M_\bullet^3$, and similarly for all other multipole moments; they are all completely determined by the first two moments, the black hole mass and spin. This is nothing more than the black hole “no-hair” theorem: the properties of a black hole are entirely determined by its mass and spin.

For inspiraling trajectories that are slightly eccentric and slightly non-equatorial, in principle all the multipole moments are redundantly encoded in the emitted gravitational waves (RYAN, 1995), through the time-evolution of the three fundamental frequencies of the orbit: the fundamental frequencies associated with the r , θ , and ϕ motions (DRASCO & HUGHES, 2004), or, equivalently, the radial frequency and the two precession frequencies.

The mass quadrupole moment M_2 of a Kerr black hole can be measured to within $\Delta M_2 \approx 10^{-2} M_\bullet^3 - 10^{-4} M_\bullet^3$ for signal with an **SNR** of 30 (BARACK & CUTLER, 2004). At the same time $\Delta M_\bullet/M_\bullet$ and $\Delta S_1/M_\bullet^2$ to will be estimated to an accuracy of 10^{-4} to 10^{-3} . Any inconsistency with the Kerr multipole structure could signal a failure of **GR**, the discovery of a new type of compact object, or a surprisingly strong perturbation from some other material or object. For a review of the different hypotheses regarding the nature of the central object see (BABAK ET AL., 2011; SPUERTA, 2010).

Other tests of the Kerr nature of the central massive object have also been proposed. **EMRI** signals can be used to distinguish definitively between a central massive black hole and a boson star (KESDEN ET AL., 2005). In the

black hole case the **GW** signal “shuts off” shortly after the inspiraling body reaches the last stable orbit (and then plunges through the event horizon), while for a massive boson star, the signal does not fade, and its frequency derivative changes sign, as the body enters the boson star and spirals toward its centre. Similarly, if the central object’s horizon is replaced by some kind of membrane (this is the case for the so-called gravastars) the orbital radiation produced by the orbiting body could resonantly excite the **QNMs** of the gravastar, with characteristic signatures in the gravitational wave energy spectrum that would be detectable by **NGO** (PANI ET AL., 2009).

Other studies within **GR** considered axisymmetric solutions of the Einstein field equations for which the multipole moments can differ from the Kerr metric, such as the Manko-Novikov solution. These studies revealed ergodic orbital motion in some parts of the parameter space (GAIR, 2009B) as a result of the loss of the third integral of motion. A similar study suggested that the inspiraling body could experience an extended resonance in the orbital evolution when the ratio of intrinsic frequencies of the system is a rational number (LUKES-GERAKOPOULOS ET AL., 2010). If detected, these features would be a robust signature of a deviation from the Kerr metric.

These and similar studies of “bumpy” Kerr black holes – spacetime metrics with a multipolar structure that deviates from the Kerr spacetime by some “tunable” amount (COLLINS & HUGHES, 2004; GLAMPEDAKIS & BABAK, 2006; HUGHES, 2006; RYAN, 1995; VIGELAND & HUGHES, 2010; VIGELAND ET AL., 2011) – focussed on understanding whether the best fit to **NGO** data is consistent with the Kerr solution *within general relativity*. However, an even more exciting prospect is that modifications in **EMRI** waveforms might arise because the true theory of gravity is in fact different from **GR**. For example, black holes in dynamical Chern-Simons theory (a parity-violating, quantum-gravity inspired extension of **GR**) deviate from Kerr black holes in the fourth multipole moment $\ell = 4$. This affects geodesic motion, and therefore the phasing of the gravitational wave signal (PANI ET AL., 2011; SPUERTA & YUNES, 2009). Gravitational wave observations of black hole-black hole binaries cannot discriminate between **GR** and scalar-tensor theories of gravity. The reason is that black holes do not support scalar fields; *i.e.*, they have no scalar hair. However, **NGO** could place interesting bounds on scalar-tensor theories using observations of neutron stars spiralling into massive black holes (BERTI ET AL., 2005; YAGI & TANAKA, 2010). These limits will be competitive with – but probably not much more stringent than – Solar System and binary pulsar measurements (ESPOSITO-FARÈSE, 2004). Finally, **NGO** observations of compact binaries could provide interesting bounds on Randall-Sundrum inspired braneworld models (MCWILLIAMS, 2010; YAGI ET AL., 2011). A general framework to describe deviations from **GR** in different alternative theories and their imprint on the **GW** signal from **EMRIs** can be found in (GAIR & YUNES, 2011).

Most high-energy modifications to **GR** predict the existence of light scalar fields (axions). If such scalar fields exist, as pointed out long ago by Detweiler and others (DETWEILER, 1980), rotating black holes could undergo a superradiant “black hole bomb” instability for some values of their spin parameter. Depending on the mass of axions, string-theory motivated “string axiverse” scenarios predict that stable black holes cannot exist in certain regions of the mass/angular momentum plane (ARVANITAKI & DUBOVSKY, 2011). Furthermore, this superradiant instability could produce a surprising result: close to the resonances corresponding to a superradiant instability the inspiral of **EMRI** would stop, and the orbiting body would float around the central black hole. These “floating orbits” (for which the net gravitational energy loss at infinity is entirely provided by the black hole’s rotational energy) are potentially observable by **NGO**, and they could provide a smoking gun of high-energy deviations from general relativity (CARDOSO ET AL., 2011).

In conclusion we remark that, if **GR** must be modified, the “true” theory of gravity should lead to similar deviations in all observed **EMRIs**. For this reason, statistical studies of **EMRIs** to test **GR** would alleviate possible disturbances that may cause deviations in individual systems, such as interactions with an accretion disk (BARAUSSE & REZZOLLA, 2008; BARAUSSE ET AL., 2007; KOCSIS ET AL., 2011) or perturbations due to a second nearby black hole (YUNES ET AL., 2011).

2.6.4. Intermediate mass ratio binaries

NGO will give us a unique opportunity to observe middleweight mass black holes in the local Universe. If observed these systems would provide an additional testbed for **GR**.

A loud gravitational wave source for **NGO** would be the intermediate mass-ratio inspiral (IMRI) of binaries comprising a middleweight (or equivalently intermediate-mass) black hole, with mass in the range of a few

times $10^2 M_\odot$ to a few times $10^4 M_\odot$, along with either a massive black hole ($10^6 M_\odot$) or a solar-mass black hole. Currently there is no fully convincing evidence for the existence of intermediate-mass black holes, primarily due to the enormous observational difficulties of resolving the central region of dwarf galaxies and/or globular clusters, the two most likely places where they might reside. **NGO** is one of the most promising observatories for discovering these middleweight black holes.

The strength of the **GW** signal from an **IMRI** lies between that of massive black hole binaries and **EMRIs**, and the signal itself carries features of both limiting types, including a relatively fast frequency evolution and comparable contribution of several harmonics to the total strength of the signal. According to the proposed **NGO** sensitivity, **IMRIs** could be seen up to redshift $z \sim 4$. There are good reasons to expect that **IMRI** orbits may have measurable eccentricity (AMARO-SEOANE & SANTAMARÍA, 2010; SESANA, 2010). It may also be possible in some cases to observe the gravitational spin-spin coupling between the two black holes (equivalent to the Lense-Thirring effect). The precision in the measurements of the source parameters will lie between that of **EMRI** and comparable-mass binaries.

2.6.5. The mass of the graviton

NGO will be capable of setting an upper limit on the mass of graviton that is at least four orders of magnitude better than the current limit based on observations in the Solar System.

In **GR**, gravitational waves travel with the speed of light and the graviton is hence massless. Alternative theories with a massive graviton predict an additional frequency-dependent phase shift of the observed waveform. The dominant effect can be expressed at 1-**PN** order, and would change the **PN** coefficient ψ_2 to

$$\psi_2 \rightarrow \psi_2 - \frac{128\pi^2 G\eta^{3/5}M}{3c^2} \frac{D}{\lambda_g^2(1+z)}, \quad (2.6)$$

where η is again the symmetric mass ratio. This term alters the time of arrival of waves of different frequencies, causing a dispersion, and a corresponding modulation in the phase of the signal that depends on the Compton wavelength λ_g and the distance D to the binary. Hence, by tracking the phase of the inspiral waves, **NGO** should set bounds in the range $\lambda_g \in [2 \times 10^{16} \text{ km}, 10^{18} \text{ km}]$ on the graviton Compton wavelength (BERTI ET AL., 2011), improving current Solar System bound on the graviton mass, $m_g < 4 \times 10^{-22} \text{ eV}$ ($\lambda_g > 3 \times 10^{12} \text{ m}$) by several orders of magnitude.

Statistical observations of an ensemble of black hole coalescence events could be used to yield stringent constraints on other theories whose deviations from **GR** are parametrized by a set of global parameters: examples considered so far in the literature include theories with an evolving gravitational constant (YUNES ET AL., 2010) and Lorentz-violating modifications of **GR** (MIRSHEKARI ET AL., 2011).

2.7. Cosmology

NGO science objectives and investigations relevant to this section

5. Confront General Relativity with observations
 - 5.1 Detect gravitational waves directly and measure their properties precisely
 - 5.2 Test whether the central massive objects in galactic nuclei are consistent with the Kerr black holes of General Relativity.
 - 5.3 Perform precision tests of dynamical strong-field gravity.

Cosmic Vision scientific questions addressed by this section

- 3.2 The gravitational wave universe
Make a key step toward detecting the gravitational radiation background generated at the Big Bang
- 4.1 The early universe
Define the physical processes that led to the inflationary phase in the early universe, during which a drastic expansion supposedly took place.

The NGO Science Objectives are listed in chapter 2.

2.7.1. New physics and the early universe

Gravitational waves penetrate all of cosmic history, which allows NGO to explore scales, epochs, and new physical effects not accessible in any other way (see figure 2.24). Indeed a detectable gravitational wave background in the NGO band is predicted by a number of new physical ideas for early cosmological evolution (HOGAN, 2006; MAGGIORE, 2000). Two important mechanisms for generating stochastic backgrounds are phase transitions in the early universe and cosmic strings.

Gravitational wave produced after the Big Bang form a fossile radiation: expansion prevents them from coming in thermal equilibrium with the other components. Important information on the first instants of the universe is thus imprinted in these relics and can be decoded. The mechanical effect of expansion is simply to redshift the corresponding frequency. Assuming that the wavelength is set by the apparent horizon size $c/H_* = ca/\dot{a}$ at the time of production (when the temperature of the universe is T_*), the redshifted frequency is

$$f_0 = \dot{a}(t) \approx 10^{-4} \text{ Hz} \sqrt{H_*(t) \times \frac{1 \text{ mm}}{c}} \approx 10^{-4} \text{ Hz} \left(\frac{k_B T_*}{1 \text{ TeV}} \right) \quad (2.7)$$

Thus, NGO frequency band of about 0.1 mHz to 100 mHz today corresponds to the horizon at and beyond the Terascale frontier of fundamental physics. This allows NGO to probe bulk motions at times about $3 \times 10^{-18} \text{ s} - 3 \times 10^{-10} \text{ s}$ seconds after the Big Bang, a period not directly accessible with any other technique. Taking a typical broad spectrum into account, NGO has the sensitivity to detect cosmological backgrounds caused by new physics active in the range of energy from 0.1 TeV to 1000 TeV, if more than a modest fraction of about 10^{-5} of the energy density is converted to gravitational radiation at the time of production. A standard example of new physics is a first-order phase transition resulting in bubble nucleation and growth, and subsequent bubble collisions and turbulence.

Phase transitions often lead to symmetry breaking and the formation of one-dimensional topological defects known as strings. Among possible topological defects, strings are unique from a cosmological point of view because, whereas their energy density should grow with expansion, they interact and form loops which decay into gravitational waves. Thus cosmic strings tend to form networks with a typical scaling behaviour, losing energy principally through gravitational radiation with a very broad and uniquely identifiable spectrum. Besides this type of phase transition, strings could find their origin among the fundamental objects of string theory, the theory that is aiming at providing a unified framework for all particles and forces of nature. Indeed, although fundamental strings were devised as submicroscopic objects, it has been progressively realized (COPELAND ET AL.,

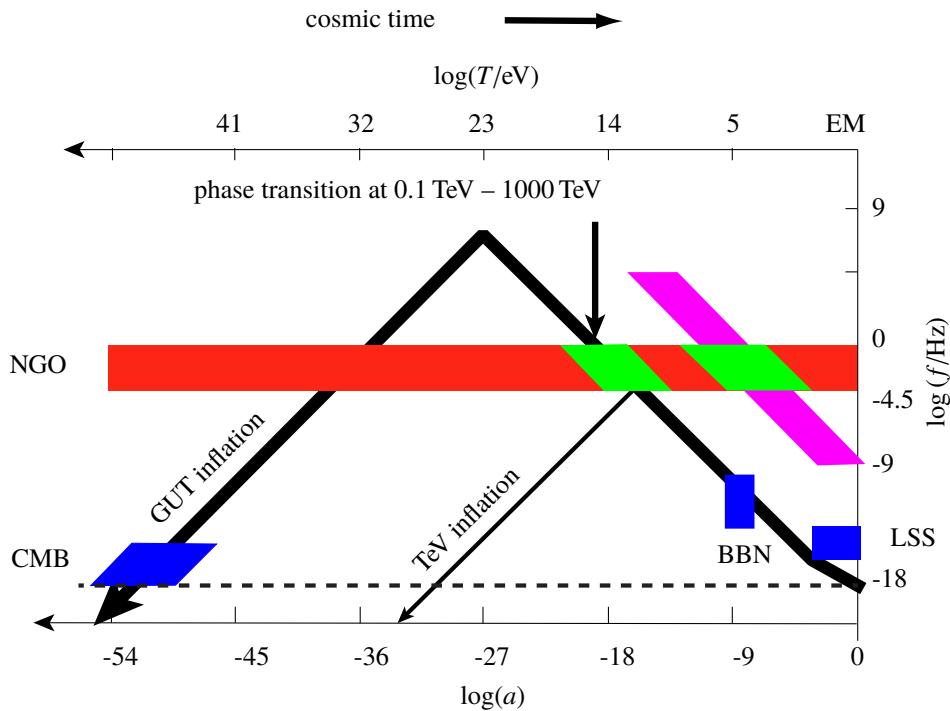


Figure 2.24.: The observed (redshifted) frequency of wave-generating phenomena is shown as a function of cosmic scale factor a , with the present epoch at the right. The redshifted Hubble rate (horizon scale) is shown in black for a standard Grand Unified Theory (GUT) and a lower temperature Terascale (TeV) inflationary cosmology. Blue regions are accessible to electromagnetic (EM) observations: the universe since recombination (right box) and cosmic microwave background (CMB) fluctuations (left box). The red bar shows the range of cosmic history accessible through NGO, from processes within the horizon up to about 1000 TeV, as well as inflation different from CMB observations.

2004) that some of these strings could be stretched to astronomical size by the cosmic expansion. NGO will be our most sensitive probe for these objects by several orders of magnitude and so offers the possibility of detecting direct evidence of fundamental strings.

In order to distinguish backgrounds of gravitational waves from those waves emitted by point sources, it is essential to make use of the successive positions of NGO around the Sun, and thus to wait a sufficient amount of time (of the order of a few months). It is more difficult to disentangle an isotropic cosmological (or astrophysical) background from an instrumental one, all the more because the NGO “Mother-Daughter” configuration, providing only two measurement arms, does not allow to use Sagnac calibration (HOGAN & BENDER, 2001). Luckily, in the case of phase transitions as well as cosmic strings, the spectral dependence of the signal is well predicted and may allow to distinguish cosmological backgrounds as long as they lie above the NGO sensitivity curve.

First-order cosmological phase transitions: Bulk motion from bubble nucleation, cavitation, collisions, turbulence

Abundant evidence suggests that the physical vacuum was not always in its current state, but once had a significantly higher free energy. This idea is fundamental and general: it underlies symmetry breaking in theories such as the Standard Model and its supersymmetric extensions, and cosmological models including almost all versions of inflation. Common to all these schemes is the feature that a cold, nearly uniform free energy contained in the original (*false*) vacuum is liberated in a phase transition to a final (*true*) vacuum, and eventually converted into thermal energy of radiation and hot plasma.

In many theories beyond the Standard Model, the conversion between vacuum states corresponds to a first-order phase transition. In an expanding universe this leads to a cataclysmic process. After supercooling below the critical temperature T_* for the transition, a thermal or quantum jump across an energy barrier leads to the formation of bubbles of the new phase. The bubbles rapidly expand and collide. The internal energy is thus

converted to organised flows of mass-energy, whose bulk kinetic energy eventually dissipates via turbulence and finally thermalises. The initial bubble collision and subsequent turbulent cascade lead to relativistic flows and acceleration of matter that radiate gravitational waves on a scale not far below the horizon scale (CAPRINI ET AL., 2009; HOGAN, 1986; HUBER & KONSTANDIN, 2008; KAMIONKOWSKI ET AL., 1994; WITTEN, 1984).

The gravitational wave energy density Ω_{GW} typically depends on two parameters: H_*/β is the duration of the transition in Hubble units and α is the fraction of energy density available in the source (false vacuum, relativistic motion). Typically $\Omega_{\text{GW}} \sim \Omega_{\text{rad}} (H_*/\beta)^2 (\alpha/1 + \alpha)^2$, where Ω_{rad} is the the fraction of radiation energy today. Strong first order phase transitions are obtained for $\alpha \gg 1$ but, in the context of specific models, increasing α may increase β as well.

Dynamics of warped sub-millimetre extra dimensions

Superstring theory provides examples of strong first order phase transitions in the Terascale region. It requires, for mathematical consistency, several extra dimensions. The sizes of these dimensions, their shapes, and how they are stabilised are yet to be determined. If they exist, gravity can penetrate into them, so they must be small or warped – with a size below the sub-millimetre scale limit set by direct laboratory tests of the gravitational inverse-square law. The scales probed by Standard Model particles and fields are much smaller than this, but fields other than gravity might be confined to a 3-dimensional subspace or (mem)brane plunged in the higher dimensional space.

Since the Hubble length at the Terascale is about a millimetre, the current threshold where possible new effects of extra dimensions might appear happens to be about the same for experimental gravity in the laboratory as for the cosmological regime accessible to **NGO**. It is even possible that new properties of gravity on this scale are related to cosmic dark energy, whose energy density is about $(0.1 \text{ mm})^{-4}$ in particle physics units.

The dynamics associated with the stabilisation of extra dimensions at a certain size or warp radius might introduce a source of free internal energy released coherently on a *mesoscopic*, *i.e.* sub-millimetre to nanometre scale, leading to a detectable background (HOGAN, 2000; RANDALL & SERVANT, 2007). If the extra dimensions are much smaller than the Hubble length when the stabilisation occurs, the behaviour of the extra dimensions is nearly equivalent to scalar field behaviour as viewed in conventional 3-dimensional space, with effects similar to the phase transitions discussed above (see figure 2.25).

Backgrounds, bursts, and harmonic notes from cosmic strings

As we have seen above, models of physics and cosmology based on string theory, as well as their field-theory counterparts, often predict the cosmological formation of cosmic superstrings (COPELAND ET AL., 2004) that form after inflation and are stretched to enormous length by the cosmic expansion. Cosmic strings also arise from certain types of phase transitions, and stable relics of the high-energy phase persist as topological defects: in the form of one-dimensional strings that resemble flux tubes or trapped vortex lines.

The primordial network of strings spawns isolated, oscillating loops that ultimately radiate almost all of their energy into gravitational waves. Their gravitational radiation is mainly governed by a single dimensionless parameter $G\mu/c^4$ reflecting the fundamental physics of the strings, where G is Newton's constant and μ is the energy per unit length, or tension. This parameter is known to be very small, as current limits on gravitational wave backgrounds already indicate that if cosmic strings existed, they must be so light that they would have few observable effects apart from their gravitational radiation.

Figure 2.26 compares **NGO** sensitivity (in red) with predicted stochastic background spectra in two distinct scenarios: large loops in blue (where newly formed loops are about $\alpha = 0.1$ times the horizon size) for two values of $G\mu/c^4$ spanning a range of scenarios motivated by brane world inflation, and small loops in dashed (with $\alpha = 50\epsilon G\mu$) for one value of $G\mu/c^4$. We note that the spectrum from cosmic strings is distinguishably different from that of phase transitions or any other predicted source: it has nearly constant energy per logarithmic frequency interval over many decades at high frequencies, and falls off after a peak at low frequencies since large string loops are rare and radiate slowly. In the small loop scenario, the peak frequency shifts to lower values when increasing ϵ , whereas the amplitude decreases with $G\mu/c^4$. This allows an interesting interplay between measurements at **NGO**, ground interferometers and millisecond pulsar arrays: depending on the parameters, one

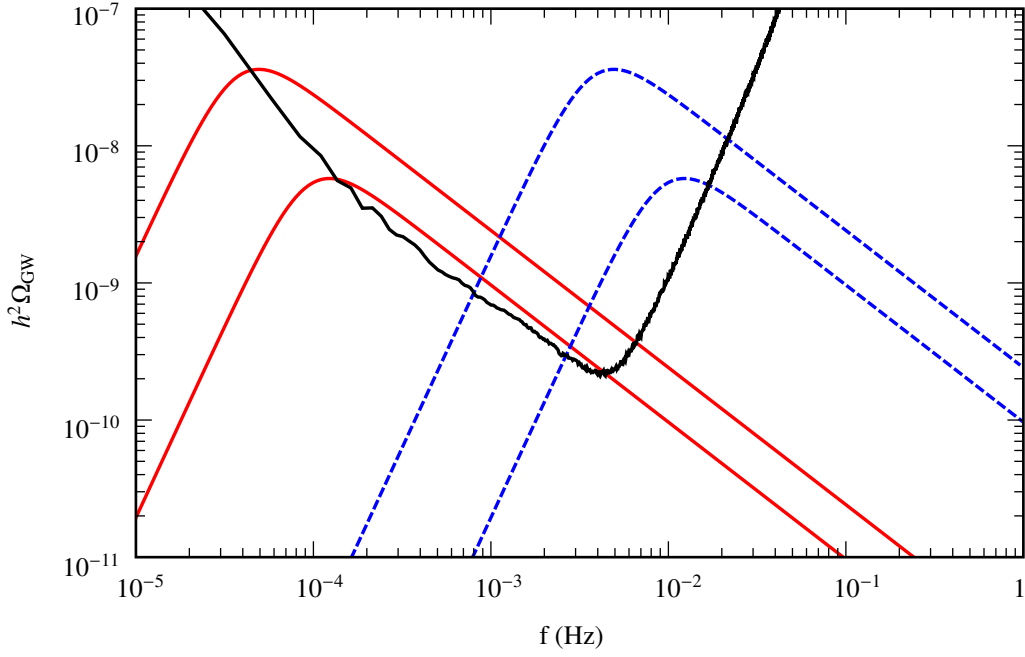


Figure 2.25.: Predictions for the holographic phase transition (KONSTANDIN ET AL., 2010) corresponding to the model of Randall and Sundrum with a TeV brane stabilized. In black, the sensitivity curve of NGO expressed in terms of the gravitational wave background density Ω_{GW} . In red, signals corresponding to a phase transition temperature of 10^2 GeV. In dashed blue, a transition temperature of 10^4 GeV. From bottom to top, curves correspond to $\beta/H_* = 6$ and $\beta/H_* = 15$.

may have detection of the string background at one, two or three of these different types of detectors. In the large loop scenario, NGO sensitivity in terms of $G\mu/c^4$ is several orders of magnitude deeper than even the best possible future sensitivity from pulsar timing.

If the strings are not too much lighter than $G\mu/c^4 \sim 10^{-10}$, occasional distinctive bursts might be seen from loops, produced by a sharply bent bit of string moving at nearly the speed of light (DAMOUR & VILENKIN, 2005; SIEMENS ET AL., 2006). These rare events, known as kinks or cusps, are recognisable, if they are intense enough to stand out above the background, from their universal waveform which derives just from the geometry of the string. Cusps are localized in time whereas kinks are propagating along the strings. In the case of fundamental strings, the presence of junctions between strings leads to a proliferation of kinks (BINÉTRUY ET AL., 2010; BOHÉ, 2011).

Although individual burst events, if detected, give the clearest signature of a string source, the first detectable sign of a superstring loop population is likely their integrated stochastic background as shown in figure 2.26.

Terascale inflationary reheating

Inflation represents an extraordinarily coherent behaviour of an energetic scalar field that is nearly uniform across the observable universe. After inflation, the internal potential energy of this field is converted into a thermal mix of relativistic particles, in a process known as reheating. The reheating temperature might be as cool as 1 TeV, especially in some brane-world models where the Planck scale is itself not far above the Terascale.

There is no reason to assume a quiet, orderly reheating process: the decay of the inflaton energy may be violently unstable. In many scenarios, the conversion begins with macroscopically coherent but inhomogeneous motions that eventually cascade to microscopic scales. Quantum coherent processes such as preheating transform the energy into coherent classical motions that can generate backgrounds on the order of 10^{-3} of the overall density (DUFAUX ET AL., 2007, 2009; GARCÍA-BELLIDO & FIGUEROA, 2007; KHLEBNIKOV & TKACHEV, 1997). As with these transitions, the characteristic frequency of the background matches the NGO band if the final reheating occurred at 0.1 TeV to 1000 TeV.

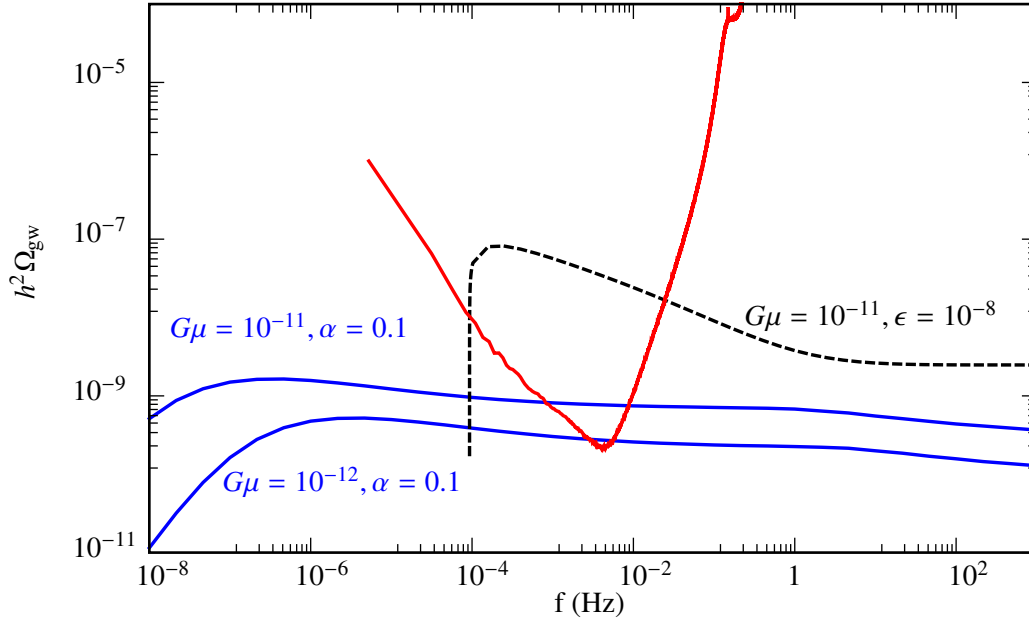


Figure 2.26.: Typical string background expected for *NGO* (whose sensitivity curve is in red) in the large loop scenario in blue (α determines the loop size as a fraction of the horizon size) and in the small loop scenario in dashed ($\epsilon \equiv \alpha/(50G\mu)$).

Exotic inflationary quantum vacuum fluctuations

The amplification of quantum vacuum fluctuations during inflation leads to a background of primordial gravitational waves. An optimistic estimate of this background in the case of conventional inflation limits these to less than about 10^{-10} of the cosmic microwave background (CMB) energy density, far below *NGO*'s sensitivity; in many inflation models it is much less (CHONGCHITNAN & EFSTATHIOU, 2006). However, some unconventional versions of inflation, particularly pre-Big-Bang or bouncing brane scenarios, predict possibly detectable backgrounds in the *NGO* band (SEE *e.g.* BRUSTEIN ET AL., 1995; BUONANNO, 2003; BUONANNO ET AL., 1997). Although some key parameters remain unknown, which limits the predictive power of these models, they are significantly constrained by gravitational wave backgrounds. If such a background is detected, its spectrum also contains information about the universe at the time perturbations re-enter the horizon (the second horizon intersection in figure 2.24).

2.7.2. Cosmological measurements with *NGO*

The discovery of coalescing binary black holes, signposts of (pre-)galactic mergers, will test, albeit indirectly, the hypothesis which is at the heart of the current paradigm of galaxy formation, *i.e.* their assembly in a bottom-up fashion. But not only that. Coalescing binary black holes are standard sirens, and this will allow for the direct measurement of the luminosity distance to the source. If coalescence is accompanied by an electromagnetic signal that permits the measure of the optical redshift of the source, then *NGO* will improve upon the estimation of cosmological parameters, such as the Hubble constant and the dark-energy parameter w .

NGO will have unique capabilities in detecting signatures from or setting meaningful constraints on a wide range of new cosmological phenomena and new fundamental physics. Gravitational radiation backgrounds are predicted in cosmologies that include first order phase transitions, late-ending inflation, and dynamically active mesoscopic extra dimensions. *NGO* will provide the most sensitive direct probes of such phenomena near TeV energies or Terascale.

As discussed in section 2.4 we can probe the assembly of cosmic structures through observations of black hole binaries up to high redshifts. In addition to that, gravitational wave sources could serve as standard sirens for cosmography (HOLZ & HUGHES, 2005), because chirping binary systems allow direct measurements of the luminosity distance to the source. The principle is elegant and simple (SCHUTZ, 1986): the chirping time τ of an inspiral/merger event, together with its orbital frequency ω and strain h , gives the absolute luminosity distance to the source, $D_L \sim c/(\omega^2\tau h)$, with a numerical factor depending on details of the system that are precisely

determined by the measured waveform. However, *NGO* cannot independently determine the redshift of a source, since in gravitational wave astronomy, the measured source frequency and chirp time are always combined with cosmic redshift $\omega = \omega_{\text{source}}/(1+z)$, $\tau = (1+z)\tau_{\text{source}}$, *i.e.*, the redshift is degenerate with the source intrinsic parameters. An independent measurement of redshift is therefore needed. This may be accomplished by getting the optical redshift to the host galaxy, for instance by identifying an electromagnetic radiation counterpart to the event.

In the last decade, several mechanisms producing electromagnetic counterparts to black hole binary coalescences have been proposed (*e.g.*, ARMITAGE & NATARAJAN, 2002; MILOSAVLJEVIĆ & PHINNEY, 2005; PHINNEY, 2009); an exhaustive review can be found in (SCHNITTMAN, 2011). While there are still uncertainties in the nature and strength of such counterparts, we might expect some of them to be observable at least in the local universe (say, $z \leq 1$). Our parameter estimation simulations show that, at low redshift, we could expect to localize at least 50 % of the inspiralling black holes to better than 400 square degrees and about 11 % to better than 10 square degrees. Merger and ringdown (if observed) should further improve those numbers. As a practical example, wide area surveys like **Large Synoptic Survey Telescope** (LSST) (LSST SCIENCE COLLABORATIONS ET AL., 2009) in optical or the **VAST** project using the Australian Square Kilometer Array Pathfinder (JOHNSTON ET AL., 2007) in radio will have the capability of covering such large area in the sky to high depth several times per day during and right after the merger event, looking for distinctive transients. Any identified counterpart will provide precise measurements of the source redshift and sky location. We can use this information to perform directional search (fixing the sky location of GW source) in the *NGO* data and the resulting uncertainty in the luminosity distance drops to less than 1 % for 60 % (5 % for 87 %) of the sources. Those numbers are comparable with (or even lower than) the weak lensing error at these low redshifts (WANG ET AL., 2002). Ultra-precise measurements of the redshift and the luminosity distance will allow us to cross-check the SNIa measurements (PERLMUTTER & RIESS, 1999; RIESS ET AL., 1998B), and because of the very different systematics from the usual cosmological distance ladder estimates, will be a strong check on hidden systematic errors in these measurements. This will improve the estimation of cosmological parameters, such as H_0 and w .

Without electromagnetic identification of the host, we can check statistical consistency between all the possible hosts detected within the measurement error box, to infer cosmological parameters as suggested in (PETITEAU ET AL., 2011). To realize this scheme one needs a rather good source sky location and distance determination, which is possible with *NGO* only at low redshifts ($z < 2$). In the local universe, the same technique applied to **EMRIs** will allow precision measurement of H_0 (MACLEOD & HOGAN, 2008) at a level of a few percent.

3. The NGO concept

The **NGO** concept for directly detecting the oscillating strain in spacetime caused by gravitational waves shares the scheme used in all laser interferometer-based gravitational wave detectors: the passage of the wave is detected by measuring the time-varying changes of optical pathlength between free-falling mirrors.

Gravitational wave detectors based on laser interferometers measure the change in length (δL) directly. The strain ($\delta L/L$) produced by the sources accessible with **NGO** (see chapter 2) may be as small as 10^{-24} . This argues simultaneously for a measurement length L as large as possible and long integration times, the primary impetus for a space-borne detector millions of kilometres long. Interferometry is the only measurement system known that can operate over these distances and with the required sensitivity.

“Free-falling” or inertial masses are not only an important conceptual detail in the detection of gravitational waves, but are an essential for achieving the required sensitivity for **NGO**. Free-falling masses are, by definition, undisturbed by forces other than gravitation. Keeping the test masses in free-fall conditions allows avoiding disturbances to the test masses causing time-varying movements that in turn could be confused with the apparent displacements caused by gravitational radiation: The residual disturbances of the masses must be sufficiently small such that the resulting motions are less than the apparent length changes associated with gravitational waves to be detected. To achieve free-fall conditions, the detector must be located in a very quiet environment. Space can provide a very stable, benign environment if careful design choices for science instrumentation, spacecraft and orbits are made.

Free-fall also implies that no station-keeping or formation-flying is needed. This is not strictly true for **NGO**. Firstly it is not the satellites that are in free fall, but the test masses, so the satellites will have to be actuated to follow the test masses, which is the task of the drag-free attitude control system (DFACS) described in some detail in chapter 5. Secondly, the satellites need to *rotate* over the course of the mission to keep the “**Mother**” spacecraft (or “**Daughter**” spacecraft, respectively) in the field of view. Both manoeuvres are purely *local*, *i.e.* no coordination between the satellites is needed. Other than those manoeuvres, there is no station-keeping foreseen. The distance between the satellites as well as the angles (*i.e.* the shape of the constellation) is evolving freely under the action of gravity alone, so **NGO** requires *no* formation-flying in any phase of the mission lifetime.

3.1. NGO design concept

NGO’s two measurement arms are defined by three spacecraft orbiting the Sun (figure 3.1) in a triangular configuration. A key feature of the **NGO** concept is a set of three orbits that maintain a near-equilateral triangular formation, without the need for station-keeping. Depending on the initial conditions of the spacecraft, the formation can be kept in an almost constant distance to the Earth or be allowed to slowly drift away to about 70×10^6 km,

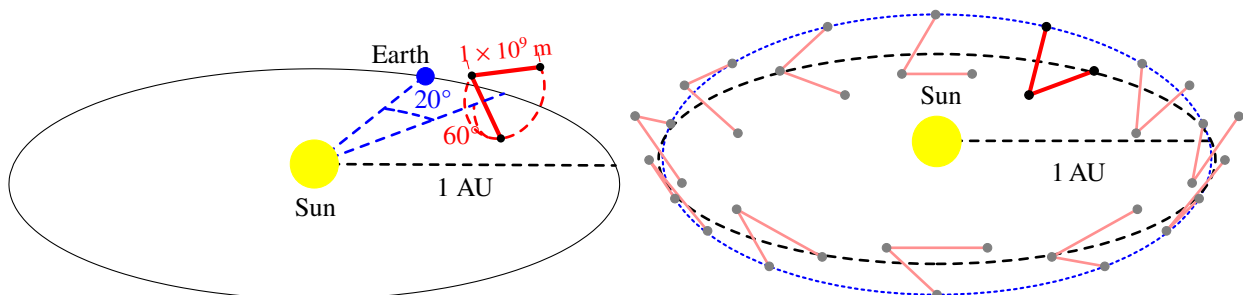


Figure 3.1.: *The NGO orbits: The constellation is shown trailing the earth Earth by about 20° (or 5×10^7 km) and is inclined by 60° with respect to the ecliptic. The trailing angle will vary over the course of the mission duration from 10° to 25° . The separation between the S/C is 1×10^6 km.*

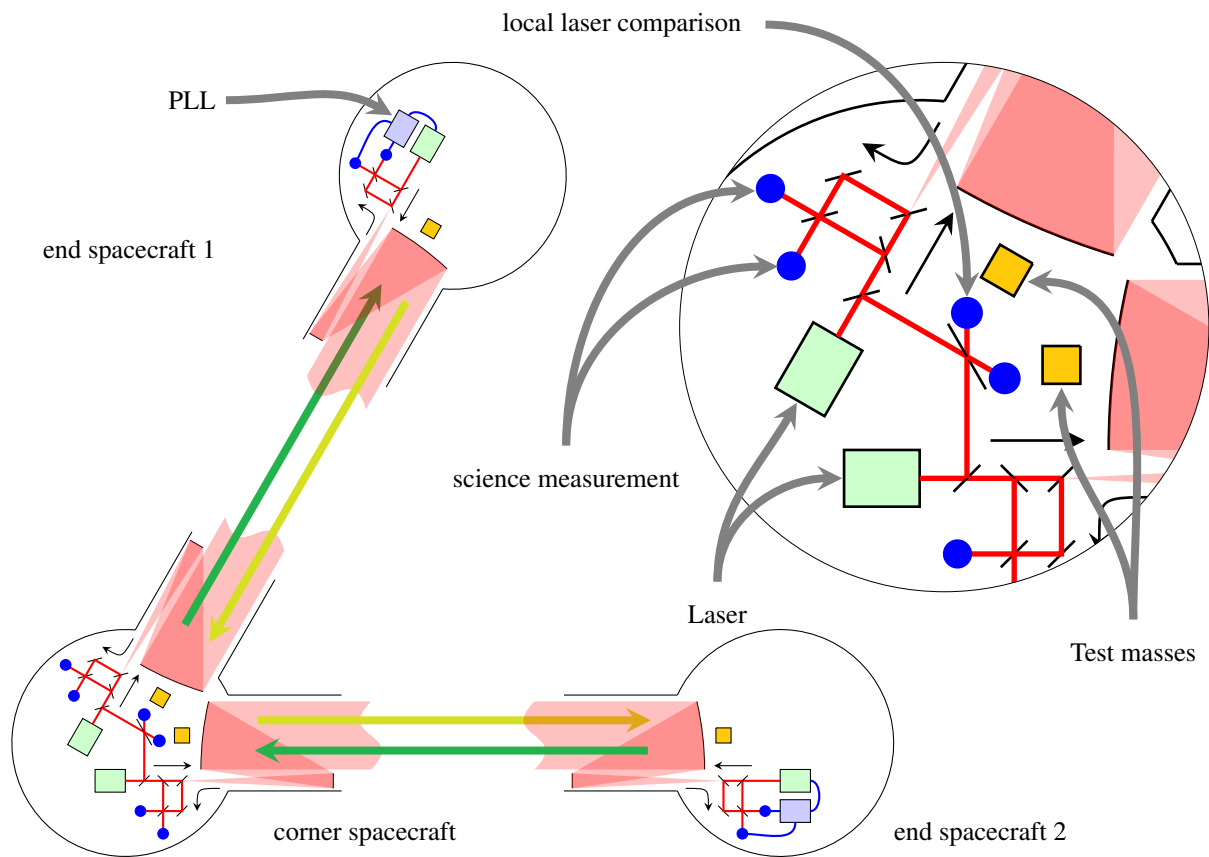


Figure 3.2.: The constellation of the three NGO spacecraft constitutes the science instrument. The central spacecraft houses two send/receive laser ranging terminals, the end spacecraft one each. The laser in the end spacecraft is phaselocked to the incoming laser light. The blue dots indicate where interferometric measurements are taken. The sketch leaves out the test mass interferometers for clarity.

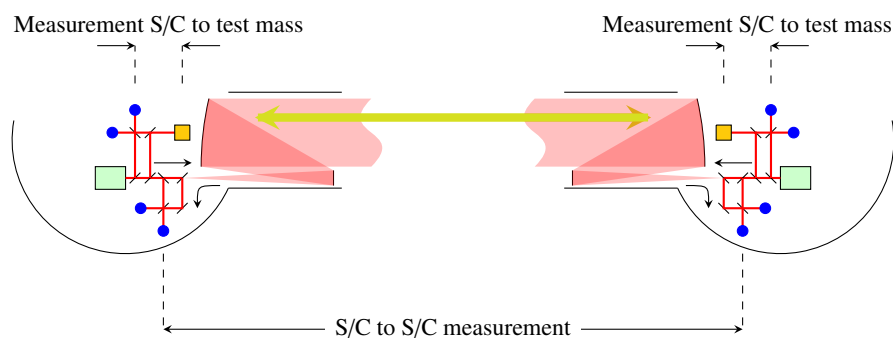


Figure 3.3.: Partition of the NGO measurement. Each measurement between two test masses is broken up into three different measurements: two between the respective test mass and the spacecraft and one between the two spacecraft. As the noise in the measurement is dominated by the shot noise in the S/C-S/C measurement, the noise penalty for the partitioning of the measurement is negligible. The blue (solid) dots indicate where the interferometric measurements are taken.

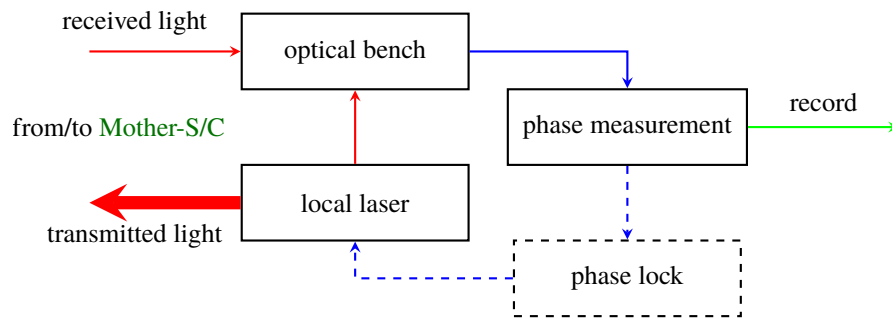


Figure 3.4.: Measurement scheme for the inter-spacecraft link at the Daughter-S/C. The received light (red) and the light from the local laser are combined on the optical bench and the beat note is fed to the phasemeter. The phasemeter determines the relative phase and hands the data (green) off to the data management (and eventually to ground). The phasemeter can also feed an error signal (blue) to a control electronics that will keep the local laser at a fixed frequency offset to the received light. While this is not required for the measurement scheme, it reduces the amount of data to be stored and downloaded, as in this case the phasemeter always registers a constant number.

which is the practical limit for communication purposes given moderate antenna gains and amplifiers on board the spacecraft.

The “Mother” spacecraft, serves as the “central hub” and defines the apex of a V, two other, simpler spacecraft (“Daughter” spacecraft) are situated at the ends of the V-shaped constellation. The Mother-S/C houses two free-falling test masses that define the one set of endpoints of the two arms, the Daughter-S/C house one test mass each, defining the two other endpoints (figure 3.2). In addition, each spacecraft accomodates the interferometry equipment needed to measure changes in the arm length.

A second key feature of the NGO concept is that the test masses are protected from disturbances as much as possible by careful design and “drag-free” operation. To establish drag-free operation, a housing around the test mass senses the relative position of test mass and spacecraft, and a control system commands the spacecraft’s thrusters to follow the free-falling mass. Drag-free operation reduces time-varying disturbances to the test masses caused by force gradients arising in a spacecraft that is moving with respect to the test masses. The amplitude spectral density of the residual acceleration of the test mass characterises the disturbance reduction, the first basic function of the science instrument. An additional benefit of the NGO orbits is the almost constant sun-angle of 30° of the spacecraft, thereby resulting in an extremely stable thermal environment within, minimising thermal disturbances on the spacecraft.

NGO achieves the requisite approximate $3 \times 10^{-20} / \sqrt{\text{Hz}}$ strain sensitivity (averaged over all sky locations and polarisations), which allows to detect a strain of about 3.7×10^{-24} in a 2-year measurement with an SNR of 1, in part, through a phase resolution of about $10 \mu\text{cycle}/\sqrt{\text{Hz}}$ with $1 \mu\text{m}$ wavelength light, resulting in a displacement sensitivity of $11 \times 10^{-12} \text{ m}/\sqrt{\text{Hz}}$ over a path length of $1 \times 10^9 \text{ m}$. The achievable reductions of disturbances on test masses and the achievable displacement sensitivities by the laser ranging system yield a useful measurement bandwidth in the frequency range from $3 \times 10^{-5} \text{ Hz}$ to 1 Hz . (The requirement is 10^{-4} Hz to 1 Hz ; the goal is $3 \times 10^{-5} \text{ Hz}$ to 1 Hz .)

3.2. Measurement scheme

The distance measuring system is a continuous interferometric laser ranging scheme, similar to that used for radar-tracking of spacecraft. The direct reflection of laser light, such as in a normal Michelson interferometer, is not feasible due to the large distance between the spacecraft. Diffraction widens the laser beam so that for each Watt of laserpower sent, about 250 pW are received. Direct reflection would thus result in a attenuation factor of about 6.25×10^{-20} , yielding about one photon in every three days. Therefore, lasers at each end of each arm operate in a “transponder” mode. A laser beam is sent out from the Mother-S/C to the Daughter-S/C. The laser in the Daughter-S/C is then phase-locked to the incoming beam thus returning a high-power phase replica (see figure 3.4). The returned beam is received by the Mother-S/C and its phase in turn compared with the phase

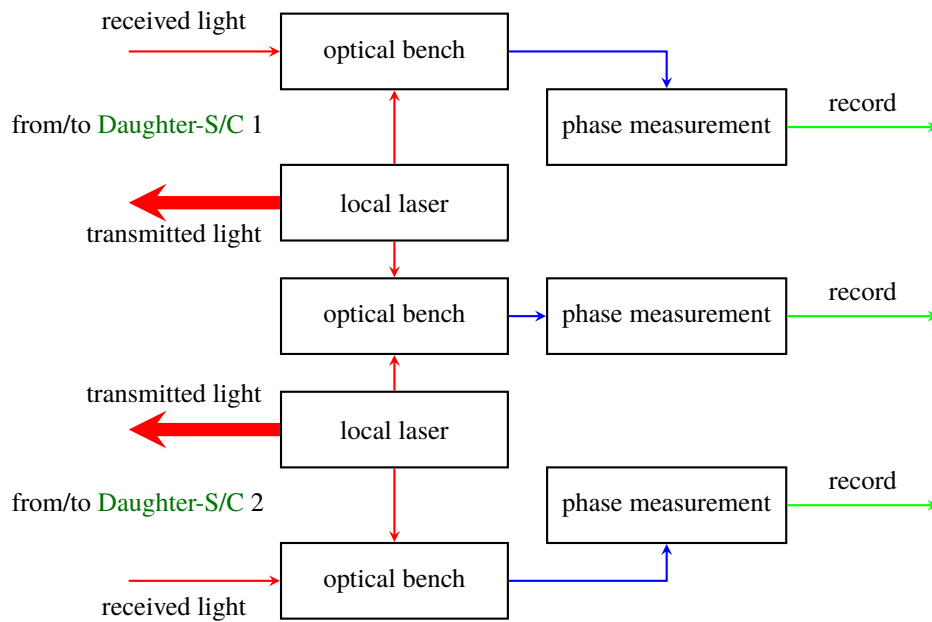


Figure 3.5.: Measurement scheme for the inter-spacecraft links at the Mother-S/C. The received light (red) and the light from the local laser are combined on the optical bench for each of the links and the beat note is fed to the phasemeter. The phasemeter determines the relative phase and hands the data (green) off to the data management (and eventually to ground). In addition, the phases of the local lasers are compared and recorded as well.

of the local laser. A similar scheme is employed for the second arm. In addition, the phases of the two lasers serving the two arms are compared in the central spacecraft (see figure 3.5).

Two additional measurements are needed for the data analysis. One is the absolute distance between the test masses. The main measurement registers *changes* in the distance with picometre accuracy. In contrast, the *absolute* distance is needed only to an accuracy of a few metres, which is easily achieved by imprint a simple ranging code on the laser light. The other additional measurement concerns the *time* on each spacecraft. As spacecraft clocks with sufficient stability do not exist (and are not likely to come in existence in the next decade) the *relative* clock error between the spacecraft has to be recorded. For that purpose, the clock signal is imprinted on the laser light as well, allowing an easy comparison between the clocks on **Mother-S/C** and **Daughter-S/C**. Both additional measurements are performed by the phasemeter that is described in more detail in section 5.2.

The set of phase measurements together with the additional measurements then allows to determine the changes in optical path difference, laser frequency noise, and clock noise.

For practical reasons, this measurement is broken up into three distinct parts: the measurement between the spacecraft, *i.e.* between the optical benches that are fixed to the spacecraft, and the measurement between each of the test masses and its respective optical bench (see figure 3.3). By combining the three measurements, the measurement of the distance between the test masses is reconstructed and kept insensitive to the noise in the position of the spacecraft with respect to the test masses. Normally, such a partitioning would be avoided as it increases the noise due to the number of detectors involved. However, the detector noise is generally negligible in **NGO**, the partitioning of the measurement has no significant degrading impact on the overall sensitivity.

3.3. Data Analysis

As **NGO** does not have the ability for dedicated observational campaigns but observes all the sky all the time, the extraction of the science from the data requires a special effort.

All the data analysis in **NGO** happens on the ground. The first step in the data analysis, after some calibration and data quality inspection, is to combine the data streams from the **Mother-S/C** and **Daughter-S/C** appropriately to reject the frequency noise of the lasers. This is achieved by employing a technique known as time-delay

interferometry (TDI) (DHURANDHAR, 2009; DHURANDHAR & TINTO, 2005), synthesising an equal-arm Michelson Interferometer (using information about the absolute arm length obtained via the ranging code) that is insensitive to frequency noise. This TDI-stream, together with other auxiliary information as, *e.g.*, the spacecraft ephemerides are the input to the following steps of data analysis.

The goal of the data analysis is to determine the astrophysical parameters of the sources of the various gravitational wave (GW) signals in the data stream; more generally, the output of the data analysis is a posterior probability density function (PDF) for the source parameters, encoding not only the most likely value, but the full probabilistic information.

While the problem is well defined and well understood in principle, the large number of parameters per source, *e.g.* 14 for extreme mass-ratio inspirals (EMRIs) or 17 for black hole binaries, and the even larger number of potential sources (tens of millions Galactic binaries) in the data stream prohibits an exhaustive search of the parameter space. The identification of sources in the data stream requires a reasonably large signal-to-noise ratio (SNR) that are well “separated” in the parameter space. Typically, an $\text{SNR} > 5$ is assumed as a threshold for detectability, but higher SNR can be required if the signal is not well modelled and thus the “effective” SNR is somewhat smaller than the “true” SNR.

3.3.1. General principles

Almost all of the detection algorithms for *known* sources rely on *matched filtering*, a correlation of a signal template $q(\vec{p}, t)$ depending on parameters \vec{p} with the data stream $s(t)$, weighted by the inverse of the spectral density of the noise $S_n(f)$:

$$\langle q(\vec{p}, t), s(t) \rangle = \int \frac{\tilde{q}(f)\tilde{s}(f)^* + \tilde{q}(f)^*\tilde{s}(f)}{S_n(f)} df \quad (3.1)$$

where $\tilde{s}(f)$ and $\tilde{q}(f)$ are the Fourier transforms of $s(t)$ and $q(\vec{p}, t)$, respectively. Finding the parameters \vec{p}_0 for a given source is then reduced to maximising $\langle q(\vec{p}, t), s(t) \rangle$ with respect to \vec{p} using the proper waveform q for the source. The *effective* SNR is then given by that maximum,

$$\text{SNR} = \langle q(\vec{p}_0, t), s(t) \rangle \quad (3.2)$$

The keys to the NGO data analysis are therefore fast and reliable search algorithms and high-fidelity waveform templates that allow to have the SNR to be as close as possible to the *true* SNR $\langle Q(\vec{p}_0, t), s(t) \rangle$ where $Q(\vec{p}_0, t)$ describes the source’s waveform perfectly.

Searching the data stream for unknown, or just unmodelled, signals such as GW bursts makes use of methods that do not use templates, but rather search for excess power or use maximum-likelihood methods, such as the coherent waveburst pipeline currently in use for LIGO (KLIMENKO ET AL., 2008).

3.3.2. Templates

The largest number of sources are Galactic binaries, which have a relatively simple signal structure (see section 2.3) – an almost monochromatic signal with only a very small frequency change over the lifetime of NGO:

$$A = \frac{2}{D_L} (\pi f)^{2/3} \mathcal{M}^{5/3} \quad \phi(t) = 2\pi(ft + \frac{f\dot{t}^2}{2}) \quad (3.3)$$

$$h_+ = A(1 + \cos^2 \iota) \cos(\phi(t) + \phi_0) \quad h_\times = -2A \cos \iota \sin(\phi(t) + \phi_0)$$

where D_L is the luminosity distance, f the frequency, ι the inclination of the binary’s orbit with respect to the direction to the Solar System barycenter (SSB), and \mathcal{M} the chirp mass. These signals can be very easily modeled with high fidelity, so that essentially all galactic binaries with a SNR larger than the threshold will be detected, resulting in thousands of sources.

Signals from massive black hole binaries have a more complex signal structure, are much less numerous (tens to hundreds), and have an SNR of up to 10^4 . Signals from massive black hole binaries are numerically

expensive to model, however, the very high SNR allows for using simplified signal models for the initial search so that the calculation of high-fidelity waveforms can be limited to a very much reduced parameter space. During the inspiralling phase, they can be described sufficiently well using, *e.g.*, post-Newtonian (PN)-approximation, and the signal can be calculated by integrating the resulting differential equations (LANG & HUGHES, 2006). The signal during coalescing and the ringdown can be calculated only through numerical relativity (NR). Fortunately, NR has made significant progress in the last decade (BAKER ET AL., 2006A, 2007A,B, 2008A; BUONANNO ET AL., 2007B; CAMPANELLI ET AL., 2006A,B; PRETORIUS, 2005), so that waveforms from coalescing massive black hole binary (MBHB) and the ringdown phase are available. The two different phases can be combined to provide a continuous waveform from early inspiral to ringdown (BAKER ET AL., 2007C; BUONANNO ET AL., 2007A; CAMPANELLI ET AL., 2009).

The most complex signals are emitted by EMRIs, which have a relatively low SNR of about 100 or less. Until recently, the lack of a full understanding of the effect of radiation-reaction and self-force on the waveform, hampered the calculation of high-fidelity waveforms. For that reason, the threshold for the detection of EMRIs has been assumed throughout the document to be $\text{SNR} > 30$. With this threshold, the so called “Analytic Kludge” (AK) waveforms can be used (BABAK ET AL., 2007) that approximate the “real” waveforms sufficiently well to allow detection. While the complexity of the waveform makes the detection of EMRIs more difficult, once detection has been achieved, parameter estimation actually benefits from the complexity. This is due to the fact that even small changes in the parameters changes the waveform significantly, so the parameters can be established with high accuracy. Recently, the understanding of the self-force has been advanced significantly, allowing to calculate more accurate waveforms, potentially allowing sources with $\text{SNR} < 30$ to be detected (BARACK & SAGO, 2011; WARBURTON ET AL., 2011).

3.3.3. Algorithms

The algorithms that are currently used to search for the optimal source parameters and to calculate the posterior PDF range from straight-forward optimisers to elaborated statistical and genetic algorithms.

Methods employed include time-frequency searches (BROWN ET AL., 2007; GAIR & JONES, 2007; GAIR & WEN, 2005; GAIR ET AL., 2008B), Markov-chain Monte Carlo (MCMC) searches (CHRISTENSEN & MEYER, 1998; CHRISTENSEN ET AL., 2004; CORNISH & CROWDER, 2005; CORNISH & PORTER, 2006; CROWDER & CORNISH, 2007; STROEER ET AL., 2006; TRIAS ET AL., 2008) and its variants, such as reversible jump Markov-chain Monte Carlo (MCMC) (STROEER & VEITCH, 2009), and parallel tempered MCMC (KEY & CORNISH, 2009; LITTENBERG & CORNISH, 2010) as well as a combination of simulated annealing and MCMC (CORNISH & PORTER, 2007A,B,C; GAIR ET AL., 2008A).

Furthermore, nested sampling (FEROZ ET AL., 2010; GAIR ET AL., 2010B) and its extension MultiNest (FEROZ ET AL., 2009) as well as genetic algorithms (CROWDER ET AL., 2006; PETITEAU ET AL., 2010), and combinations of these algorithms are used (GAIR & PORTER, 2009).

Owing to the complexity of the data, it is highly likely that there is no single “optimal” algorithm but that a combination of different search strategies and parameter extraction algorithms will have to be employed.

3.3.4. Mock Data Challenge

The data-analysis for any gravitational-wave mission is challenging and has been perceived in the past as a potentially insurmountable problem for the LISA mission in particular. In response to that, the Mock LISA Data Challenge (MLDC) had been proposed and discussed at meetings organised by the then US and European LISA Project that were attended by a broad cross section of the international gravitational-wave community. The challenges are meant to be blind tests, but not really a contest and serve the dual purposes of fostering the development of data analysis tools and capabilities, and of demonstrating the technical readiness already achieved by the gravitational-wave community in being able to distill a rich science payoff from the data.

The MLDC Task force has been working since 2006 to formulate challenge problems of maximum efficacy, to establish criteria for the evaluation of the analyses, to develop standard models of the mission (orbit, noises) and of the sources (waveforms, parametrisation), to provide computing tools such as response simulators, source waveform generators, and a Mock Data Challenge file format, and more generally to provide any technical support necessary to the challengers, including moderated discussion forums and a software repository. The challenges

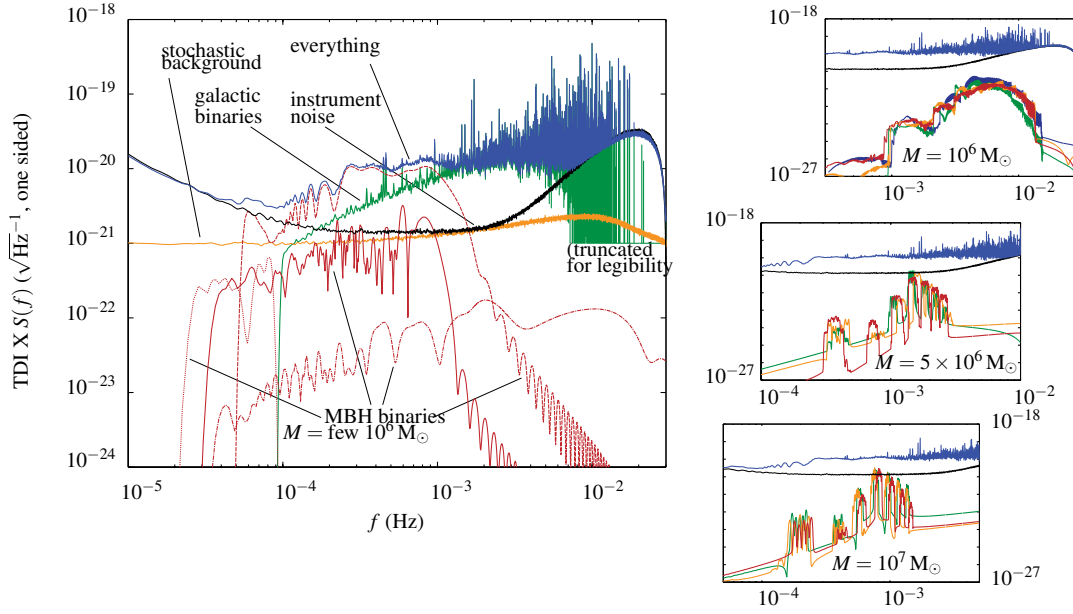


Figure 3.6.: A graphic representation of a Round 4 training dataset. This particular realisation includes more than 60 million chirping Galactic binaries, 4 MBH binaries, 9 EMRIs, 15 cosmic-string bursts, an isotropic stochastic background, and of course instrument noise.

Table 3.1.: Characteristics of the different rounds of the MLDC

	MLDC 1	MLDC 2	MLDC 1b	MLDC 3	MLDC 4
Galactic Binaries	Verification binaries, isolated systems	Galaxy with 3×10^6 binaries	Verification binaries, isolated systems	Galaxy with 6×10^7 chirping binaries	Galaxy with 6×10^7 chirping binaries
MBHB	Isolated systems	4–6 systems over simulated Galaxy and EMRI signals	Isolated systems	4–6 spinning systems, over simulated Galaxy and EMRI signals	4–6 spinning, precessing systems, extended to low mass, over simulated Galaxy and EMRI signals
EMRI		4–6 isolated systems, over simulated Galaxy and MBH signals	Isolated systems	5 signals all in one set, weaker signals	3 frequency bands, expected 2 EMRI per band (Poisson statistics)
Bursts				Cosmic string cusps	Cosmic string cusps (20 expected, Poisson statistics)
Stochastic background				Isotropic	Isotropic
Participants	40	39	25	27	
Institutions	10	13	10	15	

involve the distribution of several data-sets, encoded in a simple standard format, and containing combinations of realistic simulated noise with the signals from one or more gravitational-wave sources of parameters unknown to the challenge participants. The first round of challenges focused on parameter estimation for examples of several sources in otherwise clean noise. Subsequent challenge data-sets have addressed increasingly ambitious data-analysis problems. Round 2, completed in 2007, focused on the global analysis problem. A re-issue of challenge 1, called Round 1B, also ran in 2007 to provide an easy opportunity for new groups to develop analysis codes. A similar challenge, Round 1C, oriented toward students of gravitational-wave astronomy, is ongoing. Round 3, with new sources and source models finished in Spring 2009 (see table 3.1). The current challenge Round 4 returns to the global analysis problem. While the third round of the MLDC was focused on increasing the complexity and variety of GW sources, this current iteration is devoted to the global-fit problem of detecting and analysing sources of different types superposed in the data. All sources classes (*i.e.* galactic binaries, EMRIs, MBHB, cosmic-string bursts and stochastic background) are included, with a larger numbers of EMRIs and cosmic-string bursts and larger parameter ranges for massive black hole (MBH) binaries and EMRIs than in previous rounds (see figure 3.6). The different rounds, their challenges, sources and parameter constraints are described in a series of papers (ARNAUD ET AL., 2007A,B; ARNAUD ET AL., 2006A,B; BABAK ET AL., 2008A,B, 2010).

4. Scientific Requirements

4.1. Science Requirements Overview

NGO will be the first space-borne gravitational wave detector, which means that some of the functional and performance requirements for the science instrument are somewhat uncommon. A gravitational wave detector based on laser interferometry and undisturbed, free-falling test masses is characterised by parameters different from those characterising common space science instruments such as telescopes, spectrographs and cameras. The requirements described here are the product of a considerable effort to create a clear, robust and verifiable interface between the science and the engineering teams.

This chapter summarises the logical flow from science objectives, to science investigations, to observation requirements, to the instrument sensitivity model (ISM), to top-level performance requirements, and their flow-down to instrument performance.

The set of observation requirements quantitatively specifies the observation performance that is necessary for a particular source type to carry out the science investigations and to realise the science objectives. However, the observation requirements do not unambiguously define the instrument performance; many different detectors with equally different performances are, in principle, able to meet the observation requirements. Therefore, the choice was made to show that the observation requirements are met by a specifically chosen instrument performance, the **ISM**. The **ISM** has been shown to meet all of the observation requirements. It is based on an analytic description of a gravitational wave detector employing laser interferometry for displacement measurements, free-falling test masses, unique orbits that approximately preserve a constellation of three spacecraft in an equilateral triangle, and a laser frequency noise cancellation scheme that mimics Michelson’s “white-light fringe” condition. The **ISM**, in effect, has nominal performance requirements for the instrument built-in. The engineering team has to verify that the design for the **NGO** mission allows to meet, or to exceed, the performance of the **ISM**.

4.1.1. Science requirements rationale

The most important consideration that affects **NGO** science requirements is the complex interaction of many different source waveforms with the instrumental sensitivity curve. All gravitational wave detectors have usable sensitivity only over some limited frequency band. Some gravitational wave sources generate signals in a narrow fixed frequency band; others chirp upwards in frequency during an inspiral. The particular waveform can be a very complicated function of masses, redshifts, spins, etc. Where lots of different kinds of sources are present – as is the case with **NGO** – changes in the instrumental sensitivity curve have different consequences for the signal-to-noise ratio (SNR) depending on the source type and on the individual source parameters. The complexity is even greater when considering how well the astrophysical parameters of the source can be determined with a given instrumental sensitivity, since information on each parameter accumulates at different rates during the integration. Consequently, there is no unique inversion from available instrumental sensitivity to accessible science. Therefore, a *forward* calculation of the SNR, or the uncertainty in estimation of astrophysical parameters for the different sources, given a certain **ISM**, has been performed. To do astrophysics with gravitational wave observations, it is best to characterise a gravitational wave detector in terms of how well astrophysical parameters of the source, such as mass or luminosity distance, can be determined. Hence, for a particular source of interest, the effectiveness of a detector design can be evaluated in terms of the uncertainty of a given parameter, such as the luminosity distance, which is frequently the source parameter that is most difficult to determine. With this insight, the **NGO** science requirements were organised around the following rationale:

1. The science objectives are given in the following section.
2. For each science objective, science investigations necessary to reach that objective were mapped out.
3. For each science investigation, observations were developed with quantitative requirements on the astrophysical parameters to be measured.

4. An **ISM** and a model of the astrophysical noise, coming from the close white-dwarf binary background, were assumed.
5. The ability of the model instrument to perform the required observations is then validated by calculating the parameter uncertainty from waveforms of anticipated sources with the instrument sensitivity model. The following sections trace this rationale in some detail.

4.2. Observation Requirements

The **NGO** science objectives and investigations were introduced and motivated with the scientific context in section 2.1. The scientific objectives are the formal statement of the mission’s scientific purpose; the investigations are the research needed to fulfil these objectives.

For each science investigation, one or more observation requirements are defined. The observation requirements are stated (table 4.1) in terms of observable quantities necessary for the science investigation and the precision with which they must be measured, using formal requirements language.

Table 4.1.: *NGO Science Investigations and Associated Observation Requirements*

Science Investigation	Observation requirements
<p>SR 1.1 Elucidate the formation and evolution of Galactic stellar-mass compact binaries and thus constrain the outcome of the common envelope phase and the progenitors of (type Ia) supernovae.</p>	<p>OR 1.1.1 NGO shall have the capability to detect at least 1000 binaries at SNR > 10 with orbital periods shorter than approximately six hours and determine their period. NGO shall maintain this detection capability for at least one year.</p> <p>OR 1.1.2 NGO shall detect all neutron star and black hole binaries in the Milky Way with periods shorter than 35 minutes if they exist.</p> <p>OR 1.1.3 NGO shall have the capability to measure the level of the the unresolved Galactic foreground. NGO shall maintain this detection capability for at least one year.</p>
<p>SR 1.2 Determine the spatial distribution of stellar mass binaries in the Milky Way.</p>	<p>OR 1.2.1 NGO shall have the capability to: determine the position of at least 500 sources with better than ten square degree angular resolution and the frequency derivative to a fractional uncertainty of 10 %.</p> <p>OR 1.2.2 NGO shall measure the inclination of at least 500 binaries to better than 10°.</p> <p>OR 1.2.3 OR 1.2.3 NGO shall determine the distance to at least 50 binaries to 1 % or better and to at least 500 binaries to 10 % or better.</p>
<p>SR 1.3 Improve our understanding of white dwarfs, their masses, and their interactions in binaries, and enable combined gravitational and electromagnetic observations.</p>	<p>OR 1.3 NGO shall have the capability to measure the frequency derivative of all detected binary systems with gravitational wave frequencies above 10 mHz to better than 10 %.</p>
<p>SR 2.1 Trace the formation, growth and merger history of MBH with masses $10^5 M_{\odot} - 10^7 M_{\odot}$ during the epoch of growth of QSO and widespread star formation ($0 < z < 5$) through their coalescence in galactic halos. Capture the signal of coalescing binaries up to redshift $z = 20$, prior to the recombination epoch.</p>	<p>OR 2.1.1 NGO shall have the capability to detect the mergers of similar masses massive black hole (MBH) (mass ratio $m_2/m_1 > 0.1$) with total mass in the range $10^5 M_{\odot} < m_1 + m_2 < 2 \times 10^7 M_{\odot}$ up to redshift $z = 20$. The SNR of those sources with redshift $z < 5$ should be sufficient to enable determination of the MBH masses (relative errors smaller than 1 %) and the spin of the largest MBH (error smaller than 0.1) and an estimation of the luminosity distance (relative error smaller than 50 %)</p> <p>OR 2.1.2 NGO shall have the capability to detect the mergers of MBH with total mass in the range $10^5 M_{\odot} < m_1 + m_2 < 2 \times 10^7 M_{\odot}$ and mass ratio m_2/m_1 about 0.01 up to redshift $z = 8$. The SNR of those sources with redshift $z < 5$ shall be sufficient to enable determination of the MBH masses (relative errors smaller than a few percents).</p>

continued on next page

continued from previous page

Science Investigation	Observation requirements
<p>SR 2.2 Capture the signal of coalescing MBH binaries with masses $2 \times 10^4 M_{\odot} - 10^5 M_{\odot}$ in the range of $5 < z < 10$ when the universe is less than 1 Gyr old.</p>	<p>OR 2.2.1 NGO shall have the capability to detect the mergers of comparable mass MBH (mass ratio $m_2/m_1 > 0.1$) with total mass in the range $2 \times 10^4 M_{\odot} < m_1 + m_2 < 10^5 M_{\odot}$ beyond redshift $z = 5$ and up to $z = 15$ for equal mass systems with sufficient SNR to enable determination of the MBH masses (relative errors smaller than 1 %) and the spin of the largest MBH (error smaller than 0.1) and an estimation of the luminosity distance (relative error smaller than 50 %).</p> <p>OR 2.2.2 NGO shall have the capability to detect some of the mergers of MBH with total mass in the range $2 \times 10^4 M_{\odot} < m_1 + m_2 < 10^5 M_{\odot}$ and mass ratio $0.01 < m_2/m_1 < 0.1$ beyond redshift $z = 5$ with sufficient SNR to enable determination of the MBH masses with relative errors smaller than a few percent.</p>
<p>SR 3.1 Characterise the immediate environment of MBH in $z < 0.7$ galactic nuclei from EMRI capture signals.</p>	<p>OR 3.1 NGO shall have the capability to detect gravitational waves emitted during the last two years of inspiral for a stellar-mass compact object ($m_2 \sim 5 M_{\odot} - 20 M_{\odot}$) orbiting a massive black hole ($m_1 \sim 10^5 M_{\odot} - 10^6 M_{\odot}$) up to $z = 0.7$ with an SNR > 20. The detection of those sources shall be sufficient to determine the mass with an relative error smaller than 0.1 %, the spin of the MBH with an error smaller than 10^{-3}, and the mass of the compact object with a relative error smaller than 0.1 %, as well as the orbital eccentricity before the plunge with an error smaller than 10^{-3}.</p>
<p>SR 3.2 Discovery of intermediate-mass black holes from their captures by MBH.</p>	<p>OR 3.2 NGO shall have the capability to detect gravitational waves emitted by a $10^2 M_{\odot} - 10^4 M_{\odot}$ IMBH spiralling into an MBH with mass $3 \times 10^5 M_{\odot} - 10^7 M_{\odot}$ out to $z \sim 2 - 4$ (for a mass ratio around 10^{-2} to 10^{-3}).</p>
<p>SR 4.1 Detect gravitational waves directly and measure their properties precisely.</p>	<p>OR 4.1.1 NGO shall have capability to detect and study three or more optically observable verification binaries between 1 mHz and 10 mHz with SNR > 10 in two years of mission lifetime.</p> <p>OR 4.1.2 NGO shall be capable of observing the gravitational waves from at least 50 % of all $z \sim 2$ coalescing binary systems consisting of compact objects with masses between $10^5 M_{\odot}$ and $10^6 M_{\odot}$ and mass ratios between 1 : 1 and 1 : 3. NGO shall detect these systems with SNR ≥ 5 in each of five equal logarithmic frequency bands between 0.1 mHz (or the lowest observed frequency) and the highest inspiral frequency.</p>
<p>SR 4.2 Test whether the central massive objects in galactic nuclei are consistent with the Kerr black holes of GR.</p>	<p>OR 4.2 NGO shall have the capability to detect gravitational waves emitted during the last year of inspiral for a $10 M_{\odot}$ black hole orbiting a $10^5 M_{\odot}$ to $10^6 M_{\odot}$ black hole up to $z = 0.7$ with SNR > 20. NGO shall have a science mission duration with adequate observation time for extreme mass-ratio inspirals (EMRIs) to sweep over a range of r/M to map space-time.</p>
<p>SR 4.3 Perform precision tests of dynamical strong-field gravity.</p>	<p>OR 4.3.1 Observe the inspiral radiation from MBH with masses between $10^5 M_{\odot} - 10^6 M_{\odot}$ and mass ratio $m_2/m_1 > 1/3$ to $z \leq 5$ with an average SNR > 30, measuring the mass to better than 1 % and spin parameters to better than 0.1. The SNR should be sufficient to check consistency in the inspiral rate with prediction of General Theory of Relativity (GR).</p> <p>OR 4.3.2 Observe the merger and ring-down radiation from MBH with masses between $10^5 M_{\odot} - 10^6 M_{\odot}$ and mass ratio $m_2/m_1 > 1/3$ to $z \leq 8$ with an average SNR > 60, measuring the mass to better than 1 % and spin parameters to better than 0.3. The SNR should be sufficient to check consistency with GR prediction based on inspiral estimation.</p>
<p>SR 5.1 Measure the spectrum of cosmological backgrounds, or set upper limits on them in the $10^{-4} \text{ Hz} - 10^{-1} \text{ Hz}$ band.</p>	<p>OR 5.1 NGO shall be capable of setting an upper limit on the spectrum of a stochastic gravitational wave background in the $10^{-4} \text{ Hz} - 10^{-1} \text{ Hz}$ band.</p>
<p>SR 5.2 Search for GW bursts from cosmic string cusps and kinks.</p>	<p>OR 5.2 NGO shall be capable of detecting gravitational wave bursts from cosmic (super-)strings, or of setting cosmologically interesting upper limits on the loops.</p>

continued on next page

continued from previous page

Science Investigation	Observation requirements
SR 6.1 Search for unforeseen sources of gravitational waves	OR 6.1 NGO shall be sensitive over discovery space for unforeseen effects (e.g. even at frequencies where we cannot predict likely signals from known classes of astrophysical sources). NGO shall allow for reliable separation of real strain signals from instrumental and environmental artifacts.

4.3. Instrument Sensitivity Model

As described above, the **instrument sensitivity model (ISM)** is the central constituent of the science requirements, as it connects the science objectives with the astrophysical information obtainable with NGO.

The **ISM** combines an instrument noise model with the antenna's transfer function and serves two main purposes: the engineering team can derive performance requirements for the elements of the flight and ground systems, and the science team can validate the **ISM** against the observation requirements. The following subsections describe the **ISM**, the instrument noise model, the instrument transfer function, the **ISM** validation and the noise model validation.

4.3.1. ISM Description

The noise model for the NGO instrument calculates the strain noise amplitude spectral density (ASD) $\sqrt{S_h(f)} = \tilde{h}(f) = 2\delta\tilde{L}(f)/L$ as the product of several terms:

$$\tilde{h}(f) = \sqrt{5} \frac{2}{\sqrt{3}} T(f) \frac{\sqrt{S_{\delta x, \text{IMS}}(f) + S_{\delta x, \text{DRS}}(f)}}{L} \quad (4.1)$$

where the measurement band is defined from 0.03 mHz to 1 Hz. This frequency range corresponds to the *goal*, whereas the *requirement* is for a smaller frequency band of 10^{-4} Hz to 1 Hz.

The crucial difference between the *requirement* and the *goal* lies in the testing and verification procedures: Performances are fully tested and verified against the *requirements*, whereas *goals* are observed only in terms of design and analysis, *i.e.* the mission design must allow for measurements over the wider frequency band. The distinction between goals and requirements is made to prevent excessive efforts on testing and verification, in particular at low frequencies.

The first term in equation (4.1), $\sqrt{5}$, results from averaging the antenna response over the full sky. The second term, $1/\sin(60^\circ) = 2/\sqrt{3}$, accounts for the projection effect of the equilateral triangular geometry of the detector onto the response of the optimum detector, which is an L-shaped Michelson interferometer. The sensitivity function $T(f)$, described in section 4.3.2, represents the conversion of single-link position uncertainty into the detector strain response, including the finite light travel time of the arm and time-delay interferometry (TDI), using the response of the Michelson X variable. The terms $\delta\tilde{x}_{\text{IMS}}(f)$, $\delta\tilde{x}_{\text{DRS}}(f)$, (or $S_{\delta x, \text{IMS}}(f)$ and $S_{\delta x, \text{DRS}}(f)$, respectively) and L are the power spectral density of the displacement noise from the measuring system, the power spectral density of the displacement noise from spurious accelerations on the test masses and the arm length of the interferometer, respectively. It must be noted that the noise contributions of the interferometric measurement system (IMS) and the disturbance reduction system (DRS) comprise not only some physical model of the noise, but also frequency-dependent factors to allow for a balanced allocation of the noise contributions. The NGO sensitivity model is plotted in figure 4.1.

4.3.2. Instrument sensitivity function

The instrument sensitivity function $T(f)$ in section 4.3.1 describes the instrument's sensitivity due to the response to gravitational waves of different frequencies. Traditionally, transfer functions describe the response of a detector to an external stimulus, here gravitational waves. The sensitivity function is the *inverse* of the normal transfer function, as it describes the sensitivity rather than the response, *i.e.* how small the signal is allowed to be while

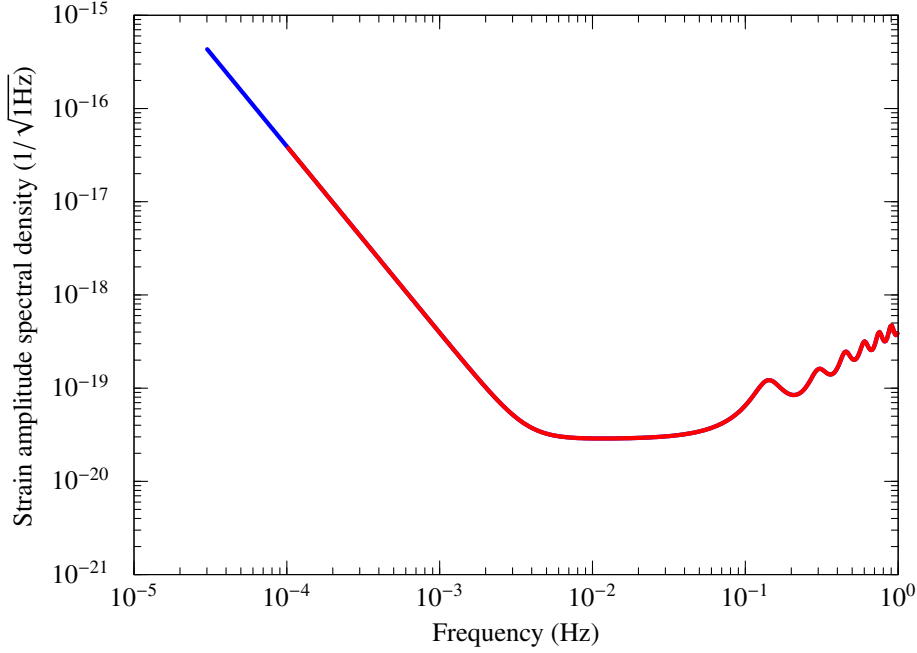


Figure 4.1.: *NGO Sensitivity Curve. The strain amplitude spectral density of the Instrument Sensitivity Model is plotted. The required measurement bandwidth extends from 0.1 mHz to 1 Hz (red line), and as a goal is extended down to 0.03 mHz and up to 1 Hz (blue lines).*

still distinguishable from the noise. As *NGO*'s response to gravitational waves depends in a complex way on the position of the source in the sky, the polarisation of the wave and its frequency, the sensitivity is conventionally averaged over all possible sky locations and polarisations. The instrument transfer function, as discussed in *e.g.* SCHILLING (1997) or LARSON ET AL. (2000), is often written containing all the effects of the averaging, but it is clear that any transfer function can always be normalised to equal 1 at a given frequency and the remaining numerical factor be absorbed in the instrument sensitivity.

The choice made in this document is to normalise the sensitivity function at low frequencies, where it shows a flat frequency dependence, *i.e.* *NGO*'s response does not depend on the frequency of the gravitational wave if that frequency is low enough. For high frequencies ($f > c/(2L)$), where L is the arm length, the response of *NGO* decreases and the sensitivity transfer function therefore increases. When the arm length L is an integer multiple of half of the wavelength of the gravitational wave, the effect of the wave on that arm vanishes. So only an effective arm length L_{eff} is affected by the gravitational wave, where L_{eff} is defined such that

$$L_{\text{eff}} = L - n \frac{\lambda_g}{2} \quad (4.2)$$

and n is chosen so that

$$n \frac{\lambda_g}{2} < L \leq (n + 1) \frac{\lambda_g}{2} \quad (4.3)$$

holds (*i.e.* L_{eff} is the *remainder* of L with respect to $\lambda_g/2$). The higher the frequency of the gravitational wave, and consequently the shorter its wavelength, the smaller the effective arm length becomes and the smaller the absolute change of the effective arm length becomes.

So, in general, a decrease proportional to $1/f$ of the response (and an increase proportional to f of the sensitivity) should be expected, with a transition between the constant part at low frequencies and the high frequency decline at $f_0 = c/(2L)$. Furthermore, at frequencies where the wavelength of the gravitational wave is an exact integer multiple of the arm length, the effect in this arm vanishes, and in an interferometer with two identical arms, the overall effect vanishes, which would cause the sensitivity function to diverge. As gravitational waves from sources at different sky positions but same frequency have different angles of incidence on *NGO*,

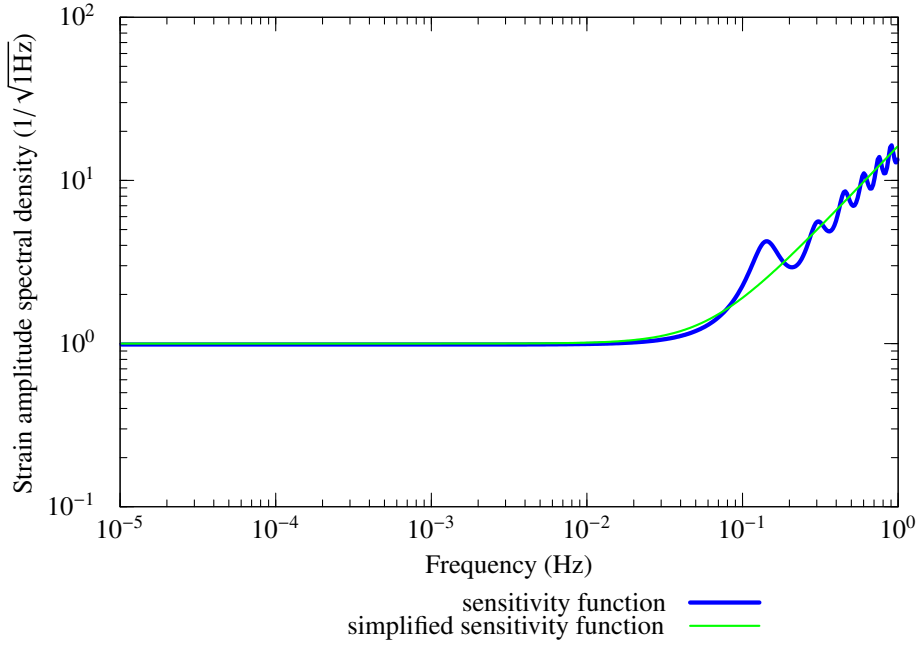


Figure 4.2.: Instrument sensitivity function and its simplified version (see equation (4.4)), relating the sensitivity of the instrument to a normalised gravitational wave strain to the frequency.

their effective wavelength, *i.e.* the wavelength projected on the arm, differs. This removes the divergence of the sensitivity function, however, it still increases by about a factor of 2 at these frequencies. There is no simple analytic model of the instrument sensitivity function that accurately displays all its features, however, numerical representation of the sensitivity function is plotted in figure 4.2. If the more complex structure at higher frequencies is not of interest, the following approximation can be used

$$T(f) \approx \sqrt{1 + \left(\frac{f}{af_0}\right)^2} \quad (4.4)$$

where $f_0 = c/(2L) = 150$ mHz and $a = 0.41$, leading to an onset of the effect of the arm length at about 60 mHz.

4.3.3. Instrument Noise Model

The single-link equivalent position uncertainty $\widetilde{\delta x}_{\text{single-link}}(f)$ is expressed as an ASD which is the root of the sum of two terms – the displacement noise of the IMS, and the acceleration noise of the DRS, which is responsible for minimising the residual acceleration of the test masses:

$$\widetilde{\delta x}_{\text{single-link}}(f) = \sqrt{S_{\delta x, \text{IMS}}(f) + S_{\delta x, \text{DRS}}(f)} \quad (4.5)$$

For each of the terms exists a *budget*, *i.e.*, the amount of noise permitted so that the science requirements can be fulfilled and an *allocation*, *i.e.* the amount of noise that a certain subsystem is foreseen to contribute, which differs from the budget by the system margin. In the following, the budget is given, the subsequent allocations, *i.e.* budget minus margin, are listed in table 4.3 and table 4.4.

The displacement noise amplitude spectral density $\widetilde{\delta x}_{\text{IMS}}(f)$ for the uncertainty in the DRS is calculated from an amplitude spectral density for the residual *acceleration* on each test mass

$$\widetilde{\delta a}_{\text{DRS}}(f) = \Delta a_0 \times 10^{-15} \frac{\text{m}}{\text{s}^2 \sqrt{\text{Hz}}} \times \sqrt{1 + \left(\frac{f}{f_H}\right)^4} \sqrt{1 + \frac{f_L}{f}} \quad \text{for } 3 \times 10^{-5} \text{ Hz} \leq f \leq 1 \text{ Hz} \quad (4.6)$$

with $\Delta a_0 = 3$, $f_L = 0.1$ mHz, and $f_H = 8$ mHz. The noise model of the acceleration contains a “reddening” factor $\sqrt{1 + f_L/f}$ to allow for noise sources at lower frequencies. The origin of that precautionary term lies with the

fact that low frequency behaviour can only be assessed with extreme difficulties during ground demonstration, testing and verification. The factor $\sqrt{1 + (f/f_H)^4}$ relaxes the *requirement* (but not the expected performance) to higher frequencies above f_H , as the sensitivity of **NGO** is reduced to higher frequencies anyway, which allows to relax the requirements on the acceleration noise accordingly. The equivalent displacement noise amplitude spectral density is then given by:

$$\widetilde{\delta x}_{\text{DRS}}(f) = 2 \frac{\widetilde{\delta a}_{\text{DRS}}(f)}{(2\pi f)^2} \quad \text{for } 3 \times 10^{-5} \text{ Hz} \leq f \leq 1 \text{ Hz} \quad (4.7)$$

where the factor of two accounts for the presence of four test masses in the measurement of the difference in length of two arms, and the $1/(2\pi f)^2$ is the conversion from acceleration to position in Fourier space.

The displacement noise amplitude spectral density $\widetilde{\delta x}_{\text{IMS}}(f)$ resulting from the uncertainty in the **IMS** is given by:

$$\widetilde{\delta x}_{\text{IMS}}(f) = \Delta x_0 \times 10^{-12} \frac{\text{m}}{\sqrt{\text{Hz}}} \times \sqrt{1 + \left(\frac{f_0}{f}\right)^4} \quad \text{for } 3 \times 10^{-5} \text{ Hz} \leq f \leq 1 \text{ Hz} \quad (4.8)$$

with $\Delta x_0 = 12$ and $f_0 = 2.8$ mHz. A sizable contribution to that noise is made up by shot-noise, whose (frequency independent) contribution is

$$\widetilde{\delta x}_{\text{SN}}(f) = \sqrt{\frac{\hbar c}{2\pi} \frac{\lambda}{P_{\text{avail}}}} = 7 \text{ pm}/\sqrt{\text{Hz}} \sqrt{\frac{100 \text{ pW}}{P_{\text{avail}}}} \quad (4.9)$$

As the equivalent **DRS** displacement noise starts to dominate at lower frequencies, it allows us to relax the **IMS** displacement noise model below f_0 with $\sqrt{1 + (f_0/f)^4}$.

4.3.4. **ISM** validation

The **instrument sensitivity model** is the core of the baseline requirements derived from the mission science. Since the observation requirements cannot be inverted for the required instrument performance, it is necessary to calculate the instrument performance with the **ISM** to verify that the observation requirements can be met. The process of verifying that the **ISM** will in fact enable the required observations is generically summarised in this section. This section is not intended to provide all technical details of the calculation, but rather give a sense of the undertaking. An extensive literature on the gravitational wave emission, propagation and detection has developed over the last thirty years. The desired products are predictions of the **SNR** in the detector and the uncertainty of source parameters extracted from the data, ideally the full posterior probability density functions (PDFs) for the chosen parameters. The number of extractable source parameters depends on the specific source, but may be as large as seventeen. Examples of parameters that might be extracted from the full waveform of a chirping binary are polar location (θ), azimuthal location (ϕ), inclination (ι), polarisation (ψ), initial orbital phase (ϕ_o), coalescence time (t_c), luminosity distance (D_L), spin vectors (\vec{s}_1, \vec{s}_2) of both compact objects, chirp mass (M_c), and reduced mass (μ).

Generically, the process involves computing waveforms for the source of interest, taking account of the relative orientation and separation of the source and the detector, invoking the response of the detector with both astrophysical and instrumental noise, and taking into account the estimation of the many parameters in the signal. The **ISM** enters this process as the instrument response and noise.

This general process differs from source to source with assumptions and methodologies appropriate to the source being considered. A good example of this process for binary black holes in many of the observation requirements is LANG & HUGHES (2006). The **NGO** science working team (**NGO SWT**) has carried out extensive calculations (ARUN ET AL., 2009) to validate each observation requirement.

Many considerations enter into the details of this process. For example where binaries are concerned, the mass ratios, redshift, spin and precession effects, merger and ring-down signals, sky and polarisation averaging, orbital eccentricity all affect choices in how the calculations are done. Background and burst detection pivots on still other considerations. The following assumptions are made for the calculations supporting the science requirements:

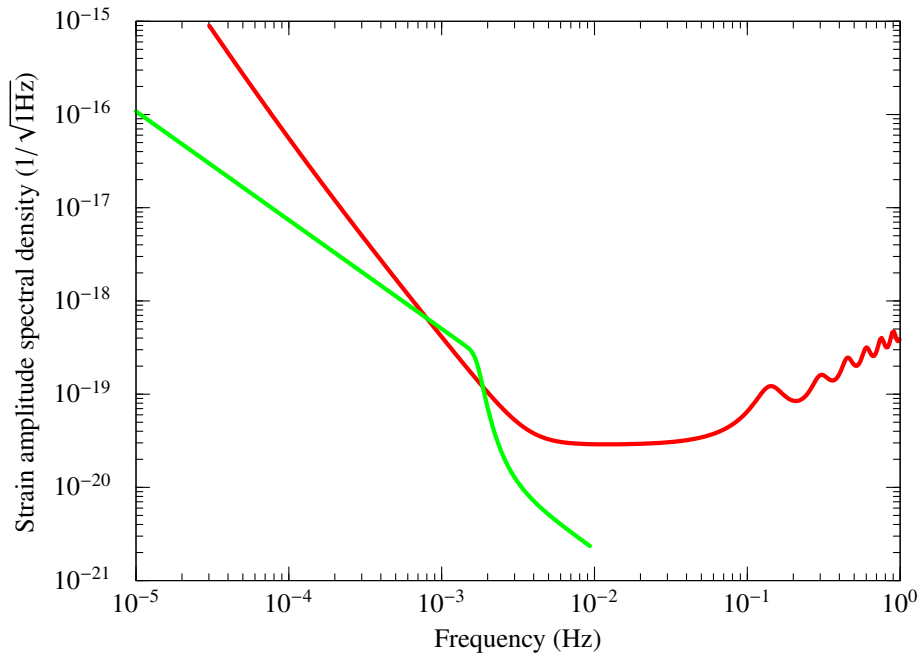


Figure 4.3.: Standard instrument sensitivity model and binary confusion noise. The red curve is the product of the standard instrument noise model given above multiplied by the instrument transfer function shown in figure 4.2. The green curve is the expected confusion noise threshold from galactic and extragalactic binaries.

- Both galactic and extragalactic binaries of compact stellar mass objects will be so numerous as to give confusion noise background at some level. While confusion noise plays a lesser role in **NGO**, a complete noise model for the detection and parameter estimation process must include the astrophysical noise; figure 4.3 illustrates a typical model of the galactic confusion noise backgrounds relative to the **ISM** from section 4.3.1
- In all cases, the **ISM** is assumed to have no useful sensitivity below 0.03 mHz.
- Except where specific sources are known, these calculations usually average over the sky position of the source and its orientation.

4.3.5. Noise Model validation

In **NGO**, requirements are closely connected to noise models. Complete and accurate noise models inform the allocation of requirements; the designer must know what can be achieved and judge the comparative difficulty of achieving different aspects of performance to balance competing requirements. So, while the previous subsection described how the performance of the **ISM** satisfies the science requirements, this subsection will address how the **NGO** Project will ensure that a realisable **NGO** instrument can meet or exceed the **ISM** performance.

The design of the **NGO** concept started with models for residual acceleration noise and displacement noise before a sensitivity curve or science requirements were formulated. The **ISM** is an allocation of residual acceleration noise and displacement noise informed by these detailed noise models. The flow-down of performance requirements (Tables 4.3 and 4.4) is also based on these detailed noise models. These models must be demonstrably correct and complete. Their calculation must be correct to much better than the associated contingency, and no substantive effect must be missed.

This situation demands disciplined maintenance of noise models and current best estimates (CBEs) of effects and, most importantly, experimental validation wherever possible. As described below, laboratory measurements and results from the **LISA Pathfinder** (LPF) test campaigns are being used to validate the instrument noise model. **LPF** flight results will be an important, in some cases crucial, contribution.

Laboratory Tests

High-level contributions to the displacement noise model are shown in table 4.3. These values are CBEs based on various combinations of measurements and calculations.

By the end of 2011, most of the CBEs in table 4.3 have some basis in laboratory measurement. For example, the residual laser frequency error is a critical performance parameter for NGO; the final laser frequency noise must be reduced by nearly 11 orders of magnitude over the natural laser frequency noise. The CBE is validated by a demonstration of laser frequency prestabilisation in a candidate master oscillator laser, a measurement of frequency noise added by a candidate fibre amplifier and a system level demonstration of laser frequency noise suppression by application of TDI to data taken with a TRL 5 NGO phasemeter in a testbed simulating two NGO spacecraft (DE VINE ET AL., 2010). The system level demonstration of the phase measurement sets substantial limits on unanticipated contributions to the displacement noise.

There are laboratory measurements in progress on pointing errors, telescope path-length stability, photoreceiver errors, residual laser frequency noise, residual clock frequency noise and phasemeter noise. Some laboratory measurements relevant to shot-noise (*e.g.*, optical system efficiency) and experience-based estimates have already been made, and three independent models of scattered light are roughly in agreement.

High-level contributions to the residual acceleration noise model are shown in table 4.4. Comprehensive measurements of the contributions to the residual acceleration budget are more difficult. Most of the laboratory work has been done as part of the LPF development and testing, and is described in part in chapter 5. The torsion pendulum is the preferred tool to measure very small spurious forces in the 1 g laboratory environment. In addition to the LPF work, there have been several measurements of various thermal, pressure and electrostatic effects with specialised torsion pendulums. In addition to confirming analytic models for these known effects, pendulum measurements rule out unanticipated force effects related to the GRS at the level of 30 fm/s²/rtHz at 1 mHz, thus forming a solid experimental starting point for the more complete LPF flight test.

LISA Pathfinder

LISA Pathfinder (LPF) contributes to the validation of the displacement and acceleration noise models in two ways: through validation during future flight operations and through extensive ground-test campaigns in the past and present development phase.

One of the top-level goals of LPF is to validate the acceleration noise model in a high-fidelity flight environment. The flight system incorporates an extensive set of environmental stimuli, actuators, and sensors that can be used to measure the response of the test mass to various disturbances. The master test plan foresees an extensive testing campaign to validate the error model. This ultimate validation awaits flight operations in April 2014.

The development of the gravitational reference sensor (GRS) and interferometer for LPF has included an extensive campaign of test and verification on the ground. The status of the LPF flight hardware can be found in *The LISA Pathfinder Mission (S2-EST-RP-1087)*. The results of the LPF ground testing of displacement noise and acceleration noise are too voluminous to include here.

The requirements on the Optical Metrology System (OMS) for LPF differ from those on the NGO IMS; hence, the OMS noise model is not the same as the IMS noise model. However, the tests performed on the flight model of the LPF “X1” interferometer demonstrate that the requirements on the NGO local interferometer, *i.e.*, the interferometer between optical bench and test mass, can be fulfilled. This validates the optical bench pathlength stability contribution in table 4.3 and excludes unanticipated noise sources in the NGO local interferometer.

The LPF GRS is designed to meet the acceleration noise requirements of the NGO GRS. However, in the interest of cost containment, LPF requirements are relaxed an order of magnitude in both amplitude spectral density ($3 \times 10^{-14} \text{ m/s}^2/\sqrt{\text{Hz}}$) and frequency (1 mHz... 100 mHz). In general, LPF ground-testing with torsion pendulums and hollow test masses has shown that the spurious forces in table 4.4 associated with surface effects (*e.g.*, thermal effects, pressure effects, patch fields) are as described by the error model. One effect observed in ground testing forced a revision of the previous noise model: dissipation and the associated TM Brownian motion caused by residual gas is increased considerably due to the proximity of the GRS surfaces. This requires a more stringent residual gas pressure requirement of 10^{-8} mbar, which can be accommodated by NGO by venting the GRS to space, a solution that will also be implemented and tested by LPF. This illustrates the value of a

Table 4.2.: *Principal Science Requirements*

Quantity	Summary	Details
Measurement band	0.1 mHz to 0.1 Hz	
Operational lifetime	2 years	Extendable to 5 years. All consumables based on a 5 year mission
Nominal arm length	1×10^9 m	
Single link IMS displacement noise ASD	$11 \times 10^{-12} \frac{\text{m}}{\sqrt{\text{Hz}}}$ at 10 mHz	$\widetilde{\delta x}_{\text{IMS}}(f) = \Delta x_0 \times 10^{-12} \frac{\text{m}}{\sqrt{\text{Hz}}} \times \sqrt{1 + (f_0/f)^4}$ for $\Delta x_0 = 11$ and $f_0 = 2.8$ mHz
Single test mass DRS acceleration noise ASD	$3 \times 10^{-15} \frac{\text{m}}{\text{s}^2 \sqrt{\text{Hz}}}$ at 10 mHz	$\widetilde{\delta a}_{\text{DRS}}(f) = \Delta a_0 \times 10^{-15} \frac{\text{m}}{\text{s}^2 \sqrt{\text{Hz}}} \times \sqrt{1 + (f/f_H)^4} \sqrt{1 + f_L/f}$ for $\Delta a_0 = 3$, $f_L = 0.1$ mHz, and $f_H = 8$ mHz
Strain ASD	$30 \times 10^{-20} \frac{1}{\sqrt{\text{Hz}}}$ at 10 mHz	$\tilde{h}(f) = 2\sqrt{5}T(f)/(L\sqrt{3}) \times \sqrt{S_{\delta x, \text{IMS}}(f) + S_{\delta x, \text{DRS}}(f)}$, where $T(f)$ is the sensitivity function representing the NGO sensitivity to a normalised gravitational wave strain

Table 4.3.: *Summary of IMS Subsystem Noise Allocations*

Effect	Total per group $\times 10^{-12} \frac{\text{m}}{\sqrt{\text{Hz}}} \sqrt{1 + (2.8 \text{ mHz}/f)^4}$	Sub-allocation	Comments
Total IMS error/noise budget	11		
Total of subsystem allocations	7		RSS of subsystems
Subsystem allocations			
Shot noise	4.7		270 pW received power
Other measurement noise	5.2		

vigorous validation programme based on both ground and in-flight measurements.

Astrophysical noise

The noise model for the astrophysical contribution from galactic binaries is not easily validated. The model in figure 4.3 is typical of those derived from BENDER & HILS (1997). Since these binaries are faint, not enough have been observed electromagnetically to reliably establish their numbers, and hence the confusion level, from observations alone. Consequently, the confusion level is derived from population synthesis models, with some constraints from observations. There are reasons to believe that the model in figure 4.3 is a factor 3 to 10 too high, resulting in a conservative noise estimate.

4.4. Performance Requirements

Table 4.2 provides the details of the principal science requirements. These requirements are derived from the **ISM** and the ensemble of observation requirements. The **ISM** – by virtue of being an analytical performance model of the **NGO** concept – can naturally be decomposed into performance requirements on the **IMS** and requirements on the **DRS**. Table 4.3 provides a flow-down of the noise budget to individual subsystems of the **IMS**, starting with the overall **IMS** displacement noise of $18 \text{ pm}/\sqrt{\text{Hz}}$. Table 4.4 provides a flow-down of the **DRS** noise budget to individual components arising in the instrument and spacecraft (S/C), starting with the overall **DRS** acceleration noise of $3 \times 10^{-15} \text{ m/s}^2/\sqrt{\text{Hz}}$.

Table 4.4.: Summary of DRS Subsystem Noise Allocations

Effect	Total per group	Sub-allocation	Comments
	$\times 10^{-16} \frac{\text{m}}{\text{s}^2 \sqrt{\text{Hz}}} \sqrt{1 + (f/8 \text{ mHz})^4} \sqrt{1 + 0.1 \text{ mHz}/f}$		
Total acceleration noise budget	30		
Total of subsystem allocations	19.5		RSS of subsystems
Electrostatics		12.0	
Brownian		9.1	
S/C magnetic		7.0	
S/C coupling		6.0	
S/C cross-coupling		4.5	
Thermal		4.0	
Interplanetary magnetic		4.0	
Misc small effects		4.0	

5. Payload

The top-level requirement for the **NGO** payload is that it has to enable gravitational wave (GW) detection at low frequencies with the strain sensitivities shown in table 5.1. The values are given in terms of a spectral density of the gravitational strain measurement, where the strain sensitivity h is a measure for the gravitational wave amplitude and is proportional to the relative arm length change: $h = 2\delta L/L$. Here, L is the arm-length expressed in m and δL the arm-length variation in $\text{m}/\sqrt{\text{Hz}}$. At high frequency, the sensitivity is dominated by the **NGO** interferometric measurement system (IMS) that has to provide an absolute accuracy in the range of $10 \text{ pm}/\sqrt{\text{Hz}}$ for a single arm laser link. At low frequencies, the disturbance reduction system (DRS) dominates the sensitivity. The equivalent displacement noise corresponds to an acceleration noise of $3 \times 10^{-15} \text{ m}/(\text{s}^2 \sqrt{\text{Hz}})$.

The accurate determination of arm length variations is complicated by the fact that the shape of the formation triangle undergoes residual seasonal changes which cannot be completely removed by orbit optimisation. These changes not only affect the nominal 60° between the lines of sight, but also the so called point-ahead angle, which describes the offset between received and transmitted beam for each individual spacecraft (S/C). This offset is required to account for the comparatively long travel time $L/c \approx 3.3 \text{ s}$ of the laser light to the respective remote S/C.

The combination of picometre resolution, a transmission path of $1 \times 10^6 \text{ km}$ and the need for active elements in the optical science chain makes the physical realisation of the **NGO** metrology system extremely challenging and has severe implications for the design of all associated subsystems:

Laser Metrology System Measurement noise and the required distance between S/C imposes stringent requirements on the laser-interferometer system, which will have to exhibit very high stability, reliability and power efficiency.

Thermal Control Both the measurement system and the test masses must be protected from thermal noise and gradients that could swamp the signal from gravitational waves. The thermal environment of the payload must be extremely stable, and thus requires that the payload is thermally decoupled from the S/C.

Structural and Mechanical A very stiff and stable structure will be required such that mHz-level disturbances are avoided. This could preclude or limit the use and operations of mechanical components that will introduce mHz-level noise, such as mechanically steered antennas on the communication subsystem.

Propulsion System The propulsion system must be essentially vibration-free and be able to produce thrust levels, both in range and controllability, compatible with the requirements of the drag-free control system for the S/C (*i.e.* capable of compensating, at a minimum, solar-radiation pressure on the S/C structure). Currently there are three possible technologies that can in principle be used for **NGO**: (i) Field-emission

Table 5.1.: *NGO measurement sensitivity requirements (see chapter 4), design sensitivity (including the instrument transfer function), and allocation to the DRS and IMS. The design sensitivity shows a margin of at least 25 % with respect to the requirements. Note that the numbers at 0.03 mHz refer to a goal.*

Frequency (mHz)	Sensitivity ($1/\sqrt{\text{Hz}}$) required	Displacement ($\text{pm}/\sqrt{\text{Hz}}$)		
		single link	DRS	IMS
0.03	1.4×10^{-15}	1.4×10^6	5.4×10^5	4.8×10^4
0.1	8.5×10^{-17}	8.5×10^4	3.3×10^4	4.3×10^3
1	6.3×10^{-19}	6.3×10^2	2.5×10^2	4.4×10^1
3	7.4×10^{-20}	7.4×10^1	2.7×10^1	1.2×10^1
5	3.7×10^{-20}	3.7×10^1	1.0×10^1	1.1×10^1
10	2.9×10^{-20}	2.9×10^1	4.4	1.1×10^1
30	3.1×10^{-20}	3.1×10^1	3.7	1.1×10^1
100	5.3×10^{-20}	5.3×10^1	3.7	1.1×10^1
1000	4.5×10^{-19}	4.5×10^2	3.7	1.1×10^1

electric propulsion (FEEP) based on ionised atoms, molecules or droplets, (ii) cold-gas thrusters, and (iii) radio frequency (RF) based ion thrusters.

Electromagnetic The measurement instrumentation and test masses must be shielded from EMC disturbances: this leads to the requirement for extremely strict policing of the electrical and magnetic components of the S/C, and the EMC environment due to the natural space environment and secondary effects such as charging.

Gravitational The gravitational environment of the test masses must be carefully considered: this includes the direct gravity gradient forces due to relative movement between the test masses. Additionally, the self-gravity environment of the S/C must be carefully analysed and designed to ensure that the summed gravity field at the test masses does not interfere with the GW measurement. Additionally displacement of S/C elements (such as mechanically steered antennas) will have to be carefully analysed to assess their impact on the self-gravity field of the S/C.

Test Mass Control Although the test masses are essentially free-flying they need to maintain their orientation with respect to the line of sight (LOS) of the respective telescope. This means that a certain degree of test mass control is necessary. In addition, the “mother”-S/C houses two test masses that cannot be kept in free-fall simultaneously in all degrees of freedom. Test mass control is provided through electrostatic actuation from the test mass cage.

Autonomy The spacecraft must possess a substantial degree of autonomy due to the frequent periods where communication with the ground segment is not possible. This autonomy extends to the ability to communicate with the other S/C in the constellation, and perform autonomous science operations. This requirement for autonomy and operations within a constellation heavily influences the subsequent choice of the data-handling architecture selected for the S/C.

The further organisation of this chapter follows the definition of the *instrument* given in chapter 8. The instrument is procured, developed, implemented, and tested by nationally funded instrument providers and consists of the optical bench (see section 5.1), the phasemeter (see section 5.2) and the DRS (see section 5.3). The two additional components of the payload, the telescope (section 5.4) and the laser (section 5.5) are considered to be part of the industrial procurement. They are described in this chapter as well, as their performance requirements are critical to achieve the required sensitivity.

The micropropulsion system is not considered part of the instrument and is described in the chapter on mission design (section 6.3).

5.1. Optical System

The optical system of NGO contains all the optical components that are needed for the interferometry and the required support. The optical system differs between the “Daughter” spacecraft (Daughter-S/C) and the “Mother” spacecraft (Mother-S/C). The Mother-S/C houses one *optical assembly* (figure 5.1, lower row) that consists of two units (figure 5.1, upper row), each consisting of the *optical bench*, the *telescope*, and the *gravitational reference sensor* as well as the associated mounting structures. The Daughter-S/C contains only one telescope, therefore the mounting structure that holds the two telescopes is not needed in this form and a single optical assembly can be mounted directly to the S/C.

The optical bench is mounted parallel to the primary mirror of the telescope, requiring a non-planar beam path, where the light from the optical bench to the telescope has to be directed “up” to the telescope. Whereas the gravitational reference sensor (GRS) is mounted behind the optical bench such that the light from the optical bench to the GRS has to pass through the optical bench (“down”), also resulting in a non-planar beam path.

5.1.1. Optical bench

The main function of the optical bench is to direct the various laser beams to the relevant positions in 3-dimensional space, to bring beams together for interference, and provide stable mechanical support to the electro-optical components such as photodiodes and CCD sensors without adding any significant noise to the measurement path (figure 5.4). The primary optical bench requirement is that the pathlength noise induced by the components on

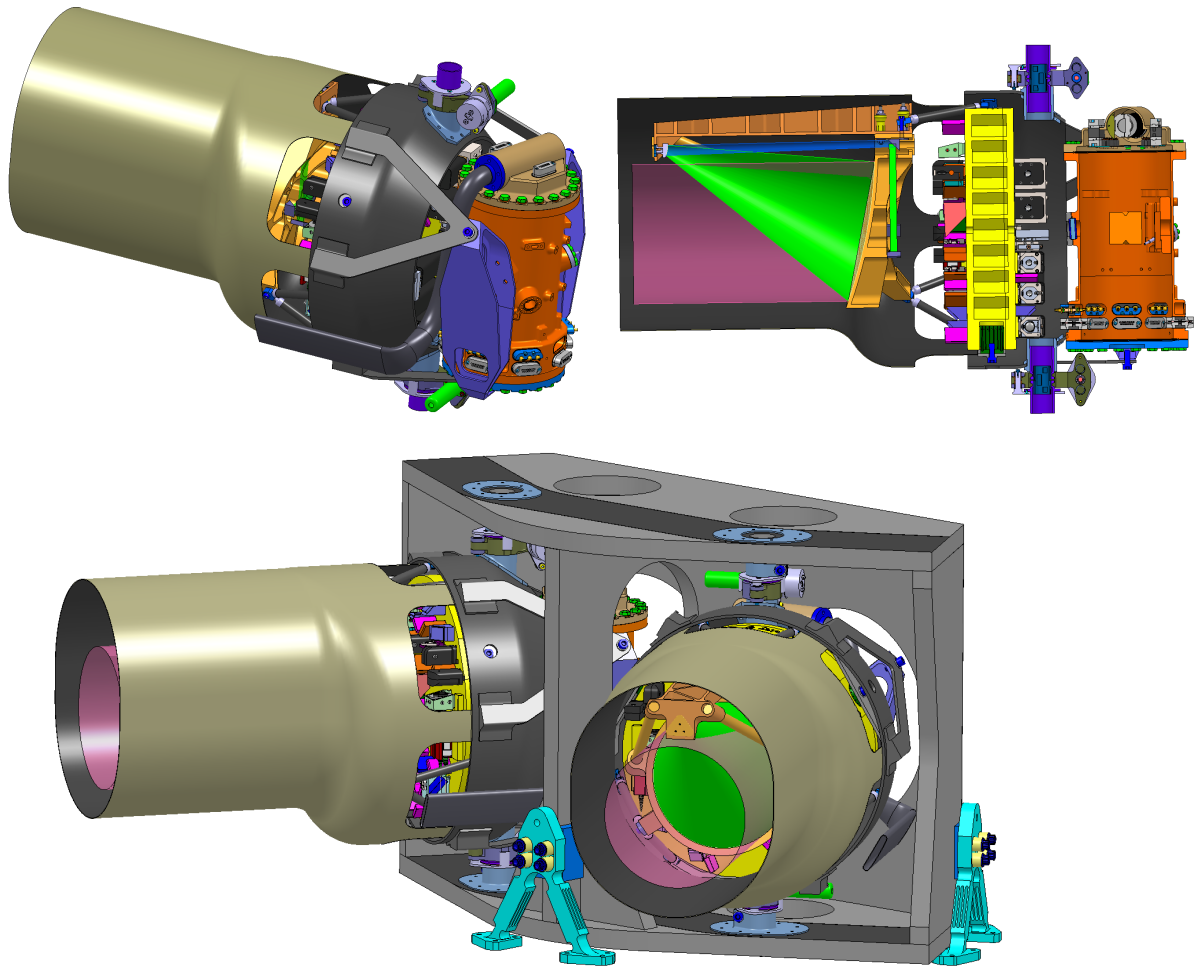


Figure 5.1.: *Optical assembly. Telescope with optical bench attached (upper row). The optical bench is orthogonal to the telescope axis with the optical components facing the back of the primary mirror of the telescope. The gravitational reference sensor is attached behind the optical bench to a support ring also holding the optical bench. A support structure takes the two sub-units (lower row), forming the optical assembly for the Mother-S/C. The angle between the two telescopes is nominally 60° , but can be varied by $\pm 1.5^\circ$ using the optical assembly tracking mechanism.*

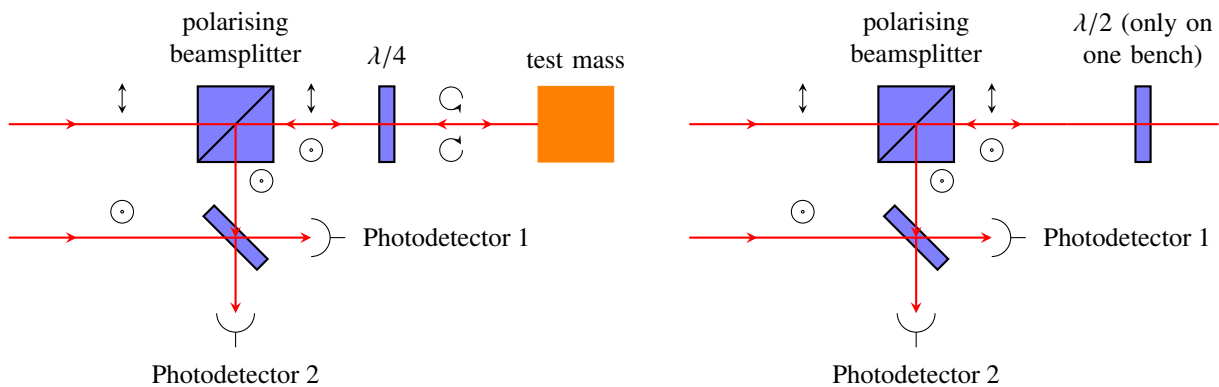


Figure 5.2.: *Separation of incoming and outgoing beam through polarisation in the test mass interferometer (left panel) and in the send/receive path of the telescope (right panel). The test mass interferometer employs a quarter-wave plate to rotate the polarisation, in the send/receive path only one optical bench has a half-wave plate.*

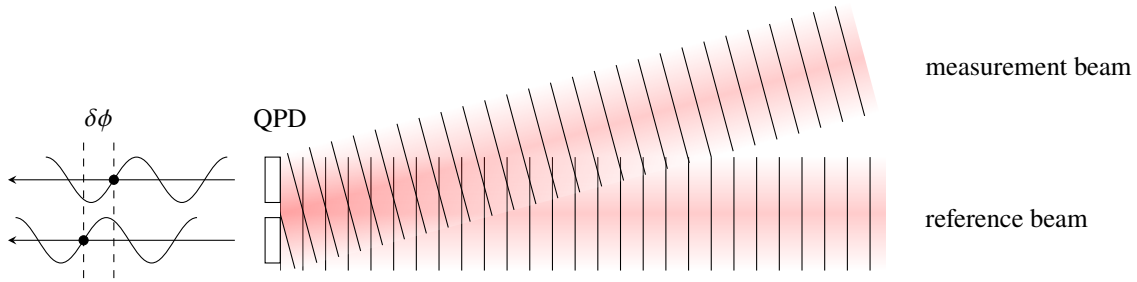


Figure 5.3.: Differential wavefront sensing. The angle between reference beam and measurement beam causes a phaseshift $\delta\phi$ between the signals in the different quadrants of the QPD.

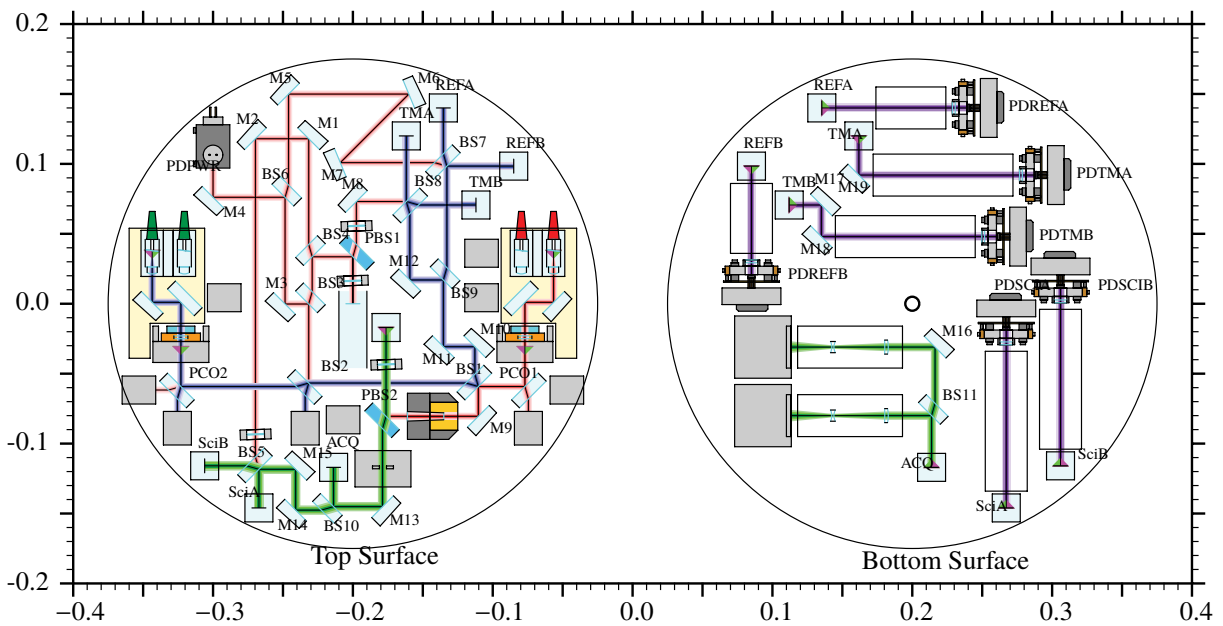


Figure 5.4.: Optical bench design front and back. The backside contains all the photodetectors.

the optical bench should not exceed $1 \text{ pm}/\sqrt{\text{Hz}}$ at frequencies above 3 mHz.

The optical bench is constructed using the same techniques employed in the construction of the optical bench for the LISA Pathfinder technology package (LTP) experiment on board **LISA Pathfinder** (LPF) (BRAXMAIER ET AL., 2004; KILLOW ET AL., 2006; MIDDLETON ET AL., 2006). The optical bench is constructed from a block of Zerodur ceramic glass with a diameter of approximately 560 mm, with fused silica mirrors and beamsplitters bonded to the bench using hydroxy catalysis bonding (ELLIFFE ET AL., 2005), a technology first developed for the GP-B mission (GWO, 1998; TURNEAURE ET AL., 2003). This technology has found broad applications in ground-based gravitational wave detectors (AMICO ET AL., 2002; SMITH ET AL., 2003) as well as in LPF (ELLIFFE ET AL., 2005) due to its excellent properties regarding dimensional stability of the components and rigidity and durability of the bond itself.

While Zerodur has the advantage of a very low coefficient of thermal expansion (CTE) of about 2×10^{-8} , it is quite brittle, and care has to be taken to restrict the mechanical load on the bench by an appropriate design of the surrounding structure. The necessary expertise has been developed during the construction of the optical bench for LTP. The few differences between the construction of the optical bench for NGO with respect to the optical bench for LPF lie in the use of polarising components and lenses for NGO (requiring mounting technology for the different optical materials), and in including non-planar optical paths, as the telescope and the GRS are placed “above” and “below” the optical bench.

Interferometric measurement techniques

The interferometric measurements in **NGO** are based on heterodyne interferometry, where two laser beams with respective frequencies ν_0 and $\nu_0 + \Delta\nu$ are combined to yield a beat note with the frequency $\Delta\nu$, the phase of which is then detected. Measurements of longitudinal displacements can be performed by directing the combined light on a single element photo detector, whereas for the measurements of angular displacements, *differential wavefront sensing* (HEINZEL ET AL., 2003) is needed. Here, the quadrant photodetector (QPD) and the differential phase between the signals from the different quadrants is used to determine the angle of the wavefront arriving at the photodiode (see figure 5.3). In practise, taking the sum of the signals from the QPDs is used to emulate a single element photodetector so that one photodetector can measure both angular displacements and the longitudinal displacement simultaneously.

All the interferometers on the optical bench (science, test mass, reference, point ahead mechanism, and optical truss) are read out by two photodetectors, located at the output ports of the combination beamsplitters, providing redundancy and an increase of the signal-to-noise ratio by a factor of $\sqrt{2}$ in the nominal case, *i.e.* with both detectors working.

Science interferometer

The science interferometer (figure 5.4, panel d) measures the distance between optical benches (*i.e.* **S/C**) located at opposing ends of a constellation arm. The primary laser associated to that optical bench (depicted in red in figure 5.4, panels a and d) provides the reference beam (or local oscillator) for the science interferometer, hence part of the light is split off after the beam expander and its polarisation rotated by 90° , via a half-wave plate, to match the polarisation of the received beam. The light received from the far spacecraft (≈ 280 pW) enters through the telescope and is directed to the optical bench via the telescope back optics, directly to the science interferometer, where about 100 pW reach each detector.

While the optical benches are designed to be as identical as possible, the polarisation multiplexing scheme (see figure 5.2) causes a slight difference, as one of the optical benches on a spacecraft will have a half-wave plate in the transmit/receive path whereas the other does not. An alternative scheme with the beam in free space being either circularly polarised or under 45° is under investigation.

Test mass interferometer

The test mass interferometer is used to determine the position of the test mass of the **GRS** with respect to the optical bench. The measurements from the test mass interferometers on the transmitting and the receiving optical bench are combined with measurements from the science interferometer to perform the measurement of the distance between the free-falling test masses. Thus, the test mass interferometer provides an integral part of the science measurement; its performance will be demonstrated on **LPF**.

For the test mass interferometer, the reference beam is taken from the secondary laser (blue in figure 5.4) and the measurement beam (orange) from the primary laser. The measurement beam is directed through the optical bench to the test mass situated in the gravitational reference sensor at the backside of the optical bench. The test mass acts as a mirror and reflects the measurement beam back to the optical bench. Separation of the beam going to the test mass and the reflected beam is again done through polarisation. This scheme is different from the setup used in **LTP** which relies on a geometrical separation of the two beams (HEINZEL ET AL., 2003). In **NGO**, an additional quarter-wave plate is therefore needed that is passed twice by the light, effectively resulting in a rotation of the polarisation by 90° . Another half-wave plate rotates the polarisation of the measurement beam back by 90° to coincide with the polarisation of the reference beam and allow the beams to interfere. The impact of these additional polarising components on the pathlength stability has been experimentally checked and found to be negligible (DEHNE ET AL., 2009).

The test mass interferometer provides information on both longitudinal movement of the test mass with respect to the optical bench (and hence the spacecraft) and rotation through differential wavefront sensing. The readout of the test mass interferometer will therefore be used to feed into the control law of the **DRS**, augmenting the signals from the capacitive readout (see section 5.3).

Reference Interferometer

The reference interferometer (figure 5.4, panel c) provides information on the frequency noise of the primary laser with respect to the secondary laser and its output signal of this interferometer is used to provide an error signal for the phase-locking of the primary and the secondary laser. It also provides a phase reference for the other interferometers, thus allowing to cancel disturbances that do not originate on the optical bench, *e.g.* in the fibres that deliver the laser beams.

Optical truss

Optical truss interferometry is a method to assess the stability of the telescope structure (see section 5.4) on orbit. The interferometers consist of three pick-off mirrors separated by 120° on the mounting structure of the secondary mirror of the telescope, each using a sample of the outgoing light for a measurement beam. A beamsplitter and photo detector are co-located with the sampling mirror, while the reference beam is taken from the secondary laser on the optical bench. Taking the measurements at three points allows to reconstruct the alignment of the wavefront of the outgoing light as is needed for diagnosis and correction in post-processing.

Point-ahead angle

The point-ahead angle is the angle between the transmitted and received beams on each optical bench. The angle between the beams is due to the fact that the velocity of the far spacecraft has a component perpendicular to the line of sight, *i.e.* the far spacecraft appears to move sideways during the travel time of the light between the spacecraft. This component changes amplitude and direction over the course of time, causing a time-varying angle between transmitted and received beam.

With the currently planned armlength of 10^6 km, the variation of that angle does not exceed the field of view of the quadrant photo diodes and the loss of contrast due to the angle between the wavefronts can be tolerated. Accordingly, the current payload design does not foresee an on-orbit mechanism to compensate for the variation of the point-ahead angle.

5.1.2. Optical assembly tracking mechanism

In addition to the time variation of the angle between the received and the transmitted beams, the angle between the two telescopes on board one spacecraft changes over time as well. Nominally 60° , it varies by about 1.5° over the course of a year due to orbital mechanics. To compensate for that variation, a mechanism that changes the angle between the two telescopes is required, the so-called optical assembly tracking mechanism (OATM), as can be seen in the lower left of figure 5.1, connecting the rear ends of the two single assemblies. The OATM acts upon the complete assembly of GRS, optical bench and telescope, rotating the assembly around an axis perpendicular to the plane of the constellation. This way, the OATM is *not* part of the optical path of an interferometer, therefore relaxing the requirements on the angular jitter of the mechanism significantly, making them similar to the residual spacecraft jitter, *i.e.* on the order of a few nrad/ $\sqrt{\text{Hz}}$.

5.2. Phase measurement

The phasemeter for NGO is one of the few payload items that can claim no or very little heritage from LPF. The main reason lies with the fact that LPF uses a constant and relatively low heterodyne frequency of 1.6 kHz to 2 kHz (HEINZEL ET AL., 2003, 2004, 2006) in its interferometers, whereas the heterodyne frequency for NGO is much higher due to the relative motion of the spacecraft and the resulting Doppler effect. The requirement for the NGO phasemeter calls for a maximum admissible frequency heterodyne frequency of 15 MHz and for a frequency rate of change up to 1 Hz/s. Additionally, the phasemeter must be compatible with data transfer and ranging tones on the laser link between the spacecraft as well as with the transmission of the clock signal, none of which are present on LPF. Furthermore, the NGO phasemeter requires significantly more independent channels than the LPF phasemeter, as NGO has a much larger number of photoreceivers, most of them quadrant diodes. In the current baseline architecture, NGO requires 58 phasemeter channels, not counting redundancy.

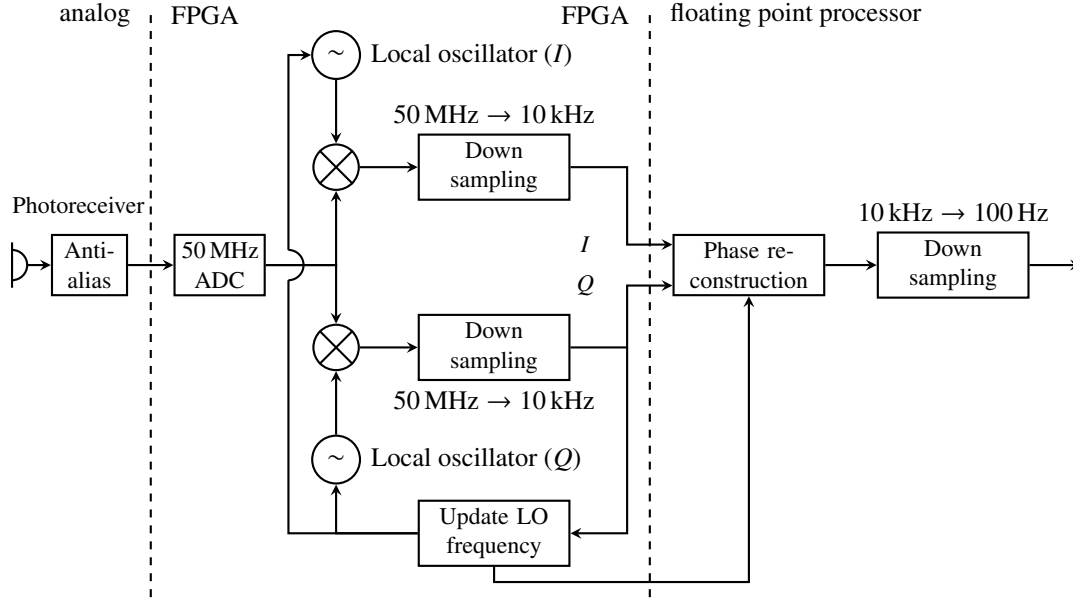


Figure 5.5.: Block diagram of the NGO phasemeter. Signals from the photodetector pass an analogue anti-alias filter before digitisation in a 50 MHz analog-to-digital converter (ADC) and further processing to determine phase and frequency, based on integer arithmetic in a field-programmable gate array (FPGA). A phase reconstruction algorithm to correct residual tracking errors is implemented in a floating point processor and feeds back to the local oscillator.

The phasemeter architecture foreseen for NGO is based on a digital phase locked loop (DPLL) as sketched in figure 5.5. The signal from the photoreceiver passes through an analog anti-alias filter and is then digitised at 50 MHz. The digitisation frequency has to be chosen high enough to exceed the Nyquist frequency for the highest occurring beat note in the system. The signal is then multiplied with a local oscillator whose frequency is made to track the signal frequency. The low-pass filtered output of this multiplication is directly proportional to the *phase* difference between signal and local oscillator and is used as an error signal to drive the frequency and phase of the local oscillator to be the same as for the signal. The DPLL needs to update the local oscillator quickly enough (~ 0.1 ms) to follow the frequency changes occurring in NGO. For performance reasons, these operations are implemented in a field-programmable gate array (FPGA), and all operations are based on integer arithmetic. Residual tracking errors are corrected by evaluating the information in the two quadratures of the error signal in a floating point processor and combine them with the local oscillator phase. Further filtering of the signal yields the output at a rate of 100 Hz for recording. A more detailed insight into the principle of operation of the phasemeter including initial results on simulated data is given in (SHADDOCK ET AL., 2006).

5.2.1. Clock noise removal

An ultra-stable oscillator (USO) is required onboard to trigger the analog-to-digital converters (ADCs) in the phasemeter, assigning timestamps to all measurements, and for providing offset frequencies for laser phase locking. Because of phase noise limitations for available space-qualified USOs, the USO phase noise must be measured. Current USOs have a stability (Allan standard deviation) of 1×10^{-13} to 2×10^{-13} for periods of 1 s to 1000 s. At 1 mHz, this corresponds to a fractional frequency noise level of about $7 \times 10^{-12}/\sqrt{\text{Hz}}$.

To remove the clock phase (*i.e.* USO) noise, the absolute distance between the spacecraft needs to be known to about 1 m, and the clock offset between spacecraft to a few ns. These measurements are performed by applying two different phase modulations on the laser link. To measure the clock noise, the phase noise of each of the three spacecraft master clocks is multiplied by an integer factor and modulated as high frequency (GHz) phase modulation sidebands onto each laser link using 10 % of the light power. After interference between local and incoming lasers, the phase measurement of the resulting sideband-to-sideband beat note contains the amplified clock noise information necessary to remove the clock noise by time-delay interferometry (TDI). Absolute inter-spacecraft distances are determined with a pseudo-random noise (PRN) phase modulation on each laser

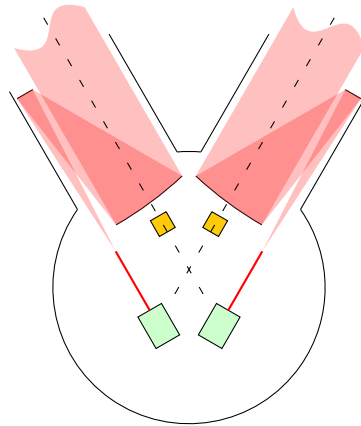


Figure 5.6.: Position and orientation of the two test masses (dark grey) in the Mother-S/C. The sensitive axes of the sensors are indicated with the dashed lines and are aligned with the direction to the far spacecraft.

carrier using 0.1 % to 1 % of the light power. The distance is measured via correlation of the demodulated carrier phase with a local copy of the original PRN code. An important benefit of such a modulation is the possibility of additional data encoding on top of the PRN codes to enable inter-spacecraft communication. A direct measurement of the clock offsets between the three spacecraft to a few nanoseconds is an automatic by-product of this technique.

5.3. Disturbance Reduction System

The DRS of NGO is one of the main components of the mission. Whereas the IMS allows to measure the distance between the test masses to picometer accuracy, the DRS is responsible to render these measurements meaningful, as it ensures that the test masses follow gravitational orbits as much as possible, limiting the residual stray acceleration error. Thus, the DRS consists of the GRS and its ancillary structures, and the drag-free attitude control system (DFACS). While the latter is not, in a strict sense, part of the payload, the main components of the DFACS will be discussed in this section: the micro-newton propulsion system that is used to provide the thrust for the fine attitude and position control of the spacecraft, and the control law that takes the data from the gravitational reference sensor and controls the micro-newton thrusters such as to keep the spacecraft centred on the test mass while keeping alignment of the telescopes to each other.

5.3.1. Principle of operation

The main objective of the DRS is to maintain the free fall of a test mass that serves as nominal reference point for the measurement of the inter-spacecraft distance. To keep the test mass in free fall, the DRS measures the position and orientation of the test mass with respect to the spacecraft, applies a control law and commands micro-newton thrusters such that the test mass remains in its nominal position with respect to the spacecraft. Situated inside the spacecraft, the test mass is shielded from the external effects, such as solar radiation pressure and (to a certain degree) the interplanetary magnetic field. In addition, the spacecraft architecture has to ensure that the forces on the test mass are as small as possible, requiring special design precautions regarding the mass distribution, the thermal balance and the magnetic cleanliness. Each spacecraft has two GRSs, each mounted in the line of sight of the corresponding telescope (see figure 5.1, upper right panel), behind the optical bench. The sensitive axis of the DRS denotes the axis aligned with the line of sight to the telescope and consequently to the test mass in the remote spacecraft (see figure 5.6). As the Mother-S/C employs two test masses per spacecraft, it is impossible to keep both of them in free fall condition in all degrees of freedom and ensure at the same time that the test masses stay close to their nominal position. However, it is sufficient to maintain free fall in the direction of the sensitive axes which can be achieved by controlling the “non-sensitive” degrees of freedom of the test masses and the position and attitude of the spacecraft. While the Daughter-S/C houses only one test mass, in

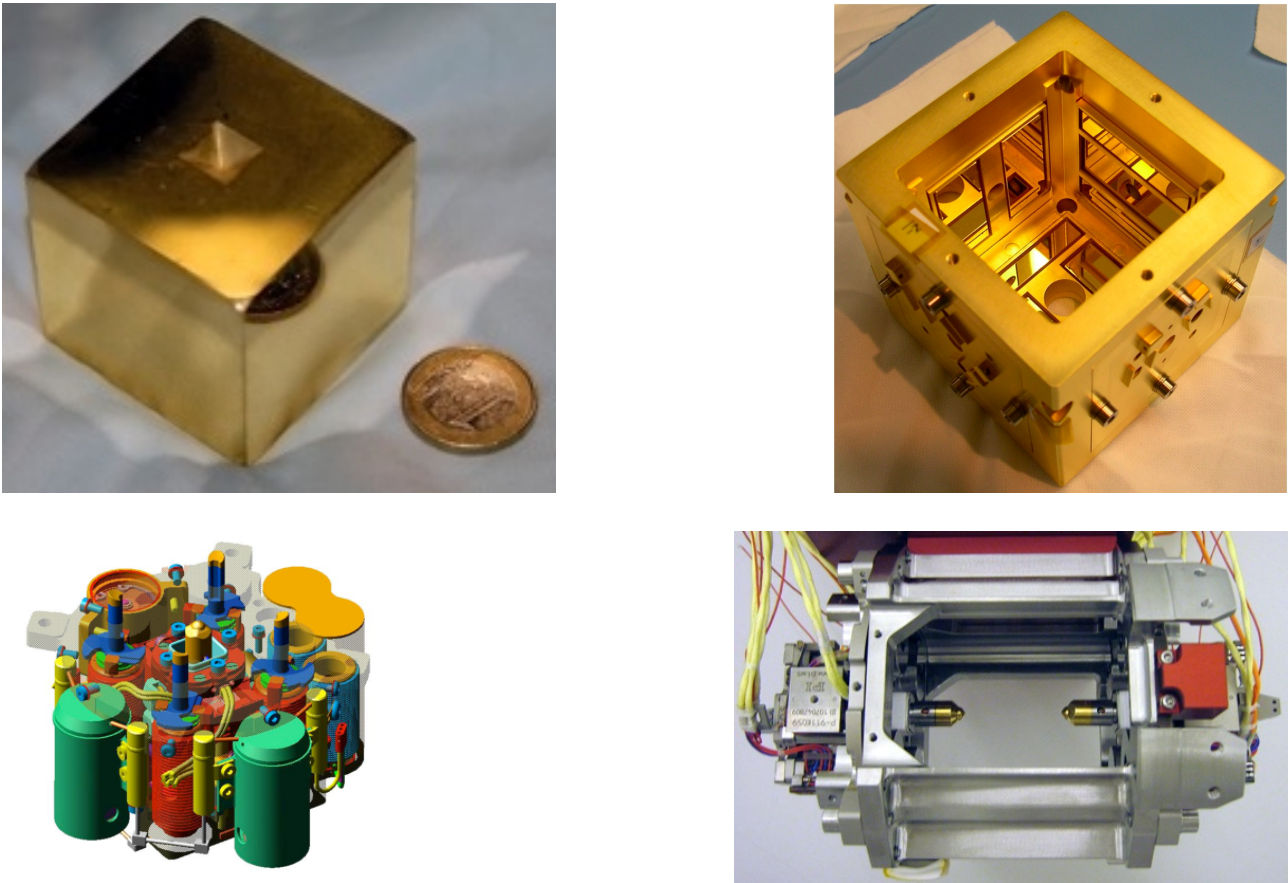


Figure 5.7.: Upper left: *LISA Pathfinder test mass made of a mono-phasic alloy of 73 % gold and 27 % platinum, coated with gold. The inverted prism-like impression at the centre of the top face takes the plunger of the caging system and allows centering of the test mass, the chamfered corners accept the fingers of the launch lock. Edges are chamfered to prevent damage during caging.* Upper Right: *Electrode Housing.* Lower left: *Schematic drawing of the bottom half of the caging mechanism, with the central plunger in the centre and the four hydraulically actuated fingers that grab onto the corners of the test mass.* Lower right: *Flight model of the Grabbing, Positioning, and Release Mechanism (GPRM) of the caging mechanism assembly (side view) with both plungers visible.*

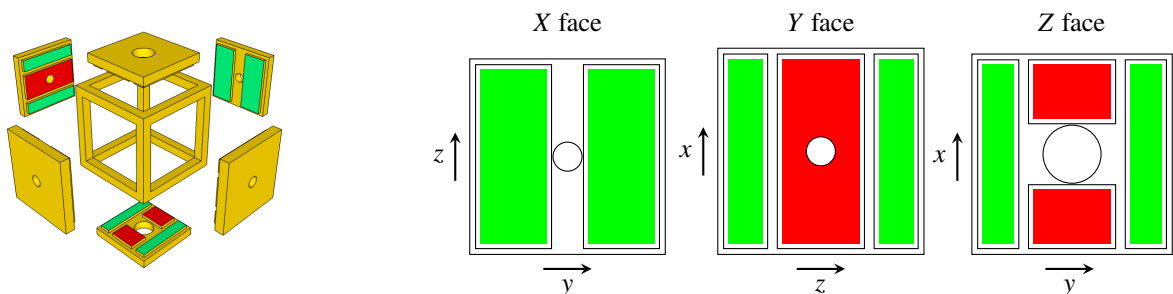


Figure 5.8.: Left: *Exploded schematic view of the electrode housing, showing the structure of the electrode housing and the electrodes mounted on the inner faces.* Right: *Placement of the electrodes onto the inner surfaces of the electrode housing. Control electrodes are given in green (light grey), injection electrodes in red (dark grey). The central holes in the X- and Y-faces admit the laser, the central hole in the Z face admits the plunger. The electrodes differ slightly in overall size on the different faces.*

both cases small forces have to be applied as well to keep the test mass aligned with the line of sight of the telescope. These forces only apply to the non-sensitive axes.

The measurement of the test mass position is provided by a capacitive readout system, augmented in the sensitive axes by the measurement provided by the test mass interferometer.

The **DRS** can claim substantial heritage from **LPF**, as the gravitational reference sensor will be identical and the micro-Newton thrusters and the control law will be similar, requiring adaptation to the larger mass of the **NGO** spacecraft and the different geometry of the test mass arrangement. Similarly, lifetime requirements for the propulsion system are more stringent as **NGO**'s nominal design life-time is 2 years compared to the 11 months of **LPF**.

5.3.2. Environmental requirements

As gravitational forces cannot be shielded, the mass distribution of the spacecraft can cause significant disturbances on the test mass, both through direct gravitation as well as through gravity gradients. To be able to compensate both mass imbalance and gravity gradient, the mass distribution on the spacecraft has to be known accurately enough to be able to use the correct amount of compensation mass in the correct position. On ground, a measurement of the self-gravity is not feasible to the precision necessary for **NGO**, verification of the self-gravity relies on analyses. Such analyses on self-gravity and the design of compensation masses has been successfully performed on **LPF** (ARMANO ET AL., 2005; BRANDT ET AL., 2005) and the corresponding analysis tools have been developed for **NGO** (MERKOWITZ ET AL., 2004, 2005).

Of similar importance is the magnetic cleanliness of the spacecraft, as magnetic fields can cause a non-gravitational acceleration of the test mass coupling to its non-zero magnetic susceptibility. In addition, they create an acceleration noise as soon as the test mass carries an electric charge. As neither the magnetic susceptibility of the test mass nor its electric charge can be controlled to be precisely zero, strict magnetic cleanliness has to be enacted, requiring the use of only non-magnetic materials in the vicinity of the **GRS**.

Temperature fluctuations at the **GRS** have the potential to cause acceleration noise, as they will cause a time varying gas pressure in the electrode housing leading to varying radiometer effect. The thermal variations allowed are at the level of $10^{-5} \text{ K}/\sqrt{\text{Hz}}$.

LPF will provide a direct readout of the spacecraft gravitational forces and torques, as well as the total force and torque gradients, in many degrees of freedom. It will also provide high resolution readouts of temperatures and magnetic fields in key locations near the test masses. As such, **LPF** will test the capabilities for achieving the necessary gravitational, magnetic, and thermal environments in orbit with a science craft similar to that of **NGO**.

5.3.3. Gravitational Reference Sensor

The **GRS** forms a crucial part of the **NGO** mission and is one of the major components of the **DRS**, providing it with the data necessary to keep the spacecraft in a (nearly) gravitational orbit. The **GRS** includes the test mass (figure 5.7, upper left), enclosed in a housing (figure 5.7, upper right) that contains the electrodes needed for the capacitive readout of the test mass position. The electrodes are arranged in such a way that all relevant degrees of freedom can be capacitively measured (CARBONE ET AL., 2003; STANGA ET AL., 2006; WEBER ET AL., 2002). The **GRS** further contains the launch lock mechanism (figure 5.7, lower row) and the charge control system.

Forcing of the test mass to control its orientation and position in the non-sensitive directions is achieved by applying additional **AC** voltages to the electrodes; the unavoidable cross-coupling of the actuation from non-sensitive directions into the sensitive directions has to be as small as possible (on the order of 10^{-3}) to avoid "leakage" into the sensitive axis that causes acceleration noise of the test mass. Knowledge of the correct cross-coupling coefficients and an effective diagonalisation of the control matrix is an important task during on-orbit commissioning of the instrument.

Other important noise sources in the **GRS** to consider include electrostatic forces from stray "patch" fields and random charging processes (SHAUL ET AL., 2004, 2005); Brownian forces associated with gas damping (CAVALLERI ET AL., 2009B); forces induced by thermal gradients, such as thermal radiation pressure, or asymmetric outgassing (CARBONE ET AL., 2007A); coupling to the satellite motion via the electrostatic force gradient in the capacitive sensor housing (CARBONE ET AL., 2005). This last noise source has been found to be much smaller than originally

Table 5.2.: Summary of the environmental and performance requirements on the DRS

Condition	Requirement
Acceleration	
DC	$3 \times 10^{-9} \text{ m/s}^2$
residual variation	$3 \times 10^{-15} \text{ m/(s}^2 \sqrt{\text{Hz}})$
Capacitive readout noise	
Displacement (sensitive axis)	$1.8 \text{ nm}/\sqrt{\text{Hz}}$
Displacement (non-sensitive axes)	$3.0 \text{ nm}/\sqrt{\text{Hz}}$
Rotation	$200 \text{ nrad}/\sqrt{\text{Hz}}$
Forcing noise	
Sensitive axis	$2 \times 10^{-15} \text{ m/(s}^2 \sqrt{\text{Hz}})$
Non-sensitive axes	$3 \times 10^{-14} \text{ m/(s}^2 \sqrt{\text{Hz}})$
Rotation	$7.3 \times 10^{-13} \text{ rad/(s}^2 \sqrt{\text{Hz}})$
Thermal variation across sensor	$10^{-5} \text{ K}/\sqrt{\text{Hz}}$
Magnetic field	
DC field	$4 \times 10^{-6} \text{ T}$
DC gradient	10^{-6} T/m
Variation	$72 \times 10^{-9} \text{ T}/\sqrt{\text{Hz}}$
Variation of gradient	$25 \times 10^{-9} \text{ T/(m } \sqrt{\text{Hz}})$
Charge on test mass	$10^7 \text{ electron charge}$
Absolute position of test mass inside electrode housing	$1.5 \times 10^{-9} \text{ m}/\sqrt{\text{Hz}} \times \sqrt{1 + \left(\frac{8 \text{ mHz}}{f}\right)^4}$

feared, due to the small measured magnitude of the stray electrostatic coupling (CAVALLERI ET AL., 2009A) and to the possibility to subtract this noise with the interferometric measurement of the motion of the test mass relative to the spacecraft (ARMANO ET AL., 2009).

The patch field effect, caused by spatial (and temporal) variation of the work function, can be a major source of noise to drag-free sensors (EVERITT ET AL., 2008). The work function of the test mass contributes to stray DC electrostatic fields that couple to the time-varying charge of the surrounding electrode housing (and vice versa), introducing both forcing and sensing noise. A technique to measure the stray DC field imbalances has been proposed (WEBER ET AL., 2007) and experimentally verified (CARBONE ET AL., 2003) that simulates a sinusoidally varying charge on the test mass by applying a dither voltage to selected electrodes. Using this method, the average bias voltage that results from the spatial variation of the work function can be suppressed by a factor of about 100 by applying a DC compensation voltage, resulting in a reduction of the respective acceleration noise to levels negligible for NGO.

The GRS is a direct heritage from the LTP experiment on LPF; a detailed review on the working principle of the GRS can be found in (DOLESI ET AL., 2003), and a detailed analysis of the GRS from the standpoint of test mass acceleration noise can be found in (ANTONUCCI ET AL., 2011). An extensive ground-testing campaign evaluating the performance and the noise sources on the GRS employing a low-frequency torsion pendulum is under way and results and more detailed descriptions of noise sources and their effect can be found in (CARBONE ET AL., 2003, 2005, 2006; HUELLER ET AL., 2005); requirements on the sensor and the environmental conditions are summarised in table 5.2. The current status of the GRS subsystem on LPF can be found in *The LISA Pathfinder Mission* (S2-EST-RP-1087).

Test mass and housing

The test mass is a cube made of an alloy of about 73 % gold and 27 % platinum with a mass of 1.96 kg and dimension 46 mm × 46 mm × 46 mm. The mixing ratio of the two metals is chosen such that the magnetic susceptibility χ can be made very small (BUDWORTH ET AL., 1960; SILVESTRI ET AL., 2003). As the susceptibility depends on the mixing ratio and the manufacturing process, a small residual magnetic susceptibility of $\chi \approx$

Table 5.3.: Summary of the physical parameters of the test mass and the housing.

Element	Property
Test mass	
Size	46 mm × 46 mm × 46 mm
Material	gold-coated AuPt (73 % Au, 27 % Pt)
Mass	1.96 kg
Magnetic susceptibility	$ \chi \leq 2 \times 10^{-5}$
Housing	
Material	gold-coated molybdenum
Gaps Electrodes/Test mass	4 mm (x), 2.9 mm (y), 3.5 mm (z)
Electrodes	
Material	gold-coated sapphire
Size and Arrangement	see figure 5.8

-2×10^{-5} remains in the test mass, requiring a certain amount of magnetic cleanliness of the whole spacecraft that prohibits the use of ferro-magnetic materials in the vicinity of the GRS. The surface of the test mass is coated with a thin layer of gold that provides reflectivity for the laser light of the local interferometer. In addition gold proves to be the material of choice to minimise the patch field effect.

The test mass is surrounded by a housing that contains the electrodes for the capacitive sensing and actuation. The housing is slightly larger than the test mass, with the gap between the test mass and the electrodes measuring between 3 mm and 4 mm, providing a further reduction of the patch field effect, as the noise forces decrease with the distance. An additional benefit of the large gaps is a reduction of the dissipation due to gas flow around the test mass. The electrode housing admits the fingers and the plunger of the launch lock and repositioning mechanism (see section 5.3.3) in the Z faces and the laser of the test mass interferometer through a hole in the X face. The electrodes are made from a gold-coated sapphire substrate, surrounded by a molybdenum guard ring; the electrode housing structure is also manufactured from molybdenum.

The physical properties of test mass and housing are summarised in table 5.3.

Capacitive sensing

The capacitive sensing of the test mass position is designed to provide a measurement of the test mass position in the sensitive axis with noise levels of $1.8 \text{ nm}/\sqrt{\text{Hz}}$, while at the same time minimise the back-action on the test mass. Six opposing pairs of electrodes form a differential capacitive-inductive bridge with a resonance frequency of about $\omega_0 = 2\pi \times 100 \text{ kHz}$. Combinations of the obtained signals yield all relevant displacement and rotation measurements. In order to apply the AC bias to the test mass, injection electrodes are placed on the +Z and -Z as well as on the +Y and -Y surfaces of the electrode housing (figure 5.8). The capacitive sensing achieves a sensitivity of $2 \text{ nm}/\sqrt{\text{Hz}}$ in displacement and $200 \text{ nrad}/\sqrt{\text{Hz}}$ in rotation (CARBONE ET AL., 2007B) in ground tests, matching or exceeding the requirements for NGO.

The details of the sensor design and a detailed discussion of the noise can be found in CAVALLERI ET AL. (2001).

Launch lock and repositioning

The relatively large gaps make it necessary that the test mass is held during launch by the *caging mechanism* to avoid damage to the test mass or the electrode housing due to the vibrations during launch. The caging mechanism comprises three actuators: a launch lock; a grabbing/positioning actuator; and the release mechanism. The launch lock consists of eight hydraulically actuated fingers that connect to the eight corners of the cubical test mass, each pushing with a force of 1200 N to keep the test mass securely in place (see figure 5.7, lower left panel for a drawing of the caging mechanism).

Releasing the test mass from the launch lock requires to break the adhesion present between the fingers and the surface of the test mass. The necessary force to break the adhesion can be up to 10 N per finger (on the order of 1 % of the load), so that without a way to push the test mass off the fingers, it would remain stuck to the launch

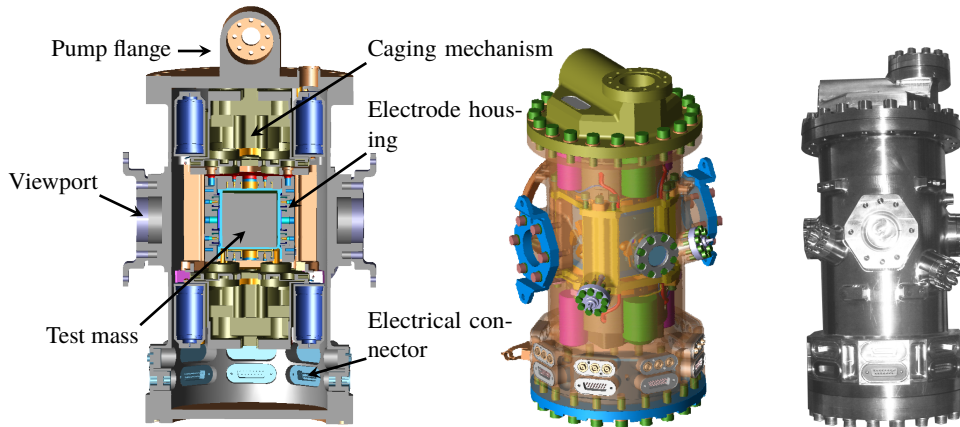


Figure 5.9.: *Left: Schematic drawing of the vacuum housing of the inertial sensor of LPF. Centre: Schematic drawing, external view. Right: Flight model of the vacuum housing for the inertial sensor of LPF. The inertial sensor for NGO is foreseen to be identical to the sensor used in LPF.*

lock. In addition, the residual momentum of the test mass after release needs to be smaller than 10^{-5} N s for the electro-static actuator to be able to slow down and centre the test mass in the electrode housing. To overcome the adhesion between the fingers and the test mass, two piezo-driven plungers, acting centrally on the $+Z$ and $-Z$ surface of the test mass, respectively, are used to push the test mass off the fingers. The Z surfaces of the test mass have inverted pyramidal indentations to allow for an auto-centring and auto-aligning of the test mass during engagement of the plungers (see figure 5.7, upper left panel). As the plungers push with up to 40 N into the indentations, an adhesion force of about 0.5 N will have to be overcome when attempting to retract the plungers. For that purpose, the plungers accommodate a release tip at their end (much like a retractable ball-point pen) that can be pushed out by a piezo-electric element to deliver the necessary force. The remaining adhesion, still too large to be overcome by the electro-static actuator (BENEDETTI ET AL., 2006), is then broken using the inertia of the test mass by quickly retracting the plungers, leaving the test mass with residual momentum below the specified 10^{-5} N s. After launch, only the plungers are employed to grab and position the test mass during spacecraft safe mode or any other circumstance that makes it necessary to re-position the test mass.

The breaking of the adhesion between plungers and test mass has been the topic of intense ground-based testing, showing the feasibility of a test mass release within the required limits of the transferred momentum (BORTOLUZZI ET AL., 2009).

Vacuum system

It is a peculiarity of NGO (and LPF) that despite the fact that the mission will operate in interplanetary space, it needs to carry a vacuum system. The residual gas pressure within the spacecraft due to outgassing is too high for the GRS to tolerate, as it creates spurious noise due to the radiometric effect (CARBONE ET AL., 2007A) and through gas damping. Therefore, a vacuum chamber, made entirely from titanium for magnetic cleanliness in the vicinity of the test masses, will contain the electrode housing and auxiliary elements (figure 5.9). During the transfer orbit phase, a gate valve connecting the vacuum enclosure to a pipe leading to the outside of the spacecraft will be opened, allowing the vacuum enclosure to vent to space, maintaining the internal pressure at, or below, the required 10^{-8} mbar.

Charge control system

Test mass charging creates acceleration noise by coupling to noisy electrostatic patch fields and by introducing a time-varying force gradient coupling to satellite motion. As such, a charge control system is needed to discharge the test mass.

Charging of the test mass occurs mainly when secondary particles created by interaction of either protons

Table 5.4.: Main requirements on the telescope. The full field of view is required for acquisition. The wavefront quality is required only for the smaller field of view in the science mode.

Characteristics	Requirement
Aperture	20 cm
Optical efficiency	≥ 0.853
Field of view	
acquisition mode	400 μ rad full angle
science mode (out of plane)	$\pm 7 \mu$ rad
(in plane)	$\pm 4.2 \mu$ rad in-plane
Optical pathlength stability	$1 \frac{\text{pm}}{\sqrt{\text{Hz}}} \times \sqrt{1 + \left(\frac{3 \text{ mHz}}{f}\right)^4}$
Magnification	40
Far-field wavefront quality	$\lambda/20$

or α -particles from cosmic radiation with the spacecraft materials hit the test mass (JAFRY & SUMNER, 1997; SUMNER ET AL., 2004). The charging rates incurred are on the order of 50 e/s. A standard way to discharge test masses in similar setups is to connect a thin wire of conductive material to the test mass (TOUBOUL ET AL., 1996), however, such a mechanical connection introduces spurious accelerations and proves to be too noisy for the NGO requirements. Another well proven way to remove surface charge is through the photo-electric effect. In the case of NGO, UV light will be used to irradiate test mass and electrode housing, removing surface charges from electrodes and test mass. The charge control system for NGO is based on the heritage from LPF (SCHULTE ET AL., 2006), which itself is based on the charge control system flown on the GP-B mission, and whose functionality and performance has been demonstrated (WASS ET AL., 2006). The LPF charge control system consists of six mercury discharge lamps, producing UV light at 254 nm coupled into optical fibres and brought to the test mass (2 lamps) and electrode housing (1 lamp). An identical setup controls the charge of the second test mass, bringing the number of lamps up to the total of six. Due to the reflectivity of both the electrodes and the test mass, light shone on any surface will eventually reach most of the other surfaces as well and release electrons, so that the discharge rate is determined by the net current between electrodes and test mass. The polarity of the discharge is determined by the digitally controlled output power of the UV lamps received by the test mass and the electrode housing, respectively, and can be further controlled by applying bias voltages to the electrodes. Operationally, the discharging can occur episodically or continuously, depending on the observed charge rate. Both methods will be demonstrated during the LPF mission. The charge itself is measured by applying an AC voltage to the electrodes and measuring the ensuing displacement of the test mass (SCHULTE ET AL., 2006; SUMNER ET AL., 2004). For NGO the development of UV LED (SUN ET AL., 2006) opens the possibility to replace the mercury discharge lamps with LED requiring less power and having less mass.

5.4. Telescope

The telescope foreseen for NGO is an off-axis telescope with a 20 cm aperture, a mechanical length of about 60 cm, and a field of view of $\pm 7 \mu$ rad out-of-plane and $\pm 4 \mu$ rad in plane in which the most stringent wavefront requirements have to be met. With an off-axis telescope, the requirements on stray light are easier to achieve than for a telescope with a secondary mirror in normal incidence. Additionally, the off-axis design has the advantage of not blocking part of the incoming light, thus allowing more light for the measurement process and resulting in less wavefront distortion.

The size of the telescope's aperture is determined by the amount of light power needed to achieve a given sensitivity, as its size determines both the widening of the beam due to diffraction and the amount of laser power collected from the received beam. As a rough guideline, the displacement noise due to shot noise for a telescope with diameter D , a laser with power P_0 , wavelength λ and "optical efficiency" ϵ (*i.e.* the ratio between the power

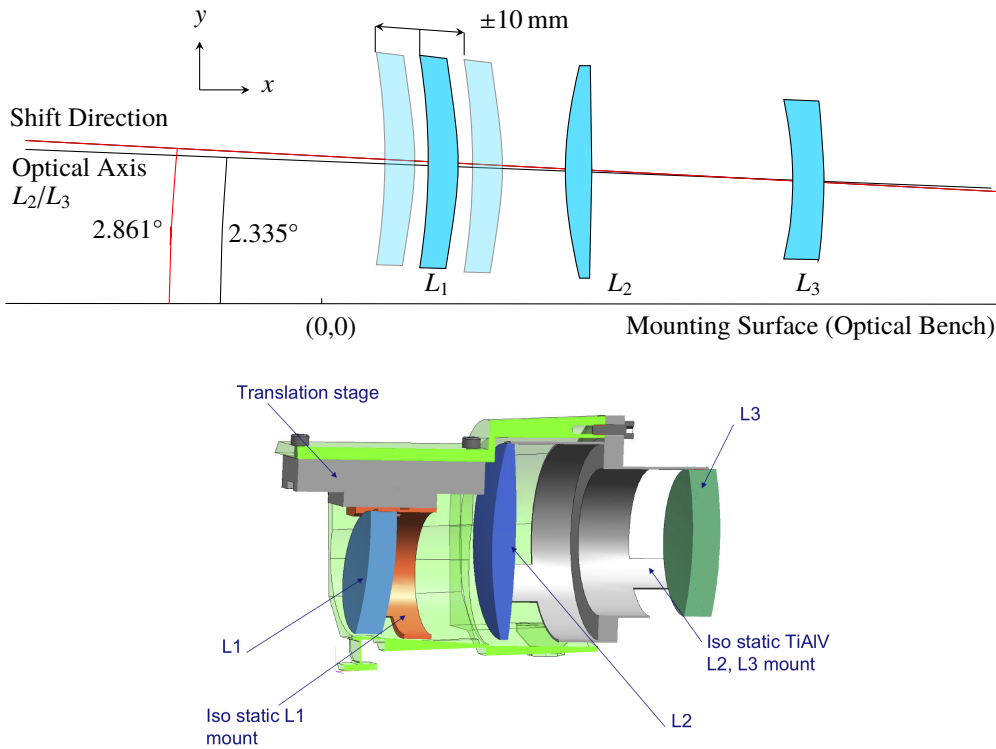


Figure 5.10.: Upper panel: *Refocusing mechanism, industrial concept (EADS Astrium)*. Lower panel: *Design of Refocusing mechanism (TNO)*

sent out by the telescope and the power delivered to the optical bench), and a distance between the *S/C* of *L* is given by

$$\widetilde{x}_{\text{SN}} = 4.35 \times 10^{-12} \left(\frac{\lambda}{1064 \text{ nm}} \right)^{\frac{3}{2}} \left(\frac{0.25 \text{ W}}{\epsilon P_0} \right)^{\frac{1}{2}} \left(\frac{L}{1 \times 10^9 \text{ m}} \right) \left(\frac{0.2 \text{ m}}{D} \right)^2 \frac{\text{m}}{\sqrt{\text{Hz}}} \quad (5.1)$$

A diameter of 20 cm results in an equivalent pathlength noise due to shot-noise of about 4.3 pm/ $\sqrt{\text{Hz}}$, the dominating contribution to the noise budget at frequencies above 3 mHz.

With a magnification of the telescope of 40 and a diameter of the outgoing beam of 200 mm, the input beam to the telescope has a diameter of 5 mm. A beam expander, situated on the optical bench (figure 5.4), matches the typical beam diameter on the optical bench (1 mm) to the diameter required by the telescope. Equally important as the telescope's ability to gather light is the quality of the wavefront leaving the telescope. An ideal, perfectly spherical wavefront with its centre at the position of the test mass would render the measurement of the optical pathlength insensitive to any pointing jitter of the sending spacecraft. Any deviation from such an ideal wavefront, however, will translate a spacecraft jitter into an equivalent pathlength noise. As the wavefront errors depend critically on the position of the beam waist with respect to the telescope, the telescope can be refocused on orbit by adjusting the position of two lenses in the telescope "back-optics". Additionally, the back-optics images the exit pupil of the telescope to the test mass and the photodetectors of the science interferometers, minimising the effect of spacecraft rotation on the science measurement.

An additional complication arises from the fact that the telescopes for *NGO* form part of the interferometric path of the science interferometer. Any change in optical pathlength between, *e.g.*, the primary and secondary mirror, directly contributes to noise degrading the science signal. To reduce the impact of any geometrical distortions, optical truss interferometry (see section 5.1.1) can be used to directly measure the wavefront and phase of the outgoing beam for later correction in post-processing.

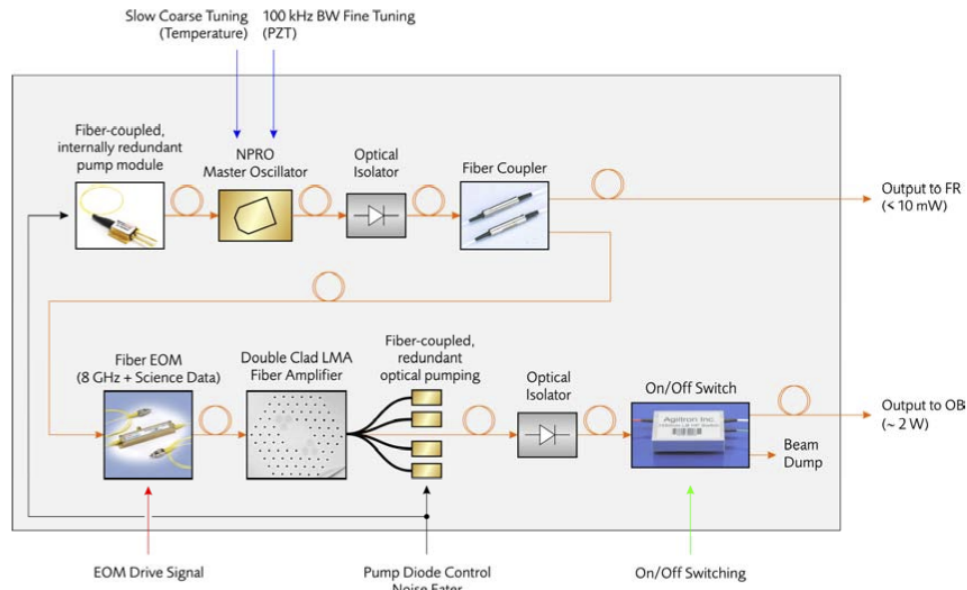


Figure 5.11.: Baseline architecture for the laser system. The output of a diode-pumped NPRO laser (~ 50 mW) is amplified by a double-clad fibre amplifier to the required 2 W. A fibre-coupled EOM imprints communication signals on the low-power light to avoid thermal stress or damage to the EOM. Courtesy of EADS Astrium.

5.5. Laser System

The laser system currently envisaged for **NGO** makes use of the Master Oscillator Fibre Power Amplifier (MOFPA) approach (WESSELS ET AL., 2002; ZAWISCHA ET AL., 1999). For **NGO**, the low-power master oscillator is largely identical to the laser used by the **LTP** experiment on board **LPF** (McNAMARA ET AL., 2008), a Nd:YAG non-planar ring oscillator (NPRO) pumped by an internally redundant, fibre-coupled arrangement of laser diodes. The **LTP** laser is manufactured by Tesat GmbH (BARTELT-BERGER ET AL., 2001), emitting 40 mW of 1064 nm light and has been used in a similar configuration as proposed for **NGO** on board the TerraSAR-X and N-Fire satellites (LANGE & SMUTNY, 2004; ROTH & WERNINGHAUS, 2006; SODNIK ET AL., 2006).

The light of the **NPRO** passes an optical isolator to suppress optical feedback and is coupled into two optical single-mode fibres, the smaller fraction of the light is taken to be used for prestabilisation purposes, the larger fraction fed into a fibre-based electro-optical modulator (EOM) that imprints phase modulation sidebands used for clock-transfer and ranging. From there, it enters a double-clad fibre amplifier, pumped by a redundant array of fibre-coupled laser diodes, bringing the laser power up to the required 2 W. After passing another optical isolator and an on/off switch controlled by the spacecraft computer, the light is then delivered via an optical fibre directly to the optical bench (figure 5.11).

The laser system is fully redundant, providing two identical, assemblies that feed into a fibre switcher on the optical bench that in the case of a laser failure will be used to switch over to the redundant laser without compromising the alignment on the optical bench.

As polarisation encoding is used in **NGO** to distinguish transmitted from received light (see 5.2), the light entering the optical bench needs to be linearly polarised. This is ensured by a polariser as the first component on the optical bench. To avoid unnecessary stray-light, 98 % of the light power arriving on the optical bench needs to be in the linear polarisation transmitted by the polariser.

The position of the test masses is read out interferometrically in the test mass interferometer, using the test masses as a mirror. Thus, the requirement on the permissible acceleration noise for the test masses leads to a requirement on the power stability of the laser, as a variation in laser power δP causes a variation in radiation pressure on the test masses and therefore a variation in the acceleration δa

$$\delta a = \frac{2\delta P}{mc} \quad (5.2)$$

Table 5.5.: Laser requirements, specified at end-of-life.

	Requirement
Wavelength	1064.5 nm
Output power (EOL) delivered to OB	2 W 1.2 W
Polarisation	linear, containing more than 98 % of optical power in main polarisation
Fractional power stability	$10^{-3}/\sqrt{\text{Hz}}$ in the NGO band

Table 5.6.: Frequency stabilisation requirements

Stabilisation stage	Performance after stabilisation in $\text{Hz}/\sqrt{\text{Hz}}$
Free running	$\frac{10^4}{f}$
Pre-stabilisation	$\frac{280}{f} \times \sqrt{1 + \left(\frac{2.8 \text{ mHz}}{f}\right)^4}$
Arm locking	$0.3 \times \sqrt{1 + \left(\frac{2.8 \text{ mHz}}{f}\right)^4}$
TDI	$4 \times 10^{-7} \times \sqrt{1 + \left(\frac{2.8 \text{ mHz}}{f}\right)^4}$

Consequently, the relative intensity noise (RIN) $\widetilde{\delta P}/P$ for the laser has to be smaller than $10^{-3}/\sqrt{\text{Hz}}$ in the **NGO** band, given the allocated acceleration noise of $\widetilde{\delta a} = 3.4 \times 10^{-16} \text{ m}/(\text{s}^2 \sqrt{\text{Hz}})$ and an absolute power of $100 \mu\text{W}$ for the readout of the test mass. A summary of the requirements on the laser at end-of-life is given in table 5.5.

5.5.1. Laser frequency noise suppression

Frequency stabilisation of the lasers is a vital part of the **NGO** measurement scheme. As in any interferometric length measurement, a frequency noise $\delta\nu$ causes an equivalent noise in the length measurement δx that is proportional to the difference of optical pathlength ΔL and the fractional frequency noise.

$$\delta x = \Delta L \frac{\delta\nu}{\nu} \quad (5.3)$$

The difference in optical pathlength in **NGO** can be as large as $\Delta L = 10^8 \text{ m}$ due to the orbital motion of the spacecraft, and the equivalent pathlength noise contribution allocated to frequency noise is around $\widetilde{\delta x} = 0.4 \text{ pm}/\sqrt{\text{Hz}}$ at 3 mHz. This results in a required frequency stability of $\widetilde{\delta\nu} = 1.2 \times 10^{-6} \text{ Hz}/\sqrt{\text{Hz}}$ at 3 mHz. Starting from a free-running laser that has a typical frequency noise of $\widetilde{\delta\nu}_{\text{free}} = 3 \text{ MHz}/\sqrt{\text{Hz}}$ at 3 mHz, such a reduction of frequency noise by about 12 orders of magnitude is difficult to achieve in a single step.

Therefore, a three-level approach has been chosen for **NGO**. First, a pre-stabilisation of the free-running laser to a level of $280 \text{ Hz}/\sqrt{\text{Hz}}$, then a stabilisation of the laser to the **NGO** arms, and finally the post-processing stage as a last step.

Prestabilisation

The prestabilisation is the first stage of the frequency stabilisation scheme for **NGO**. It requires a local frequency reference, such as a cavity (LIVAS ET AL., 2007; MUELLER ET AL., 2005; THORPE ET AL., 2008), a molecular resonance (ARGENCE ET AL., 2010; LEONHARDT & CAMP, 2006; LEONHARDT ET AL., 2006) or a dedicated heterodyne interferometer with unequal arms, much like the one employed in the **LPF** (HEINZEL ET AL., 2006; WAND ET AL., 2006).

Laser stabilisation to a cavity using a variety of techniques, most prominently **RF**-sideband locking, has been demonstrated to well beyond the required stability for **NGO** (see *e.g.* NOTCUTT ET AL. (2005) for a demonstration of a

stability of $\delta\tilde{\nu} = 1 \text{ Hz}/\sqrt{\text{Hz}}$ for frequencies above 1 Hz) at frequencies somewhat higher than the **NGO** frequency band. In the **NGO** frequency band, thermally driven changes of the cavity length are a major contributor to the residual frequency noise. As the thermal environment for **NGO** will be exceptionally stable, this is mainly a problem for laboratory-based demonstration or verification experiments, as these need sophisticated thermal insulation to reach an equivalent stability. Using multiple-stage insulation systems, a frequency stability of $\delta\tilde{\nu} = 30 \text{ Hz}/\sqrt{\text{Hz}}$ at 3 mHz has been demonstrated at NASA's Goddard Space Flight Center (GSFC) (MUELLER ET AL., 2005). The cavities used in this experiment underwent environmental testing and the stated performance has been reached before and after the testing cycle.

The stabilisation of a frequency-doubled Nd:YAG laser to a hyperfine absorption line of the I_2 molecule has a long history as well. Typically used for comparing absolute frequencies in metrology (HONG ET AL., 1998; NEVSKY ET AL., 2001), iodine stabilisation has been employed in ground-based gravitational wave detectors (MUSHA ET AL., 2000) and is currently under investigation for applications in **NGO** (LEONHARDT & CAMP, 2006; LEONHARDT ET AL., 2006; MONDIN ET AL., 2004). where frequency stability of around $10 \text{ Hz}/\sqrt{\text{Hz}}$ to $100 \text{ Hz}/\sqrt{\text{Hz}}$ in the frequency range of 1 mHz to 100 mHz has been demonstrated in tabletop experiments (LEONHARDT ET AL., 2006; MUSHA ET AL., 2000). In contrast to the stabilisation on a cavity resonance, stabilisation on a molecular line provides an absolute frequency reference; the drawback is some added complexity due to the need of frequency-doubled light and gas cell. Recently, a frequency-doubling system has been qualified for space application in the framework of the technology development for the **SIM** mission (CHANG ET AL., 2007), greatly reducing the impact of frequency doubling on the technology development for **NGO**.

Heterodyne interferometry, as opposed to the “homodyne” stabilisation schemes described above, does not require a tuning of the laser to the reference, as it provides an error signal largely independent of the common-mode frequency of the light used. The drawbacks are the need for two light fields, separated by the heterodyne frequency and the comparatively low sensitivity. The use of a heterodyne interferometer with optical paths deliberately chosen to be unequal has been proposed for **NGO**, using a scheme much like the frequency interferometer in the LTP experiment on board **LPF**.

Arm-locking

The second stage of the frequency stabilisation scheme uses the interferometer arms of **NGO** as a frequency reference. By design, the fractional stability of the arms in the frequency range of around 1 mHz is on the order of $\delta\tilde{x}/L \sim 10^{-21}/\sqrt{\text{Hz}}$ as it has to fulfil the science requirements for **NGO**.

Arm-locking therefore makes use of this stability and derives an error signal from the phase-difference of the local laser and the received light. As the received light is phase-locked to the local laser at the remote spacecraft, it can be regarded to carry a replica of the noise of the local laser delayed by one full round-trip time $\tau = 33 \text{ s}$ (SHEARD ET AL., 2003). After choosing a suitable control law, the noise is suppressed at frequencies f smaller than the corresponding round-trip frequency $f_0 = 1/\tau = 30 \text{ mHz}$ but causes significant amplification of the noise at integer multiples of f_0 (SYLVESTRE, 2004) as well as a long decay time for the initial conditions. A more elaborate implementation of arm-locking (HERZ, 2005) uses the phase-differences from the two arms in sum and difference to suppress the noise spiking. The main advantage of the arm-locking scheme is the additional suppression of the laser frequency noise. The only additional functionality required is a tunable frequency reference, as the sensors for the required phase measurements and the actuators for setting the laser frequency are already present. The control law is fully implemented in software and requires no additional resources.

A proof-of-concept implementation in hardware uses **RF** signals instead of light and a 300 m coaxial cable to simulate the **NGO** arm (GARCÍA MARÍN ET AL., 2005) and shows the feasibility of unity gain frequencies above the inverse of the delay time ($\tau = 1.6 \mu\text{s}$) as well as the predicted amplification of the noise and the “ringing” after lock acquisition. Similar experiments, using light in optical fibres ($L = 10 \text{ km}$, $\tau = 100 \mu\text{s}$) and purely electronic delays (THORPE ET AL., 2006) yield comparable results.

Time delay interferometry

The third stage of the frequency stabilisation scheme, **TDI**, does not reduce the laser frequency noise *in situ*, but rather suppresses the effects of laser frequency noise in a post-processing stage. In contrast to standard

interferometers, where the light from the two arms is combined optically and the phase of the individual light impinging on the recombining beamsplitter is not known, in **NGO** each incoming light field is combined optically with a reference beam individually, so that the phase of the incoming light is separately measured and recorded. This allows to make use of correlations in the frequency noise and to remove the frequency noise down to the level of the measurement accuracy provided for the individual phase measurements by algebraically combining phase measurements delayed by multiples of the light travel time between the spacecraft to the so called **TDI variables**. The ability to use the individual phase measurements in post-processing does *not* depend on the actual values of the measurements. This means that **TDI** is not in any way restricted by arm-locking (or does in any way restrict arm-locking, for that matter) (SHADDOCK ET AL., 2004).

The first implementation of the algorithm was based in the frequency domain and dealt with a much simplified constellation (GIAMPIERI ET AL., 1996). Such a frequency-domain based implementation is difficult to generalise to the case of changing arm-length differences and more complex interferometric schemes. Subsequent implementations of the algorithm have therefore been based in the time-domain and include signals from all three spacecraft (ARMSTRONG ET AL., 1999; TINTO & ARMSTRONG, 1999). The simple time-domain implementation of the **TDI** algorithm (“first generation **TDI**”) using only phase measurement data delayed by the respective distances between the spacecraft cancels the frequency noise *exactly* only for fixed inter-spacecraft distances (much like the algorithm in the frequency domain) and requires an initial frequency noise of the lasers not larger than $5 \text{ Hz}/\sqrt{\text{Hz}}$ (CORNISH & HELLINGS, 2003). Further refinements of the algorithm (“second generation **TDI**”) allow to deal with changing arm-lengths as well (SHADDOCK ET AL., 2003; TINTO ET AL., 2002) by using phase measurement data that are delayed by multiples of the inter-spacecraft distances. Using **TDI** with changing arm-lengths requires in addition the ability to perform phase measurements at arbitrary times to accommodate for the fact that the travel time of the light between the spacecraft will not only be different for each arm, but also changing over time. This additional complication can be overcome by oversampling and subsequent high-precision interpolation (SHADDOCK ET AL., 2004) of the phase measurements.

A rigorous algebraic approach to the mathematics of **TDI** progressed as well from considering a purely static constellation (DHURANDHAR ET AL., 2002) to coping with changing arm-lengths (NAYAK & VINET, 2004) and a fully relativistic treatment of the optical links (DHURANDHAR, 2009). The set of **TDI** variables forms a complete set of interferometric observables, so that any interferometric combination can be retrieved by linearly combining suitable **TDI** variables (DHURANDHAR ET AL., 2002). Furthermore, suitably chosen linear combinations of **TDI** variables correspond to optimal statistical inference (ROMANO & WOAN, 2006). An in-depth review of the current state-of-the-art techniques and the mathematical understanding of the algorithm has been conducted by DHURANDHAR & TINTO (2005).

A full experimental demonstration of **TDI** poses some difficulties, mainly because of the need to provide sufficient, or at least representative, time delays between the data streams. Two main experimental routes have been explored in the past and have proceeded to demonstrate the full performance of **TDI**. One experimental approach uses electronic delays of the measured signal to emulate the optical delay. Starting with a delay of 2 s and later 16 s a reduction of the laser phase noise to within a factor of two of the requirements in the **NGO** bandwidth (see figure 5.13) has been shown (CRUZ ET AL., 2006; CRUZ ET AL., 2006; MITRYK ET AL., 2010). Another approach employs an all-optical setup, using smaller delays of order 10 ns. With this technique, DE VINE ET AL. (2010) achieved a reduction of the laser frequency noise to the **NGO** requirements (see figure 5.12).

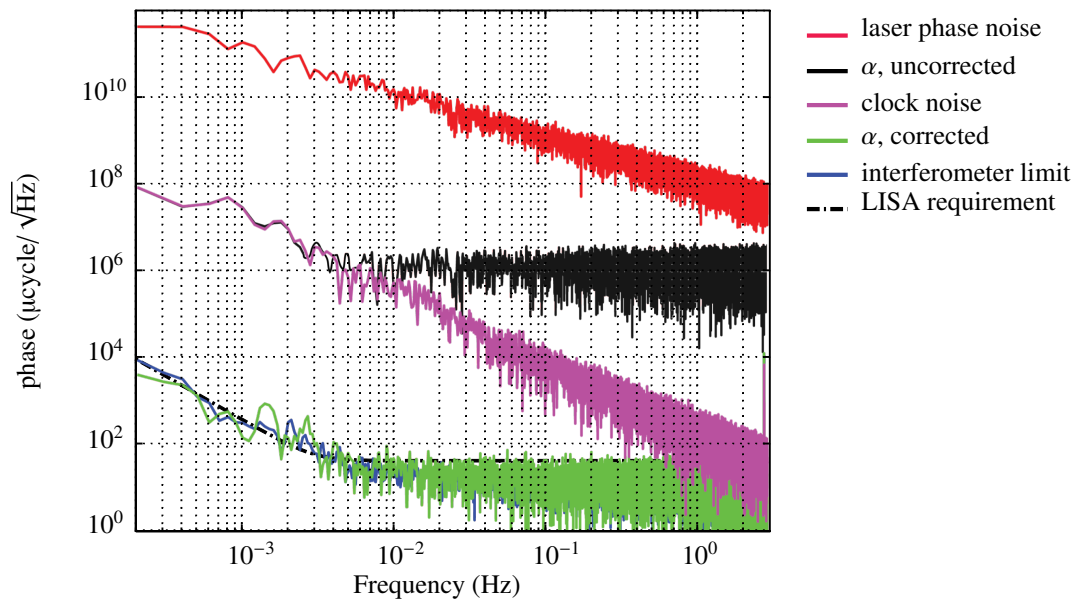


Figure 5.12.: Displacement measurements of the NGO interferometry test bed, showing injected laser phase noise (red); interpolated and clock noise corrected Sagnac TDI variable α (green), demonstrating phase noise cancellation by about 9 orders-of-magnitude, down to the interferometer noise floor (blue). Note: $1 \mu\text{cycle} \approx 1 \text{ pm}$ displacement equivalent. Adapted from DE VINE ET AL. (2010).

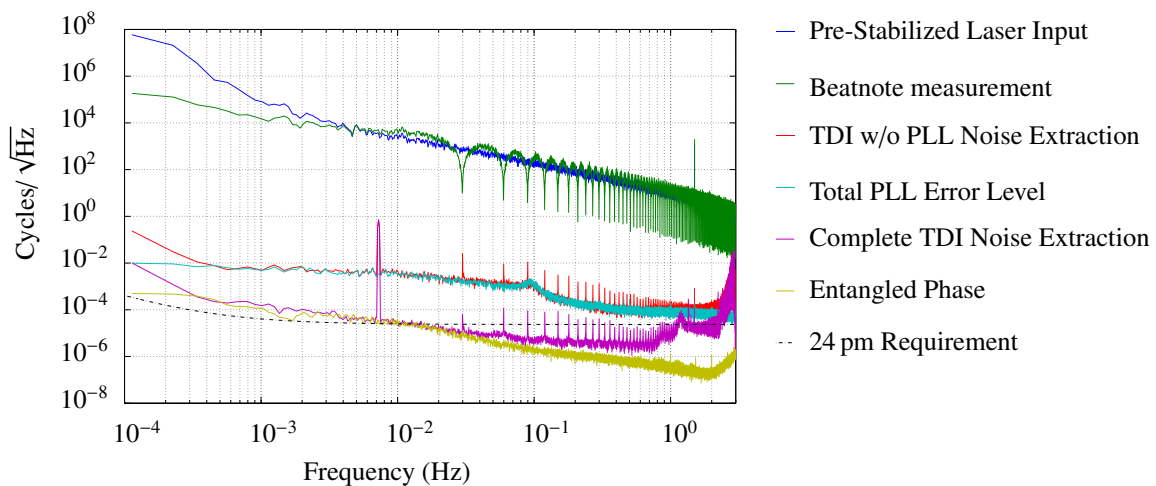


Figure 5.13.: TDI Simulation results showing the laser input noise level with the applied ranging tone (blue), the sensor signals' spectral analysis with zeros at frequencies of $nc/(2L)$ (green), the TDI noise cancellation both with (purple) and without (red) the PLL noise extraction compared with the PM noise (yellow) and PLL noise (cyan) respectively. Adapted from MITRYK ET AL. (2010).

6. Mission Design

6.1. Overview

The baseline scenario for the launch of the three **NGO** spacecraft foresees two Soyuz launch vehicles, one carrying the “Mother” spacecraft (Mother-S/C), one the two “Daughter” spacecraft (Daughter-S/C), including propulsion modules. In order to reach the final operational orbit, each science spacecraft is equipped with an additional propulsion module (P/M) which is separated when the target orbit is obtained after approximately 14 months. The P/M are designed to form the launch stack, isolating the spacecraft (S/C) from the quasi-static load at launch. Figure 6.1 depicts the launch stack configuration and illustrates the science spacecraft and the propulsion module.

The space segment consists of two distinct elements: the S/C which carries the payload, and the P/M which is responsible for delivering the S/C to the selected orbit. Following final orbit acquisition the elements are separated to ensure that no disturbances generated by the P/M will affect the payload. The P/M is closely derived from the **LISA Pathfinder** (LPF) P/M, making as much use as possible of the existing development.

6.2. Spacecraft Design

The starting point for the spacecraft design is the accommodation of the optical payload. The primary launch load path is through the P/M cone to the 800 mm diameter separation ring of the S/C. It is therefore natural to start with the payload assembly placed on a stiff structural panel above the interface to the P/M. This panel will form the primary structural reference of the S/C and enables the payload assembly to be supported and accessed for integration. The next step is to build a spacecraft structure around it which:

- Provides a vertical load path through the spacecraft (*i.e.* from top to bottom) which bypasses the payload, to enable lifting of the complete stack
- Allows to accommodate all units (payload and platform), preferably separating platform from payload to allow parallel integration and test as far as possible
- Complies with other “standard” **NGO** requirements (providing, on-station, complete 30° shading, ensure that the Inertial Sensor Test Masses are roughly placed near the spacecraft centre of mass, etc...)

On **LPF** the entire core payload assembly can be contained inside a central cylindrical support structure, enabling lifting loads to be carried by a simple cylinder through the centre of the S/C. For **NGO**, the volume and complex geometry of the payload assembly precludes the use of a central cylinder, and the primary lifting loads must therefore be transferred in a different fashion. Furthermore, the **LPF** S/C design provides too little space for

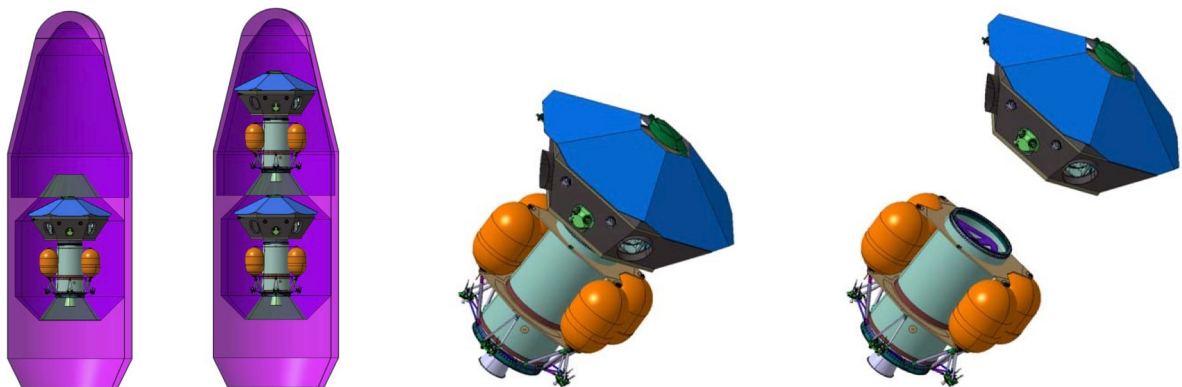


Figure 6.1.: *Mother/Daughter configuration in the Soyuz fairing (left) and S/C-P/M assembly (centre) separated (right).* (EADS Astrium)

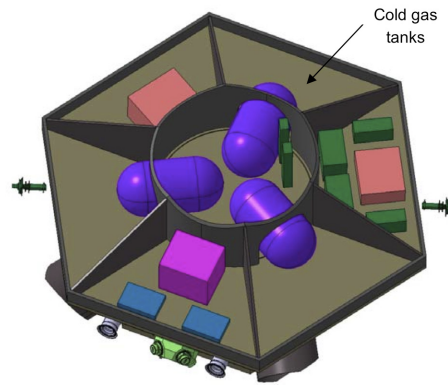


Figure 6.2.: View of the platform deck of the S/C. Shown is the “mother” S/C. (EADS Astrium)

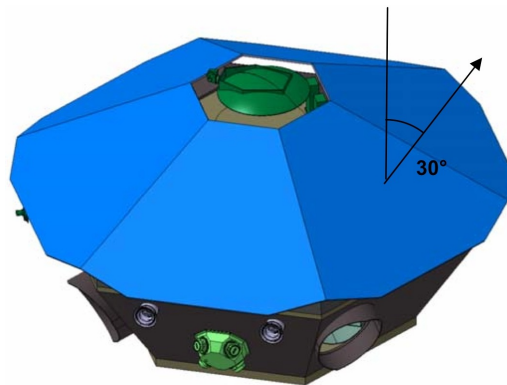


Figure 6.3.: S/C with solar array, implemented as a faceted hexagon with a canting angle of 30°

the avionics and associated associated payload electronics needed in **NGO**, so a different **S/C** design was chosen.

The approach that has been adopted has been to transfer the primary load through strut bipods attaching to the payload floor at a few discrete strong points, which connect to the bottom spacecraft panel just above the interface ring, but then spread out to an increased diameter of 1000 mm above the payload. The angle that is gained in this way allows to accommodate these load-bearing struts without violating the payload envelope. Shear panels support the sloping outer panels and the upper floor, creating a stiff overall structure similar in configuration to **LPF**. In addition, a non-planar solar panel and solar array have been chosen that will be discussed in more detail later. A side effect is that the spacecraft can effectively be subdivided into two “decks”, with one floor defining primarily the “payload deck”, and the other one primarily the “platform deck”. Currently, the payload deck accommodates also some platform units, such as star trackers, gyroscopes and elements of the micro propulsion system. A complete payload/platform separation has therefore not yet been achieved, but it is expected that eventually the platform equipment will be mounted below the platform floor to provide near complete separation. This allows the payload to be “dropped in” as a unit, without interfering with other units or structural elements, which simplifies assembly, integration, and testing (AIT) greatly. Effectively, the payload deck can be closed off once the payload has been integrated.

From a structural point of view, the payload deck is identical for both considered micropropulsion systems, Radio-frequency Ion Thruster (RIT) and Cold Gas; all that changes is some of the equipment. The sloped sides of the payload deck provide the main radiator area of the spacecraft. Even with some blockage due to the micropropulsion thrusters, the available radiator area exceeds 4 m^2 , easily sufficient for a total dissipation from payload and platform of less than 700 W (including 20 % system margin, but excluding the directed radiation from the traveling-wave tube amplifier (TWTA)). The top deck, or platform deck, differs between between the two micropropulsion systems, since the cold gas tanks represent a very substantial mass and volume that need to be accommodated. Figure 6.2 depicts the cold gas version, which requires the larger volume.

Table 6.1.: Summary of the micro-Newton thruster requirements.

	Requirement
Maximum thrust	100 μN
Thrust resolution	0.3 μN
Thrust noise	$0.1 \mu\text{N}/\sqrt{\text{Hz}} \times \sqrt{1 + \left(\frac{10\text{mHz}}{f}\right)^4}$
Lifetime	> 5 yr
Total impulse	7800 Ns per year

It should be noted that there many possible tank combinations, other than the three tank configuration shown in figure 6.2. A total of 35 kg of cold gas need to be accommodated with a typical storage pressure of 310 bar, setting the basic volume requirements. Although smaller, more numerous tanks offer larger accommodation flexibility, it also carries a penalty in terms of tank mass, and in terms of complexity and additional hardware, such as connecting pipes, valves, etc. The approach here has therefore been use as few tanks as possible. The smallest number for which a solution based on commercially available tanks could be physically accommodated is three. The structural impact of selecting the RIT as a micro-propulsion system would be a reduction in height by approximately 50 mm with no further structural impact.

One question that also needs to be addressed is the change in self-gravity that results as 35 kg of cold gas are being depleted over the mission life time. For the chosen configuration, the dominant effect is in the vertical direction (z -direction). A quick estimate reveals that the self-gravity will change by approximately $4 \times 10^{-9} \text{ ms}^{-2}$ in z during the mission. This level can be tolerated, as it provides a common acceleration on the two test mass (TM), and does not exceed any electrostatic actuation authority.

The S/C is completed by closure panels closing off the platform deck, which can be used as access panels as long as the solar array panel is not installed. The solar array is constructed as 6 separate flat panels, thermally isolated by multilayer insulation above the closure panels and mounted on thermally isolating blade stand-offs, in order to provide thermal insulation to the spacecraft, a concept taken from LPF. The solar array and the structural panel it is mounted on, form a faceted hexagon, with an canting angle of 30° (see figure 6.3).

This approach has allowed increasing the available volume inside the spacecraft, while at the same time still fitting inside the Soyuz fairing. As can be seen, the solar array corners have been trimmed for this purpose as well; neither the shading nor the power generation capacity are affected by this. This approach has several potential consequences that need to be considered:

- Since the formation plane is inclined at 60° to the ecliptic and the formation rotates once per year, each facet will have a time varying different angle of incidence of solar radiation, so that there will be a slow annual modulation of the temperature of each panel. This needs to be taken into account in the thermal and power system design.
- The different temperature and also angle of incidence will result in different efficiencies for each panel; the power subsystem design takes this into account
- The solar radiation will exert a net lateral radiation force and torque which is larger than if a flat panel is used, but a lower axial force than if a flat panel of the same total power output. The drag-free attitude control system (DFACS) and micropropulsion budgets must account for this
- The pyramidal configuration means that solar array output is relatively insensitive to solar aspect angle in the range $\pm 40^\circ$ from the z axis, and some power is available even with the sun at 90° from the z axis, increasing the range of sun angles that can be tolerated in safe modes.

6.3. Micropropulsion design

NGO will make full use of the micropropulsion developments for LPF and the guiding principle for the mission design has therefore been to maintain compatibility with all three of the technologies currently under development for LPF, cold gas, field-emission electric propulsion (FEED), and RIT.

Table 6.2.: *NGO cold gas budget for 4 years operation*

Component	Comment	Impulse budget Ns	Number of thrusters	average thrust μN	I_{sp} s	Mass kg	Mass (+ mar.) kg
Initial nutation damping and despin	Scaled from original LISA	110	11	58	50	0.2	0.2
Separation correction manoeuvre	allocation 0.2 m/s	306	11	161	50	0.6	0.9
Laser beam acquisition	negligible						
Antenna rotations	35 Ns allocation	35	11	45	50	0.1	0.1
Safe mode	included in DFACS						
Commissioning	included in DFACS						
DFACS science operations	DFACS simulations, 4 years ops, 2 μN minimum thrust, one thruster failed	10 300	5	16	46	22.8	34.2
Total		10 751				23.7	35.6

6.3.1. FEFP thrusters

In the original LISA mission formulation study, the long mission and the limited throughput capability of any one thruster prompted the adoption of a cold redundant thruster arrangement in which 3 clusters of 4 thrusters were operational until a single failure, after which operation would shift to a redundant set of 3 clusters. Since that time, studies on LPF have demonstrated that cant angle optimisation, and the use of quasi-symmetric 8 thruster configurations after a failure, can substantially reduce the required impulse, enabling a three cluster arrangement to be retained, although this is ultimately dependent on the successful demonstration of required individual lifetime.

6.3.2. Cold gas thrusters

A cold gas micropropulsion system has been developed and qualified for GAIA, and has recently completed a preliminary design review for potential application to LPF. Although the noise performance is about two times higher than the FEFP specification, studies for both LPF and NGO have shown that overall performance requirements can be met using such a thruster. The primary impact is on the accommodation and mass of the necessary gas and gas storage. The LPF architecture can be applied directly to NGO, using the following configuration, based entirely on qualified components. Only the tank size and possibly thruster cant angle need to be adapted specifically for NGO.

The most critical issue for micropropulsion budgets is the impulse budget for cold gas. Extensive work on LPF as part of the preparation for a preliminary design review of a cold gas system has produced the tools necessary to analyse the required impulse and cant angle optimisation.

On LPF, the impact of test mass DC forces is a significant contributor to the impulse budget. Therefore, the impact of test mass DC forces for NGO has been reviewed. The total mass of the spacecraft including payload is 721 kg. The required maximum residual DC acceleration on a proof mass is $8 \times 10^{-10} \text{ m/s}^2$ for NGO (including contingency and dominated by self gravity. By comparison, the specification for LPF is 10^{-9} m/s^2 axis, and this gives rise to the sensitivity). For NGO, this yields a resulting force that needs to be compensated by the S/C of $0.6 \mu\text{N}$. Even if a factor of two margin is considered, this is well below the accuracy of the solar force and torque model (amounts to approx. 2.5 % of the DC force due to the solar pressure). Therefore, the effect of proof mass DC forces can be neglected for the calculation of the total impulse on NGO. Note that the DC forces acting on the proof mass are compensated by the existing suspension control loops in wide range during accelerometer mode. A summary of the cold gas budget is given in table 6.2.

6.3.3. Radiofrequency ion thrusters

A mini-RIT configuration is being studied for LPF. Development is likely to be complete in time for the NGO mission, and this therefore can be considered as a potentially credible candidate. The mini-RIT system uses a cut down version of the gas supply system for the cold gas (tank size is substantially reduced, since the mini-RIT is based on constant flow at 4 microgram/second level for each thruster and the pressurant is Xenon). For the mini-RIT, the key parameter is power consumption, which is strongly dependent on number of thrusters operating, and then proportional to total thrust. It was found in studies for LPF that using a quasi symmetric 8-operating configuration enabled the power requirement to be lower than the equivalent FEPP system. Although noise is expected to be similar to FEPP, the minimum thrust level due to the constant flow is of order 10 μN , but since total pressurant mass is small, the impact of this on pressurant budget and overall mass is not large.

The primary issue for RIT is the high minimum thrust. This results in the minimum total thrust of the anti-sun thrusters exceeding the solar radiation pressure, requiring the sun facing thrusters to be used. The RIT model for thrust versus power consumption at constant flow rate is approximately of the form $P = n \times 15 \text{ W} + (F/\mu\text{N}) \times 0.07 \text{ W}$ where n is the number of thrusters operating and F is the total required thrust. Minimising total power is then driven by minimising the number of thrusters operating and the total thrust over all thrusters. For mini-RIT, there is a strong incentive to use 8 thrusters at all times. In addition, the cant angle needs to be optimised for the high minimum thrust. A number of cant angles were assessed by ESA in the original LPF RIT study. Results for the proposed cant angle were found in the New Gravitational wave Observatory (NGO) study to be similar to those obtained with in the LPF case.

The baseline design for NGO accommodates the power requirements of the RIT.

6.4. Propulsion module design

At launch, the NGO launch composite (LCM) consists of two elements, the spacecraft (S/C) and the propulsion module (P/M). The S/C is mounted on top of the P/M and secured by a low shock separation system, which allows the S/C to be released once the operational orbit around has been reached. The principal role of the P/M is to provide the propulsive Δv and attitude control following launcher separation to transfer the S/C to an initial escape orbit, and then through a series of deep space manoeuvres to acquire its operational orbit, in response to commands from the attitude and orbit control system (AOCS) on the S/C.

For the NGO mission, maximum advantage is taken of the development of a propulsion module for LPF, based on proven Eurostar communications satellite technology, and specifically qualified for the needs of a science mission in which practically all propellant is used for main engine manoeuvres. The only change from the LPF P/M proposed for NGO is the adaptation of the propellant capacity to the needs of the NGO mission. The LPF P/M has a propellant capacity of 1285 kg, carried in four 288 l tanks, capable of providing more than 3200 m/s Δv to a 500 kg S/C. For the NGO mission, the requirement is to provide about 1800 m/s Δv to a 700 kg (including margin) S/C, and the required propellant load is no more than 700 kg. The tank propellant management system places a limitation that the fill capacity must exceed 80 % to ensure that ullage gas does not reach under the membrane. The tanks used for LPF are much too large, and it is necessary to use another in the family of Eurostar tanks, with a smaller capacity but same diameter in order to comply with this requirement. An existing 175 l tank would meet this requirement, and accommodating it is readily accomplished by shortening the P/M structure and tanks by 330 mm, leaving all the propulsion system components and the separation system components, and all subsystem operations untouched. The spherical EADS 51 l pressurant tank replaces the stretched 90 l tank of LPF, with identical interfaces. The shortened cone is stiffer than the LPF unit one and will require an adapted upper machined ring to match the separation system of 800 mm diameter. An overview of the external configuration of the LPF P/M, minus thermal blanketing, is shown in figure 6.4. The NGO P/M would be identical in appearance, apart from the shortened cylindrical sections of the propellant tanks.

The main features of the system architecture are:

- A simple, conical central tube to support the S/C and provide the primary load path for the propulsion equipment
- Tank support structure assemblies for the five boss-mounted tanks: four externally mounted propellant tanks and a single pressurant tank

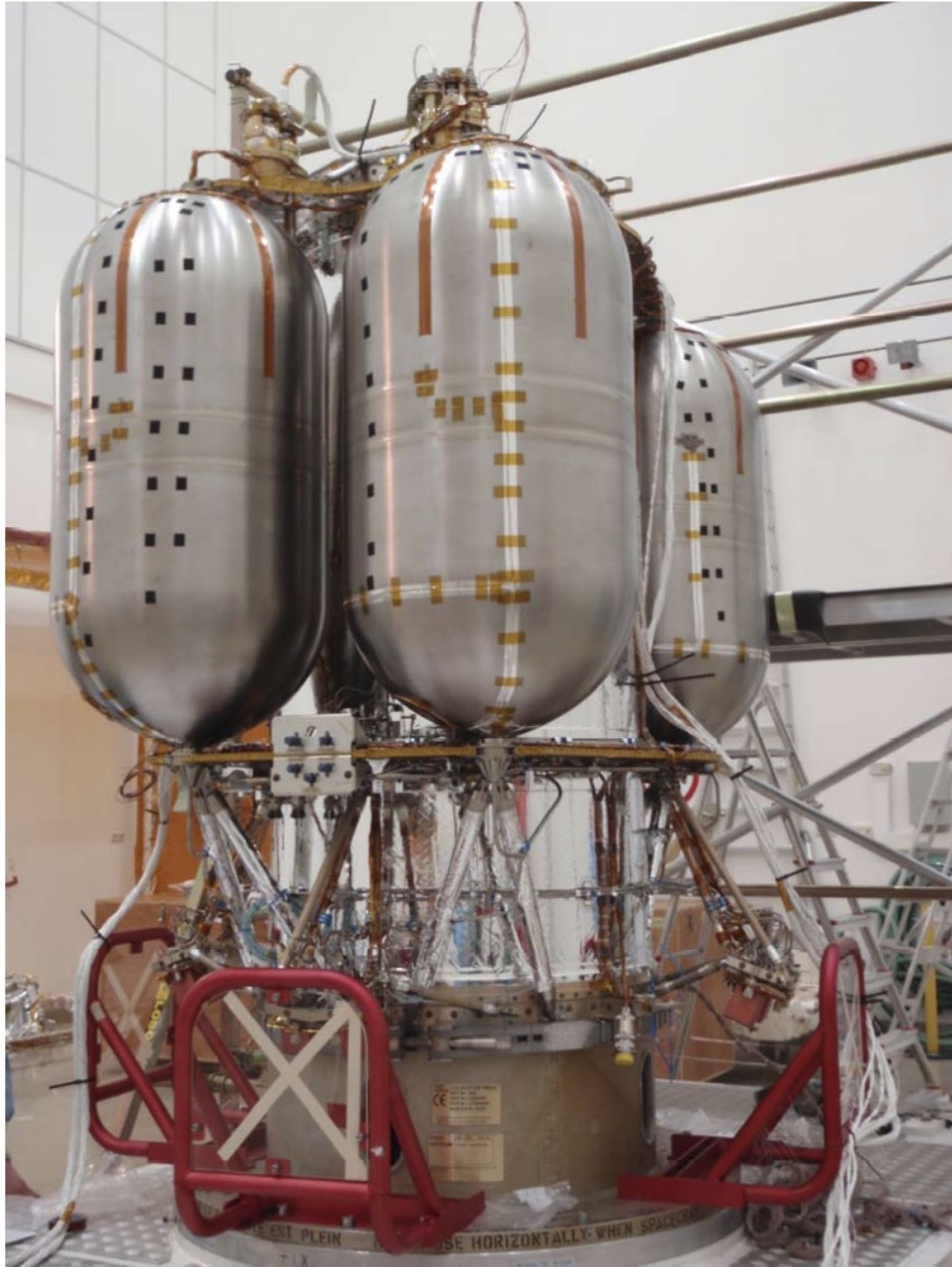


Figure 6.4.: LPF propulsion module with thermal blanket removed. The propulsion module for NGO will be 330 mm shorter due to the required smaller tanks.

- Four 175 l propellant tanks with a maximum capacity storing a total of approximately 780 kg of nitrogen tetroxide and monomethyl hydrazine propellants
- A single 51 l, 310 bar maximum expected operating pressure (MEOP) pressurant tank
- A single high performance, 450 N, 323 s maximum specific impulse main engine for Δv manoeuvres
- Four pairs of 10 N bipropellant thrusters for attitude control
- Propulsion manifold equipment supported from the lower tank platform to avoid the need for extra mounting structure
- No external structural panels (to minimize the mass and complexity)
- Conventional thermal control of the propulsion subsystem; essentially isolated and controlled via distributed heaters and thermistors
- Thermal blanketing of the P/M tanks and other elements.

The thermal control subsystem uses passive means to control the upper temperatures of sensitive equipments,

with electrical heaters to control the lower temperatures. However, because there are very few dissipating components on the P/M (2.5 W total during non-firing periods) the P/M has been designed to absolutely minimise its heat loss. The outer multi layer insulation (MLI) surfaces reject heat directly to space, and performance is selected to minimise the heat loss and hence heater power consumption. The minimum necessary heater power is applied in the cold cases so that the lower temperatures of the components of the chemical propulsion system are maintained towards the bottom of their allowable range allowing for control uncertainty.

The P/M components are primarily mounted on the lower floor of the P/M, utilising both the upper and lower surfaces of the floor. The floor is then heated to maintain the required temperatures of the chemical propulsion system equipment and an enclosure is created to retain heat from the lower surface of the floor. The main engine heat shield has been optimised to maximise the heat rejection during main engine firing to maintain the engine temperature within limits. Internal surfaces are highly reflective to additionally increase radiative couplings and heat loss from the engine valves during main engine firing.

P/M thermal control is provided by two circuits which maintain the temperature of the propulsion elements throughout the Launch and Early Operations Phase (LEOP) and transfer phases of the mission. With redundancy, two heater circuits for thermal control translate to four circuits for the power subsystem.

To ensure that propellant mass transfer between like tanks is minimised, the tank heater circuits have been arranged so that the tanks can not be heated out of phase of each other. Electrical heaters are also used on the lower floor, pressurant tanks, main engine valves, flange and pipes, propellant tank upper pipes, fill and drain valve, umbilical brackets, and thrusters to maintain all equipment temperature limits are met. The control of the heater circuits is by thermostats in series, and thermistors are only provided for temperature monitoring.

Heater powers are sized to maintain all equipment above their minimum temperature limit plus modelling uncertainty. The actual heater switch-on temperatures are set to 5 °C above the lower allowable temperature limit, and the over sizing ensures that the heater is powerful enough to cycle in the coldest flight conditions. Redundant heaters are used in the case of a prime heater circuit failure only.

6.4.1. S/C-P/M Separation System

The separation system interfaces the S/C and the P/M Propulsion Module. and it separates and jettisons the P/M upon command from the S/C. The LPF separation system is fully qualified for launch on VEGA and Eurockot, which have more severe acceleration environments than Soyuz. The more benign environment can be traded against the higher mass of the NGO S/C. The separation system is a system designed for low shock at release. This is achieved with a device called clamp band opening device (CBOD). This device releases the clamp band pre-load in a controlled way, transforming the main part of the elastic strain energy in the band and rings into rotational energy in the CBOD flywheel. The CBOD is qualified and has flown several times.

6.4.2. Propulsion Subsystem

The P/M chemical propulsion system is a helium pressurised bipropellant system using monomethyl hydrazine (MMH) as the fuel and mixed oxides of nitrogen with 3 % nitric oxide (MON-3) as the oxidant. A common propellant storage and feed system supplies the main engine and the eight reaction control thrusters. The design builds on the heritage gain through the Eurostar programs of which there are more than 30 platforms in flight with all propulsion systems performing satisfactorily. The system is designed to operate in a constant pressure mode during the main engine firings using a regulated helium supply. Following completion of the orbital injection manoeuvres, the system will remain in a regulated helium supply mode. The pressurant subsystem comprises a single helium tank, a series of normally closed pyrovalves, a pressure regulator, four non-return valves, three fill and vent valves, four test ports and a high pressure transducer. The single pressurant tank is fitted inside the central structural cylinder and provides sufficient helium storage capacity to meet the P/M pressurant requirements. The other pressurisation subsystem components are all located on the +z surface of the lower tank floor. Four propellant tanks, specifically sized to meet the total propellant load requirement for the mission, are fitted in the P/M configuration as with one propellant tank per quadrant. All propulsion components are located on the lower tank floors. The components downstream of the propellant tanks (*i.e.* latch valves, filters, orifices, pressure transducers, fill and drain valves, and pyrovalves) are located between the stub tube and the thrusters on

Table 6.3.: Required Δv for the Mother-S/C and the Daughter-S/C spacecraft, including allocations for loss and margins. The Mother-S/C requires less Δv than the Daughter-S/C due to the different transfer orbits (20 000 km apogee for the Daughter-S/C, GTO for the Mother-S/C)

Manoeuvre	Daughter 1	Daughter 2	Mother
GTO to escape	1274	1274	851
Deep Space manoeuvres	439	402	479
Perigee control	11	11	53
Dispersion control	32	32	32
Transfer navigation	32	32	32
Total	1786	1750	1445

the $-z$ face of the lower tank floor ($+y/ - y$ sides). The pressurant components are located on the $+Z$ face of the lower tank floor ($+x/ - x$ sides).

6.5. Mission Analysis

6.5.1. Overview

The different operational phases of the NGO mission are

- Launch and Early Operations Phase (LEOP)
- Cruise Phase
- Commissioning Phase
- Acquisition Phase
- Constellation Commissioning Phase
- Operational Phase
- Decommissioning Phase.

The NGO launch composite (LCM) will be launched on two separate Soyuz launch into an transfer orbit with an apogee of 20 000 km (for the daughters) and geostationary transfer orbit (GTO) (mother), respectively. Transfer first into an escape orbit and then to the final science orbits takes about 14 months for both, mother and daughters. During this time, a chemical propulsion system will provide manoeuvrability to the LCM.

6.5.2. Launch and Early Operations Phase

The LEOP operations consist of those essential activities that are necessary to configure the spacecraft for cruise after separation from the launcher (where this cannot be done prior to launch) and to monitor the health of the composite spacecraft systems. Following separation, each launch composite will acquire a basic sun-pointing attitude using its sun sensors. The final configuration actions for the LEOP phase are to switch on the star trackers, upload the inertial pointing guidance and command the AOCS to an inertial pointing mode.

During the LEOP phase, communication between the ground segment and the S/C uses conventional omnidirectional antennas to provide coverage for any spacecraft attitude. This will be provided by two low-gain antennas (LGAs) which are mounted on the outer shroud of the propulsion module, and optimised to give a maximum field of view.

6.5.3. Transfer

During the 14 month transfer phase, starting from launcher separation, the spacecraft/propulsion-module (S/C-P/M) composites are travelling toward the target orbits, using a chemical propulsion system for manoeuvring. During the transfer an out-of-plane manoeuvre is needed in order to set up the required inclination.

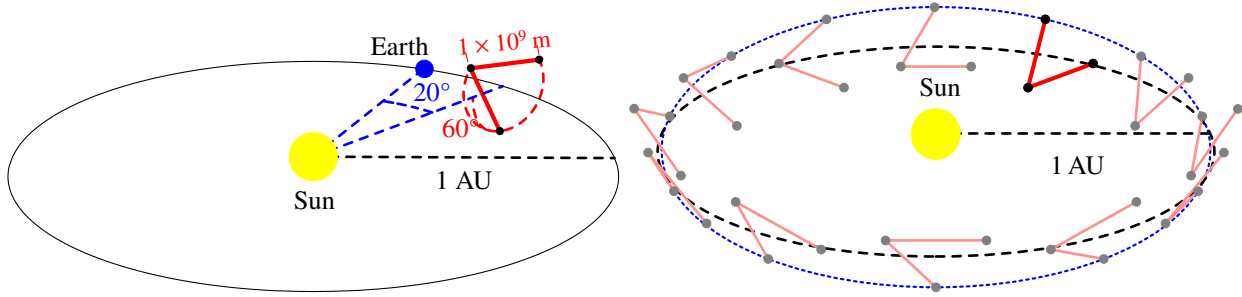


Figure 6.5.: *NGO Science Orbit*. The three spacecraft form an equilateral triangle with 1×10^6 km armlength, inclined by 60° with respect to the ecliptic. The constellation trails the Earth by about 20° and orbits the Sun in a distance of about 1 AU. The exact constellation parameters are optimised so that a mission duration of up to 5 years is feasible without exceeding the requirements on relative velocities and Doppler shift.

Table 6.4.: *Main parameters and constraints of the constellation for a typical science orbits.*

Parameter	nominal value	actual value/deviation	
Arm length	10^6 km	$\delta L_{\max} = 18.31 \times 10^3$ km	$\delta L_{\max} = -30.66 \times 10^3$ km
Relative velocities	0 m/s	$\delta v_{\max} = 7.06$ m/s	
Trailing angle	10°	$\Phi_{\max} = 19.81^\circ$	$\Phi_{\min} = 9.34^\circ$
Inner angle	60°	$\alpha_{\max} = 61.59^\circ$	$\alpha_{\min} = 58.44^\circ$

6.5.4. Science orbit

Orbit selection for the **NGO** mission is influenced by a number of drivers: the requirement for a benign environment for the payload; non-gravitational perturbations should be minimised to allow accurate micro-propulsion control; the thermal character of the orbit should be stable to avoid widely varying or sudden thermal shocks; the orbit must allow a quasi-static equilateral triangular constellation with arm lengths of 1×10^6 km to be maintained without active maintenance; distance from the Earth must be accounted for by the communications subsystem design and the requirement is to not exceed absolute distances between any **S/C** and Earth of 75×10^6 km.

The baseline **NGO** orbits for the three **NGO S/C** are Heliocentric Earth Trailing Orbits (HETOs), providing a good compromise between the orbit drivers. In their **HETO** constellation, the three **S/C** form a constellation with a plane of rotation that is inclined by 60° to the ecliptic (see figure 6.5). Nominally, that would lead to orbits with identical eccentricity $e = 0.001930$ and inclination of $i = 0.191500^\circ$. However, the influence of mainly the Earth, and to a much lesser degree of the Moon and the large planets results in slightly perturbed orbital parameters (see table 6.5).

The optimisation process has taken into account the requirements for range and range rate. It has also aimed to minimise the maximum angular excursion from the basic equilateral triangle solution. The target is a peak to peak value of no more than 3° (*i.e.* $\pm 1.5^\circ$) for the vertex of the **Mother-S/C**.

Table 6.5.: *Initial orbital elements of the spacecraft for a typical science orbit*

	S/C 1	S/C 2	S/C 3	nominal
a (AU)	1.000 300	1.000 338	1.000 338	1.0000
e	0.013 687	0.012 148	0.010 378	0.001 930
i (degree)	0.170 053	0.224 875	0.184 510	0.191 500
Ω (degree)	57.085 376	170.167 241	-81.932 021	—
ω (degree)	286.316 625	186.415 367	64.078 461	270
M (degree)	7.196 537	-5.970 331	8.462 198	—

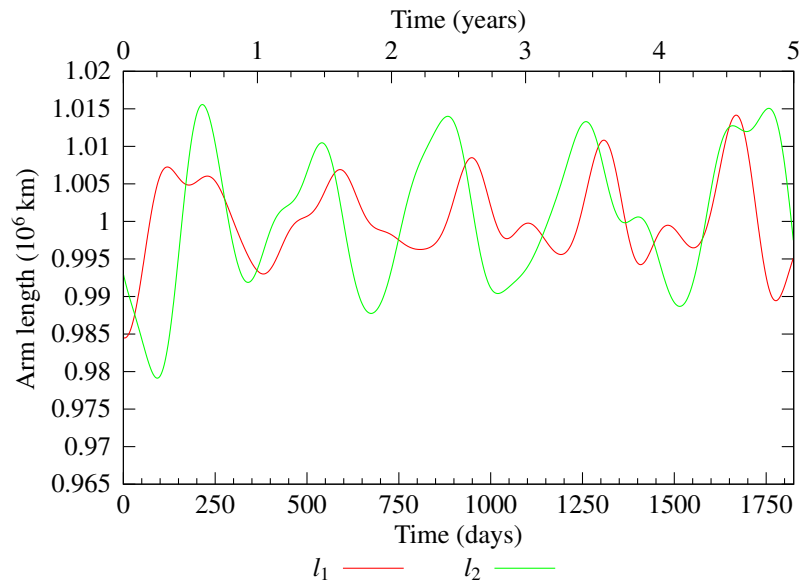


Figure 6.6.: Variation in inter-S/C distance for a 5-year mission duration. Notional armlength is 1×10^6 km, variations are withing $\pm 10^5$ km, or 2%. Earth offset is between 9° and 20° .

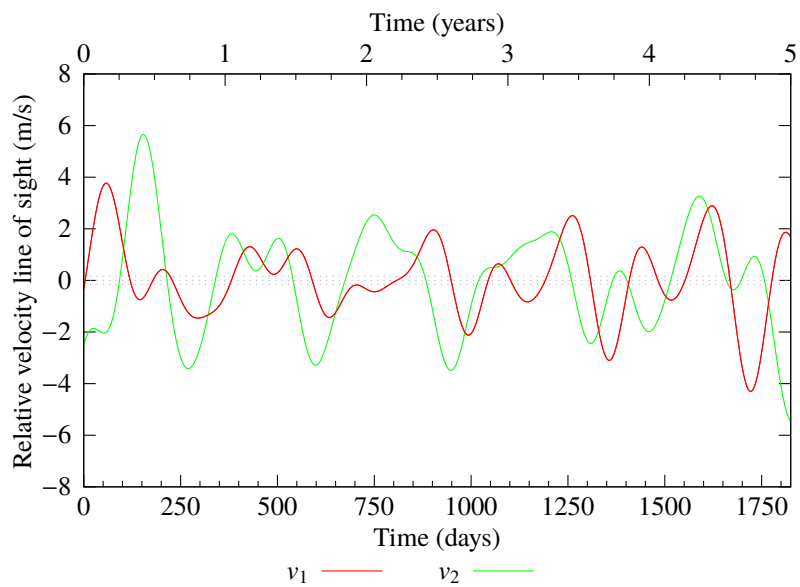


Figure 6.7.: Variation in the velocity in line-of-sight between the satellites for a 5-year mission. This variation determines the Doppler shift between received and emitted beam. For the wavelength chosen for *NGO*, 1 m/s corresponds to 1 MHz Doppler shift. The dashed line indicate the “natural” oscillation without gravitational disturbances from Earth, Moon and the planets.

Table 6.6.: Mass and power budget for the baseline architecture. Note that there are two Daughter-S/C on a launcher.

	Mother		Daughters	
	Mass (kg)	Power (W)	Mass (kg)	Power (W)
Total per launcher	1703	638	3585	1096
Adaptor	45	–	430	–
Wet mass per composite	1685	–	1577	–
Propellant	619	–	691	–
Composite (dry)	835	638	707	548
S/C	624	638	694	548
Bus	342	356	342	356
Payload	282	282	154	192
P/M (dry)	211	–	211	–

6.6. Mission budgets

6.6.1. Mass and power budget

The total available launch mass is limited by the capabilities of the foreseen launcher, Soyuz, whose relevant payload mass capability (including launch vehicle adaptor) for the assumed transfer orbit (apogee 20 000 km) is 3650 kg. The wet mass of the baseline launch composite including all margins is 1703 kg (**Mother-S/C**) and 3585 kg (**Daughter-S/C**), showing the feasibility of the launcher baseline. The mass budget includes a 20 % margin and is, wherever possible, derived from as-built hardware from, e.g., **LPF**. The mass budget for the micro-propulsion system has been based on the worst case estimate, which is give by the cold gas system. Thus, the mass budget is compatible with both alternatives, cold gas and **RIT** micro-propulsion.

The available power is limited by the total area and the efficiency of the solar array. The baseline design with the faceted hexagon has a minimum power output of 864 W, whereas the maximum power requirement of the **S/C** is 638 W (**Mother-S/C**) and 548 W (**Daughter-S/C**), including all margins. The power budget has been compiled based on consumption numbers from similar projects including **LPF**. A system margin of 20 % has been applied on all power estimates except those of the thermal subsystem (effectively heaters); as the consumption of other units increases, the required heater power is expected to decrease, and hence adding a margin to both entries would be overly conservative. The power consumption of the micro-propulsion has been taken from the worst case, which is given in this case by the **RIT** system. Thus, the power budget is compatible with both alternatives, cold gas and **RIT** micropropulsion. Harness losses are included and internal switching distribution of the power subsystem equipments is also incorporated into the budget calculation. Mission (*i.e.* launch date, orbit altitude, etc.), seasonal and ageing criteria impact on the power required and have been taken into account when producing the overall system budget. A more detailed power and mass budget is given in table 6.6.

Battery

The battery acts as storage reservoir of electrical energy to provide power for the **NGO** spacecraft when solar array power is not available. The **NGO** battery requirements can be met with the existing **LPF** battery, which contains of a total of 22 strings, each consisting of 7 cells in series. The size of the battery is driven by the energy requirements during the early part of the **LEOP**, whereas the solar array size is determined by the operational power requirements of about 650 W.

6.6.2. RF link budgets

The communication between the spacecraft and ground station during the operational phase uses high-gain antenna (HGA) (+25 dB gain) on the spacecraft and the 35 m antenna in Cebreros with a backup in New Norcia

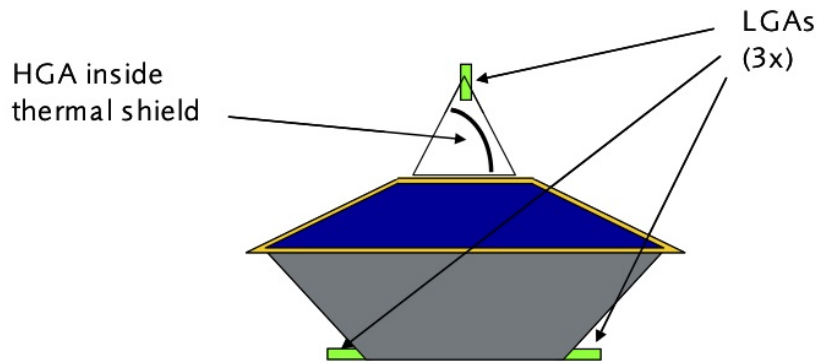


Figure 6.8.: *Antenna concept. One high-gain antenna in a thermal shield is used for communications in the nominal case. In an emergency, three low-gain antennas are used to communicate with the S/C.*

for up- and downlink in the nominal scenario. In the case of an emergency, communication is conducted via three omnidirectional LGA (-2 dB antenna gain) on the spacecraft. The maximum distance between spacecraft and the ground station is assumed to be 65×10^6 km, the data rate is 200 kbps, compared to the data generation rate of about 17 kbps. This allows for contact time of about 8 h in every 48 h.

The **Mother-S/C** has approximately twice the data generation rate of each **Daughter-S/C** (the platform house-keeping parts will be identical, but the payload parts almost double). This difference can be exploited as follows (many other schemes are possible):

- **Mother-S/C**: 4 h window on any given day,
- **Daughter-S/C**: 2×2 h windows on the same day

Alternatively, an 8 hour window for the **Mother-S/C** on any given day, followed by 2×4 h windows for the **Daughter-S/C** two days later gives the same effective capacity. In this way the downlink data rates and thus TT&C power requirements on the **Mother-S/C** and the **Daughter-S/C** will be virtually identical.

The data latency will be between two days (first scheme) and four days (second scheme). If all spacecraft communicate every two days, then HGA re-pointing would also take place nominally once every two days. However the antenna beamwidth is sufficient to support a strategy of pointing ahead by four days. Even longer quiet periods will also be possible at the expense of data rate and data latency.

7. Mission Operations

7.1. Introduction

Science operation for **NGO** will be conducted Science Operation Centre (SOC) under the responsibility of **ESAC**. The scientific analysis of the data and the production of the higher level data products is the task of the data centre, for which an Announcement of Opportunity (AO) for nationally funded development, implementation, and operation is proposed.

7.2. Science Products

The consolidation of the science products is under the responsibility of the **SOC** and the guiding principle for publication of the data products is to enable the scientific community to re-do any analysis of the data, starting from the Level 0 products to Level 2 products (and, if applicable, to Level 3 data). It is therefore required to not limit the publication to the data, but to also make available the algorithms, the software, and the models used for processing the data as well as ensuring that the data processing history for any data published is traceable and retrievable. All data products will be public, the associated software under an open source license. A proprietary period of 6 month (TBD) is foreseen to ensure the quality and consistency of the data. The data centres will make the data available in regular intervals, *e.g.* 3 months (to be defined).

Raw data streams (Level 0) Level 0 data are the raw data streams necessary to obtain the basic time-delay interferometry (TDI) data streams and the relevant data streams of the gravitational reference sensor (GRS), the interferometric measurement system (IMS) and the science housekeeping. The Level 0 data contain all the data from each of the phase-meter channels, all the data from the **GRS**, and the complete science and payload housekeeping data. This includes, *e.g.*, the phasemeter outputs of the **Daughter-S/C** and **Mother-S/C**, ranging and clock noise information, the state of the **DFACS** on all spacecraft, and the attitude of the spacecraft with respect to the received laser light.

Processed data streams (Level 1) Level 1 data are the fully processed data streams that are needed to isolate individual gravitational wave signals using parametrised source models or other data analysis techniques. The Level 1 data consist of fully calibrated and corrected **TDI** data streams, augmented by the spacecraft ephemerides. In addition, Level 1 data contain the software and the models used to produce Level 1 data from Level 0 data, in particular the full dynamical model of the **GRS**, the relevant time shifts for the construction of the **TDI** data streams, and any other relevant information on changes on the effective optical pathlength.

Processed data streams (Level 2) Level 2 data are the result of source identification and parameter extraction. Level 2 data consist of the model parameters and their posterior probability density function (PDF) (where applicable) of identified gravitational wave sources or other identifiable events. They include the reconstructed waveforms and detector signals for identified sources as well as regular updates on the critical parameters of transient sources, such as coalescence time and sky location.

In addition, Level 2 data contain the software and the models used to produce Level 2 data from Level 1 data, in particular the waveform models, and search algorithms.

Source catalogue (Level 3) Level 3 data are the result of a scientific evaluation of the lower level data products. Level 3 data consist of a catalogue of sources, their physical and astrophysical parameters and their strain time series $h(t)$. Level 3 data also include the “residual” data stream, *i.e.* the Level 1 data stream with the contribution of identified sources removed. Level 3 data may be regularly updated during the mission lifetime and ensuing operational and archival periods.

In addition, Level 3 data contain the software and the models used to produce Level 3 data from Level 2 data.

Table 7.1.: *NGO Operations Characteristics*

Metric	Comment
Number of spacecraft	3
Ground station pass frequency	every 48 h
On-board data storage per spacecraft	5 GB
Recorded data per day (3 spacecraft)	§1470Mbit (17 kbps for 24 h)
Total mission data for 3 spacecraft	135 GB
Down-link schedule	8 h at 200 kbps every 48 h
Frequency of required commanding	Once every six days

Additional products Although not the main scientific product of the **NGO** mission, the measured performance and the physics model of the inertial sensor are of potential use for future space missions. Therefore, the respective data will be made available in a form yet to be determined.

7.3. Mission Phases

The operational phase of the **NGO** mission can be broken up into the following phases

Launch and early operations phase This phase covers the first 30 days after each of the two foreseen launches.

The activities include all the launch-related activities leading to the separation of the three spacecraft on their trajectories.

Cruise phase This phase covers the 14-month period during which the three spacecraft move away from the Earth to their respective operational orbits. The major cruise activities are the spacecraft manoeuvres that are required to change the spacecraft trajectory.

Commissioning phase This phase covers the three-month period to achieve the science mode configuration required for science operations. Key activities include acquisition, drag-free testing, and instrument calibration.

Calibration phase This phase covers a three-month period during which the characteristics of the instrument will be established. The activities performed in this phase can be fully or partly repeated during the science operations phase as needed.

Science operations phase This phase covers the nominal two-year period during which science data are collected. Activities for this phase include the generation of science data products, health monitoring of the spacecraft and instrument, and the planning and execution of downlinks every other day with one spacecraft.

Post-operational phase This phase covers the period after the Science Operations Phase comes to an end. During this phase, the main activities are in the data centres and the data archive. The duration of this phase is at least two years.

Archive phase During the Archive phase support will be provided to the scientific community for the usage of the **NGO** data products. It is foreseen that the **NGO** archive will continue to be operated beyond the end of the Archive phase.

7.3.1. Launch and Early Operations Phase

The three spacecraft (S/C)-propulsion module (P/M) composites will be launched by two Soyuz launchers from Kourou into an geostationary transfer orbit (GTO) from which the composites will transfer into an escape orbit.

7.3.2. Cruise Phase

During the cruise phase the following activities take place.

Spacecraft health monitoring During the majority of the cruise phase the spacecraft are in a sun-pointing attitude with minimal active operations. Engineering telemetry is collected during this time and formulated into packets for storage and transmission to the ground at the next communication window. The spacecraft

health monitoring telemetry will include spacecraft attitude, propulsion module thruster usage, solar array output, and temperature monitoring. It is unlikely that much payload commissioning can be performed during the cruise phase. However there is plenty of time if useful functional checks can be done that are compatible with the cruise configuration.

Manoeuvre design and execution The major cruise activities for the spacecraft are the planning and execution of eight manoeuvres per spacecraft over a 14-month time period. Each of the spacecraft will require three large deterministic transfer manoeuvres (DTMs) to transfer from launch to its respective operations orbit that establishes the triangular configuration. Fortunately these manoeuvres may be designed to occur at different times to smooth out the operations team workload. Each of these DTMs will require a correction manoeuvre one week afterwards to compensate for execution errors.

Operations orbit delivery At the end of the cruise phase each spacecraft performs the final DTM which establishes the operational orbit for the next 2 years. The cruise trajectories are designed to provide staggered arrivals with a two week separation. This final DTM for each spacecraft will be preceded by a correction manoeuvre seven days earlier to correct any position delivery error. An additional final cleanup manoeuvre will be scheduled for two weeks after the DTM, adjusting the spacecraft velocity so that the period of the achieved orbit will preserve the stability of the triangular configuration for the mission duration. Final delivery of each spacecraft is accomplished by separation of the propulsion module using a spring mechanism to impart a 3 cm/s separation velocity. The delivery target for each spacecraft is rendezvous with a point on its respective operations orbit within 500 km in position and 0.1 m/s in velocity and with an achieved heliocentric period within 38 s of nominal.

Ground station passes Communications during most of the interplanetary transfer will be a pass weekly for each spacecraft with Doppler and range data being taken for orbit determination.

7.3.3. Commissioning Phase

In the commissioning phase, the overall mission performance will be tested. The commissioning phase ends with a formal in-orbit commissioning review (IOCR) and responsibility of the mission will be handed over from the project manager to the mission manager. During the commissioning phase the following activities take place.

Drag-free attitude control system (DFACS) commissioning DFACS commissioning starts upon reaching the operational orbits. The test masses will be uncaged and the spacecraft attitude and orbit control system (AOCS) will be handed over to the DFACS control. The performance of the DFACS will be established and a number of commissioning procedures will be initiated, such as test on magnetic and thermal disturbances, actuation noise and parasitic stiffness. These tests will be derived from the previous experiences with the LISA Pathfinder (LPF) operations. DFACS commissioning requires intense ground support, both in commanding for the commissioning procedures and in instrument operations. Upon completion of DFACS commissioning, each spacecraft can be put in autonomous drag-free mode and the test mass interferometry has been established.

Laser commissioning The commissioning of the laser system includes establishing the necessary laser power and the required amplitude and frequency noise.

Acquisition During acquisition, the three spacecraft are brought to a science mode configuration and all laser links between the three spacecraft are established. Acquisition of the laser links between the spacecraft will make use of a collaborative strategy. The coarse pointing of the spacecraft is established through star trackers. The outgoing laser of the first (“mother”) spacecraft is then scanned in a slow spiral pattern over the pointing uncertainty cone. The remote (second, “daughter”) spacecraft signals the reception of light to ground control which then commands the first spacecraft to return to the sending direction corresponding to the time of reception (corrected for run-time delays), establishing the link from S/C 1 to S/C 2. The second spacecraft now enters the spiral search procedure, establishing the link from S/C 2 to S/C 1 in the same way. The link between S/C 1 and S/C 3, the “mother” and the other “daughter”, are established in a similar way. The main task of ground operations during the acquisition phase is to provide relative position and velocity information of all spacecraft to each of the three spacecraft and to command the commissioning procedure. Upon completion of the acquisition, each spacecraft receives laser light from each other spacecraft, and the S/C–S/C interferometry is established.

Measurement system commissioning With both the test mass interferometry and the inter-spacecraft interferometry established, the commissioning of the measurement system commences. This includes the commissioning of the phase measurement system, establishing clock transfer, data transfer and ranging, as well as the commissioning of the **TDI** procedure. The latter is a ground based activity, demonstrating the necessary corrections for laser frequency noise to verify the required sensitivity.

Ground communication Communications during this phase will be required for up to eight hours for each spacecraft.

This phase is complete when all spacecraft and payload functions have been checked in the operational mode and the **IOCR** has been successfully completed.

7.3.4. Calibration phase

During the calibration phase, final instrument characterisation and calibrations are performed. This includes:

Far-field characterisation The characterisation of the far-field quality of the received laser beam can be done only after the laser links are fully established and the measurement system is fully functional. Assessing the beam quality will require actuation of the spacecraft and of payload mechanisms.

Phase-centre characterisation The characterisation of the phase-centre requires actuation of the test masses and of the spacecraft to minimise the coupling between spacecraft jitter and length measurement.

Determination of instrument noise levels The noise levels of the instruments depend on the precise operational parameters and need to be assessed to optimise the science return.

Ground communication Communications during this phase will be required for up to eight hours for each spacecraft.

This phase is complete when the instrument calibration data are fully retrieved. Any of the activities required in this phase may need to be repeated either periodically in routine science operation or after incidents that are likely to change the calibration data (*e.g.* spacecraft safe-mode or loss of laser link).

7.3.5. Science Operations Phase

During the science operations phase the following activities take place.

Data Collection Collection of the science data (main, and auxiliary) will continue until end of mission.

Communications planning Nominal communication is scheduled every second day to one of the spacecraft. The nominal communication schedule will be superseded by an extended communication schedule in case of an upcoming merger event. Extended communication requires complete download from *all* spacecraft six days, four days, two days, and six hours before the merger event. The communications planning is performed by the Operations Planning Team.

Preliminary noise analysis The science data undergo a preliminary noise analysis to ensure data integrity. The preliminary noise analysis is performed by the Data Analysis Team.

Data validity monitoring and maintenance The validity of the data is monitored by the Instrument Operations Team using the instrument health data received from the Mission Operations Centre (MOC) and the preliminary noise analysis. Invalid data will be flagged.

Announcements of upcoming merger events Notices of transient events are published (and updated) through standard astronomy alert services (*e.g.* **The Astronomer's Telegram**). The responsibility for these notices lies with the **SOC**.

Science product generation The science products, as described in section 7.1, are generated by the Data Processing Centre (DPC).

Archiving The science data products, including the related code will be archived by the Data Archiving Team.

Decommissioning At the end of the science operations phase decommissioning activities are performed by which the the spacecraft is placed in a well determined passive state. All systems will be powered off.

7.3.6. Post-operations Phase

During the post-operations phase, the collection of science data and the mission operations has ceased, with the only activities in the data centres, the **SOC** and the data archive. The following activities are still performed:

Science Product Generation Generation of science products continues to make full use of the data collected

Archiving The science data products, including the related code will be archived in the data archive.

7.4. Mission Operations Elements

7.4.1. Ground Segment

The ground segment will provide command uplink, telemetry reception, and navigation services to the **NGO** mission. Specific services that are provided are

- Prior to launch, supporting the design and development of the spacecraft telecommunications hardware, the mission operations system, and the operations concept
- Providing a simulator for verifying compatibility of the flight hardware during integration and test
- Receiving requests for contacts, files and command sequences from the **MOC**
- Transmitting commands and files to the three spacecraft
- Scheduling passes with the network of antennas, reconciling competing demands from other users
- Delivering tracking and navigation data, de-commutated telemetry, and event logs back to the **MOC**

7.4.2. Flight Operations

The **MOC** is responsible for all aspects of the command, control and maintenance of the spacecraft in flight. The key operations functions are described next.

Mission control

- Uplink the master schedule of commands to the spacecraft for later execution onboard.
- Monitor the spacecraft status and the health and safety of both the platform and the payload using the house-keeping telemetry.
- In case of anomalies, trigger the appropriate recovery procedure and follow-up.
- Perform off-line performance analysis.
- Reception and storage of the platform and payload housekeeping and science telemetry.

Mission operations planning

- Generate the master schedule using the inputs from the **SOC** and adding the necessary platform commanding.
- Validate the master schedule against the mission resources (power, data storage, ...).

Orbit and Attitude Control

- Perform trajectory and attitude analyses.
- Prepare the command sequences for input to the master schedule updates related to all orbit and attitude manoeuvres.

Ground Stations and Communication Network

- Provide ground station coverage during the science operations phase (8h every second day, New Norcia is assumed as the prime ground station).
- Provide the TM/TC links to and from the ground stations.

7.5. Science Operations Elements

7.5.1. Science Operation Centre

The **SOC** will coordinate the development of the science operations ground segment and its operations to optimise the scientific return of the **NGO** mission. During operation, it generates Level 1 data products from the Level 0

data products that are received from the **MOC**. It will also perform the planning and the coordination for the extended communication in the case of upcoming transient events. The extended communication schedule ensures that information on the sky position of the upcoming mergers can be assessed by the **DPC** (section 7.5.2).

In many cases, the precise time of occurrence of a transient event can be determined many weeks or even months before the event to within about a second. The error bars on the sky position collapse only in the last few hours to within a size that can be usefully covered with electro-magnetic telescopes. The extended data schedule therefore foresees download periods of six days, four days, two days and six hours before the transient event (see figure 7.2).

The **SOC** will be developed and operated by ESA. It will coordinate the development of the science operations ground segment and its operations to optimise the scientific return of the mission.

SOC will host the archive, used during operations as the central “hub” between the **MOC**, the **DPC** and the Instrument Operations Teams (**IOTs**) for the repository and exchange of all the data required. The archive will also to be used as the **NGO** Legacy Archive containing all the products generated by **MOC** (raw and Level 0 data), **SOC** (Level 1 data), **Instrument Operations Teams** (Instrument calibration files) and the **Data Processing Centre** (level 2 and level 3 data), freely and publicly accessible by the scientific community after a proprietary period of six months (TBD). The activities of the **SOC** include

Science planning **SOC** is the unique point of contact with **MOC** on matters relevant for the payload uplink chain. This includes:

- Planning the instrument operations requests to update the configuration of the instruments
- Planning the calibration activities
- Planning the extended Ground Station communication in case of upcoming merger events

Data processing The **SOC** is responsible for the generation of the Level 1 data products. This includes:

- Ingestion of the Level 0 data from **MOC**
- Quick-Look Analysis of the data to confirm that the Level 0 data are fine
- Level 1 data products are generated by a data processing pipeline
- Transfer of the Level 1 data to the **DPC**

Data archive All the science data products of all levels will be available in the **SOC** data archive. The activities include :

- To populate the archive with the data products generated by **MOC**, **SOC**, **IOTs**, and **DPC** as soon as they are available
- Quality checks of the products before being ingested into the archive

User Support The **SOC** will provide support to the scientific community on their queries related to the data products available in the archive.

7.5.2. Data processing centre

The task of the **Data Processing Centre (DPC)** is to generate and provide the main science products to the **SOC**. The **DPC** is assumed to be developed and operated under national funds. Its activities includes:

- Retrieving the Level 1 data from the **SOC**
- Generating the Level 2 and Level 3 science data products
- Releasing the Level 2 and 3 data to the **SOC** as soon as they are available
- Supporting the assessment of the quality of the science data products they generated
- Generation of the event notices containing all the relevant parameters of the transient events (*e.g.* for upcoming super-massive black hole mergers)
- Transfer of the event notices to the **SOC** for screening and issuing.

7.5.3. Instrument Operations Teams

The **Instrument Operations Teams (IOTs)** are responsible for the payload related activities to be performed during the operations. The **IOTs** are assumed to be developed and operated under national funds. ESA will support these activities through the Instruments Operations Scientists that will be partly co-located with the **IOTs**

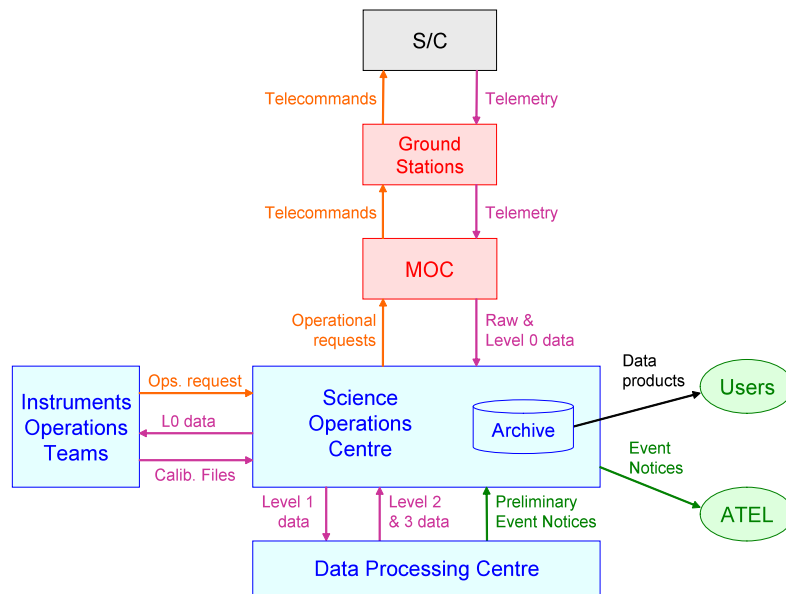


Figure 7.1.: Overview of the NGO Ground Segment including the data flow between the various elements of the Ground Segment. Data flows from S/C through MOC and SOC to the data centres (black). The data centres and the SOC issue data products (blue) that are archived and are accessible to the users. Merger Event Notices are issued by the SOC that receives preliminary event notices by the data centres.

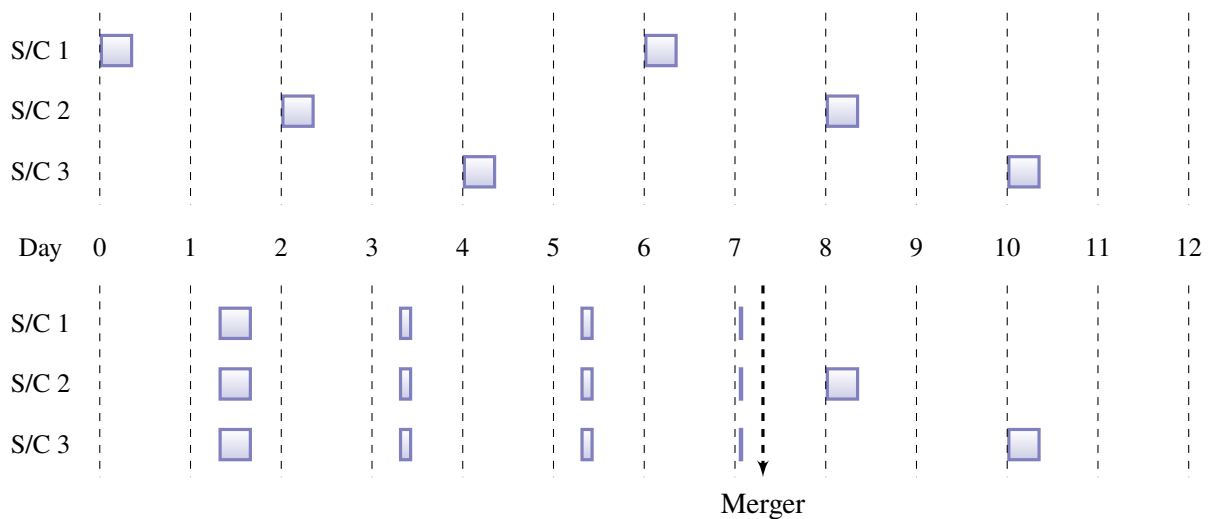


Figure 7.2.: Communication schedule. In nominal communications (upper half), the constellation is contacted every second day for eight hours, iterating through the three spacecraft, resulting in a six day sequence for each spacecraft. In extended communications (lower half), each spacecraft is contacted six days, four days, two days and six hours before a merger event, after which the nominal schedule continues.

during development and operations and that will provide full visibility of the detailed instruments calibration and monitoring aspects. The activities of the **IOTs** include:

- Monitoring the operations of the payload and look for trends in their behaviour in order to decide if/when changes in their configuration are needed and provide these instrument operations requests to the **SOC**
- Monitoring of the payload calibration to decide if/when dedicated calibration activities are needed and provide these calibration operations requests to the **SOC**
- Maintenance of all the payload calibration files used in the data processing throughout the operations

7.5.4. Data Archive

The data archive is the primary repository for all the science data products of all levels. The data archive is freely and publicly accessible and provides standard interfaces to the data. The data are available in standard formats, the associated software is available in open source. The activities of the data archive include:

- Development, operation and maintenance of the archive system
- Populate the archive with the data products (Level 0 from the **MOC**, Level 1 from the **SOC** and subsequent levels from the **DPC**).
- Providing free and public access to the archive

8. Management

The overarching responsibility for all aspects of the NGO mission rests with ESA's Directorate of Science and Robotic Exploration and its director (D-SRE). ESA is responsible for the development, integration, test, verification and timely delivery of the three fully integrated spacecraft, and for the development, integration and verification of the Mission Operations Centre (MOC) and Science Operation Centre (SOC). During the development phase, ESA appoints a Project Manager, who is responsible for implementing and managing ESA's activities during this phase. After commissioning, the ESA Mission Manager assumes responsibility for operations of the spacecraft (S/C), its payload, and the ground segment, with the exclusion of the Data Processing Centre (DPC), which is nationally funded.

The experiences in the development and the implementation of **LISA Pathfinder** (LPF) have played an important role in identifying a management scheme for **NGO**. Much like in **LPF**, the performance of **NGO** hinges critically on the performance of the complete instrument and to a certain extent of the spacecraft. In addition, the performance of **NGO** depends as well on the joint performance of the three **S/C**, *i.e.* as a constellation.

The proposed instrument procurement scheme for **NGO** focuses on ensuring the performance of the payload across the different providers. It provides a coherent, and centralised, approach to the system engineering, the flow-down of the performance requirements, the allocation of errors, and – most importantly – clear and simple interfaces.

8.1. Instrument procurement strategy

The preliminary procurement scheme foresees the *instrument* procurement by the member states. For this purpose, the instrument is defined to consist of the following components

- the optical bench with all the optical elements,
- the disturbance reduction system (DRS), including the test masses, the **charge management system** and the **front-end electronics** as well as the vacuum system and the associated structural elements
- the phasemeter

The procurement of the telescope and the laser (as described in chapter 5) are considered to be part of the spacecraft procurement.

The required mechanical support structures, interfaces, the harness, associated electronics and payload computer procedures of each element are considered to be part of the instrument. The mechanical structure connecting the instrument to the spacecraft and the “global” harness, supplying the instrument with power and data connections is considered part of the *spacecraft*. The functions and performance of the elements are described in greater detail in chapter 5.

The instrument and its components are foreseen to be developed, implemented, and tested by nationally funded instrument providers. The instrument components will be integrated by the consortium and then delivered to the industrial prime contractor for integration on the spacecraft bus.

The proposed participation scheme would be subject to the usual Agency procedures, *i.e.* a call for a statement of interest, followed by an Announcement of Opportunity (AO) for the instruments, the data analysis (see section 8.3), and scientific support for the Instrument Operations Team (IOT) (see section 7.5.3). Subsequently, a Multi-lateral agreement (MLA) would be established between ESA and the instruments funding agencies to formalise the commitments and deliverables of all parties.

8.2. Project Scientist and Science Team

The **NGO** Project Scientist is ESA's interface with the instrument consortia and the general scientific community for all scientific matters. The Project Scientist chairs the Science Team and coordinates its activities. The Project Scientist – with the help of the Science Team - advises the Project Manager during the development phase on all issues that affect the scientific performance of **NGO**, and advises the Mission Manager during operations on all issues that affect the scientific output of the mission. The Project Scientist pays special attention to those aspects that are directly related to the scientific productivity of **NGO**, in particular the status and performance of the payload, the timely analysis and reduction of the data, the generation of scientifically optimal mission products, and their archival and distribution to the scientific community.

The Science Team supports the Project Scientist in monitoring the correct implementation of the scientific objectives of the mission and in maximising its scientific return. The Science Team acts as a focus for the interest of the scientific community in **NGO**. It is foreseen that the Science Team, in addition to representatives of the **Data Processing Centre** and the instrument providers, contains members of the community at large to serve as *independent mission scientists* whose terms of reference would be subject to the usual Agency procedures.

8.3. Data analysis

Similar to the procurement of the instrument, nationally funded groups are foreseen to contribute to the data analysis for **NGO**. Thanks to the last decade of joint development efforts for the gravitational wave data analysis both for ground-based detectors (**LIGO** and **Virgo**) and space-borne detectors, quite a lot of the techniques, algorithms and codes are now at hand (see also section 3.3), so that the required investment for the **DPC** can be well defined.

The **DPC** (as defined in section 7.5.2) are developed and maintained by nationally funded groups with the overall requirements, interfaces to the **SOC** etc. to be defined by ESA. The data products and therefore the scope of the activities that the **DPC** is foreseen to deliver is described in chapter 7.

8.3.1. Data Rights

By virtue of its science goals, **NGO** resembles more closely a survey mission than an observatory, as it observes all the sky all the time. It is therefore the intention is to make the data products (see section 7.2) public after a rolling proprietary period of 6 months (TBD), *i.e.* data obtained at a given date enter the publicly accessible archive latest after the defined proprietary period.

The proprietary period is required for initial quality assurance of the data. During this period, access to the data falling under this period is limited to

- Members of the **Science Operation Centre**
- Members of the **Data Processing Centre**
- Members of the **Instrument Operations Team**
- Members of the Science Team, and their support teams
- Members of the Instrument consortia

Critical information on transient events, such as coalescence time and sky position can be exempt from the proprietary period and access limitation to allow for electro-magnetic co-observation of merger events.

A. The Evolution of LISA to NGO

This appendix provides an overview of the differences and communalities of the required capabilities of **NGO** and LISA, which in some cases might go beyond the stated *science objectives* as the mission design makes is particularly sensitive to some sources as a result of an objective placed on another source type.

In many cases, the science capabilities are very similar and differ only in so far as the capabilities of **NGO** are stated more precisely, despite the fact that the sensitivity of **NGO** is worse than the sensitivity for LISA. This is made possible by the progress in data analysis, and hence the ability to predict the science performance, and in the understanding of the physics of the sources. Both allow to give the capabilities of **NGO** in a more quantified way than has been possible in the past for LISA and recover some of the very conservative safety margin that has been applied in the capabilities of LISA. The capabilities of LISA have not been reanalysed during the scope of this study, but it is safe to say that, had this been done, the performance of LISA would have exceeded the performance of NGO significantly.

Some of the performance of LISA cannot be retrieved by **NGO**, such as the instantaneous measurement of the polarisation and thus the precise measurement of the luminosity distance of distant source, which impacts the return in cosmology.

In the following tables, we use a colour code where measurements that are essentially unaffected are marked in **green**, those that are significantly affected, but can still be performed in **yellow** and those that cannot be performed or are severely degraded with respect to the observational requirements of LISA are coloured **red**. For those measurements a short explanation is provided in *italics*.

The colour **blue** is used for those measurements that **NGO** will perform and that were either not explicitly specified for LISA or are a result of advances in understanding and data analysis. For those measurements a short explanation is provided in *italics*.

A.1. General architecture

The general mission architecture of **NGO** differs from LISA in three key areas: (i) the reduced armlength, (ii) the smaller number of laser links, and (iii) the shortened mission lifetime. The instruments, *i.e.* the optical bench, the phasemeter and the disturbance reduction system (DRS) are as much as possible inherited from LISA to maximise the return from the ongoing technology development programme.

NGO	LISA
Triangular constellation of 3 satellites in a Mother-Daughter configuration	Triangular constellation of 3 identical satellites
Inter-spacecraft distance 10^6 km	Inter-spacecraft distance 5×10^6 km
Single Michelson-type interferometer (4 laser links)	Many possible interferometer configurations (up to 6 links)
Direct amplitude measurement, polarisation measurement only via orbital evolution	Direct amplitude measurement, instantaneous polarisation measurement
2 years nominal mission lifetime, extendable to 5 years	5 years nominal mission lifetime, extendable to 10 years

A.2. Galactic binaries

The measurements on the galactic binaries are mainly affected due to the reduced sensitivity, which is due to the shorter arms. In general, less binaries will be detected, however, many of them will have a large enough **SNR** so that the observational requirement is unaffected.

The measurement of the second derivative of the frequency is most likely not possible in the nominal mission duration and might be possible during a possible mission extension. The galactic foreground that was clearly detectable with LISA is marginal for NGO due to the reduced sensitivity, so that no quantitative measurements such as moments or frequency dependency are expected.

NGO	LISA
expected number: about 3000 expected number of verification binaries: more than 8	expected number: about 10 000 expected number of verification binaries: more than 20
Detection of more than 1000 binaries at $\text{SNR} > 10$ with orbital periods shorter than approximately six hours and determine their period.	Detection of more than 1000 binaries at $\text{SNR} > 10$ with orbital periods shorter than approximately six hours and determine their period.
Detection of <i>all</i> neutron star and black hole binaries in the Milky Way with periods shorter than 35 minutes.	Detection of <i>all</i> neutron star and black hole binaries in the Milky Way with periods shorter than 35 minutes.
Determine the position of at least 500 sources with better than ten square degree angular resolution, the inclination to better than 10° degree, and the frequency derivative to 10 %.	Determine the position of more than a hundred sources with better than a square degree angular resolution and the frequency derivative to a fractional uncertainty of 10 %
Measure the frequency derivative of <i>all</i> detected binary systems with gravitational wave frequencies above 10 mHz to better than 10 %.	<i>Shorter arms allow better sensitivities at higher frequencies</i>
<i>Reduced sensitivity due to shorter arms</i>	Measure the distance to 10 % for the binaries for which an EM counterpart is available.
<i>Limited mission duration. Possible measurement during mission extension</i>	Measure the second frequency derivative of binary systems with gravitational wave frequencies above 20 mHz to 10 % and their sky location to better than 0.1 square degree.
Measure the level of the the unresolved Galactic foreground.	Measure the spectral amplitude and frequency dependency of the unresolved Galactic foreground below 1 mHz and constrain the spectral amplitude of the unresolved extragalactic foreground in the frequency region 2 mHz to 5 mHz.
<i>Reduced sensitivity due to shorter arms</i>	Measure the first two moments of the distribution of the Galactic unresolved foreground.

A.3. Astrophysical Black Holes

The measurement of the astrophysical black holes is mainly affected by the lack of the laser link between the two “Daughter” spacecraft (Daughter-S/C) that causes the loss of instantaneous polarisation information. This makes it more difficult to determine the luminosity distance precisely, as polarisation and amplitude of the signals are degenerate.

The main effect of the shorter arms and the reduced sensitivity is a shift in the observable masses, quite generally to lower masses, as the optimum sensitivity moves toward higher frequencies, and a smaller rate. The lower end of that rate (10 yr^{-1}), though, is made up of very massive black hole binaries that can be seen with a large signal-to-noise ratio (SNR) out to a redshift of $z = 20$ or more and is thus not affected by the reduced sensitivity. For this reason, the rate and expected number is marked essentially unaffected.

The science return of the massive black hole mergers is not much affected, as the loss in signal and numbers is partly compensated by the better understanding and availability of waveforms and because the identification of a particular model for the structure formation does not depend on a measurement of the luminosity distances. This is the reason for marking the measurements as essentially unaffected, despite the fact that massive black hole binaries of different masses will be observed.

The reduced sensitivity still allows for a very precise determination of the coalescence *time* but the position information is essentially unavailable.

NGO	LISA
expected rate: 10 yr^{-1} to 100 yr^{-1} expected number (2 year mission duration): 20 to 200	expected rate: 10 yr^{-1} to 1000 yr^{-1} expected number (5 year mission duration): 50 to 5000
Capability to detect the mergers of comparable mass black hole binaries (mass ratio $m_2/m_1 > 0.1$) with total mass in the range $10^5 M_\odot < m_1 + m_2 < 2 \times 10^7 M_\odot$ up to redshift $z = 20$. Determine the spin of the largest massive black hole (MBH) (error smaller than 0.1) and the luminosity distance (relative error smaller than 50 %).	Capability to detect the mergers black hole binaries with masses in the range $300 M_\odot < m_2 < m_1 < 3 \times 10^4 M_\odot$ with $m_2/m_1 > 0.01$, out to redshift $z = 15$.
Capability to detect the mergers of comparable mass black hole binaries (mass ratio $m_2/m_1 > 0.1$) with total mass in the range $2 \times 10^4 M_\odot < m_1 + m_2 < 10^5 M_\odot$ beyond redshift $z = 5$ and up to $z = 15$. Determine the MBH masses (relative errors smaller than 1 %) and the spin of the largest MBH (error smaller than 0.1) and the luminosity distance (relative error smaller than 50 %).	Capability to detect the mergers of black hole binaries with masses in the range $10^4 M_\odot < m_2 < m_1 < 3 \times 10^5 M_\odot$ out to redshift $z = 16$.
Capability to detect some of the mergers of MBH with total mass in the range $2 \times 10^4 M_\odot < m_1 + m_2 < 10^5 M_\odot$ and mass ratio $0.01 < m_2/m_1 < 0.1$ beyond redshift $z = 5$. Determine the masses with relative errors smaller than a few percent.	Capability to detect the mergers of black hole binaries with masses in the range $3 \times 10^5 M_\odot < m_1 < 10^7 M_\odot$ and $10^3 M_\odot < m_2 < m_1$, at redshifts $z < 6$.
<i>Instantaneous polarisation measurement required for precision measurement of luminosity distance</i>	Determination of MBH masses, the spin of the larger MBH, and the luminosity distance to the binary.
Capability of providing advance warning of mergers of $5 \times 10^5 M_\odot$ to $3 \times 10^6 M_\odot$ black holes at $z = 1$.	Capability of providing advance warning and localisation of mergers of $5 \times 10^5 M_\odot$ to $3 \times 10^6 M_\odot$ black holes at $z = 1$ with an accuracy of less than 15 square degrees one week before merger.

A.4. EMRI

The detection of extreme mass-ratio inspiral (EMRI) is mainly affected by the reduced sensitivity of New Gravitational wave Observatory (NGO), which results in a reduction of the rate that is partly compensated by progress in the data analysis, requiring a lower SNR for a detection. As for LISA, any EMRI detected will yield extremely precise measurements of the parameters. Note that the rate on EMRI has a very high astrophysical uncertainty.

NGO	LISA
expected rate: 1 yr^{-1} to 100 yr^{-1} expected number (2 year mission duration): 10 to 20	expected rate: 10 yr^{-1} to 1000 yr^{-1} expected number (5 year mission duration): a few tens
Capability to detect gravitational waves emitted during the last two years of inspiral for a stellar-mass compact object ($m_2 \sim 5 M_\odot - 20 M_\odot$) orbiting a massive black hole ($m_1 \sim 10^5 M_\odot - 10^6 M_\odot$) up to $z = 0.7$ with an SNR > 20 . Determine the mass with an relative error smaller than 0.1 %, the spin of the MBH with an error smaller than 10^{-3} , and the mass of the compact object with a relative error smaller than 0.1 %, as well as the orbital eccentricity before the plunge with an error smaller than 10^{-3} .	Capability to detect gravitational waves emitted during the last year of inspiral for a stellar-mass compact object ($m_2 \sim 5 M_\odot \dots 100 M_\odot$) orbiting a massive black hole (with $m_1 \sim 10^5 M_\odot \dots \text{few} \times 10^6 M_\odot$) at $z = 1$ with SNR > 30 (averaged over source locations and orientations)
Capability to detect gravitational waves emitted by a $10^2 M_\odot - 10^4 M_\odot$ IMBH spiralling into an MBH with mass $3 \times 10^5 M_\odot - 10^7 M_\odot$ out to $z \sim 2 - 4$ (for a mass ratio around 10^{-2} to 10^{-3}).	Capability to detect gravitational waves emitted by a $10^3 M_\odot - 10^4 M_\odot$ intermediate-mass black hole (IMBH) spiralling into an MBH with mass in the range $3 \times 10^5 M_\odot - 10^6 M_\odot$ out to $z = 3$ (with SNR ~ 30).

A.5. Testing General Relativity

The tests of General Theory of Relativity (GR) are relying on a highly precise determination of the system parameters, which is usually possible for either systems with a very large SNR or for EMRI. Therefore, the quality

of the tests are not very much affected, as NGO will see massive black hole coalescences with very high SNR and EMRI, but the total number of those tests will be reduced, as NGO will observe fewer high-SNR systems than LISA.

Here, the advances in data analysis and understanding of the sources allow to reduce the required SNR, partly or fully compensating for the reduced sensitivity.

NGO	LISA
Capability to detect and study three or more (expected more than 8) optically observable verification binaries between 1 mHz and 10 mHz with SNR > 10.	Capability to detect and study three or more (expected around 20) optically observable verification binaries between 1 mHz and 10 mHz with SNR > 20.
Capability to observe the gravitational waves from at least 50 % of all $z \sim 2$ coalescing binary systems consisting of compact objects with masses between $10^5 M_\odot$ and $10^6 M_\odot$ and mass ratios between 1:1 and 1:3.	Capability to observe the gravitational waves from at least 50 % of all $z \sim 2$ coalescing binary systems consisting of compact objects with masses between $10^5 M_\odot$ and $10^6 M_\odot$ and mass ratios between 1:1 and 1:3.
Capability to detect gravitational waves emitted during the last year of inspiral for a $10 M_\odot$ black hole orbiting a $10^5 M_\odot$ to $10^6 M_\odot$ black hole up to $z = 0.7$ with SNR > 20.	Capability to detect gravitational waves emitted during the last year of inspiral for a $10 M_\odot$ black hole orbiting a $3 \times 10^5 M_\odot$ to $3 \times 10^6 M_\odot$ black hole at 1 Gpc with SNR > 30.
Observe the inspiral radiation from MBH with masses between $10^5 M_\odot - 10^6 M_\odot$ and mass ratio $m_2/m_1 > 1/3$ to $z \leq 5$ with an average SNR > 30, measuring the mass to better than 1 % and spin parameters to better than 0.1.	Observe the merger and ring-down radiation from all $1 \times 10^5 M_\odot$ to $1 \times 10^6 M_\odot$ black holes formed from approximately equal mass, $M_1 < 3M_2$, mergers to $z \leq 8$, measuring the mass and spin parameters, M_\bullet and a_\bullet , of the final black hole to $0.1M$.
Observe the merger and ring-down radiation from MBH with masses between $10^5 M_\odot - 10^6 M_\odot$ and mass ratio $m_2/m_1 > 1/3$ to $z \leq 8$ with an average SNR > 60, measuring the mass to better than 1 % and spin parameters to better than 0.3.	<i>Advances in data analysis</i>

A.6. Cosmology

The measurements on cosmology are mainly affected by the lack of instantaneous polarisation information that renders the measurements of the luminosity distances much less precise, making it much more difficult to establish the distance-redshift relationship.

NGO	LISA
Capability of setting an upper limit on the spectrum of a stochastic gravitational wave background in the 10^{-4} Hz – 10^{-1} Hz band.	Capability of detecting or setting an upper limit on the spectrum of a stochastic gravitational wave background in the 10^{-4} Hz – 10^{-1} Hz band.
Capability of detecting gravitational wave bursts from cosmic (super-)strings, or of setting cosmologically interesting upper limits on the loops.	Capability of detecting gravitational wave bursts from cosmic (super-)strings, or of setting cosmologically interesting upper limits on the loops.
<i>Instantaneous polarisation measurement required for precision measurement of luminosity distance; Reduced sensitivity due to shorter arms, thus less SNR</i>	Capability of providing sky localisation of 3.5° (not squared degrees) or better, for MBH mergers with component masses in the range $10^5 M_\odot$ to $10^6 M_\odot$ at $z \lesssim 2$. Determine the luminosity distance to these mergers better than 5 %
<i>Instantaneous polarisation measurement required for precision measurement of luminosity distance; Reduced sensitivity due to shorter arms, thus less SNR</i>	Capability to provide sky location of 10 square degrees or better, and luminosity-distance measurements to 3 % or better, for EMRI or intermediate mass-ratio inspiral (IMRI) binary sources with SNR > 50.

Acronyms

- AC** alternating current; *fig* referring to oscillating processes or entities.
- ADC** analog-to-digital converter.
- AGN** active galactic nuclei.
- AIT** assembly, integration, and testing.
- AK** “Analytic Kludge”.
- AM CVn** class of cataclysmic variable stars.
- AO** Announcement of Opportunity.
- AOCS** attitude and orbit control system.
- ASD** amplitude spectral density.
- CBE** current best estimate.
- CBOD** clamp band opening device.
- CCD** charge-coupled device.
- CDM** cold dark matter.
- CMB** cosmic microwave background.
- CMS** charge management system.
- COMBO** **Classifying Objects by Medium-Band Observations.**
- COSMOS** **Cosmic Evolution Survey.**
- CTE** coefficient of thermal expansion.
- Daughter-S/C** “Daughter” spacecraft.
- DC** direct current; *fig* referring to quasi-static processes or quasi-constant entities.
- DEEP2** **Deep Extragalactic Evolutionary Probe 2.**
- DFACS** drag-free attitude control system.
- DPC** Data Processing Centre.
- DPLL** digital phase locked loop.
- DRS** disturbance reduction system.
- DTM** deterministic transfer manoeuvre.
- EGAPS** European Galactic Plane Surveys.
- EM** electro-magnetic.
- EMC** electro-magnetic compatibility.
- EMRI** extreme mass-ratio inspiral.
- EOL** end-of-life.
- EOM** electro-optical modulator.
- EPS** extended Press-Schechter formalism.
- ESAC** European Space Astronomy Centre in Madrid, Spain.
- FEE** front-end electronics.
- FEPP** field-emission electric propulsion.
- FPAG** Fundamental Physics Advisory Group.
- FPGA** field-programmable gate array.
- GR** General Theory of Relativity.
- GRS** gravitational reference sensor.
- GSFC** Goddard Space Flight Center.
- GTO** geostationary transfer orbit.
- GW** gravitational wave.
- HETO** Heliocentric Earth Trailing Orbit.
- HGA** high-gain antenna.
- HST** **Hubble Space Telescope.**
- IMBH** intermediate-mass black hole.
- IMRI** intermediate mass-ratio inspiral.
- IMS** interferometric measurement system.
- IOCR** in-orbit commissioning review.
- IOT** Instrument Operations Team.
- ISM** instrument sensitivity model.
- JILA** **Joint Institute for Laboratory Astrophysics.**
- LAGOS** Laser Antenna for Gravitational-radiation Observation in Space.
- LCM** NGO launch composite.
- LED** light-emitting diode.
- LEOP** Launch and Early Operations Phase.
- LGA** low-gain antenna.
- LIGO** **Laser Interferometer Gravitational Wave Observatory.**
- LOS** line of sight.
- LPF** **LISA Pathfinder.**
- LSST** **Large Synoptic Survey Telescope.**
- LTP** LISA Pathfinder technology package.
- MAXI** **Monitor of All-sky X-ray Image.**
- MBH** massive black hole.
- MBHB** massive black hole binary.
- MCMC** Markov-chain Monte Carlo.
- MEOP** maximum expected operating pressure.
- MLA** Multi-lateral agreement.
- MLDC** **Mock LISA Data Challenge.**
- MLI** multi layer insulation.
- MMH** monomethyl hydrazine.
- MOC** Mission Operations Centre.
- MOFPA** Master Oscillator Fibre Power Amplifier.
- MON-3** mixed oxides of nitrogen with 3% nitric oxide.
- Mother-S/C** “Mother” spacecraft.
- NASA** **National Aeronautic and Space Administration.**
- NGO** New Gravitational wave Observatory.
- NGO SWT** NGO science working team.
- NPRO** non-planar ring oscillator.
- NR** numerical relativity.
- OATM** optical assembly tracking mechanism.
- OMS** Optical Metrology System.
- P/M** propulsion module.
- PDF** probability density function.
- PN** post-Newtonian.
- PRN** pseudo-random *often* pseudo-noise.
- PTF** **Palomar Transient Factory.**
- QNM** quasi-normal mode.
- QPD** quadrant photodetector.
- QSO** quasi-stellar object.
- RATS** Rapid Time Survey.
- RF** radio frequency.
- RIN** relative intensity noise.
- RIT** Radio-frequency Ion Thruster.
- RSS** root sum square.
- RXTE** **Rossi X-Ray Timing Explorer.**
- S/C** spacecraft.
- S/C-P/M** spacecraft/propulsion-module.
- SDSS** **Sloan Digital Sky Survey.**
- SIM** Space Interferometry Mission.
- SNR** signal-to-noise ratio.
- SOC** Science Operation Centre.
- SSB** Solar System barycenter.
- TDI** time-delay interferometry.
- TM** test mass, *often proof mass.*
- TRL** Technology Readiness Level.
- TWTA** traveling-wave tube amplifier.
- USO** ultra-stable oscillator.
- UV** ultra-violet.
- VAST** **Variables and Slow Transients, An ASKAP Survey for Variables and Slow Transients is a Survey Science Project for the Australian SKA Pathfinder.**

Bibliography

Scientific References

- Abel, T et al. (Jan. 2002). *Science* **295**.  
- Alexander, T (Nov. 2005). *Phys. Rep.* **419**.  
- Aller, MC & D Richstone (Dec. 2002). *AJ* **124**.  
- Amaro-Seoane, P & M Freitag (Dec. 2006). *ApJ* **653**.  
- Amaro-Seoane, P & M Preto (May 2011). *Class. Quantum Grav.* **28.9**.  
- Amaro-Seoane, P & L Santamaría (Oct. 2010). *ApJ* **722**.  
- Amaro-Seoane, P et al. (Sept. 2007). *Class. Quantum Grav.* **24**.  
- Amaro-Seoane, P et al. (Feb. 2010). *MNRAS* **401**.  
- Amico, P et al. (2002). *Class. Quantum Grav.* **19** (7).  
- Antonucci, F et al. (May 2011). *Class. Quantum Grav.* **28.9**.  
- Argence, B et al. (Apr. 2010). *Phys. Rev. D* **81.8**.  
- Armano, M et al. (2005). *Class. Quantum Grav.* **22** (10).  
- Armano, M et al. (May 2009). *Class. Quantum Grav.* **26.9**.  
- Armitage, PJ & P Natarajan (Mar. 2002). *ApJ* **567**.  
- (Dec. 2005). *ApJ* **634**.  
- Armstrong, JW et al. (Dec. 1999). *ApJ* **527**.  
- Arnaud, KA et al. (Oct. 2007a). *Class. Quantum Grav.* **24**.  
- Arnaud, KA et al. (Oct. 2007b). *Class. Quantum Grav.* **24**.  
- Arnaud, KA et al. (2006a). *AIP Conf. Series.* **873**.  
- (2006b). *AIP Conf. Series.* **873**.  
- Arun, KG et al. (July 2006). *Phys. Rev. D* **74.2**, 024006.  
- Arun, KG et al. (May 2009). *Class. Quantum Grav.* **26.9**.  
- Arvanitaki, A & S Dubovsky (Feb. 2011). *Phys. Rev. D* **83.4**.  
- Babak, S et al. (Jan. 2007). *Phys. Rev. D* **75.2**.  
- Babak, S et al. (June 2008a). *Class. Quantum Grav.* **25.11**.  
- Babak, S et al. (Sept. 2008b). *Class. Quantum Grav.* **25.18**.  
- Babak, S et al. (Apr. 2010). *Class. Quantum Grav.* **27.8**.  
- Babak, S et al. (June 2011). *Class. Quantum Grav.* **28.11**.  
- Bahcall, JN & RA Wolf (Oct. 1976). *ApJ* **209**.  
- (Sept. 1977). *ApJ* **216**.  
- Baker, JG et al. (May 2006a). *Phys. Rev. D* **73.10**.  
- (Mar. 2006b). *Phys. Rev. Lett.* **96.11**.  
- Baker, JG et al. (June 2007a). *Phys. Rev. D* **75.12**.  
- Baker, JG et al. (June 2007b). *Class. Quantum Grav.* **24**.  
- Baker, JG et al. (Nov. 2007c). *Phys. Rev. Lett.* **99.18**.  
- Baker, JG et al. (Aug. 2008a). *Phys. Rev. D* **78.4**.  
- Baker, JG et al. (July 2008b). *ApJ* **682**.  
- Ballo, L et al. (Jan. 2004). *ApJ* **600**.  
- Barack, L & C Cutler (Apr. 2004). *Phys. Rev. D* **69**, 082005 (8).  
- Barack, L & N Sago (Apr. 2011). *Phys. Rev. D* **83.8**, 084023.  
- Barausse, E & L Rezzolla (May 2008). *Phys. Rev. D* **77.10**.  
- Barausse, E et al. (Mar. 2007). *Phys. Rev. D* **75.6**.  
- Barclay, T et al. (June 2011). *MNRAS* **413**.  
- Bardeen, JM (Apr. 1970). *Nature* **226**.  
- Bardeen, JM & JA Petterson (Jan. 1975). *ApJ* **195**.  
- Barrows, RS et al. (Feb. 2011). *NewA* **16**.  
- Bartelt-Berger, L et al. (2001). *IEEE Conf. Proceedings*.  
- Barth, AJ et al. (May 2004). *ApJ* **607**.  
- Barth, AJ et al. (Jan. 2009). *ApJ* **690**.  
- Begelman, MC et al. (Sept. 1980). *Nature* **287**.  
- Begelman, MC et al. (July 2006). *MNRAS* **370**.  
- Bekki, K & AW Graham (May 2010). *ApJ* **714**.  
- Belczynski, K et al. (June 2002). *ApJ* **572**.  
- Belczynski, K et al. (Dec. 2010). *ApJ* **725**.  
- Bell, EF et al. (Nov. 2006). *ApJ* **652**.  
- Benacquista, M & K Holley-Bockelmann (July 2006). *ApJ* **645** (1).  
- Bender, PL & D Hils (June 1997). *Class. Quantum Grav.* **14**.  
- Benedetti, M et al. (2006). *Journal of Tribology* **128** (4).  
- Berczik, P et al. (Nov. 2005). *ApJ* **633**.  
- Berczik, P et al. (May 2006). *ApJ* **642**.  
- Berti, E (Oct. 2006). *Class. Quantum Grav.* **23**.  
- Berti, E & M Volonteri (Sept. 2008). *ApJ* **684**.  
- Berti, E et al. (Apr. 2005). *Phys. Rev. D* **71**, 084025 (8).  
- Berti, E et al. (Mar. 2006). *Phys. Rev. D* **73** (6).  
- Berti, E et al. (Nov. 2007). *Phys. Rev. D* **76.10**.  
- Berti, E et al. (Aug. 2009). *Class. Quantum Grav.* **26.16**.  
- Berti, E et al. (July 2011). *ArXiv e-prints*.  
- Bertone, S et al. (Aug. 2007). *MNRAS* **379**.  
- Bhattacharya, D & EPJ van den Heuvel (1991). *Phys. Rep.* **203**.  
- Bildsten, L (July 1998). *ApJ* **501**.  
- Binétruy, P et al. (Dec. 2010). *Phys. Rev. D* **82.12**.  
- Blanchet, L (2006). *Living Reviews in Relativity* **9.4**.  
- Blecha, L & A Loeb (Nov. 2008). *MNRAS* **390**.  
- Blecha, L et al. (Apr. 2011). *MNRAS* **412**.  
- Bogdanović, T et al. (Feb. 2008). *ApJS* **174**.  
- Bogdanović, T et al. (May 2009). *ApJ* **697**.  
- Bohé, A (Sept. 2011). *Phys. Rev. D* **84.6**.  
- Boroson, TA & TR Lauer (Mar. 2009). *Nature* **458**.  
- Bortoluzzi, D et al. (May 2009). *Class. Quantum Grav.* **26.9**.  
- Boylan-Kolchin, M et al. (Sept. 2004). *ApJ* **613**.  
- Brandt, N et al. (2005). *Class. Quantum Grav.* **22** (10).  
- Braxmaier, C et al. (Sept. 2004).  
- Bromm, V & A Loeb (Oct. 2003). *ApJ* **596**.  
- Brown, DA et al. (Oct. 2007). *Class. Quantum Grav.* **24**.  
- Brown, WR et al. (Jan. 2009). *ApJ* **690**.  
- Brown, WR et al. (Aug. 2011). *ApJ* **737**.  
- Brustein, R et al. (Feb. 1995). *Physics Letters B* **361**.  
- Budworth, DW et al. (1960). *Proceedings of the Royal Society of London. Series A* **257**.1289.  
- Buonanno, A (Mar. 2003). *ArXiv e-prints*.  
- Buonanno, A et al. (Mar. 1997). *Phys. Rev. D* **55**.  
- Buonanno, A et al. (Nov. 2007a). *Phys. Rev. D* **76.10**.  
- Buonanno, A et al. (June 2007b). *Phys. Rev. D* **75.12**.  
- Callegari, S et al. (Mar. 2011). *ApJ* **729**.  
- Campanelli, M et al. (Mar. 2006a). *Phys. Rev. Lett.* **96.11**.  
- Campanelli, M et al. (Mar. 2006b). *Phys. Rev. D* **73.6**.  
- Campanelli, M et al. (June 2007). *Phys. Rev. Lett.* **98.23**.  
- Campanelli, M et al. (Apr. 2009). *Phys. Rev. D* **79.8**.  
- Caprini, C et al. (Dec. 2009). *Journal of Cosmology and Astroparticle Physics* **12**.  
- Carbone, L et al. (Oct. 2003). *Phys. Rev. Lett.* **91.15**.  
- (May 2005). *Class. Quantum Grav.* **22.10**.  
- Carbone, L et al. (Nov. 2006). *AIP Conf. Series.* **873**.  
- Carbone, L et al. (Nov. 2007a). *Phys. Rev. D* **76.10**.  
- Carbone, L et al. (Feb. 2007b). *Phys. Rev. D* **75.4**.  
- Cardoso, V et al. (Sept. 2011). *ArXiv e-prints*.  
- Cavalleri, A et al. (Oct. 2001). *Class. Quantum Grav.* **18** (19).  
- Cavalleri, A et al. (May 2009a). *Class. Quantum Grav.* **26.9**.  
- Cavalleri, A et al. (Oct. 2009b). *Phys. Rev. Lett.* **103.14**, 140601.  
- Centrella, J et al. (Nov. 2010). *Annual Review of Nuclear and Particle Science* **60**.  

- Chakrabarty, D et al. (July 2003). *Nature* **424**.  
- Chandrasekhar, S (Mar. 1943). *ApJ* **97**. 
- Chandrasekhar, S & S Detweiler (Aug. 1975). *Royal Soc. of London Proc. Series A* **344**. 
- Chang, DH et al. (2007). *Proc. SPIE*. **6713**. 
- Chirenti, CBMH & L Rezzolla (Aug. 2007). *Class. Quantum Grav.* **24**.  
- Chongchitnan, S & G Efstathiou (Apr. 2006). *Phys. Rev. D* **73.8**.  
- Christensen, N & R Meyer (Oct. 1998). *Phys. Rev. D* **58.8**. 
- Christensen, N et al. (July 2004). *Phys. Rev. D* **70.2**.  
- Ciotti, L et al. (July 2010). *ApJ* **717**.  
- Civano, F et al. (July 2010). *ApJ* **717**.  
- Clark, PC et al. (Feb. 2011). *ApJ* **727**.  
- Collins, NA & SA Hughes (June 2004). *Phys. Rev. D* **69.12**. 
- Colpi, M et al. (Nov. 1986). *Phys. Rev. Lett.* **57**. 
- Colpi, M et al. (Nov. 1999). *ApJ* **525**.  
- Colpi, M & M Dotti (Feb. 2011). *Advanced Science Letters* **4.2**.  
- Copeland, EJ et al. (June 2004). *Journal of High Energy Physics* **6**.  
- Cornish, NJ (May 2011). *Class. Quantum Grav.* **28.9**.  
- Cornish, NJ & J Crowder (Aug. 2005). *Phys. Rev. D* **72**, 043005 (4).  
- Cornish, NJ & RW Hellings (Nov. 2003). *Class. Quantum Grav.* **20** (22).  
- Cornish, NJ & EK Porter (Oct. 2006). *Class. Quantum Grav.* **23**.  
- (Jan. 2007a). *Phys. Rev. D* **75.2**.  
- (Oct. 2007b). *Class. Quantum Grav.* **24**.  
- (Dec. 2007c). *Class. Quantum Grav.* **24**.  
- Cornish, N et al. (Sept. 2011). *Phys. Rev. D* **84.6**.  
- Cox, TJ & A Loeb (May 2008). *MNRAS* **386**.  
- Croton, DJ et al. (Jan. 2006). *MNRAS* **365**.  
- Crowder, J & NJ Cornish (Feb. 2007). *Phys. Rev. D* **75.4**.  
- Crowder, J et al. (Mar. 2006). *Phys. Rev. D* **73** (6).  
- Cruz, RJ et al. (Oct. 2006). *Class. Quantum Grav.* **23**. 
- Cruz, RJ et al. (2006). *AIP Conf. Series*. **873**. 
- Cuadra, J et al. (Mar. 2009). *MNRAS* **393**.  
- D'Souza, MCR et al. (May 2006). *ApJ* **643**.  
- Damour, T & A Vilenkin (Mar. 2005). *Phys. Rev. D* **71.6**.  
- Damour, T et al. (Jan. 2011). *Phys. Rev. D* **83.2**.  
- Dan, M et al. (Aug. 2011). *ApJ* **737**.  
- De Lucia, G et al. (Feb. 2006). *MNRAS* **366**.  
- De Marco, O et al. (Mar. 2011). *MNRAS* **411**.  
- De Propriis, R et al. (Sept. 2007). *ApJ* **666**.  
- Decarli, R et al. (Sept. 2010). *ApJ* **720**. 
- Dehne, M et al. (Mar. 2009). *JPCS* **154.1**. 
- Detweiler, S (Nov. 1980). *Phys. Rev. D* **22**. 
- Devecchi, B et al. (Apr. 2009). *MNRAS* **394**.  
- Dhurandhar, SV (Mar. 2009). *JPCS* **154.1**.  
- Dhurandhar, SV & M Tinto (July 2005). *Living Reviews in Relativity* **8**.  
- Dhurandhar, SV et al. (May 2002). *Phys. Rev. D* **65** (10).  
- Dhurandhar, SV & M Tinto (2005). *Living Reviews in Relativity* **8.4**. 
- Di Matteo, T et al. (Feb. 2005). *Nature* **433**.  
- Di Matteo, T et al. (Mar. 2008). *ApJ* **676**.  
- Dijkstra, M et al. (Dec. 2008). *MNRAS* **391**.  
- Dolesi, R et al. (2003). *Class. Quantum Grav.* **20.10**. 
- Dotan, C et al. (Oct. 2011). *MNRAS*.  
- Dotti, M et al. (Mar. 2006). *mnras* **367**.  
- Dotti, M et al. (Aug. 2007). *MNRAS* **379**.  
- Dotti, M et al. (July 2009a). *MNRAS* **396**.  
- Dotti, M et al. (Sept. 2009b). *MNRAS* **398**.  
- Dotti, M et al. (Feb. 2010). *MNRAS* **402**.  
- Drasco, S & SA Hughes (Feb. 2004). *Phys. Rev. D* **69.4**.  
- (Jan. 2006). *Phys. Rev. D* **73.2**, 024027.  
- Dreyer, O et al. (Feb. 2004). *Class. Quantum Grav.* **21**.  
- Dufaux, JF et al. (Dec. 2007). *Phys. Rev. D* **76.12**, 123517.  
- Dufaux, JF et al. (Mar. 2009). *Journal of Cosmology and Astroparticle Physics* **3**. 
- Eardley, DM et al. (Nov. 1973). *Phys. Rev. D* **8**. 
- Edlund, JA et al. (June 2005). *Phys. Rev. D* **71** (12).  
- Einstein, A (1915). *Sitzungsberichte der Königlich Preußischen Akademie der Wissenschaften (Berlin)*.  
- Eisenhauer, F et al. (July 2005). *ApJ* **628**.  
- Elliffe, EJ et al. (2005). *Class. Quantum Grav.* **22.10**. 
- Enoki, M et al. (Nov. 2004). *ApJ* **615**.  
- Eracleous, M et al. (June 2011). *ArXiv e-prints*. 
- Escala, A et al. (June 2004). *ApJ* **607**.  
- Esposito-Farèse, G (Nov. 2004). *AIP Conf. Series*. **736**.  
- Everitt, CWF et al. (2008). *Class. Quantum Grav.* **25.11**. 
- Fabbiano, G et al. (Sept. 2011). *Nature* **477**.  
- Fan, X et al. (Mar. 2006a). *AJ* **131**.  
- Fan, X et al. (July 2006b). *AJ* **132**.  
- Farmer, AJ & ES Phinney (Dec. 2003). *MNRAS* **346**.  
- Feroz, F et al. (Nov. 2009). *Class. Quantum Grav.* **26.21**.  
- Feroz, F et al. (Apr. 2010). *Class. Quantum Grav.* **27.7**.  
- Ferrarese, L & H Ford (Feb. 2005). *Space Science Reviews* **116**.  
- Ferrarese, L & D Merritt (Aug. 2000). *ApJ* **539**.  
- Ferrarese, L et al. (June 2006). *ApJ* **644**.  
- Finn, LS & KS Thorne (Dec. 2000). *Phys. Rev. D* **62.12** (12).  
- Flanagan, ÉÉ & SA Hughes (Apr. 1998). *Phys. Rev. D* **57**.  
- (Sept. 2005). *New Journal of Physics* **7**.  
- Freitag, M et al. (Dec. 2006a). *JPCS* **54**.  
- Freitag, M et al. (May 2006b). *MNRAS* **368**.  
- Freitag, M et al. (Sept. 2006c). *ApJ* **649**.  
- Fuller, J & D Lai (Aug. 2011). *ArXiv e-prints*. 
- Gair, JR (May 2009a). *Class. Quantum Grav.* **26.9**.  
- (May 2009b). *Class. Quantum Grav.* **26.9**.  
- Gair, JR & G Jones (Mar. 2007). *Class. Quantum Grav.* **24**.  
- Gair, JR & EK Porter (Nov. 2009). *Class. Quantum Grav.* **26.22**.  
- Gair, JR & L Wen (Sept. 2005). *Class. Quantum Grav.* **22** (18).  
- Gair, JR et al. (Oct. 2004). *Class. Quantum Grav.* **21** (20).  
- Gair, JR et al. (Sept. 2008a). *Class. Quantum Grav.* **25.18**.  
- Gair, JR et al. (Sept. 2008b). *Class. Quantum Grav.* **25.18**.  
- Gair, JR et al. (May 2010a). *Phys. Rev. D* **81.10**.  
- Gair, JR et al. (May 2010b). *JPCS* **228.1**. 
- Gair, J & N Yunes (Sept. 2011). *Phys. Rev. D* **84.6**.  
- Galloway, DK et al. (Sept. 2002). *ApJ* **576**.  
- Gammie, CF et al. (Feb. 2004). *ApJ* **602**.  
- Gao, L et al. (June 2007). *MNRAS* **378**.  
- García-Bellido, J & DG Figueroa (Feb. 2007). *Phys. Rev. Lett.* **98.6**, 061302.  
- García Marín, AF et al. (May 2005). *Class. Quantum Grav.* **22**.  
- Gebhardt, K et al. (Aug. 2000). *ApJ* **539**.  
- Genzel, R et al. (Oct. 2010). *Reviews of Modern Physics* **82**.  
- Ghez, AM et al. (Apr. 2003). *ApJ* **586**.  
- Ghez, AM et al. (Feb. 2005). *ApJ* **620**.  
- Ghez, AM et al. (Dec. 2008). *ApJ* **689**.  
- Giampieri, G et al. (1996). *Opt. Commun.* **123**. 
- Gillessen, S et al. (Feb. 2009). *ApJ* **692**.  

- Glampedakis, K & S Babak (June 2006). *Class. Quantum Grav.* **23** (12).
- González, JA et al. (June 2007). *Phys. Rev. Lett.* **98**.23.
- Gould, A & HW Rix (Mar. 2000). *ApJ* **532**.
- Graham, AW & LR Spitler (Aug. 2009). *MNRAS* **397**.
- Graham, AW et al. (Apr. 2011). *MNRAS* **412**.
- Greene, JE & LC Ho (Aug. 2004). *ApJ* **610**.
- Greene, JE et al. (Nov. 2008). *ApJ* **688**.
- Greif, TH et al. (Aug. 2011). *ApJ* **737**.
- Gualandris, A & D Merritt (May 2008). *ApJ* **678**.
- Guedes, J et al. (Sept. 2009). *ApJ* **702**.
- Guedes, J et al. (Mar. 2011). *ApJ* **729**.
- Gültekin, K et al. (June 2009). *ApJ* **698**.
- Guo, Q et al. (May 2011). *MNRAS* **413**.
- Gürkan, MA & C Hopman (Aug. 2007). *MNRAS* **379**.
- Gürkan, MA et al. (Apr. 2004). *ApJ* **604**.
- Gürkan, MA et al. (Mar. 2006). *ApJ* **640**.
- Gwo, DH (Sept. 1998). *Proc. SPIE*. **3435**.
- Haehnelt, MG (July 1994). *MNRAS* **269**.
- Haehnelt, MG & MJ Rees (July 1993). *MNRAS* **263**.
- Haehnelt, MG et al. (Nov. 1998). *MNRAS* **300**.
- Haiman, Z & A Loeb (Aug. 1998). *ApJ* **503**.
- Hannam, M et al. (Dec. 2007). *Phys. Rev. Lett.* **99**.24.
- Häring, N & HW Rix (Apr. 2004). *ApJ* **604**.
- Hayasaki, K & AT Okazaki (Jan. 2009). *ApJ* **691**.
- Hayasaki, K et al. (Aug. 2008). *ApJ* **682**.
- Heger, A et al. (July 2003). *ApJ* **591**.
- Heinzel, G et al. (May 2003). *Class. Quantum Grav.* **20** (10).
- Heinzel, G et al. (Mar. 2004). *Class. Quantum Grav.* **21**.
- Heinzel, G et al. (Mar. 2006). *JPCS* **32**.
- Herz, M (Sept. 2005). *Optical Engineering* **44**.
- Hogan, CJ (Feb. 1986). *MNRAS* **218**.
- (Sept. 2000). *Phys. Rev. Lett.* **85**.
- (Nov. 2006). *AIP Conf. Proc.* **873**.
- Hogan, CJ & PL Bender (Sept. 2001). *Phys. Rev. D* **64**.6.
- Holz, DE & SA Hughes (Aug. 2005). *ApJ* **629**.
- Hong, FL et al. (Sept. 1998). *Proc. SPIE*. **3477**.
- Hopkins, PF et al. (Mar. 2006). *ApJS* **163**.
- Hopkins, PF et al. (Apr. 2008). *ApJS* **175**.
- Hopkins, PF et al. (Sept. 2009). *MNRAS* **398**.
- Hopman, C (May 2009). *Class. Quantum Grav.* **26**.9.
- Hopman, C & T Alexander (July 2006a). *ApJ* **645**.
- (July 2006b). *ApJ* **645**.
- Huber, SJ & T Konstandin (Sept. 2008). *Journal of Cosmology and Astroparticle Physics* **9**.
- Hueller, M et al. (May 2005). *Class. Quantum Grav.* **22**.
- Huerta, EA & JR Gair (Apr. 2009). *Phys. Rev. D* **79**.8.
- Hughes, SA (Jan. 2003). *Annals of Physics* **303**.
- Hughes, SA & RD Blandford (Mar. 2003). *ApJ* **585**.
- Hughes, SA (2006). *AIP Conf. Series*. **873**.
- Hulse, RA & HJ Taylor (Sept. 1974). *Bulletin of the American Astronomical Society*. **6**.
- Huwylar, C et al. (Aug. 2011). *ArXiv e-prints*.
- Ivanov, PB et al. (July 1999). *MNRAS* **307**.
- Jafry, Y & TJ Sumner (1997). *Class. Quantum Grav.* **14**.6.
- Jiang, YF et al. (Aug. 2011a). *ApJ* **737**.
- Jiang, YF et al. (July 2011b). *ArXiv e-prints*.
- Johansson, PH et al. (Jan. 2009). *ApJ* **690**.
- Johnston, S et al. (Dec. 2007). *PASA* **24**.
- Jonker, PG et al. (Sept. 2010). *MNRAS* **407**.
- Jonker, PG et al. (June 2011). *ApJS* **194**.
- Kamaretsos, I et al. (July 2011). *ArXiv e-prints*.
- Kamionkowski, M et al. (Mar. 1994). *Phys. Rev. D* **49**.
- Kasliwal, MM et al. (Nov. 2010). *ApJ* **723**.
- Kesden, M et al. (Feb. 2005). *Phys. Rev. D* **71**.4, 044015.
- Kesden, M et al. (June 2010). *ApJ* **715**.
- Key, JS & NJ Cornish (Feb. 2009). *Phys. Rev. D* **79**.4.
- Khan, FM et al. (May 2011). *ApJ* **732**.
- Khlebnikov, S & I Tkachev (July 1997). *Phys. Rev. D* **56**.
- Killow, CJ et al. (2006). *AIP Conf. Series*. **873**.
- King, AR & JE Pringle (Nov. 2006). *MNRAS* **373**.
- King, AR et al. (Oct. 2005). *MNRAS* **363**.
- King, A (Oct. 2003). *ApJ* **596**.
- Klimenko, S et al. (June 2008). *Class. Quantum Grav.* **25**.11.
- Kocsis, B et al. (July 2011). *Phys. Rev. D* **84**.2.
- Komossa, S et al. (Jan. 2003). *ApJ* **582**.
- Komossa, S et al. (May 2008). *ApJ* **678**.
- Konstandin, T et al. (Oct. 2010). *Phys. Rev. D* **82**.8.
- Konstantinidis, S et al. (Aug. 2011). *ArXiv e-prints*.
- Kormendy, J & R Bender (Feb. 2009). *ApJ* **691**.
- Koushiappas, SM & AR Zentner (Mar. 2006). *ApJ* **639**.
- Koushiappas, SM et al. (Oct. 2004). *MNRAS* **354**.
- Kramer, M & N Wex (Apr. 2009). *Class. Quantum Grav.* **26**.7.
- Kramer, M et al. (Oct. 2006). *Science* **314**.
- Krolik, JH (1999). *Active galactic nuclei: from the central black hole to the galactic environment*. Princeton University Press.
- Kuo, CY et al. (Jan. 2011). *ApJ* **727**.
- LSST Science Collaborations et al. (Dec. 2009). *ArXiv e-prints*.
- Lacey, C & S Cole (June 1993). *MNRAS* **262**.
- Lamastra, A et al. (June 2010). *MNRAS* **405**.
- Lang, RN & SA Hughes (Dec. 2006). *Phys. Rev. D* **74**.12.
- Lange, R & B Smutny (Oct. 2004). *IEEE Conf. Proceedings*. **1**.
- Larson, SL et al. (Sept. 2000). *Phys. Rev. D* **62**.6.
- Lauer, TR et al. (June 2007). *ApJ* **662**.
- Leaver, EW (Dec. 1985). *Royal Society of London Proceedings Series A* **402**.
- Leonhardt, V & JB Camp (June 2006). *Applied Optics* **45**.17.
- Leonhardt, V et al. (Nov. 2006). **873**.
- Levan, AJ et al. (May 2006). *MNRAS* **368**.
- Levin, Y (Jan. 2007). *MNRAS* **374**.
- Levitani, D et al. (Oct. 2011). *ApJ* **739**.
- Li, TGF et al. (Oct. 2011). *ArXiv e-prints*.
- Lin, L et al. (Dec. 2004). *ApJ* **617**.
- Lin, L et al. (July 2008). *ApJ* **681**.
- Littenberg, TB & NJ Cornish (Nov. 2010). *Phys. Rev. D* **82**.10.
- Liu, X et al. (Aug. 2011). *ApJ* **737**, 101.
- Livas, JC et al. (Dec. 2007). *Bulletin of the American Astronomical Society*. **211**.
- Lodato, G & P Natarajan (Oct. 2006). *MNRAS* **371**.
- Lodato, G et al. (Sept. 2009). *MNRAS* **398**.
- Loeb, A (July 2007). *Phys. Rev. Lett.* **99**.4.
- Loeb, A & FA Rasio (Sept. 1994). *ApJ* **432**.
- Lorimer, DR (Nov. 2008). *Living Reviews in Relativity* **11**.
- Lousto, CO & Y Zlochower (Aug. 2011a). *ArXiv e-prints*.
- (Jan. 2011b). *Phys. Rev. D* **83**.2.
- Lukes-Gerakopoulos, G et al. (June 2010). *Phys. Rev. D* **81**.12.
- MacFadyen, AI & M Milosavljević (Jan. 2008). *ApJ* **672**.
- MacLeod, CL & CJ Hogan (Feb. 2008). *Phys. Rev. D* **77**.4.
- Madau, P & MJ Rees (Apr. 2001). *ApJ* **551**.
- Maggiore, M (2000). *Phys. Rep.* **331**.
- Maggiore, M (Oct. 2007). *Gravitational Waves: Theory and experiments*. Vol. 1. Gravitational Waves. Oxford University Press.
- Magorrian, J et al. (June 1998). *AJ* **115**.

- Makino, J & Y Funato (Feb. 2004). *ApJ* **602**.
- Maoz, E (Feb. 1998). *ApJ* **494**.
- Marconi, A & LK Hunt (May 2003). *ApJ* **589**.
- Marconi, A et al. (June 2004). *MNRAS* **351**.
- Marronetti, P et al. (Mar. 2008). *Phys. Rev. D* **77.6**.
- Marsh, TR (May 2011). *Class. Quantum Grav.* **28.9**.
- Marsh, TR & D Steeghs (Mar. 2002). *MNRAS* **331**.
- Marsh, TR et al. (May 2004). *MNRAS* **350**.
- Mathur, S & D Grupe (Nov. 2005). *ApJ* **633**.
- Mayer, L et al. (June 2007). *Science* **316**.
- McNamara, P et al. (2008). *Class. Quantum Grav.* **25.11**.
- McWilliams, ST (Apr. 2010). *Phys. Rev. Lett.* **104.14**.
- Merkowitz, SM et al. (2004). *Class. Quantum Grav.* **21.5**.
- Merkowitz, SM et al. (2005). *Class. Quantum Grav.* **22.10**.
- Merloni, A (Oct. 2004). *MNRAS* **353**.
- Merritt, D (Sept. 2006). *ApJ* **648**.
- Merritt, D & RD Ekers (Aug. 2002). *Science* **297**.
- Merritt, D & M Milosavljević (Nov. 2005). *Living Reviews in Relativity* **8**.
- Merritt, D & MY Poon (May 2004). *ApJ* **606**.
- Merritt, D et al. (Dec. 2007). *ApJ* **671**.
- Merritt, D et al. (Mar. 2009a). *ApJ* **693**.
- Merritt, D et al. (July 2009b). *ApJ* **699**.
- Merritt, D et al. (Aug. 2011). *Phys. Rev. D* **84.4**.
- Middleton, KF et al. (Dec. 2006). *Optical Engineering* **45.12**.
- Mihos, JC & L Hernquist (June 1996). *ApJ* **464**.
- Miller, MC (May 2009). *Class. Quantum Grav.* **26.9**.
- Miller, MC & EJM Colbert (Jan. 2004). *International Journal of Modern Physics D* **13**.
- Miller, MC et al. (Oct. 2005). *ApJ* **631** (2).
- Milosavljević, M & D Merritt (Dec. 2001). *ApJ* **563**.
- Milosavljević, M & ES Phinney (Apr. 2005). *ApJ* **622**.
- Miralda-Escude, J (July 1998). *ApJ* **501**.
- Miralda-Escudé, J & A Gould (Dec. 2000). *ApJ* **545**.
- Mirshakari, S et al. (Oct. 2011). *ArXiv e-prints*.
- Mishra, CK et al. (Sept. 2010). *Phys. Rev. D* **82.6**.
- Mitryk, SJ et al. (Apr. 2010). *Class. Quantum Grav.* **27.8**.
- Mo, H et al. (2010). *Galaxy Formation and Evolution*. Cambridge University Press.
- Mondin, L et al. (Nov. 2004). *Journal de Physique IV* **119**.
- Montero, PJ et al. (Aug. 2011). *ArXiv e-prints*.
- Montuori, C et al. (Mar. 2011). *MNRAS* **412**.
- Mortlock, DJ et al. (June 2011). *Nature* **474**.
- Mouawad, N et al. (Feb. 2005). *Astronomische Nachrichten* **326**.
- Mueller, G et al. (Dec. 2005). *Laser frequency stabilization for LISA*. Technical Report NASA/TM-2005-212794; Rept-2006-00387-1. Goddard Space Flight Center.
- Musha, M et al. (Sept. 2000). *Optics Communications* **183.1-4**.
- Nayak, KR & JY Vinet (Nov. 2004). *Phys. Rev. D* **70** (10).
- Nelemans, G & CA Tout (Jan. 2005). *MNRAS* **356**.
- Nelemans, G et al. (Mar. 2001). *A&A* **368**.
- Nelemans, G et al. (Mar. 2004). *MNRAS* **349**.
- Nevsky, AY et al. (June 2001). *Optics Communications* **192**.
- Notcutt, M et al. (July 2005). *Optics Letters* **30.14**.
- O'Leary, RM & A Loeb (May 2009). *MNRAS* **395**.
- Omukai, K & F Palla (June 2003). *ApJ* **589**.
- Orosz, JA (2003). *IAU Symposium*. **212**.
- Ostriker, EC (Mar. 1999). *ApJ* **513**.
- Paczynski, B (1976). *IAU Symposium*. **73**.
- Pakmor, R et al. (Jan. 2010). *Nature* **463**.
- Pan, Y et al. (June 2011). *ArXiv e-prints*.
- Pani, P & V Cardoso (Apr. 2009). *Phys. Rev. D* **79.8**, 084031.
- Pani, P et al. (Dec. 2009). *Phys. Rev. D* **80.12**.
- Pani, P et al. (May 2011). *Phys. Rev. D* **83.10**.
- Patrino, A et al. (Sept. 2011). *ArXiv e-prints*.
- Patton, DR et al. (Jan. 2002). *ApJ* **565**.
- Peng, CY (Dec. 2007). *ApJ* **671**.
- Perego, A et al. (Nov. 2009). *MNRAS* **399**.
- Perets, HB & T Alexander (Apr. 2008). *ApJ* **677**.
- Perets, HB et al. (May 2010). *Nature* **465**.
- Perets, HB et al. (Apr. 2011). *ApJ* **730**.
- Perlmutter, S & A Riess (July 1999). *AIP Conf. Series*. **478**.
- Perlmutter, S et al. (June 1999). *ApJ* **517**.
- Peters, PC (Nov. 1964). *Physical Review* **136**.
- Peterson, BM et al. (Oct. 2005). *ApJ* **632**.
- Petiteau, A et al. (May 2010). *Phys. Rev. D* **81.10**.
- Petiteau, A et al. (May 2011). *ApJ* **732**.
- Phinney, ES (2009). *Astronomy*. **2010**.
- Piro, AL (Oct. 2011). *ApJ* **740**.
- Popham, R & CF Gammie (Sept. 1998). *ApJ* **504**.
- Portegies Zwart, SF & SLW McMillan (Jan. 2000). *ApJ* **528**.
- Portegies Zwart, SF et al. (Apr. 2004). *Nature* **428**.
- Porter, EK (July 2009). *GW Notes* **1**.
- Press, WH & P Schechter (Feb. 1974). *ApJ* **187**.
- Preto, M & P Amaro-Seoane (Jan. 2010). *ApJ* **708**.
- Preto, M et al. (May 2011). *ApJ* **732**.
- Pretorius, F (Sept. 2005). *Phys. Rev. Lett.* **95.12**.
- Quinlan, GD (July 1996). *NewA* **1**.
- Racine, É et al. (Sept. 2007). *MNRAS* **380**.
- Randall, L & G Servant (May 2007). *Journal of High Energy Physics* **5**.
- Rau, A et al. (Jan. 2010). *ApJ* **708**.
- Rezzolla, L et al. (Aug. 2008a). *Phys. Rev. D* **78.4**.
- Rezzolla, L et al. (Feb. 2008b). *ApJ* **674**.
- Rhook, KJ & JSB Wyithe (Aug. 2005). *MNRAS* **361**.
- Riess, AG et al. (Sept. 1998a). *AJ* **116**.
- Riess, AG et al. (Sept. 1998b). *ApJ* **504**.
- Robertson, B et al. (Apr. 2006). *ApJ* **641**.
- Rodriguez, C et al. (July 2006). *ApJ* **646**.
- Roelofs, GHA et al. (Sept. 2006). *MNRAS* **371**.
- Roelofs, GHA et al. (Dec. 2007). *MNRAS* **382**.
- Roelofs, GHA et al. (Mar. 2010). *ApJ* **711**.
- Romano, JD & G Woan (May 2006). *Phys. Rev. D* **73** (10).
- Roth, A & R Werninghaus (2006).
- Ruiter, AJ et al. (Mar. 2009). *ApJ* **693**.
- Ruiter, AJ et al. (July 2010). *ApJ* **717**.
- Ryan, FD (Nov. 1995). *Phys. Rev. D* **52**.
- Salpeter, EE (Aug. 1964). *ApJ* **140**.
- Santamaría, L et al. (Sept. 2010). *Phys. Rev. D* **82.6**.
- Scheel, MA et al. (Jan. 2009). *Phys. Rev. D* **79.2**.
- Schilling, R (June 1997). *Class. Quantum Grav.* **14** (6).
- Schnittman, JD (Oct. 2007). *ApJ* **667**.
- (May 2011). *Class. Quantum Grav.* **28.9**.
- Schnittman, JD & A Buonanno (June 2007). *ApJ* **662**.
- Schödel, R et al. (Oct. 2003). *ApJ* **596**.
- Schulte, M et al. (Nov. 2006). *AIP Conf. Series*. **873**.
- Schutz, BF (Sept. 1986). *Nature* **323**.
- Sesana, A (Aug. 2010). *ApJ* **719**.
- Sesana, A et al. (Aug. 2004). *ApJ* **611**.
- (Apr. 2005). *ApJ* **623** (1).
- Sesana, A et al. (Nov. 2006). *ApJ* **651**.
- (May 2007a). *ApJ* **660**.
- Sesana, A et al. (June 2007b). *MNRAS* **377**.
- Sesana, A et al. (Oct. 2008a). *ApJ* **686**.
- Sesana, A et al. (Oct. 2008b). *MNRAS* **390**.

- Sesana, A et al. (Apr. 2009). MNRAS **394**.
- Sesana, A et al. (Feb. 2011). Phys. Rev. D **83**.4.
- Seth, A et al. (May 2008). ApJ **678**.
- Shaddock, DA et al. (Sept. 2003). Phys. Rev. D **68** (6).
- Shaddock, DA et al. (Oct. 2004). Phys. Rev. D **70** (8).
- Shaddock, D et al. (Nov. 2006). AIP Conf. Series. **873**.
- Shakura, NI & RA Sunyaev (1973). A&A **24**.
- Shapiro, SL & SA Teukolsky (June 1986). *Black Holes, White Dwarfs and Neutron Stars: The Physics of Compact Objects*. Wiley-VCH.
- Shaul, DNA et al. (2004). Class. Quantum Grav. **21**.5.
- Shaul, DNA et al. (2005). Class. Quantum Grav. **22**.10.
- Sheard, BS et al. (Dec. 2003). Physics Letters A **320**.
- Shen, Y & A Loeb (Dec. 2010). ApJ **725**.
- Shibata, M & SL Shapiro (June 2002). ApJ **572**.
- Shields, GA et al. (2009). ApJ **707**.2.
- Siemens, X et al. (May 2006). Phys. Rev. D **73**.10.
- Sigurdsson, S & MJ Rees (Jan. 1997). MNRAS **284**.
- Silk, J & MJ Rees (Mar. 1998). A&A **331**.
- Silvestri, Z et al. (2003). Metrologia **40**.4.
- Smith, JR et al. (2003). Class. Quantum Grav. **20**.23.
- Sodnik, Z et al. (2006). IEEE Conf. Proceedings.
- Soltan, A (July 1982). MNRAS **200**.
- Somerville, RS et al. (Dec. 2008). MNRAS **391**.
- Sopuerta, CF (Sept. 2010). GW Notes **4**.
- Sopuerta, CF & N Yunes (Sept. 2009). Phys. Rev. D **80**.6.
- Springel, V et al. (June 2005). Nature **435**.
- Stacy, A et al. (Mar. 2010). MNRAS **403**.
- Stanga, R et al. (Nov. 2006). AIP Conf. Series. **873**.
- Stroeer, A & G Nelemans (Nov. 2009). MNRAS **400**.
- Stroeer, A & A Vecchio (Oct. 2006). Class. Quantum Grav. **23**.

- Stroeer, A & J Veitch (Sept. 2009). Phys. Rev. D **80**.6.
- Stroeer, A et al. (Sept. 2006). AIP Conf. Series. **873**.
- Stroeer, A et al. (Sept. 2011). ArXiv e-prints.
- Sullivan, M et al. (May 2011). ApJ **732**.
- Sumner, T et al. (2004). Class. Quantum Grav. **21**.5.
- Sun, KX et al. (Apr. 2006). Class. Quantum Grav. **23**.
- Sylvestre, J (Nov. 2004). Phys. Rev. D **70**, 102002 (10).
- Taam, RE & PM Ricker (Mar. 2010). NewAR **54**.
- Taam, RE & EL Sandquist (2000). ARA&A **38**.
- Tegmark, M et al. (Jan. 1997). ApJ **474**.
- Teukolsky, SA (Oct. 1973). ApJ **185**.
- Thorne, KS (July 1974). ApJ **191**.
- (1987). “Gravitational radiation.” *Three Hundred Years of Gravitation*.
- Thorpe, JI et al. (2006). AIP Conf. Series. **873**.
- Thorpe, JI et al. (Sept. 2008). Optics Express **16**.
- Tinto, M & JW Armstrong (May 1999). Phys. Rev. D **59**.10.
- Tinto, M & SL Larson (May 2005). Class. Quantum Grav. **22** (10).
- Tinto, M et al. (Apr. 2002). Phys. Rev. D **65** (8).
- Touboul, P et al. (1996). Class. Quantum Grav. **13**.11A.
- Tremaine, S et al. (Aug. 2002). ApJ **574**.
- Treu, T et al. (Sept. 2007). ApJ **667**.
- Trias, M et al. (Sept. 2008). Class. Quantum Grav. **25**.18.
- Tsalmantza, P et al. (Sept. 2011). ApJ **738**.
- Turk, MJ et al. (July 2009). Science **325**.
- Turneure, JP et al. (Oct. 2003). Advances in Space Research **32**.7.

- Valsecchi, F et al. (May 2011). ArXiv e-prints. 
- Valtonen, MJ et al. (Apr. 2008). Nature **452**. 
- Vigeland, SJ & SA Hughes (Jan. 2010). Phys. Rev. D **81**.2. 
- Vigeland, S et al. (May 2011). Phys. Rev. D **83**.10. 
- Volonteri, M (July 2010). A&A Rev. **18**. 
- Volonteri, M & MC Begelman (Dec. 2010). MNRAS **409**. 
- Volonteri, M & P Natarajan (Dec. 2009). MNRAS **400**. 
- Volonteri, M et al. (Jan. 2003). ApJ **582**. 
- Volonteri, M et al. (Oct. 2007). ApJ **667**. 
- Volonteri, M et al. (Jan. 2008). MNRAS **383**. 
- Volonteri, M et al. (Sept. 2009). ApJ **703**. 
- Volonteri, M et al. (June 2010). MNRAS **404**. 
- Volonteri, M (2006). AIP Conf. Series. **873**. 
- Waldman, R et al. (Sept. 2011). ApJ **738**. 
- Wand, V et al. (Apr. 2006). Class. Quantum Grav. **23**. 
- Wang, Y et al. (June 2002). ApJ **572**. 
- Warburton, N et al. (Nov. 2011). ArXiv e-prints. 
- Wass, PJ et al. (Nov. 2006). AIP Conf. Series. **873**. 
- Watts, AL et al. (Sept. 2008). MNRAS **389**. 
- Webbink, RF (Feb. 1984). ApJ **277**. 
- (Dec. 2010). AIP Conf. Series **1314**. 
- Weber, WJ et al. (2002). Class. Quantum Grav. **19**.7. 
- Weber, W et al. (2007). Advances in Space Research **39**.2. 
- Wehner, EH & WE Harris (June 2006). ApJ **644**. 
- Weisberg, JM & JH Taylor (July 2005). Astronomical Society of the Pacific Conference Series. **328**. 
- Weßels, P et al. (Apr. 2002). Optics Communications **205**.1-3. 
- White, SDM & MJ Rees (May 1978). MNRAS **183**. 
- Wijnands, R (Nov. 2010). Highlights of Astronomy **15**. 
- Will, CM (Mar. 2006). Living Reviews in Relativity **9**. 
- Willems, B et al. (Apr. 2010). ApJ **713**. 
- Witten, E (July 1984). Phys. Rev. D **30**. 
- Woo, JH et al. (July 2008). ApJ **681**. 
- Wyithe, JSB & A Loeb (Dec. 2002). ApJ **581**. 
- Wyithe, JSB & A Loeb (June 2003). ApJ **590** (2). 
- Wyithe, JSB & A Loeb (Oct. 2003). ApJ **595**. 
- Xiao, T et al. (Sept. 2011). ApJ **739**. 
- Xu, CK et al. (Sept. 2011). ArXiv e-prints. 
- Yagi, K & T Tanaka (Mar. 2010). Phys. Rev. D **81**.6. 
- Yagi, K et al. (Apr. 2011). Phys. Rev. D **83**.8. 
- Yoshida, N et al. (Nov. 2006). ApJ **652**. 
- Yoshida, N et al. (Aug. 2008). Science **321**. 
- Yoshida, S et al. (Nov. 1994). Phys. Rev. D **50**. 
- Yu, S & CS Jeffery (Oct. 2010). A&A **521**. 
- Yunes, N & F Pretorius (Dec. 2009). Phys. Rev. D **80**.12. 
- Yunes, N et al. (Mar. 2010). Phys. Rev. D **81**.6. 
- Yunes, N et al. (Feb. 2011). Phys. Rev. D **83**.4. 
- Yungelson, LR et al. (June 2002). A&A **388**. 
- Zawischa, I et al. (Apr. 1999). Optics Letters **24**.7. 
- Zel’dovich, YB & ID Novikov (Oct. 1964). Soviet Physics Doklady **9**. 
- de Ravel, L et al. (May 2009). A&A **498**. 
- de Vine, G et al. (May 2010). Phys. Rev. Lett. **104**.21. 
- van der Marel, RP et al. (May 1994). MNRAS **268**. 

Project Documents

- ESA-SCI(2000) 11 (2000). *System and Technology Study Report*. Tech. rep.
- S2-EST-RP-1087. *The LISA Pathfinder Mission*. Tech. rep.

Index

- acceleration noise
 - conversion to displacement noise, 77
 - due to cross-coupling, 92
 - due to gas damping, 92
 - due to micro-newton thrusters noise, 92
 - due to temperature fluctuations, 92
 - due to thermal gradients, 92
 - model verification by *LISA Pathfinder* (LPF), 79
 - radiation pressure, 98
 - reddening, 76
 - relaxing at higher frequencies, 77
- accretion models
 - for black holes, 31
- acquisition, 110, 117
- adhesion, 94
 - break, 94
- AGN
 - binary
 - 0402+379, 28
 - OJ 287, 28
 - recoiling, 29
 - SDSS J092712.65+294344.0, 29
- AM CVn, 18, 21
- antenna
 - high-gain, 113
 - omnidirectional, 114
 - transfer function, 74
- apparent horizon size, 56
- archive phase, 116
- battery, 113
- Big Bang, 6
- binary
 - compact, *see* compact binaries
- black hole
 - accretion disk warping, 31
 - accretion model
 - chaotic, 31
 - coherent, 31
 - at the Galactic centre, 20
 - binary
 - signal, 67
 - template, 67
 - centre of elliptical galaxies, 29
 - centre of the Milky Way, 26
 - co-evolution with galaxies, 24
 - coalescence
 - evidence, 29
 - coalescence events in star clusters, 46–47
 - coalescence phase
 - inspiral, 33
 - merger, 33
 - ring-down, 33
 - coalescing in merging galaxies, 26–28
 - cohabiting nuclear star clusters, 26
 - connection to evolving background baryonic density field, 26
 - cosmic X-ray background, 24
 - cosmology, 24–26
 - EMRI, 53
 - evolving spin via accretion, 31
 - evolving spin via coalescence, 30–31
 - geodesy, *see* holidesy
 - gravitational influence radius, 23
 - growth via gas accretion, 24
 - Eddington Luminosity as a limit, 24
 - timescale, 24
 - hardening of the orbit, 28
 - in dwarf galaxies without a bulge, 26
 - in low-mass spiral galaxies, 26
 - inspiral, 51
 - intermediate mass, 47
 - detection rate, 47
 - formation, 47
 - Kerr, 52, 53
 - large seeds, 30
 - measuring mass with EMRI, 42–43
 - merger, 9, 51
 - changing spin direction, 29
 - final mass, 52
 - final spin, 52
 - inspiral, 50
 - ringdown, 50
 - merger in numerical simulations, 27
 - merger rate, 32
 - inferred from optical observations, 32
 - predicted by Monte Carlo merger trees, 32
 - merger scenarios, 32
 - multipolar structure, 53
 - NGO observation, 32–37
 - NGO sensitivity, 26
 - no hair, *see* no hair theorem
 - observational evidence, 23–24
 - phases during merger
 - coalescing phase, 68
 - inspiralling phase, 68
 - ringdown phase, 68
 - phases during mergers
 - binary phase, 28
 - gravitational wave phase, 28
 - pairing phase, 28
 - recoiling phase, 28, 31
 - powering QSO, 22
 - probing the environment with EMRI, 41
 - retention in galaxies, 31
 - ringdown, 52
 - spectroscopy, 52
 - seeds, 30
 - SgrA*, 40
 - size compared to galaxy, 23
 - space density, 24
 - spin alignment due to viscous accretion, 31
 - spin determine radiative efficiency, 31
 - spun down by accretion, 31
 - spun up by accretion, 31
 - stellar mass, 22
 - supermassive, 22
 - timescale for coalescence
 - gravitational waves only, 27
- brane, 58
- caging mechanism, 94
 - launch lock, 94
 - overcoming adhesion, 95
 - positioning actuator, 94
 - pushing force, 94
 - release mechanism, 94
- calibration
 - far field characterisation, 118
 - ground communication, 118
 - instrument noise, 118
 - phase-centre characterisation, 118
- calibration phase, 116
- capacitive readout, 87
- capacitive sensing
 - sensitivity, 94
- charge control system, 95–96
 - mercury discharge lamps, 96
 - polarity, 96
- chirp mass, 17, 67
- commissioning, 110, 116
 - acquisition, 117
 - DFACS, 117
 - ground communication, 118
 - Laser, 117
 - measurement system, 118
- commissioning phase, 116
- communication
 - during operational phase, 113
- communications planning, 118
- compact binaries, 12–21
 - as instrument verification, 12–13
 - at the Galactic centre, 20
 - black hole, 19–20
 - common-envelope phase, 14
 - detached, 18
 - evolution of period, 18
 - distances, 20
 - double white dwarfs, 12, 18–19
 - expected number of detections, 12
 - frequency and phase evolution, 12
 - gravitational wave foreground, 15–16
 - mass transfer, 17
 - stability, 17–18
 - neutron stars, 19–20

- new detections, 13–15
- number of known systems today, 12
- orbital inclination, 21
- resolved, 14
- Roche lobe, 18
- signal, 67
- studying galactic structure, 20–21
- supernovae Ia progenitor, 12
- template, 67
- tidal coupling
 - efficiency, 18
- tidal heating, 17
- tidal interaction, 17–18
 - frequency evolution, 17
- X-ray, 18, 19
- constellation commissioning, 110
- cosmic censorship conjecture, 30
- Cosmic Vision, 1
 - scientific questions, 22, 40, 48, 56
- cosmology
 - inflation, 57
 - Standard Model, 57
 - supersymmetry, 57
- cruise, 110
- cruise phase, 116
- dark energy, 58
- data analysis, 66–70, 124
 - algorithm
 - MultiNest, 68
 - nested sampling, 68
 - MLDC, 68–70
 - Monte-Carlo Markov chain search, *see* Monte-Carlo Markov chain
 - simulated annealing, 68
 - time-frequency search, 68
- data archive, 119, 120, 122
- data collection, 118
- data formats, 122
- data processing, 120
- data processing centre, 120
- data product, *see* science product
- data rights, 124
 - proprietary period, 124
 - exemption, 124
- data validity
 - monitoring, 118
- decommissioning, 110, 118
- detection algorithms
 - for known signals, 67
 - for unmodelled signals, 67
- detection rate
 - black holes, 9
- detector strain response, 74
- differential wavefront sensing, 87
- displacement noise
 - amplitude spectral density, 76, 77
 - conversion from acceleration noise, 77
 - from residual acceleration, 76
 - from the DRS, 76
 - from the IMS, 77
 - relaxing at lower frequencies, 77
- disturbance reduction system
 - heritage, 92
- dwarf galaxy
 - NGC 4359, 26
- Eddington limit
 - for a neutron star, 18
- Eddington Luminosity L_E , 24
- electrode housing, 94
 - electrodes
 - material, 94
 - gap, 94
 - material, 94
- environmental requirements, 92
- extreme mass ratio inspiral, 40–47
 - analytic kludge, 43, 68
 - as a probe of galactic dynamics, 41–42
 - as a probe of masses of black holes, 42–43
 - detecting with NGO, 43–45
 - determining mass from gravitational waves, 41
 - event rates, 45–46
 - in galactic nuclei, 40–41
 - modelling black holes, 46
 - phenomenological waveforms, 43
 - precession of orbital plane, 53
 - precession of periapsis, 53
 - probes of Kerr spacetime, 52–54
 - probing dense stellar systems, 41
 - probing the environment of a black hole, 41
 - production mechanisms, 41
 - imprint on eccentricity and inclination, 41
 - star formation in accretion disks, 41
 - tidal disruption of binaries, 41
 - two-body scattering, 41
 - relativistic orbits, 43
 - signal, 68
 - stellar mass black holes, 41
 - template, 68
 - test particle scenario, 41
- false vacuum, 57
- flight operations, 119
 - ground stations, 119
 - mission control, 119
 - mission operations planning, 119
 - orbit and attitude control, 119
- frequency stabilisation
 - arm-locking, 100
 - cavity resonance, 99
 - heterodyne interferometry, 100
 - molecular absorption line, 100
 - prestabilisation, 99
 - time-delay interferometry, 100
- Gaia, 12
- Galactic centre, 40
 - black hole, 20
 - cusp of stellar black holes, 42
 - imprint on stellar dynamics, 42
- Galactic components
 - bar, 20
 - bulge, 13, 20
 - velocity dispersion σ , 23
- disc, 20
 - thick, 16
 - thin, 16
- halo, 16, 20
- galaxy
 - Andromeda, 28, 40
 - M31, 28
 - major merger, 26
 - morphology after merger, 26
- gamma-ray burst, 18
- General Relativity, 5
 - strong-field, 49, 51
- test
 - EMRI, 10, 49, 53–54
 - gravitational wave polarisation, 7
 - graviton mass, 55
 - merger events, 49, 50
 - solar system, 48
 - weak-field regime, 48
- geodesic constants of integration, 53
- globular clusters, 15
 - AM CVn systems, 21
 - formation and evolution of binaries, 21
 - metal-poor population, 21
- goal vs. requirement, 74
- GP-B mission, 86, 96
- gravitational reference sensor, 92–96
 - capacitive readout system, 92
 - mounting, 90
 - non-sensitive degrees of freedom, 90
 - sensitive axis, 90
 - test mass interferometer, 92
- gravitational waves
 - anisotropic emission, 31
 - as probes for extreme conditions, 6
 - determining EMRI parameters, 41
 - foreground, 12, 15–16, 20
 - modulation, 16
 - spectral shape, 16
 - from EMRI
 - information content, 41
 - from black holes, 9
 - from capture events, 10
 - from compact binaries, 10
 - from cosmic strings, 56
 - from early universe, 11, 56
 - from EMRI, 10
 - from first-order phase transition, 57
 - from massive black hole mergers, 32–37
 - from strings, 59
 - from superstrings, 11
 - from verification binaries, 10
- generation, 7
- information content, 35
- interferometry, 7
- mass quadrupole, 7
- measurement principle, 7
- oscillations of spacetime, 6
- polarisation, 7
- primordial, 59
- propagation speed, 7
- property, 6
- radiated power, 6

- recoil, 31
- source distribution
 - halo, 20
- stochastic background, 56, 58
- strain, 8
- tidal action, 7
- transversal, 7
- waveform
 - for EMRI, 43
 - for merger and ring-down, 33
 - PhenomC, 34
 - phenomenological, 33
- wavelength, 7
- graviton
 - Compton wavelength, 55
 - mass, 55
 - Solar System bounds, 55
- gravity
 - Einstein-dilaton-Gauss-Bonnet, 52
- gravity gradient
 - compensation, 92
- ground station
 - Cerberos, 113
 - New Norcia, 113
- ground segment, 119
- ground station
 - nominal, 113
- ground-based detectors
 - data analysis heritage, 124
 - LIGO, *see* LIGO
 - Virgo, *see* Virgo
- heterodyne interferometry, 87
- holiodesy, 53
- housekeeping data
 - payload, 115
 - science, 115
- Hubble length, 58
- Hulse-Taylor, *see* pulsar, PSR1913+16
- hydroxy catalysis bonding, 86
- inflation, 59
- inflaton
 - decay, 59
- instrument noise
 - allocation, 76
 - budget, 76
 - margin, 76
- instrument noise model, 74
- instrument operations team, 120
- instrument sensitivity function, 74
 - high-frequency approximation, 76
 - inverse of transfer function, 74
 - normalisation, 75
- ISM
 - validation, 77
- Keck telescope, 13
- Kerr black hole
 - event horizon, 23
- laser
 - fibre amplifier, 98
 - frequency noise
 - free-running, 99
 - frequency stabilisation, 99, *see* frequency stabilisation
 - low-power master oscillator, 98
 - neodymium YAG, 98
 - power stability, 98
 - pump diodes
 - amplifier, 98
 - low-power seed, 98
- launch and early operations, 110
- launch mass, 113
- launch phase, 116
- launcher
 - baseline, 113
 - mass capability, 113
 - separation, 110
- Lense-Thirring precession
 - in a viscous accretion disc, 31
- LIGO, 7, 49, 50
 - advanced, 19, 49
- luminosity distance, 9, 67, 71
- M - σ relation, 24
- magnetar, 18
- manoeuvre
 - design and execution, 117
 - inclination changing, 110
- Markov-chain Monte Carlo, 68
 - parallel tempered, 68
 - reversible jump, 68
- mass imbalance
 - compensation, 92
- massive star formation, 30
- matched filtering, 67
- MAXI, 13
- mercury discharge lamps, 96
- Michelson interferometer, 7
- micro-newton propulsion system, 90
- mission operations elements, 119–122
- mission phases, 116–119
- MLDC, 68–70
 - heritage, 124
- N-Fire, 98
- neutron star, 18
 - compact binaries, 19
- NGC 4359, 26
- NGO
 - all-sky detector, 8
 - angular resolution, 15
 - antenna pattern, 8, 16
 - census of black hole population, 34
 - detecting EMRI, 43–45
 - differences to electro-magnetic observatories, 8–9
 - directional sensitivity, 21
 - displacement sensitivity, 8
 - distance measurement, 65
 - drag-free operation, 65
 - dynamical range, 8
 - evolution of constellation, 63
 - formation, 63
 - formation flying, 63, *see* formation flying
 - free fall, 63
 - frequency range, 8
 - ground segment, 115
 - high SNR instrument, 34
 - implementation, 8
 - limited by astrophysical sources, 36
 - measurement arm, 63
 - measurement concept, 7
 - measuring chirp mass, 19
 - measuring coalescence time, 19
 - mission concept, 71
 - orbits, 63
 - without station-keeping, 63
 - parameter estimation
 - for EMRI, 45
 - for black hole mergers, 34–39
 - partition of measurement, 66
 - physical parameters of the source, 35
 - residual acceleration, 65
 - science data stream, 8
 - science objectives, 12, 22, 40, 48, 56
 - science requirements, 71
 - sensitivity for black holes, 26
 - signal-to-noise ratio, 9
 - sources, 9
 - MBH, 9
 - black hole binaries, 19
 - black holes, 22–39
 - compact binaries, 10, 12–21
 - EMRI, 10
 - extreme mass ratio inspiral, 40–47
 - intermediate mass black hole, 47
 - massive black hole mergers, 32–37
 - MBH, 50
 - neutron star binaries, 19
 - ultra-compact X-ray binaries, 18
 - verification binaries, 10, 12, 13
 - spacecraft Doppler tracking, 8
 - station keeping, 63
 - strain sensitivity, 8
 - structure formation
 - model selection, 37–39
 - transfer function, 74
 - transponder mode, 65
- no-hair theorem, 30, 50, 52, 53
 - testing with QNM, 52
- noise
 - gravity-gradient, 8
 - seismic, 8
- noise analysis
 - preliminary, 118
- noise model
 - validation, 78
- numerical relativity
 - predictions for merger and ringdown, 51
 - waveforms for ringdown, 52
- observation requirement, 77
- open source, 122
- operations, 110
- operations orbit delivery, 117
- optical assembly
 - gravitational reference sensor, *see* gravitational reference sensor
 - optical bench, *see* optical bench

- telescope, *see* telescope
- optical bench, 84
 - additional half-wave plate, 87
 - construction technique, 86
 - differences to LPF, 86
 - interferometer, 87
 - optical truss, 87
 - point-ahead angle mechanism, 87
 - reference, 87
 - science, 87
 - test mass, 87
- material, *see* Zerodur
- mirrors, 86
- non-planar beam path, 84
- polarisation, 87
- polarising components, 86
- requirement, 84
- size, 86
- optical system
 - optical assembly, 84
- orbits, 111
 - eccentricity, 111
 - inclination, 111
 - influence of Earth, 111
 - selection, 111
- Pan-Starrs, 13
- patch field effect, 93
 - measuring, 93
 - reduction, 94
 - suppression, 93
- payload
 - requirement, 83
- payload housekeeping data, 115
- payload subsystem
 - autonomy, 84
 - electromagnetic, 84
 - gravitational, 84
 - laser metrology system, 83
 - mechanical, 83
 - propulsion system, 83
 - structural, 83
 - test mass control, 84
 - thermal control, 83
- perturbation theory, 52
- phase measurement
 - system level demonstration, 79
- phase transition
 - first-order, 57
- Planck scale, 59
- point-ahead angle, 88
- polarisation encoding, 98
- polarisation multiplexing, 87
- post-operational phase, 116
- posterior PDF, 67
- proof mass, *see* test mass
- pulsar
 - binary, 48
 - orbital gravitational fields, 48
 - double, 48
 - Hulse-Taylor, *see* pulsar, PSR1913+16
 - millisecond radio
 - as descendants of compact binaries, 19
 - millisecond X-ray, 19
 - PSR 1913+16, 7, 48, 49
 - PSR J0737-3039, 48
 - radio, 18
- QSO
 - housing black holes, 23
- QSO
 - powered by black holes, 22
- quantum vacuum fluctuation
 - amplification of, 59
- quasar
 - ULAS J1120+0641, 26
- Roche lobe, 18
- RXTE, 13
- scalar-tensor theories, 54
- science housekeeping data, 115
- science instrument
 - basic function, 65
- science investigation, 71
- science objectives, 71
- science observation, 71
- science operations centre, 119–120
- science operations phase, 116
- science planning, 120
- science product, 115–116
 - archiving, *see* data archive
 - consolidation, 115
 - generation, 118, 119
 - Level 0, 115
 - Level 1, 115
 - Level 2, 115
 - Level 3, 115
- science requirements, 71
- self-gravity analyses, 92
- separation system, 109
- SgrA*
 - black hole, 40
 - radio source, 40
 - stars around compact object, 40
- Shapiro delay, 48
- shot-noise, 77
- Signal to noise ratio
 - effective, 67
 - true, 67
- simulations
 - Millennium Run, 32
 - N-body, 32
- single-link position uncertainty, 74
- solar array, 113
- Space Interferometry Mission, 100
- spacecraft
 - ephemerides, 67
 - health monitoring, 116
 - magnetic cleanliness, 92
- spacecraft architecture, 90
 - magnetic cleanliness, 90
 - mass distribution, 90
 - thermal balance, 90
- spectral density
 - amplitude, 9
 - power, 9
 - units, 9
- Standard Model
 - fields, 58
 - particles, 58
- star
 - neutron, *see* neutron star
 - R Corona Borealis, 18
 - subdwarf B star, 18
- stars
 - population II, 30
 - population III, 30
- string
 - tension, 59
- string theory, 56
- supernovae
 - progenitor, 12
 - type Ia, 12, 14–15
- superstrings, 11
- survey
 - COMBO, 32
 - COSMOS, 32
 - DEEP2, 32
 - EGAPS, 13
 - European Galactic Plane Surveys, 13
 - OmegaWhite, 13
 - Palomar Transient Factory, 13
 - Pan-Starrs, 13
 - PTF, 13
 - RATS, 13
 - SDSS, 13, 28
 - Sloan Digital Sky Survey, 13
- symmetric mass ratio, 51, 55
- telescope
 - aperture, 96
 - exit pupil, 97
 - magnification, 97
 - off-axis, 96
 - wavefront quality, 97
- temperature fluctuations, 92
- Terascale, 56, 58, 59
- TerraSAR-X, 98
- test mass
 - actuation
 - cross-coupling, 92
 - capacitive sensing, *see* capacitive sensing
 - charging, 95
 - dimension, 93
 - discharging, 96
 - electrostatic coupling, 92
 - free fall, 90
 - forcing, 92
 - magnetic susceptibility, 92, 93
 - residual, 93
 - mass, 93
 - material, 93
 - surface, 94
- Teukolsky
 - equation, 44
 - horizon, 45
 - waveform, 45
- theory of everything
 - string theory, 59
- time-delay interferometry, 100
 - algebraic approach, 101

- first generation, 101
- frequency domain, 101
- second generation, 101
- time domain, 101
- transfer phase, 110
- transient events
 - announcement, 118
 - ULAS J1120+0641, 26
 - user support, 120
- vacuum
 - false, 57
- verification binaries, 13
 - RX J0806.3+1527, *see* HM Cnc
- Virgo, 7, 19, 49, 50
- Zerodur, 86
 - CTE, 86